Electrical and Electrochemical Properties of Diamond and Graphene Interfaces

Der Naturwissenschaftlichen Fakultät
der Friedrich-Alexander-Universität Erlangen-Nürnberg
zur
Erlangung des Doktorgrades

vorgelegt von
Wenying Zhang
aus Foshan, China

Als Dissertation genehmigt von der
Naturwissenschaftlichen Fakultät der Universität Erlangen-Nürnberg

Tag der mündlichen Prüfung:	11, 11, 2010
Vorsitzender der Promotionskommission:	Prof. Dr. Rainer Fink
Erstberichterstatter:	Prof. Dr. Jürgen Ristein
Zweitberichterstatter:	Prof. Dr. Patrik Schmuki

Content

Summary

Diamond and graphene are at date the two most promising carbon allotropes for electronic devices. In this work the electronic characteristics of their surfaces in contact with gaseous and liquid electrolyte are investigated. These surfaces constitute the functional interfaces for a number of chemical sensing devices based on diamond and graphene. A number of novel phenomena for these interfaces are observed and quantified in detail:

(i) Both carbon surfaces are susceptible for surface transfer doping. This is a mechanism by which the dopant, without entering the semiconductor matrix, exchanges charge with the semiconductor across the semiconductor-dopant interface. The surface dopant can be less or more complex, from isolated molecules to thin solid layers up to electrochemical phases with various sorts of solvated ionic species. Under atmospheric conditions, p-type surface conductivity is developed on hydrogen-terminated diamond surfaces (C:H) by electrochemical reactions with the red-ox couples in an absorbed water layer. This electrochemical surface transfer doping process takes place in graphene as well. On varying the pH value of humid atmosphere, in-situ Hall effect measurements show that the areal concentration of charge carriers and their mobility of C:H and graphene can be controlled efficiently: acidic conditions reduce the electron concentration of n-type epitaxial graphene on silicon carbide, while they lead to an increase of the hole concentration of p-type C:H at the surface. Alkaline atmosphere leads to opposite results on both surfaces.

(ii) For C:H the electrochemical surface transfer doping mechanism can as well be witnessed when the surface is brought in contact with (liquid) aqueous electrolyte. Simultaneous charge equilibration with the intrinsic hydrogen (H_2/H_3O^+) and oxygen (O_2/OH^-) red-ox couples of water establishes a pH dependent mixed (or corrosion) potential of the surface that is investigated by open circuit voltage measurements and quasi-static I-V characterization of the two surfaces when operated as electrochemical electrode.

(iii) Finally, two types of novel field effect transistor (FET) are produced: the metal semiconductor field effect transistor (MESFET) on C:H and the solution gated field effect transistors (SGFET) on both C:H and graphene. The study of the C:H based MESFET shows that, in contrast to the current models proposed in literature, leaking currents from

gate to source are observed that are controlled by the gate length rather than a hypothetical “separation layer” between the metal gate and semiconductor. When the gate length is large, the device behaves like a back-to-back Schottky diode; when it is small enough, in fact a field effect output characteristic is observed. The systematic transition from the one to the other device concept is demonstrated in this work proving that the C:H MESFET operates in deed as a junction field effect device.

The SGFETs based on C:H and graphene both work properly without an intentional insulator. The transfer characteristics of both devices show amazingly the same pH dependent shift of 19 ±1 mV/pH. The working principle of the SGFET is based on the fact that the surface potential of the carbon surface is strictly related to the areal density of mobile charge carriers. The concentration of ions adsorbed at the surface modifies the surface potential and thus the conductivity of the device channel which can be compensated by a corresponding change of the gate voltage. This mechanism renders the device an ion sensitive field effect transistor (ISFET). From a comprehensive analysis of these relations we derive expressions for the transfer characteristics of both the diamond and the graphene SGFET that faithfully describe the experiment. From corresponding fits to our data, characteristic parameters of the carbon surfaces are determined.

Zusammenfassung

Diamant und Graphene sind derzeit die wohl vielversprechendsten Kohlenstoff-Allotrope für elektronische Anwendungen. In dieser Arbeit wird die elektronische Charakteristik ihrer Oberflächen in Kontakt mit gasförmigen und flüssigen Elektrolyten untersucht. Diese Oberflächen bilden die funktionalen Grenzflächen für eine Reihe von chemischen Sensoren auf der Basis von Diamant und Graphen. Einige neuartige Phänomene werden für die Grenzflächen beobachtet und im Detail quantifiziert:

(i) Beide Oberflächen zeigen Oberflächen-Transferdotierung. Das ist ein Mechanismus, bei dem Dotanten, ohne in das Wirtsgitter eines Halbleiters einzudringen, Ladung mit dem Halbleiter über die Oberfläche hinweg austauschen. Der Oberflächen-Dotant kann dabei mehr oder weniger komplex aufgebaut sein, von isolierten Molekülen über dünne Festkörperschichten bis hin zu elektrochemischen Phasen mit verschiedensten Arten solvatisierter Ionen. Unter atmosphärischen Bedingungen entwickelt sich auf wasserstoff-terminierten Diamantoberflächen eine p-artige Oberflächenleitfähigkeit durch elektrochemische Reaktionen mit Red-Ox-Paaren in einer adsorbierten Wasserschicht. Diese elektrochemische Oberflächen-Transferdotierung findet auch bei Graphen statt. Wird der pH-Wert einer feuchten Atmosphäre verändert, zeigen in-situ Messungen des Hall-Effekts, dass die flächenbezogene Dichte und die Mobilität der Ladungsträger in C:H und Graphen effizient kontrolliert werden kann: saure Bedingungen verringern die Elektronenkonzentration in epitaktisch auf Siliziumkarbid gewachsenem Graphen, während sie zu einem Anstieg der Löcherkonzentration für p-artige C:H-Oberflächen führen. Alkalische Bedingungen führen auf beiden Oberflächen zu gegenteiligen Ergebnissen.

(ii) Für C:H kann eine elektrochemische Oberflächen-Transferdotierung auch beobachten werden, wenn die Oberfläche in Kontakt mit einem (flüssigen) wässrigen Elektrolyten gebracht wird. Die gleichzeitige Einstellung eines Ladungsgleichgewichts mit den intrinsischen Wasserstoff (H_2/H_3O^+) und Sauerstoff (O_2/OH^-) Red-Ox-Paaren des Wassers führt zu einem so genannten gemischten (oder Korrosions-) Potential für die Oberfläche, welches durch die Messung von offenen Klemmspannungen und quasistatischen Strom-Spannungskurven untersucht wird. Die C:H-Oberfläche wird in diesen Experimenten als Arbeitselektrode in einem galvanischen Schaltkreis eingesetzt.

(iii) Schließlich werden zwei Arten von neuartigen Feldeffekt-Transistoren (FET)

hergestellt: ein Metall-Halbleiter-FET (MESFET) auf C:H und ein elektrolyt-gesteuerter FET (SGFET) sowohl auf C:H als auch auf Graphen. Das Studium des C:H-basierten MESFET zeigt, dass, im Gegensatz zu den aktuell in der Literatur vorgeschlagenen Modellen, signifikante Leckströme zwischen Quell- und Steuerelektrode beobachtet werden, die von der Ausdehnung der Steuerelektrode und nicht von einer hypothetischen Trennschicht zwischen dem Metall der Steuerelektrode und dem Halbleiter bestimmt werden. Bei großer Steuerelektrode verhält sich das Bauelement wie zwei gegeneinander geschaltete Schottky-Dioden; bei kleiner Steuerelektrode wird in der Tat eine Feldeffekt-Ausgangscharakteristik beobachtet. Der systematische Übergang zwischen beiden Bauelementkonzepten wird in dieser Arbeit gezeigt, was beweist, dass der C:H MESFET in der Tat wie ein Verzweigungs-Feldeffektbauelement (junction FET) arbeitet.

Die elektrolyt-gesteuerten Transistoren funktionieren sowohl auf der Basis von C:H wie auch mit Graphen ohne Einbringung einer Isolationsschicht zum Steuerkontakt hin. Die Transfercharakteristik beider Bauelemente zeigt erstaunlicherweise die gleiche pH-abhängige Verschiebung von 19 ±1 mV/pH. Das Funktionsprinzip des SGFET basiert darauf, dass das Oberflächenpotential der Kohlenstoffschicht eng mit der flächenbezogenen Dichte der beweglichen Ladungsträger verknüpft ist. Die Konzentration von auf der Oberfläche adsorbierten Ionen ändert dieses Oberflächenpotential und damit die Flächenleitfähigkeit des Bauelements, was wiederum durch geeignete Anpassung der Steuerspannung kompensiert werden kann. Dieser Mechanismus macht das Bauelement zu einem Ionen-sensitiven Feldeffekt-Transistor (ISFET). Aus einer umfassenden Analyse dieser Zusammenhänge werden Beziehungen für die Transfercharakteristik des C:H und des Graphen SGFETs abgeleitet, welche die Experimente korrekt beschreiben. Aus entsprechenden Anpassungen der Daten werden charakteristische Parameter für die beiden Kohlenstoffoberflächen bestimmt.

Chapter 1 Introduction

Carbon is one of the most intriguing elements in the Periodic Table. It forms allotropes of all possible dimensionalities: three-dimensional diamond, graphite and amorphous carbon, two-dimensional graphene, one-dimensional carbon nanotubes and zero-dimensional fullerenes. Not surprisingly, carbon-based materials are attracting a great deal of attention from both scientists and engineers, especially since the new discovering of the low dimensional carbon allotropes in recent years. Among them, diamond and graphene are most interesting to semiconductor physicists, since they can be produced in high purity and with well defined crystalline perfection.

Diamond, where the carbon atoms are sp^3 hybridized and arranged in a cubic fcc lattice, has been a well-known luxurious stone since its discovery in ancient times. Although diamond reveals remarkable intrinsic properties like extreme hardness, highest known thermal conductivity at room temperature, exceptional resistance to radiation, excellent chemically stability and high values of breakdown field, charge carrier mobility, and saturation velocity compared to other semiconductors, the rarity of the material limits its application. With the development in the mid 20th century of the high pressure and high temperature (HPHT) technique, in which diamond was synthesized at a pressure of around 5 GPa at temperatures of at least 1500 °C, diamond was widely used as an engineering material. However, the high concentration of nitrogen in the HPHT synthetic diamonds (mostly type Ib)[1] restricts its application for electronic devices, due to the fact that the donor level associated with nitrogen lies relatively deep, at about 1.7 eV, while the band gap in diamond is 5.47 eV. Thus, those yellow diamonds are insulators at room temperature. Ever since the 1950s, a process known as chemical vapor deposition (CVD) was developed: a pyrolysis of hydrocarbon gases at relatively low temperature (ca. 800 °C) and under

[1] Depending on impurity concentration, diamond is classified into four types: type Ia, Ib, IIa, and IIb. Diamonds that contain nitrogen aggregates are referred to as type Ia. They are colorless or lightly yellow. Most of natural diamonds are of type Ia. If the nitrogen is present on isolated substitutional lattice sites, diamonds are referred to as type Ib. Type Ib diamond is yellow in color and is constructed mostly by synthetic high pressure high temperature method. In case that nitrogen is the major impurity and with a low concentration of less than $10^{18} cm^{-3}$, diamonds are referred to as type IIa and are normally colorless. The type IIb diamonds are those containing boron as major impurity and are usually in blue color. Type IIb diamonds, extremely rare in nature, exhibit p-type conductivity since the boron impurities act as acceptor in the diamond lattice.

low-pressure (< 50mbar). A landmark of the CVD deposition of diamond was reached is in 1971 when Angus et al. [1, 2] first introduced the use of atomic hydrogen to etch graphitic deposits during growth and to permit a high rate of sp^3 nucleation. Later, p-type or n-type bulk diamond was grown by adding dopants like boron or phosphorus during the CVD process. However, the doping for such a wide bandgap, atomic dense semiconductor remains as a tricky task since donor and acceptor levels are far away from the band edges of diamond. This yields a low degree of ionization at room temperature. In 1989, Landstrass and Ravi [3, 4] reported a novel type of conductivity on intrinsic diamond that was obviously related to the surface. With hydrogen terminated surfaces, either intentionally or automatically by the CVD process, intrinsic diamond specimens exhibit a p-type two-dimensional conductivity with a sheet resistance of the order of $10-20\mathrm{k}\Omega/\square$, a hole concentration of about $10^{13}\mathrm{cm}^{-2}$, and a hole mobility of $100-150\mathrm{cm}^2\mathrm{V}^{-1}\mathrm{s}^{-1}$ [5, 6]. The thickness of the conductive layer is estimated to be less than 10nm [7]. Since the discovery of this so-called hydrogen-induced surface conductivity, the physical origin behind the phenomenon remained a mystery for many years.

On the basic of classical concepts of doping in semiconductors, Landstrass and Ravi [3, 4] assigned the role of hydrogen to the passivation of donor like bulk or surface defects which in turn were held responsible to compensate a p-type base conductivity of unspecified origin. Later, also this base p-type conductivity was directly assigned to hydrogen by claiming hydrogen-related point defects in the subsurface region of the diamond lattice acting as shallow acceptors. These so-called sub-surface hydrogen accepters dominated the discussion of the hydrogen-induced surface conductivity for a number of years and were the basis of even more elaborated models that were developed to explain the electrical characteristics of surface field effect devices based on the hydrogen-induced surface conductivity. They remained, however, inconclusive positioning the subsurface hydrogen acceptors in a nm-range directly below the surface [8, 9] or even claiming a “separation layer” between them and the surface [10].

Moreover, the subsurface hydrogen acceptors remained speculative because -despite many efforts- no shallow acceptor-like hydrogen related lattice defect could be specified to substantiate the concept. A change of paradigm in the discussion came along with the observation of Maier et al. [11] that hydrogen termination is necessary but not sufficient for introducing surface conductivity. ONLY when the hydrogenated intrinsic diamond surfaces are exposed to normal atmosphere, the p-type conductivity is created. Based on their experimental observation as well as Hall effect results from others [5, 12], they suggested a novel electrochemical surface transfer doping model, which proposed that the hydrogen/hydronium (H_2/H_3O^+) red-ox couple in a water layer that is physically absorbed

on the surface accepts electrons from the hydrogen terminated diamond via an electrochemical reaction [11, 13]. Later, within the framework of the electrochemical transfer surface doping mechanism, Foord et al. [14] and Angus et al. [13] proposed that the oxygen/hydroxyl (O_2/OH^-) red-ox couple instead of the H_2/H_3O^+ red-ox couple in the absorbed water layer were responsible for the transfer doping process. A consequence of electrochemical reactions of either the H_2/H_3O^+ or the O_2/OH^- red-ox couple would be that acidic conditions favor surface conductivity of hydrogen terminated diamond while an alkaline ambient should lead to a decrease. The electrochemical surface transfer doping model agrees well with experimental results [12, 15] and thereby is widely accepted meanwhile. Strobel et al. first extended the model outside electrochemistry to solid phase or molecular phase surface donors [16, 17]. Similar results were demonstrated by Qi et al. [18].

Graphene, where sp^2-bonded carbon is packed in a honeycomb structure to form a one-atom-thick two-dimensional layer, is the latest carbon allotrope. Ever since the pioneering experimental production by Novoselov et al. [19] in 2004, graphene immediately and rapidly became a rising star in fields of science and industry. The honeycomb lattice of graphene in with each carbon atom is connected to its neighbors through strong covalent bonds, results in unusual properties of this new material: remarkable stable, chemically innert and crystalline under ambient conditions. The graphene sheet is a two-dimensional electronic system. The band structure of its electronically relevant π and π^* bands is represented by cones in the corners of the hexagonal Brillouin zone that touch at the Fermi energy, making graphene a zero-band-gap semiconductor or a semimetal. Due to the strictly linear dispersion relation, electrons and holes behave like massless relativistic particles. This results in the observation of a number of very peculiar electronic properties in this two-dimensional material [20]. Not surprisingly, doping of graphene in the traditional way, i.e. via replacing matrix atoms by impurities, seems to be an impossible task. Instead, the doping of graphene is realized by adsorbing atoms and/or molecules on its surface [13, 21, 22]. Experimental researchers found that exposing the surface to gases may change the resistivity of graphene, and the sign of the change indicates whether the gas is an electron acceptor or an electron donor. However, the doping mechanism of graphene is still under debate. Following computer simulations of **individual** gas molecule absorbed on graphene, a so-called “chemical doping model” is generally proposed [23], which is based on the relative position of the

Fermi level of pure graphene (the Dirac point) and the density of states (DOS) of the HOMO and LUMO of the adsorbate. Later even more complicated models that take closed-shell molecules and open-shell molecules separately into account for the doping process were presented [24, 25]. Others proposed that the mobility rather than the concentration of charge carrier is changed by molecular adsorption due to modified Coulomb scattering.

Up to now, most of the experimental work about transfer doping between graphene and gas species is based on two point conductivity measurements or on graphene MOSFET device characteristics, and few is known about the kinetics of the doping process. The electrochemical surface transfer doping mechanism, although meanwhile established for diamond surfaces, has not yet been considered as a doping mechanism for graphene. Instead, the theoretical simulations in literature about graphene doping focus on individual molecules, although in reality and especially at ambient conditions and normal pressure, molecular clusters (forming liquid or solid phases) rather than single molecules are expected to interact with surfaces. Thereby, the electrochemical surface transfer doping model may open a more general view of the doping process for graphene. Also, we will readdress some questions that remained unclear about the surface conductivity of hydrogen terminated diamond: Which of the plausible red-ox couples participates in the electrochemical equilibrium and results in the p-type character of hydrogen-terminated diamond, the H_2/H_3O^+ red-ox couple or the O_2/OH^- red-ox couple? What kinetics does the reaction follow? We will compare the electrochemical reactions as they take place on both graphene and diamond samples in contact with gas atmosphere and with liquid phase.

Finally, since the conductive region of both diamond-H and graphene is restricted to the two dimensional plane, devices based on a formation of heterojunctions with those materials can be fabricated. We will discuss field effect transistors (FET) of various type that are based on C:H and graphene: the metal semiconductor field effect transistor (MESFET) that is based on a metal-diamond Schottky contact and the solution gated field effect transistor (SGFET) that is based on the electrolyte-semiconductor interface of C:H and graphene. The performance of those devices will be studied.

The organization of the thesis is as following:

In part I, a fundamental introduction of the materials and methods is given (*chapter 2*), followed by a general description of the experimental setup (*chapter 3*).

In part II, the surface transfer doping on C:H and graphene is addressed as it occurs in gas phase (*chapter 4*) and in liquid phase (*chapter 5*).

In part III, field effect transistors (FET) based on C:H and graphene are studied. An introduction of the concept especially for the novel-type FETs (*chapter6*) is presented followed by a discussion of the diamond-based MESFET (*chapter 7*) and diamond and graphene based solution gated field effect devices (*chapter 8*).

PART I BASIC ASPECTS

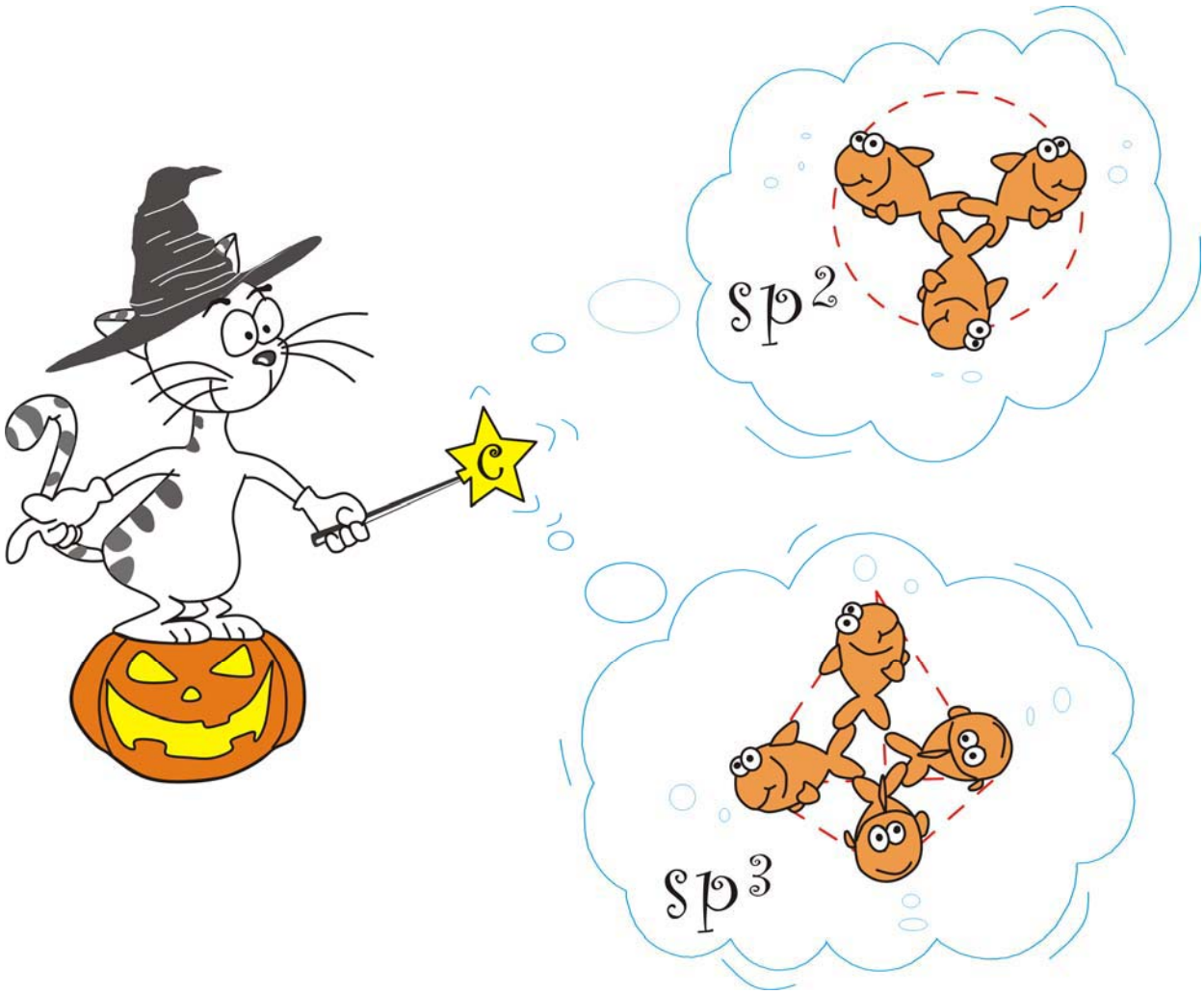

Chapter 2 Materials and Methods

2.1 Materials

2.1.1 General Introduction to Carbon Materials

Table 2.1 *Examples of carbon allotropes.*

sp^3 bonding carbon				
dimension	allotropes	structure	ilustration	discovery
3D	diamond	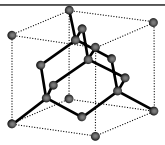		ancient times
sp^2 bonding carbon				
3D	graphite	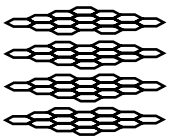		ancient times
2D	graphene	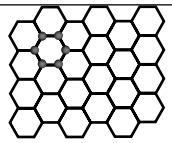	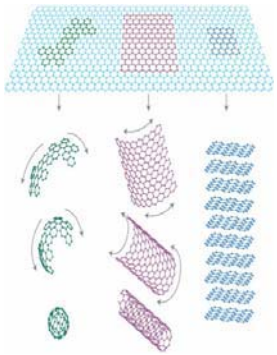 [26]	2004, Novoselov, et al. [19]
1D	carbon nanotube	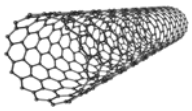		1991, Iijima [27]
0D	fullerenes	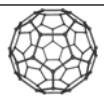		1985, Kroto et al.[28]
sp^3 and sp^2 bonding (mixture) carbon				
3D	amorphous carbon	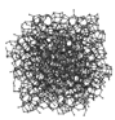	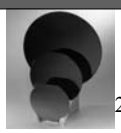 [2] [29]	NA

[2] This figure shows amorphous carbon film on silicon substrates.

Carbon is one of the most interesting and important elements in the world, not only because it forms our amazingly beautiful and colorful living beings on earth, but also thanks to its capability to form a variety of allotropes that make it important in modern scientific and technological fields. When carbon bonds with other atoms, three types of hybrid orbital may be present: sp, sp^2 and sp^3 [30]. he first two well-known carbon allotropes, graphite and diamond have been well-known for a long time [31]. Only during the last two and a half decades, the third and forth carbon allotrope, were discovered: fullerene “buckyballs” (1985) and carbon nanotube (1991). Though it was realized in 1991 that carbon nanotubes were formed by rolling a 2D graphene sheet, a single layer of a 3D graphitic crystal, the production of graphene was successless until 2004. Graphene, the latest carbon allotrope, is said to be the mother of all graphitic materials [26], since it can be (imaginarily) wrapped up into 0D buckyballs, rolled into 1D nanotubes or stacked into 3D graphite. In Table 2.1 we briefly list the most popular carbon allotropes classified by the corresponding hybrid orbital of carbon. Details of carbon materials can be found in reference [31].

2.1.2 Diamond

1) General Properties

Diamond is an old but popular star for scientists. It is a beautiful and expensive stone for jewelry since ancient times. As CVD processes based on ultra pure gases were developed for diamond during the 80’s and 90’s of the last century (see an overview by Locher et al. [32]), research has focused on the electronic properties of diamond, for its outstanding material properties that potentially provide excellent device performance. Diamond [33]:

□ is the hardest material in the world;
□ is optically transparent from deep ultraviolet (UV) to far infrared;
□ has the highest known thermal conductivity of all materials at room temperature;
□ has negative electron affinity (NEA) in case of a hydrogen terminated surface;
□ develops p-type surface conductivity under appropriate condition in case of a hydrogen terminated diamond surface;
□ shows high values of breakdown field, charge carrier mobility, and saturation velocity compared to other semiconductors;
□ is biologically compatible and very resistive to chemical corrosion;
□ is much more resistant to X-ray and nuclear radiation than any other semiconductors.

Table 2.2 *Properties of semiconductors at room temperature: a comparison [34, 35].*

Semiconductor Materials		Diamond	Si	Ge	6H-SiC
Structural properties	Lattice constant (Å)	3.567	5.431	5.658	a: 3.081 c: 15.117
	Density (gcm^{-3})	3.52	2.33	5.33	3.22
Thermal Properties	Melting point T_m (K)	4100 <1>	1687	1210.4	2810
	Specific heat C_p ($Jg^{-1}K^{-1}$)	0.51	0.71	0.33	0.58
	Debye temperature θ_D	1870	643	348	1126
	Thermal expansion coefficient α_{th} ($10^{-6}K^{-1}$)	1.05	2.616	5.75	α_a: 4.2 α_c: 4.7
	Thermal conductivity (K)	22	1.56	0.6	4.9 <2> 3.30 <3>
Elastic Properties <4>	Young's modulus (GPa)	1148.2	157.2	126.8	c⊥*l*: 4.73 c ∥*l*: 5.44
	Poisson's ratio	0.068	0.21	0.195	c⊥*l*: 0.14 c ∥*l*: 0.09
	Knoop microhardness (GPa)	56~115	2~16	9.92	21.3~27.6
Lattice Dynamic Properties	Long-wavelength optical phonon frequencies $\hbar\omega_{LO}$ (cm^{-1})	1332	519.2	301	965
	Optical phonon frequency difference $\Delta\omega_{OP} = \omega_{LO} - \omega_{TO}$ (cm^{-1})	0	0	0	167
Electronic properties	Indirect bandgap (eV)	5.50	1.12	0.67	3.00
	Electron Affinity (eV) [36] <5>	H-: -1.30 O-: 1.73	4.05	4.14	3.34
	The breakdown field (10^5 Vcm^{-1}) in Schottky barriers and p-n junctions	>200 <6>	3	1	24
	Electron mobility ($cm^2V^{-1}s^{-1}$)	2800	1750	2300	375
	Hole mobility (cm^2 $V^{-1}s^{-1}$)	1500	450	2400	100
	Electron saturation velocity ($10^7 cm.s^{-1}$)	1.5	1.02	0.7	1.9
	Hole saturation velocity (10^7 $cm.s^{-1}$)	1.1	0.72	0.63	NA
	Intrinsic resistivity (Ω.cm) [37]	$>10^{15}$	10^5	47	$>10^{15}$
	Dielectric constant	5.7	11.9	16.0	10
Optical Properties	Refractive index	2.4	3.4	4	2.55
Biological properties [33]		excellent	NA	NA	NA
Chamical resistance [33]		excellent	NA	NA	NA

Notes for Table 2.2:

<1> at p = 12.5 GPa;

<2> Heat flow parallel to the basal plane;

<3> Heat flow perpendicular to the basal plane;

<4> For cubic lattice: averaging within the crystallographic planes (100), (110) and (111) at 300K; *l*: directional vector;

<5> H-: hydrogen terminated (100) surface; O-: oxygen terminated (100) surface;

<6> CVD-diamond.

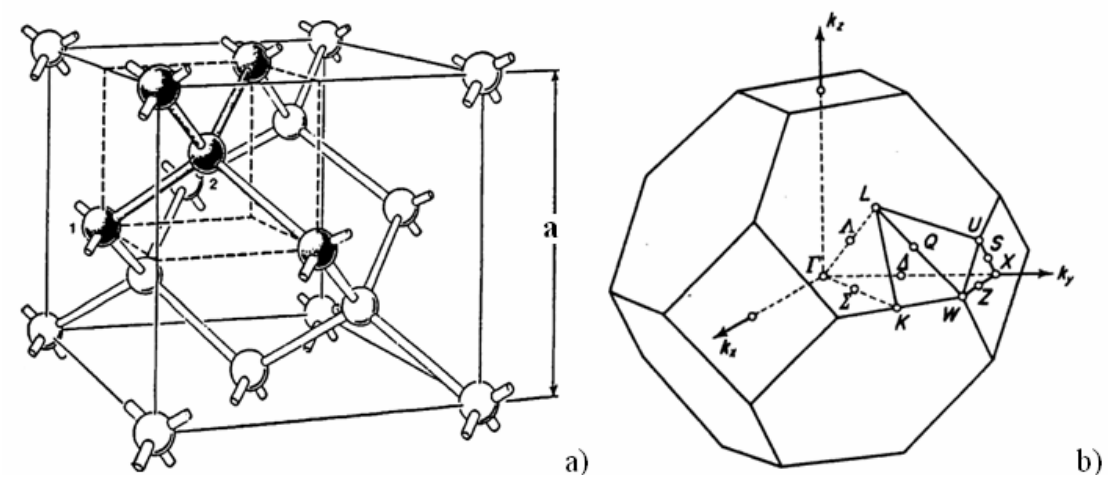

Figure 2.1 *a) Unit cell of the diamond crystal structure. Note that the tetrahedral coordination and the two interpenetrating face centered cubic (fcc) Bravais lattices occupied with one carbon atom per lattice site. The mineralogical cubic unit cell (space group Fd3m) and two inequivalent atoms (1 and 2) are indicated [38]; b) the first Brillouin zone of diamond [38].*

The crystal structure of diamond is the face centered cubic Bravais lattice with two inequivalent atoms in the unit cell (Figure 2.1a) and the Brillouin zone of the diamond structure are displayed in Figure 2.1b). The electronic band structure contributes an indirect semiconductor with a band gap of 5.5eV (Figure 2.2). The vibration properties are described by the phonon dispersion relations (Figure 2.3). The lightest phonon frequency is given by the Raman active Γ phonon corresponding to a wavenumber of 1364cm^{-1}. The phonon dispersion relations are shown in Figure 2.3. In general, the diamond phonon frequencies are higher by a factor of 2 than the frequencies of Si and Ge indicating the stronger bonds of diamonds [39]. A comparison of the properties of diamond and other typical semiconductors is shown in Table 2.2.

Thanks to the outstanding electronic and bio/electrochemical properties of diamond, progresses were made later on applying diamond in fields like environmental protection, health care and biochemical applications. The first extensive study of boron-doped diamond as an electrochemical electrode was that of Pleskov et. al [40] in 1987. Later,

various studies found that diamond electrodes have a very wide electrochemical window for water stability [41-43]. Ever since then, diamond based solid state biosensors and chemical sensors attract increasing attention of scientists and engineers [44-47].

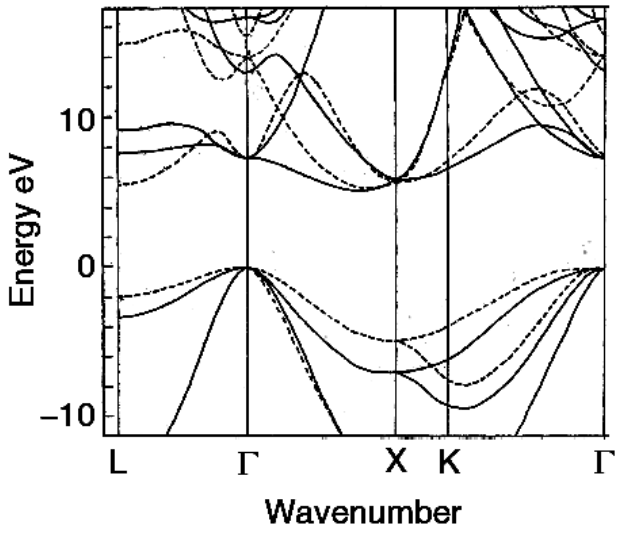

Figure 2.2 *Electronic energy bands in pure diamond [48] for wave vectors k parallel to the major crystallographic axes. Point Γ has k=0, and X, L and K are respectively at the <001>, <111> and <110> zone boundaries. The lines are calculated by Saravia et al. [49].*

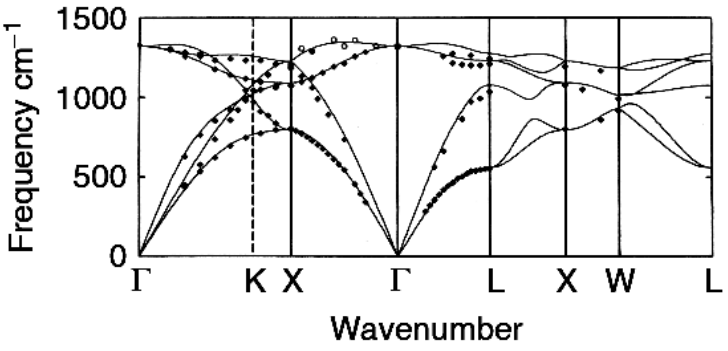

Figure 2.3 *Phonon dispersion relation for diamond at room temperature [48]. The curves are resulted from theoretical calculation. The filled circles and the open circles are neutron scattering data and X-ray scattering data, respectively [48].*

2) Hydrogen Terminated Diamond Surfaces

Recently, large interest is focus on diamond surfaces, especially on the hydrogen terminated diamond (diamond-H) surfaces, since they exhibit unique properties among the semiconductor family, i.e. 1) negative electron affinity [36] and 2) high p-type surface conductivity under appropriate conditions [3]. Experiments show that an absorbed layer from the aqueous atmosphere on the diamond-H surface is one possibility to induce surface conductivity [21]. The p-type conductive surface layer typically involves hole sheet

densities between 10^{10} and 10^{14} cm^{-2} [50], and Hall mobilities between 1 and 100 cm^2/Vs [51].

One of the most recent applications of hydrogen terminated diamond (diamond-H) is as a sensing element in electrochemical/biological sensing devices. In 1970 Bergveld first introduced the so-call ion-sensitive field effect transistor (ISFET)[3] on the basis of silicon. The ISFET device, which can measure pH or, in more general terms, the concentration of ions in solution, is in principle a MOSFET but with the gate electrode being replaced by an electrolyte and a reference electrode [52] (also see chapter 6). The first application of diamond-H as sensing element in the "oxide free" ISFETs was demonstrated by Kawarada et al. [44]. Later, Diamond-H based chemical sensors as well as biosensors have been realized by a number of research groups in the years that followed [45-47, 53-55]. However, the story behind, i.e. the working principle and physics of the diamond ISFETs were not well understood, with contradictions spread in literature [44, 56-60]. To understand the physics of diamond ISFETs is one of the motivations of our thesis (see chapter 8).

2.1.3 Graphene

Graphene, a one-atom-thick two-dimensional layer of sp^2-bonded carbon, packed in a honeycomb structure, is a rapidly rising star in condensed matter physics and material science. This material, presumed not to exist, was not studied until recently [19]. Nevertheless, the unusual material and physical properties rapidly capture the intense interest of scientists who realize that graphene could be a wonderful candidate for future electronic devices. Its honeycomb lattice, with each carbon atom connected to its neighbors through strong covalent bonds, explains its strength and rigidity: remarkable stable, chemically innert and crystalline under ambient conditions. In addition, graphene exhibits ballistic electronic transport on the micrometer scale at room temperature, and can be chemically doped [61].

1) Production of Graphene

So far, there are several methods to produce graphene. Here we summarize the main methods and list them in Table 2.3.

[3] Also called solution gated field effect transistor (SGFET), see chapter 8.

Table 2.3 *The main methods of producing graphene.*

Method	Pioneers	Discription
Peeling/drawing	2004, Novoselov et al. [19]	Mechanical exfoliation (repeated peeling) of 3D graphite crystals with Scotch tape.
Epitaxial growth	2004, Berger et al. [62]	Thermal decomposion of SiC in high vacuum and at high temperature (>1100 °C) to reduce it to graphene.
	2008, Sutter et. al [63]	Using the atomic structure of a metal substrate to seed the growth of the graphene on ruthenium [63], on iridium [64], on nickel [65] and on copper [66].
Chemical method	2009, Choucair et. al [67]	A direct chemical synthesis of graphene nanosheets in a bottom-up approach based on ethanol and sodium reagents.
Unzipping nanotubes	2009, Kosynkin et al. [68]	Unzipping multiwall carbon nanotubes by plasma etching [69] or chemical oxidation [68] of nanotubes.

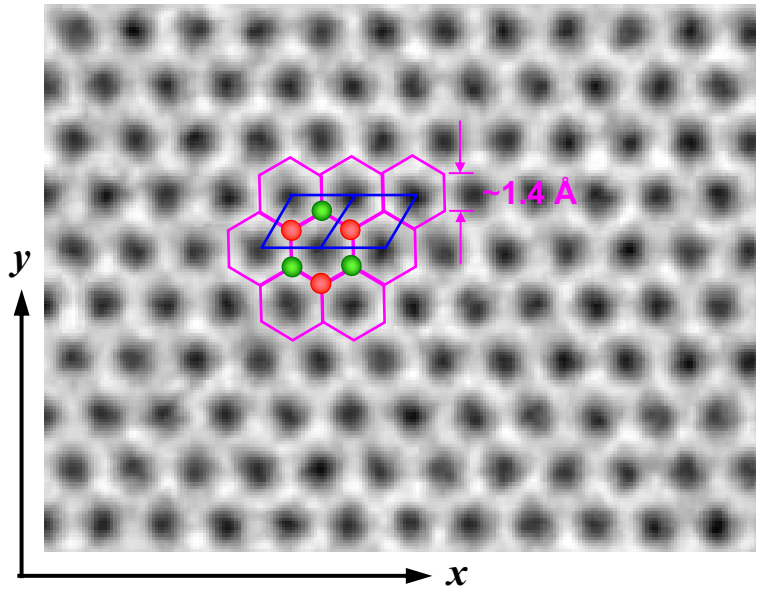

Figure 2.4 *Direct TEM image of a single-layer graphene membrane in real space [70]. The pink lines contribute the hexagonal atomic pattern. In red and green the two inequivalent atoms A and B of crystal structure, respectively, are indicated. Only atoms B are seen as bright white dots in the micrograph. In blue the unit cell of the structure is shown. The distance between atoms is around 1.4 angstrom.*

2) Atomic Structure of Graphene

The atomic structure of graphene, the single layer of carbon atoms densely packed in a honeycomb structure with the atomic distance of ca. 0.14nm, can be studied by Atomic Force Microscope (AFM) [71], Scanning Tunneling Microscope (STM) [72] and Transmission electron microscopy (TEM) [70] (see Figure 2.4).

The energy bands relevant for the material's electronic properties are constructed from atomic p_z orbitals that are perpendicular to the sheet. The conduction band π^* and valence band π touch at the "Dirac point" in the six corners of the hexagonal Brillouin zone (see Figure 2.5) and form an unusual zero-gap semiconductor with linear band dispersion, which leads to many interesting electronic phenomena, such as the fractional quantum Hall effect [73].

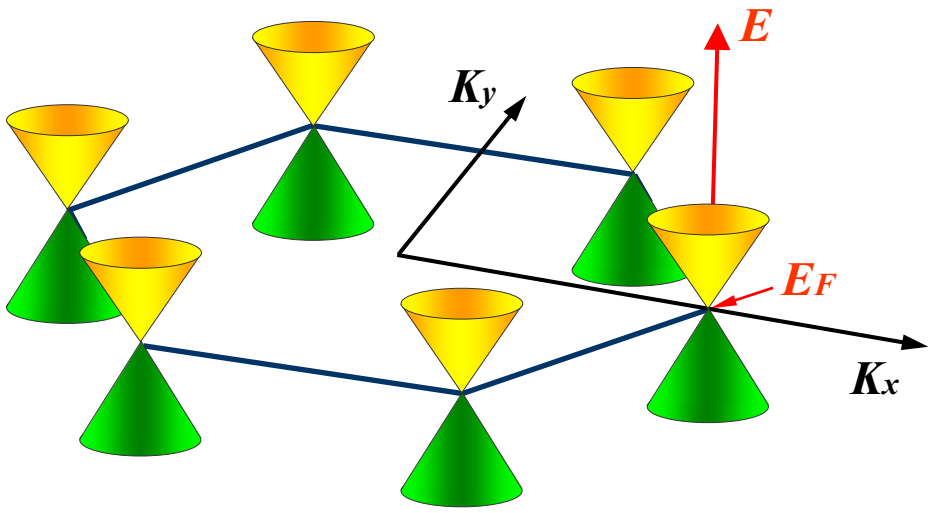

Figure 2.5 *Schematic diagram of the band structure of graphene* ***near*** *the six Brillouin Zone (BZ) corners in the three dimensional energy-momentum space (Note: the hexagonal BZ is rotated by 30° relative to the atomic carbon hexagons and identically oriented to the lattice point hexagons as shown in Figure 2.4). E: energy; Kx, Ky: wave vector component in x and y direction. The conduction bands (yellow) and valence bands (green) meet at the so-called "Dirac point".*

3) Electronic Properties of Graphene

Another interesting feature of graphene is the ambipolar electric field effect [26] (see Figure 2.6), where the position of the Fermi energy E_F can be adjusted by applying a gate voltage V_g: positive V_g induces electrons while the negative V_g induces holes. Minimum charge carrier concentration and maximum sheet resistance is achieved with a gate voltage that puts the Fermi level in the graphene at the Dirac point. A rapid decrease in resistance ρ is observed on adding charge carriers of either sign. Moreover, the observed mobilities

weakly depend on temperature T [26], which means that μ at room temperature is still limited by impurity scattering, and therefore can be improved significantly even up to $40,000 cm^2 V^{-1} s^{-1}$ [74].

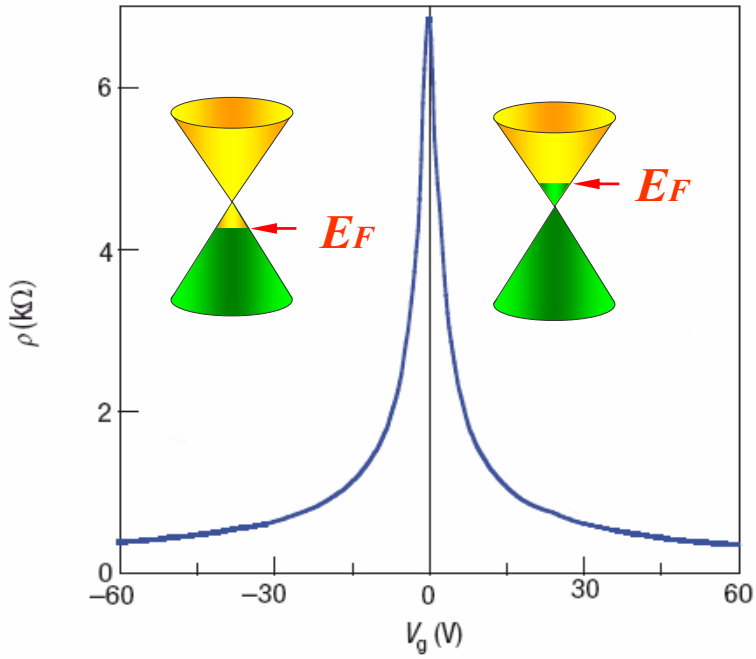

Figure 2.6 *The ambipolar electric field effect of graphene (measured at room temperature) [26]: charge carriers can be turned continuously between electrons and holes; positive V_g induces electrons while the negative V_g induces holes.*

4) Surface Sensitive Electronic Properties of Graphene

Not surprisingly, the two dimensional material, graphene, has been proven to be extremely sensitive to its environment, i.e. the supporting substrate and/or gases and chemicals in contact with its surface [61, 73]. Some effects are assigned to the broken of symmetry of the two sublattices of graphene (since graphene has two atoms per unit cell) [61]. We have performed Hall effect measurements of expitaxial graphene at different gas atmosphere that will be discussed in section 4.2. We have further analyzed solution gated field effect transistors based on single layer epitaxial graphene on silicon carbide. These results will be discussed in chapter 8. For further information from this rapidly growing field of research we refer the reader to recent review articles [26, 75, 76].

2.2 Electrical Characterization

2.2.1 The Hall Effect

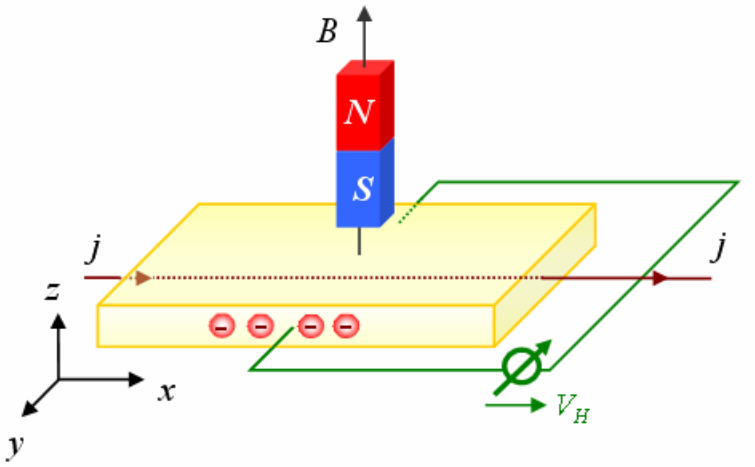

Figure 2.7 *Hall effect in an n-type semiconductor. Schematically shown is only the charge of the mobile electrons.*

The Hall effect, discovered by E.H. Hall (1879), is a phenomenon observed in metals and semiconductors [77]. When an electric current passes through a semiconductor strip there is normally no potential difference across the strip if measured perpendicularly to the current path. If, however, a magnetic field is applied perpendicularly to the plane of the strip, the electrons are deflected towards one side and such a potential difference is created. Due to the balance of the Lorentz force $F = qv \times B$ and the transverse electric field force this Hall voltage V_H, can be deduced by integrating over the transverse field E_H.

$$E_H = \left(\frac{1}{nq}\right)\frac{1}{d} jB = \left(\frac{1}{qn_s}\right) jB \tag{2.1}$$

Here B is the magnetic flux density, d is the depth of the plate, q is the charge of the carriers ($\pm e$), and n is the density of the charge carriers. The ratio of the transverse Hall field divided by the longitudinal current density and the magnetic field is called the Hall coefficient R_H.

$$R_H = \frac{V_H}{jB} \tag{2.2}$$

When the polarity of the charge carriers is invertel while keeping the sign of the current density, the charge deflection by the Lorentz force is to the same sign as the Hall voltage changes sign. Thus, with the sign convention of Figure 2.7, the Hall constant is written as:

$$R_H = -\frac{1}{ne} \tag{2.3}$$

R_H yields the polarity[4] and the concentration of the charge carriers irrespective of their mobility. It is this fact that makes the Hall effect such an important tool in semiconductor physics.

2.2.2 The Van Der Pauw Method

In 1958, Van Der Pauw [78] presented an ingenious method for carrying out conductivity and Hall-mobility measurements on thin layers with arbitrary shape if the following conditions are fulfilled [79]:

1) The layer must be perfectly flat;

2) The four contacts must be point shaped and positioned at the circumference of the sample;

3) The sample is homogeneous and uniform in thickness;

4) The area of the sample is singly connected, i.e. the sample does not contain isolated holes.

1) Conductivity

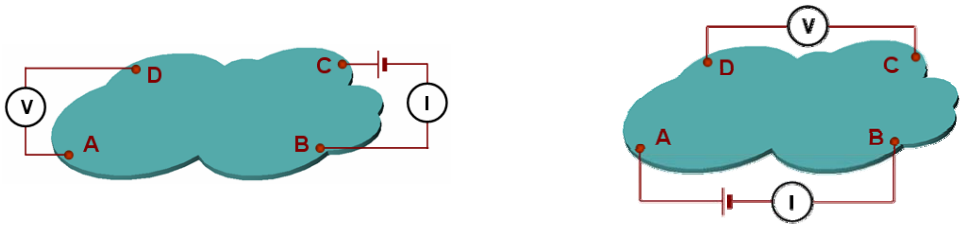

(a) (b)

Figure 2.8 *The two construction of measurements required to determine the sheet resistance of a thin layer conductor with arbitrary shape, according to the Van Der Pauw method. I denotes the current forced through the sample via two contacts, and V is the voltage which is recorded between the other two contacts.*

To determine the sheet resistance of the sample, two measurements have to be performed (Figure 2.8). In each measurement, a current I is forced through the sample between two neighboring contacts while the voltage is measured between the other two

[4] In case of a p-type semiconductor, the Hall constant has a positive sign, while for n-type it is negative.

contacts. The following ratios are calculated.

$$R_{AB,CD} = \frac{V_D - V_C}{I_{AB}} = \frac{V_{DC}}{I_{AB}}, \quad R_{BC,DA} = \frac{V_D - V_A}{I_{BC}} = \frac{V_{DA}}{I_{BC}} \tag{2.4}$$

Van Der Pauw showed that for these the following relation holds:

$$\exp(-\pi \frac{R_{AB,CD}}{R_S}) + \exp(-\pi \frac{R_{BC,DA}}{R_S}) = 1 \tag{2.5}$$

where R_s is the sheet resistance. Rewritten this equation yields the conductivity:

$$\sigma = \frac{1}{R_S} = \frac{1}{\frac{\pi}{\ln 2} \frac{R_{AB,CD} + R_{BC,DA}}{2} f(\frac{R_{AB,CD}}{R_{BC,DA}})} \tag{2.6}$$

where $f(\frac{R_{AB,CD}}{R_{BC,DA}})$ is a function of the ratio $\frac{R_{AB,CD}}{R_{BC,DA}}$=Q only. Inserting (2.6) into (2.5) yields an implicate equation for f which its argument Q is replaced by its reciprocal 1/Q. Thus, on a logarithms scale *f(logQ)* is a symmetric function of its argument and will defined by its positive branch. $f(\frac{R_{AB,CD}}{R_{BC,DA}})$ can be withdrawn graphically from the plot below (Figure 2.9)

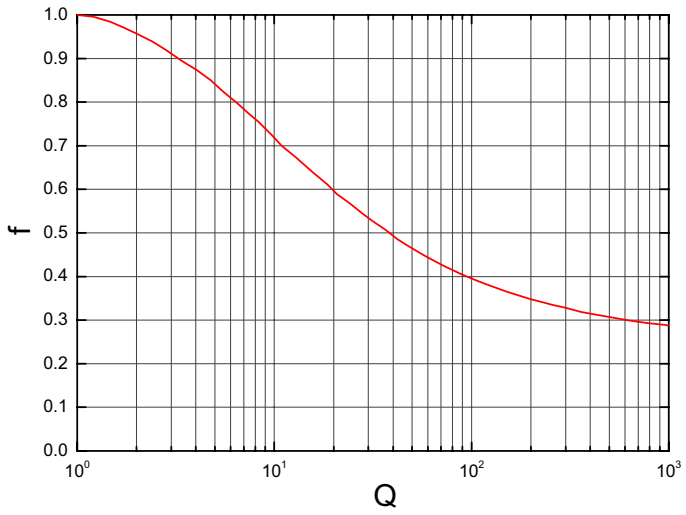

Figure 2.9 $f\left(\frac{R_{AB,CD}}{R_{BC,DA}}\right)$ *as a function of* $Q = \frac{R_{AB,CD}}{R_{BC,DA}}$, *replotted from reference [78].*

2) Hall-mobility

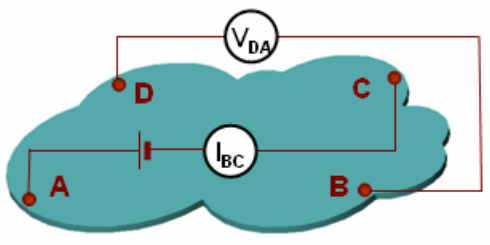

Figure 2.10 *Hall effect measurement on the Van Der Pauw geometry.*

The goal of the Hall measurement in the van der Pauw geometry is to determine the sheet carrier density n_s and their mobility μ by measuring the Hall voltage V_H and the sheet resistance simultaneously. A constant current *I* is forced through the sample between two **non**-neighboring contacts while the voltage is measured between the other two contacts. At the same time, a variable magnetic field is applied perpendicular to the conductive-sheet, which, lead to a variation of the recorded voltage. Once the Hall voltage V_H is acquired, the sheet carrier density n_s can be calculated via:

$$n_s = \frac{IB}{qV_H} = \frac{d}{qR_H} \tag{2.7}$$

with the sheet thickness *d*.

2.3 Introduction to Electrochemistry

Electrochemistry involves chemical phenomena that are associated with charge separation or charge transfer that takes place heterogeneously at electrode surfaces. For electroneutrality reasons, at least two charge transfer reactions are involved, and each of them, correspond to a so-called red-ox half-reaction at a different electrode. The two different electrodes, plus the conducting electrolyte, and the external circuit, makes up an electrochemical cell. When the sum of the free energy changes at both electrodes is negative, electrochemical energy is converted to electrical energy, and such a cell is called a battery. If it is positive, external electrical energy must supply to drive the electrode reactions. Then, electrical energy is converted to electrochemical energy, and the process is called electrolysis [80]. The later process can be considered as a branch of catalyst chemistry, in which the external power supplier is a special, controllable “catalyst”. In the following text, we give a brief overview of electrochemistry dealing with: the electrode-electrolyte interface, the thermodynamic driving forces, and the kinetics of electrochemical reactions.

2.3.1 General Structure of the Electrode-Electrolyte Interface

When a semiconductor electrode is in contact with an electrolyte an electrode-electrolyte interface is formed, where the electrochemical reactions take place. Since the thermodynamic driving forces and the kinetics of the reactions depend on the structure of the interfacial region, it is important to study how the interfacial region looks like. Generally speaking, the "contact" consists of two parts: the space-charge region of the semiconductor and the electrolyte double layer. Since the space-charge region in the solid state phase is not new but similar to other semiconductor contacts (see section 6.1), we will focus on the electrolyte double layer part. To illustrate the electrolyte double layer region, we take metal electrodes as an example, as space-charge region of metal is so narrow that its extension can be ignored.

Table 2.4 *Specific properties of "specific adsorbed ions"*

Ions	Ions in IHP (specifically adsorbed ions)	Ions in OHP
Distance to electrode	Closest to electrode (touching)	Seperated by IHP
Interaction with electrode	Form chemically stong bonding	Electrostatic force
Charges (←→electrode)	The same or opposite charge	Opposite charge
Hydration	partially loses its salvation shell	Full hydration

The concept of the existence of a double-layer at the surface of a metal in contact with an electrolyte appeared in 1879 (Helmholtz) [81] who assumed the presence of a compact layer of ions in contact with the charged metal surface. The next model by Gouy and Chapman (1910-1913), different from the Helmholtz model, suggested a diffuse layer that is made up by Boltzmann-distributed ions extending to some distance from the solid surface. Later, Stern (1924) suggested that the solid-liquid interface is a combination of the rigid Helmholtz layer and the diffuse layer. Graham (1947) [82], following consecutive experiments, made further process by taking into account specific adsorption of ions at the metal surface (see Table 2.4). The final model that is well-accepted nowadays is made by Bockris and Devanathan (1963) [83], who, in addition, considered the effect of dipolar solvents, such as water. As a consequence of the dipole-interaction with the charged metal surface, a much lower dielectric constant of the solvent in the compact layer as compared to the bulk solution is assumed. A detailed description of the double-layer models can be found in reference [80].

The simplified Bockris model of the double layer formed at the metal electrode surface is presented in Figure 2.11.

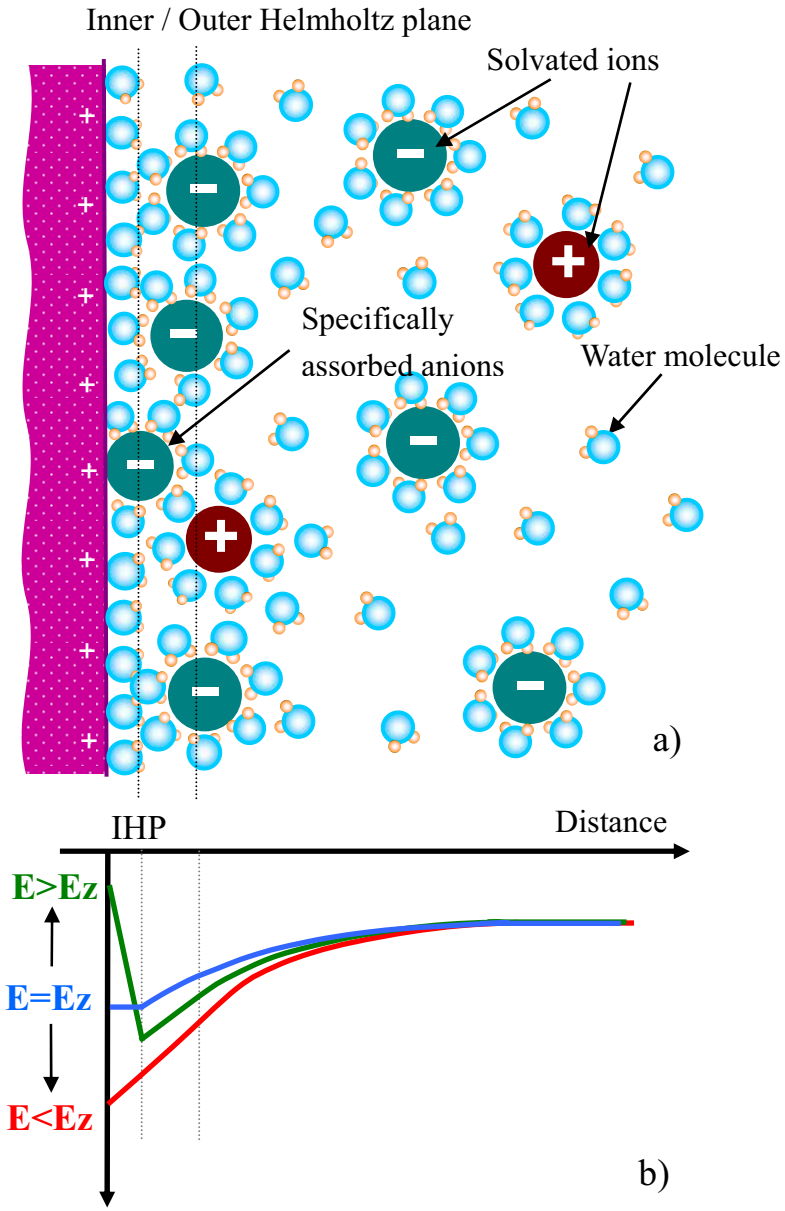

Figure 2.11 *a) Model of the electrochemical double layer formed at the metal-electrolyte interface, featuring solvated cations and anions near the anode surface; a specifically adsorbed anion is also shown [84]; b) The Variation of the electrostatic potential with distance from the electrode, according to the applied potential [80]. Ez denotes the potential of zero charge. When E=Ez the electrical charge density on the electrode surface is zero. E<Ez stands for negative charges accumulated at the electrode while E>Ez is for the opposite situation.*

Most of the electrode is covered by re-oriented water molecules, while at certain sites by specifically adsorbed ions that has been surrounded by a hydrated water shell. The so called inner Helmholtz plane (IHP) is defined by a plane going through the centers of these

ions. Next to that is a second layer, called outer Helmholtz plane (OHP), which is formed by centers of ions carrying a primary hydration shell. The concept of "specific adsorption" (or contact adsorption) is sometimes confusing. In Table 2.4, we compare them with normal ions to show the readers how "specific" they are. Between the OHP and the bulk solution is the diffused layer, constructed by ions that follow the Boltzmann distribution law.

The total excess charge density on the solution side of the double layer, $\sigma^S(\mu C/cm^2)$, is given by:

$$\sigma^S = \sigma^i + \sigma^d = -\sigma^M \tag{2.8}$$

Here σ^i is the total charge density from specifically adsorbed ions in IHP; σ^d is the excess charge density in the diffuse layer; and σ^M is the total excess charge density on the metal side of the double layer. The thickness of the diffuse layer depends on the total ionic concentration in the solution. For concentrations greater than 10^{-2} M, the thickness is less than ~10nm. We will readdress this issue in section 5.1.

2.3.2 Thermodynamics of Electrochemical Reactions

Thermodynamics describes the changes in energy and entropy, during an electrochemical reaction. The two fundamental state functions determine to what extent a reaction will processed. Nothing, however, can be said about the rate at which an equilibrium state is approached, nor the mechanism of the proceeding reaction [81]. In addition, thermodynamic information can only be obtained about systems that are in equilibrium or at least very close to it. Practically, to control an electrochemical reaction near equilibrium is to approximately limit the electric current [81].

In electrochemistry, the reference point for the chemical potential of red-ox electrons is defined by the standard hydrogen electrode (SHE) as zero potential. Then, each of the half-reactions potentially proceeding at an electrode is associated with it a standard red-ox potential $E^{\ominus}$, measured relative to SHE. The real electrochemical potential of the red-ox electrons, E, is related to $E^{\ominus}$ through the famous Nernst equation [80]:

$$E = E^{\ominus} - \frac{RT}{nF}\sum \ln q \tag{2.9}$$

where q is the reaction coefficient (see the following explanation about the term “activity”). F is the Faraday constant: $9.6485\times10^4 Cmol^{-1}$, and R is the gas constant: $8.3145 JK^{-1}mol^{-1}$. At room temperature (T = 298K), $(RT/F)\ln 10$ can be replace by 0.0592V. Hence, the Nernst equation at room temperature can be rewritten as:

$$E = E^{\Theta} - \frac{0.0592V}{n}\sum \log q \qquad (2.10)$$

Details about the derivative of the Nernst equation can be found in Appendix I.

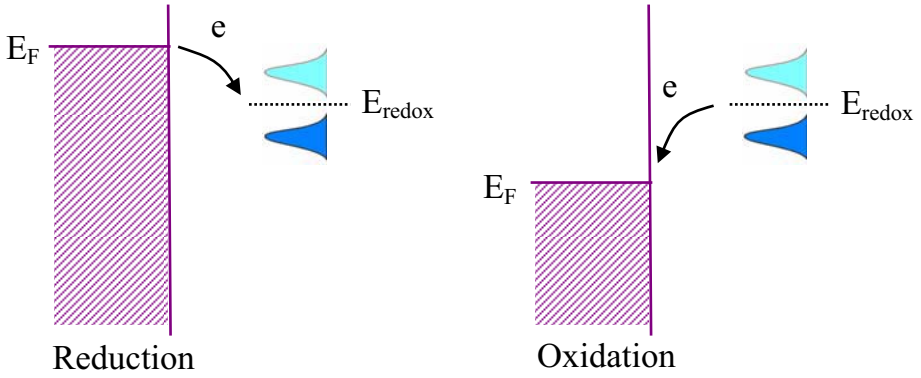

Figure 2.12 *Electron transfer at an metallic electrode [80]. The potential applied to the electrode alters the alignment between the electrochemical potential of red-ox electrons and the electrons of the electrode, E_F, facilitating (a) reduction or (b) oxidation.*

The other important terms that are commonly used in electrochemistry are:

The Gibbs Energy: it is at the heart of electrochemistry, because it can be deduced that $dG_{T,P} = dW_{electrical} = VQ = nFE$. In words, the Gibbs energy identifies the amount of work we can extract electrically from a system. Details can be found in reference [85]. The tendency for the reaction to occur ΔG^{Θ}, can be related to standard electrode potential E^{Θ}, which is relative to the SHE reference under standard conditions: $\Delta G^{\Theta} = -nFE^{\Theta}$ [80].

The Chemical Potential μ: a property that describes how much a substance contributes to the system's energy. The chemical potential is defined as $\mu = (\partial G / \partial n_i)_{T,P}$ and hence the change of Gibbs energy in a system is $dG_i = \sum \mu_i \cdot dn_i$.

The Electrochemical Potential is defined as $\bar{\mu}_i = \mu_i + z_i F\Phi$, i.e. it is the chemical potential of the charged particle (electron or ion) plus the response of it to an electrical field.

The Activity, a_i, is a generalized concentration that describes how a reactant contributes to a reaction in terms of the law of mass action. For a reaction, $wA + xB \rightarrow yC + zD$, we define the "reaction quotient"[5] as $q = \frac{a_C^y + a_D^z}{a_A^w + a_B^x}$. Activity can be related to concentrations via: $a_i = \gamma_i c_i$, where $\gamma_i \approx 1$ for small concentrations c_i.

[5] In chemistry, a reaction quotient is a function of the activities of the chemical species involved in a chemical reaction.

Reference Electrode: Reference electrodes, as their name suggests, are electrodes which have a stable and well-known electrode potential and are used to give a value of potential to which other potentials can be referred in terms of a potential difference [80]. Commonly used reference electrodes are the standard hydrogen electrode (SHE) (E^{Θ}=0.000V), the saturated calomel electrode (SCE) (E^{Θ}=0.242V against SHE), and the silver chloride electrode (E^{Θ}=0.197V against SHE)

Reduction and Oxidation: Oxidation is the loss of electrons and reduction is the gain of electrons (see Figure 2.12).

2.3.3 Kinetics of Electrochemical Reactions

1) Faradaic and Nonfaradaic Processes

To complete a certain electrochemical reaction, Faradaic and Nonfaradaic Processes at the electrode-electrolyte interface have to be distinguished. The Faradaic process is a process that involves charge transfer across the electrode-electrolyte interface. An electron transfer, causes oxidation or reduction, and the corresponding current follows Faraday's law [6]. The nonfaradaic, on the other hand, normally refers to a process in which the current is transient and does not follow the Faraday's law.

2) Factors Limiting the Reaction Rate

An electrode reaction is a multistep reaction. The current flowing across the interface is limited by the current corresponding to the slowest reaction step. There are four major types of Faradaic currents [85]: 1) Charge transfer currents; 2) Adsorption currents; 3) Kinetic currents; 4) Mass transport currents (including: diffusion currents; migration currents and convection currents), and hence the total reactions can be controlled by: i) Mass transport (diffusion, convection and migration); ii) Charge transfer (Butler-Volmer equation and Tafel plot, see text below); iii) Mixed controlled: charge transfer-mass transfer step (Butler-Volmer equation with correction for mass transport). Details of the kinetic theories of electrochemical reactions can be found in references [80, 86]. In the following section, we will take the hydrogen deposition reaction as an example to discuss its kinetics.

---

[6] Faraday's law: The amount of electricity that flows depends on the amount of species being oxidized or reduced. The Faraday current density is $j = (nF)/(At) = (F/A)\cdot k$, where n is the number of electrons in a redox reaction; F is Faraday constant; A is the area of electrode and k is the rate constant of the reaction.

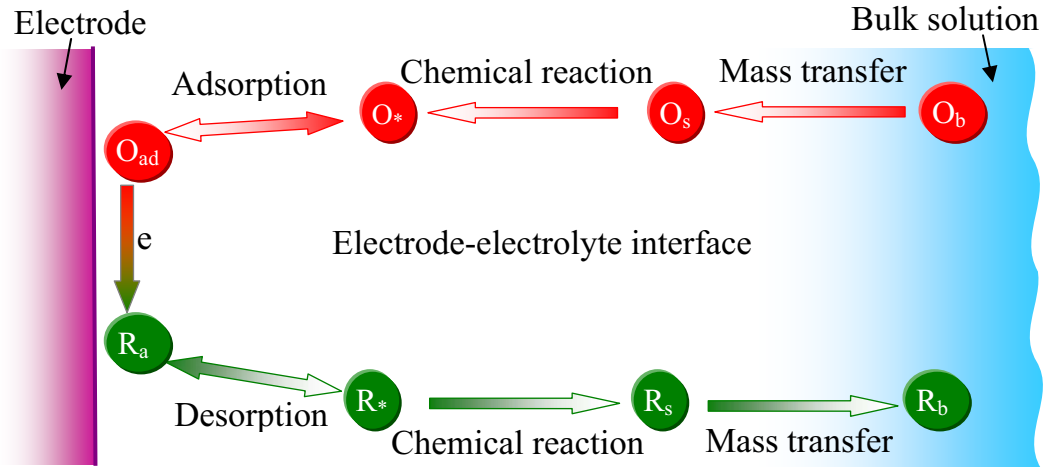

Figure 2.13 *General scheme of a Faradaic process at an electrode-electrolyte interface [86]. "O" is the oxidant and "R" is the reductant. The subscript "b" represents "bulk", "s" is for "surface", and "*" is for ions that are dehydrated and are ready for adsorption/desorption on the electrode surface.*

3) Example: Kinetics of the Hydrogen Deposition Reaction

In this section, we discuss the mechanism of hydrogen evolution at metallic surface to outline the principles of electrode reaction kinetics [87]. The complete reaction of hydrogen evolution is:

$$2H^+ + 2e^- \rightarrow H_2 \tag{2.11}$$

The first step is the mass transport of H^+ (or H_3O^+) from the bulk solution to the metal surface by diffusion, convection and electrolytic migration:

$$\text{step 1, mass transport: } H^+ \rightarrow (H^+)_* \tag{2.12}$$

The subscript "*" indicates the position of closest approach of hydronium ions (i.e. H^+ or H_3O^+) to the metal surface. Later, at this position, the ions are discharged to atomic hydrogen and adsorbed at the surface after the charge transfer reaction:

$$\text{step 2, Volmer reaction: } (H^+)_* + e^- \rightarrow H_{ad} \tag{2.13}$$

Finally, the adsorbed atomic hydrogen recombines to molecular hydrogen by the Tafel reaction:

$$\text{step 3, Tafel reaction: } H_{ad} + H_{ad} \rightarrow H_2 \tag{2.14}$$

The above sequence is called Volmer-Tafel mechanism, as shown in Figure 2.14. As we mention above, as long as there is no mixed controlled involved, the total reaction speed is limited by the slowest reaction step. In the following we will discuss each step separately, assuming the one being discussed is the limiting step.

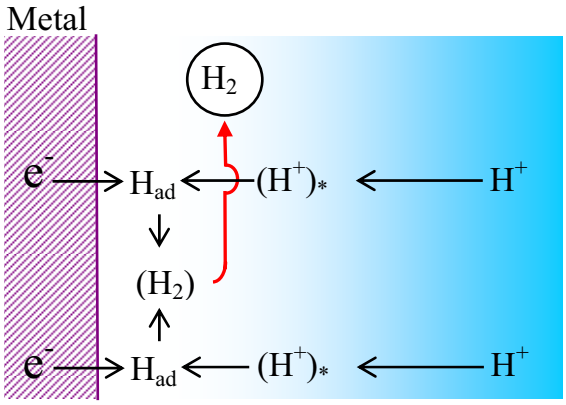

Figure 2.14 *Mechanism of cathodic hydrogen deposition, according to the Volmer-Tafel model [87].*

i) The Mass Transport Process

We use the Nernst boundary-layer model to describe the mass transfer process. The model suggests the existence of a Nernst layer, whose thickness δ_{Nernst} is by orders of magnitude larger than the thickness of the electrical double layers (i.e. the distance between the surface and the OHP) δ_{dl}. Beyond the Nernst layer, the concentration C_{H^+} of dissolved H^+ or H_3O^+ is assumed constant $(C_{H^+})_O$. Within the layer, the concentration decreases linearly to $(C_{H^+})_*$ at the distance $x = \delta_{dl} \approx 0$ from the electrode surface (see Figure 2.15). The concentration C_{H^+} varies with distance, following the Fick's first law of diffusion:

$$(\frac{n}{t}) = -D_{H^+} \cdot \frac{dC_{H^+}}{dx} \tag{2.15}$$

D_{H^+} is the diffusion coefficient of H^+ ions, in unit of $cm^2 s^{-1}$; n is the number of unit charge; the unit of $(\frac{n}{t})$ is $mol \cdot s^{-1}$ and the unit of dC_{H^+}/dx is $mol \cdot cm^{-2}$.

Inserting Faraday's law [7] yields the diffused current:

$$i_H = -FD_{H^+}\left(\frac{dC_{H^+}}{dx}\right)_{x=0} \tag{2.16}$$

For stationary conditions, dC_{H^+}/dx must be constant and can be substituted by $\left[(C_{H^+})_0 - (C_{H^+})_*\right]/\delta_{Nernst}$ and thus

$$i_H = -FD_{H^+}\frac{(C_{H^+})_0 - (C_{H^+})_*}{\delta_{Nernst}} \tag{2.17}$$

[7] Faraday constant F= 96 485.3415 s A / mol

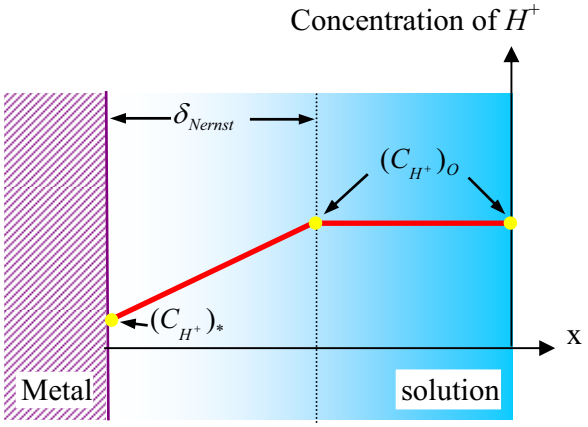

Figure 2.15 *Simple sketch of the Nernst boundary-layer model.*

For $(C_{H^+})_* = 0$, $i_H \equiv i_{H,D} = -FD_{H^+}\dfrac{(C_{H^+})_0}{\delta_{Nernst}}$; $i_{H,D}$ is called the diffusion-limited current density. Combining (2.16) and (2.17), yields:

$$\frac{(C_{H^+})_*}{(C_{H^+})_0} = 1 - \frac{i_H}{i_{H,D}} \tag{2.18}$$

Discussion of (2.18):

i) When $|i_H|$ is small compared to $i_{H,D}$, the concentration $(C_{H^+})_*$ is nearly the same as the bulk concentration, and mass transport is not the limiting reaction step.

ii) When $(C_{H^+})_* < (C_{H^+})_0$, the hydrogen deposition rate is so high that we can assume equilibrium for all other reaction steps, i.e. we can apply the Nernst equation for the charge-transfer step. The potential difference is:

$$\eta_H = E_{(a_{H^+})_*} - E_{(a_{H^+})_0} = \frac{RT}{F}\ln\frac{(a_{H^+})_*}{(a_{H^+})_0} \approx \frac{RT}{F}\ln\frac{(C_{H^+})_*}{(C_{H^+})_0} = \frac{RT}{F}\ln\left(1 - \frac{i_H}{i_{H,D}}\right) \tag{2.19}$$

This means that the passage of the current i_H has made the potential $E_{(a_{H^+})_*}$ depart from the one that corresponding to zero current value $E_{(a_{H^+})_0}$. The potential difference, $\eta_H = E_{(a_{H^+})_*} - E_{(a_{H^+})_0}$, is produced by a concentration charge at the interface, owing to diffusion holdup. This is called *diffusion overpotential* or *concentration polarization* [88]. The word *overpotential* refers to the departure of the potential of the electrode from its equilibrium value as a result of having a net flow of electric current across the interface (at equilibrium, the net flow of current is zero!).

ii) The Charge Transfer Process: Volmer reaction

● **Rate of charge transfer under zero field ($\phi_{ml} = 0$)**

Consider the Volmer reaction, and define the rate constant "$\vec{k}$" & "$\overleftarrow{k}$" as the

coefficient between rate and concentration:

$$(H^+)_* + e^- \rightarrow H_{ad} \qquad \text{with forward rate constants: } \vec{k}$$
$$H_{ad} \rightarrow (H^+)_* + e^- \qquad \text{with backward rate constants: } \overleftarrow{k} \tag{2.13}$$

Then, the total reaction (forward and backward) speed is:

$$v_H = \vec{v}_H - \overleftarrow{v}_H = \vec{k}(c_{H^+})_* - \overleftarrow{k}(\theta_H)_{ad} \tag{2.20}$$

Inserting the Faraday's law (footnote 6), and use j to represent current density yields:

$$j_H = \vec{j}_H - \overleftarrow{j}_H \tag{2.21}$$

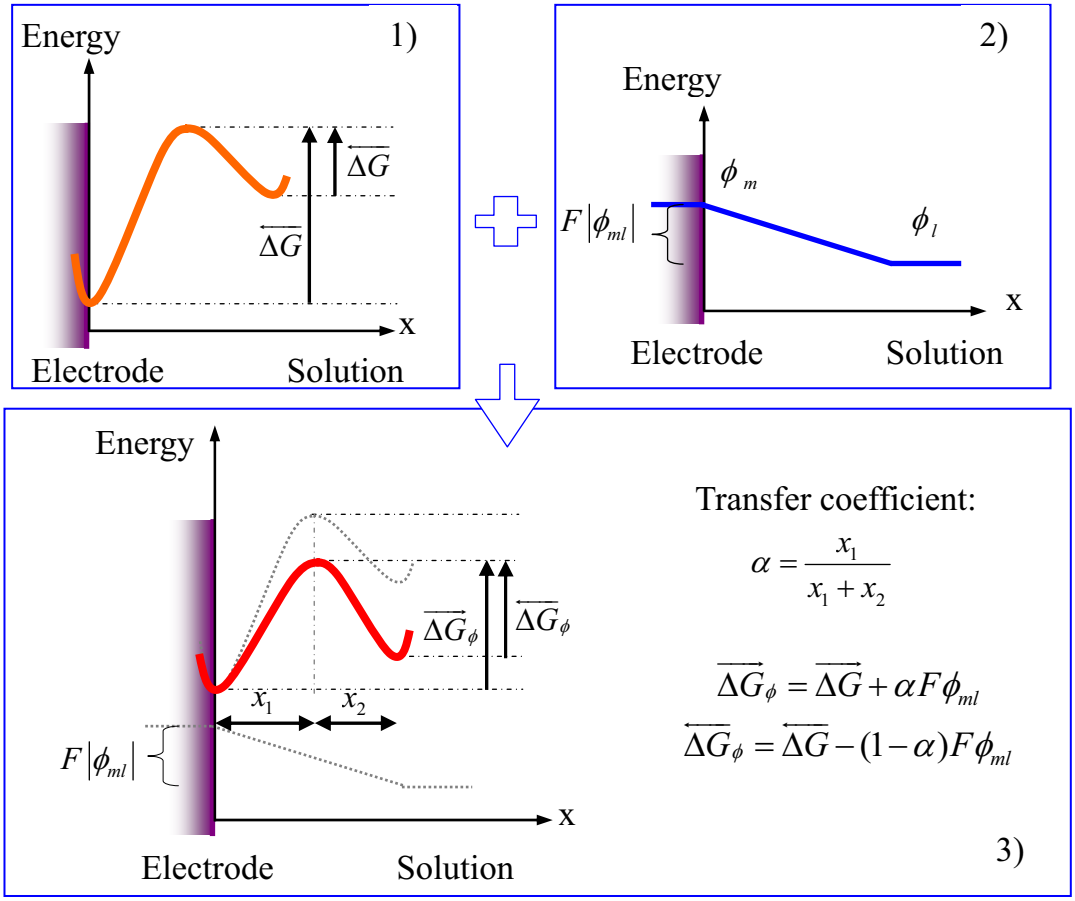

Figure 2.16 *Energy change during forward and reverse Volmer reaction, with and without external electric field. "1" corresponds to zero electronic field* $\phi_{ml} = 0$ *and "2" is the potential profile of the external field. "3" is the structure change of the interface on applying a nonzero electronic field* $\phi_{ml} \neq 0$.

For any chemical reaction, the Arrhenius equation, which links the activation energy of the reaction ΔG and Boltzmann statistics, can be applied for calculating the reaction speed [86]:

$$k = k_0 \exp(-\Delta G / RT) \tag{2.22}$$

Inserting (2.22) into (2.21) and (2.20):

$$j_H = \vec{j}_H - \overleftarrow{j}_H = F \cdot \vec{k}_0 \cdot (c_{H^+})_* \cdot \exp\left(-\frac{\overrightarrow{\Delta G}}{RT}\right) - F \cdot \overleftarrow{k}_0 \cdot (\theta_H)_{ad} \cdot \exp\left(-\frac{\overleftarrow{\Delta G}}{RT}\right) \tag{2.23}$$

● Rate of charge transfer under nonzero field ($\phi_{ml} \neq 0$)

The modified activation energies on applying a nonzero voltage between the electrode and the electrolyte ϕ_{ml} are:

$$\overrightarrow{\Delta G}_\phi = \overrightarrow{\Delta G} + \alpha F \phi_{ml}, \quad \overleftarrow{\Delta G}_\phi = \overleftarrow{\Delta G} - (1-\alpha) F \phi_{ml} \tag{2.24}$$

And the modified net current under the external field is:

$$\begin{aligned} j_H = \vec{j}_H - \overleftarrow{j}_H = & \left[F \cdot \vec{k}_0 \cdot \left(C_{(H^+)_*} \right) \cdot \exp\left(-\frac{\overrightarrow{\Delta G}}{RT} \right) \right] \exp\left((1-\alpha) \frac{F \phi_{ml}}{RT} \right) \\ & - \left[F \cdot \overleftarrow{k}_0 \cdot \left(C_{H_{ad}} \right) \cdot \exp\left(-\frac{\overleftarrow{\Delta G}}{RT} \right) \right] \exp\left(-\alpha \frac{F \phi_{ml}}{RT} \right) \end{aligned} \tag{2.25}$$

At equilibrium [8],

$$\phi_{ml} \equiv \phi_{eq.}, \; j_H = 0, \; \vec{j}_H = \overleftarrow{j}_H \equiv j_0 \tag{2.26}$$

$$\eta \equiv \phi_{ml} - \phi_{eq.} \tag{2.27}$$

Where η is the overpotential. Combining (2.25), (2.26) and (2.27), and rearranging the results, yields:

$$j_H = \vec{j}_H - \overleftarrow{j}_H = j_0 \left[\exp\left((1-\alpha) \cdot \eta \cdot \frac{F}{RT} \right) - \exp\left(-\alpha \cdot \eta \cdot \frac{F}{RT} \right) \right] \tag{2.28}$$

The (2.28) is called **the Butler-Volmer equation** (for a single electron transfer) [87]. Plotting (2.28) into current-overpotential curve as Figure 2.17:

1) Linear region- at low η, (i.e. below 50mV, since $RT/(1-\alpha)F$ is around 50mV at room temperature in most cases [88]), expense Taylor series of (2.28) yields:

$$j_H \approx j_0 \cdot \eta \cdot \frac{F}{RT} \tag{2.29}$$

i.e. the total current increase linearly with the over potential.

2) Exponential region- at high η, one of the terms in (2.28) can be neglected:

2a) η is large and positive:

$$j_H \approx j_0 \exp\left((1-\alpha) \cdot \eta \cdot \frac{F}{RT} \right) \quad \text{or:} \quad \ln j_H \approx \ln j_0 + (1-\alpha) \cdot \eta \cdot \frac{F}{RT} \tag{2.30}$$

8 **Equilibrium** does in general correspond to nonzero voltage $\phi_{eq.}$ that will be discussed in more detail in chapter5.

2b) η is large and negative:

$$j_H \approx -j_0 \exp\left(-\alpha \cdot \eta \cdot \frac{F}{RT}\right) \quad \text{or:} \quad \ln j_H \approx \ln j_0 - \alpha \cdot \eta \cdot \frac{F}{RT} \tag{2.31}$$

A plot of $\ln j$ vs. η is called a Tafel plot (Figure 2.17b). The slope of such a curve is, obviously, $(1-\alpha)\cdot\frac{F}{RT} \approx (1-\alpha)\bullet 38.92\ [V]$, from which the transfer coefficient α can be extracted (see (2.30), (2.31) and Figure 2.18).

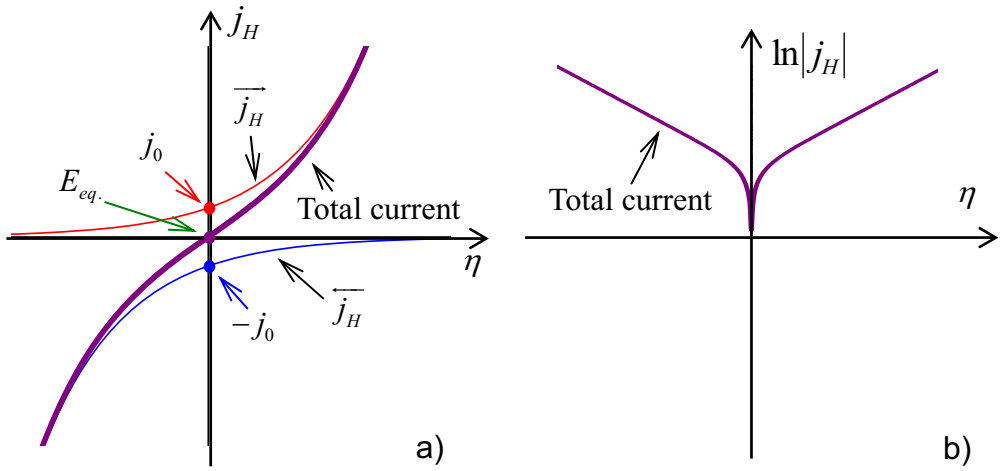

Figure 2.17 *Current-overpotential curves for a single electron transfer reaction. The current is in linear scale (a) and natural logarithm scale (b).* η *is the overpotential, with* $\eta > 0$ *on the anodic side and* $\eta < 0$ *on the cathodic side.*

iii) Absorbance Process: Tafel Reaction

Similarly, if we assumed that the mass transport process (2.12) and the preceding Volmer reaction (2.13) is close to equilibrium while the Tafel reaction (2.14) is out of equilibrium, then we have the electrochemical potentials (following the definition of electrochemical potential and (2.13)) as [87]:

$$\bar{\mu}_{H^+} + \bar{\mu}_{e^-} = (\mu_{H^+} + F\phi_l) + (\mu_{e^-} - F\phi_m) = (\mu_H)_{ad} \tag{2.32}$$

Inserting the Nernst equation (2.9) and neglecting the activity coefficients, i.e., assuming $a_{H^+} = c_{H^+}$ and $(a_H)_{ad} = \theta_H$, and rearranging (2.32) yields:

$$F\phi_{ml} = F\phi_m - F\phi_l = \left[(\mu_{H^+})^{\ominus} + RT\ln c_{H^+}\right] + \mu_{e^-} - \left[(\mu_H)^{\ominus}_{ad} + RT\ln\theta_H\right] \tag{2.33}$$

In the working electrode/reference electrode circuit, constant contributions in the above equation can be combined into a constant, and results in a new Nernst equation:

$$\varepsilon = E_{H_{ad}/H^+} = const + \frac{RT}{F}\ln\frac{c_{H^+}}{\theta_H} \tag{2.34}$$

Following the Tafel's assumption: the rate of the recombination reaction should be proportional to θ^2 [87], i.e.

$$i_H \sim \theta^2 \tag{2.35}$$

Combining (2.34) and (2.35) yields:

$$i_H = const' \cdot c_{H^+}^2 \cdot \exp\left(-\frac{2F}{RT}\varepsilon\right) \tag{2.36}$$

From the above equations, obviously, if the Tafel reaction is rate limiting, the $\log|i| - \varepsilon$ plot (Figure 2.18) has a slope of: $d\varepsilon / d\log|i_H| = 2.303RT / 2F = 0.029V$.

iv) Summary: A Comparison of the Three Different Limiting Steps

To sum up, provided the hydrogen evolution reaction is a single-step-controlled process, i.e., not of mixed-control, the current-potential curves look like Figure 2.18. And hence by measuring and plot such a curve, we can predict which one is the limiting step.

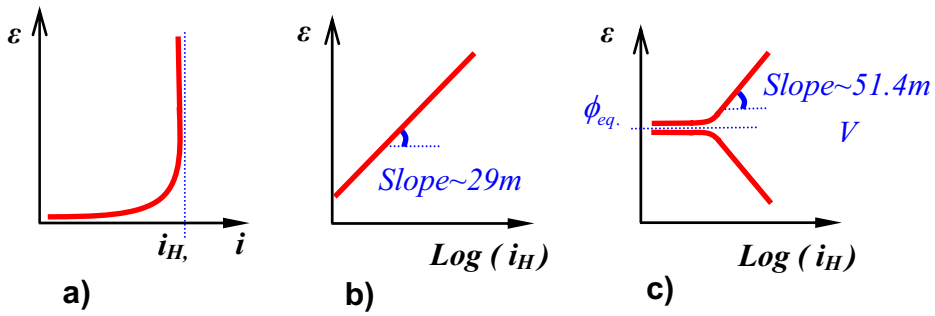

Figure 2.18 *Current-potential curves for hydrogen deposition governed by rate-determination of diffusion controlled a), adsorption controlled b) and charge transfer controlled c). i_H is the current density in arbitrary unit; ε is the electrode potential in arbitrary unit.*

Chapter 3 Sample Preparation

3.1 Hydrogen Terminated Diamond Surfaces

Smooth, well polished single crystal diamond plates type Ib or IIa with (100) surface are used in the experiments. Atomic Force Microscopy (AFM) shows that the RMS (Root Mean Square) roughness of the samples is below 0.3nm. For type Ib samples, an 80 nm thick intrinsic diamond film is epitaxially grown on top of the (100) surface as the active layer. The samples are wet-chemically cleaned and then treated with hydrogen microwave plasma. The experimental processes are shown in Table 3.1 and Table 3.2. After hydrogen termination, the samples were stored in normal atmosphere for one day to allow a stable state conductivity.

Table 3.1 *Wet chemical cleaning.*

Step	Purpose	Chemicals	Temperature	Time
1	Dissolving metallic contamination	$HCl:HNO_3 = 3:1$	150°C	30mins
2	Dissolving graphitic contamination	$H_2SO_4:HNO_3 = 4:1$	300°C	30mins
3	Removing chemical solvents	deionized water	RT	~
4	Drying the sample	flowing N_2 gas	RT	3mins

Table 3.2 *Microwave assisted hydrogen plasma treating.*

Step	Gas	Pressure	Microwave	Temperature	Time
1	H_2 flux: 100 ml/min	50 mbar	500 W	600 °C	30mins
2			500 W	350 °C	5mins
3			0W	350 °C to RT	10mins

3.2 Monolayer Graphene Surfaces

The graphene samples are produced on the silicon-terminated (0001) face of a semi-insulating, hexagonal 6H-SiC single crystal by high-temperature annealing in an inert gas atmosphere [89]. The average thickness of the graphene layer was 1.05 ± 0.1

monolayer.

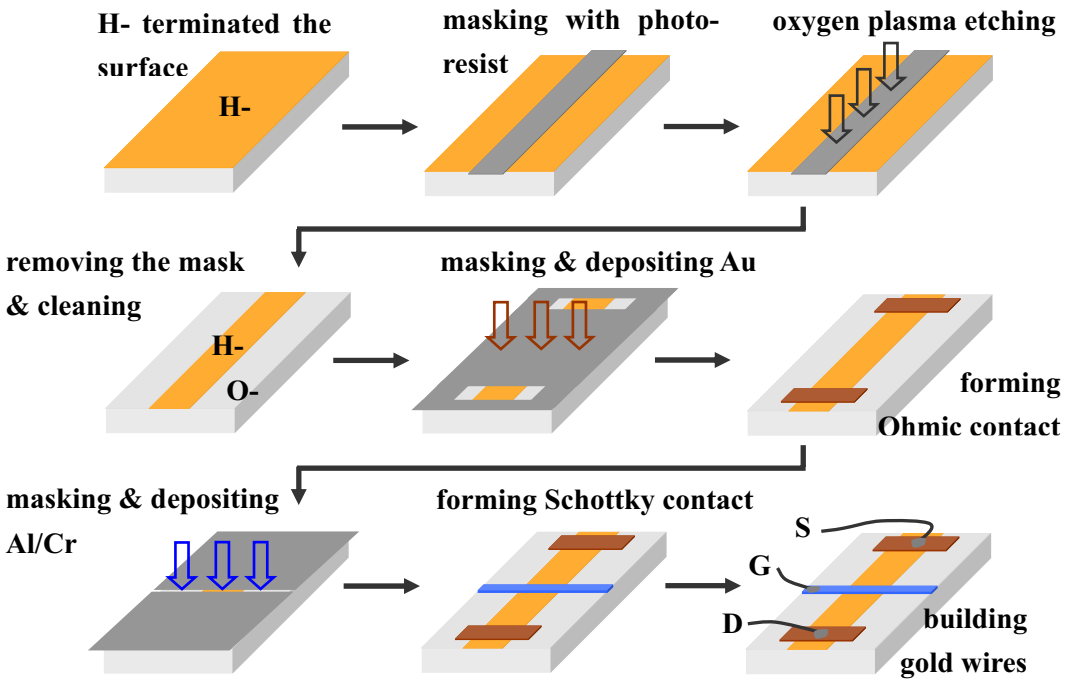

Figure 3.1 *Process steps for diamond based MESFET fabrication (description is in chapter 7).*

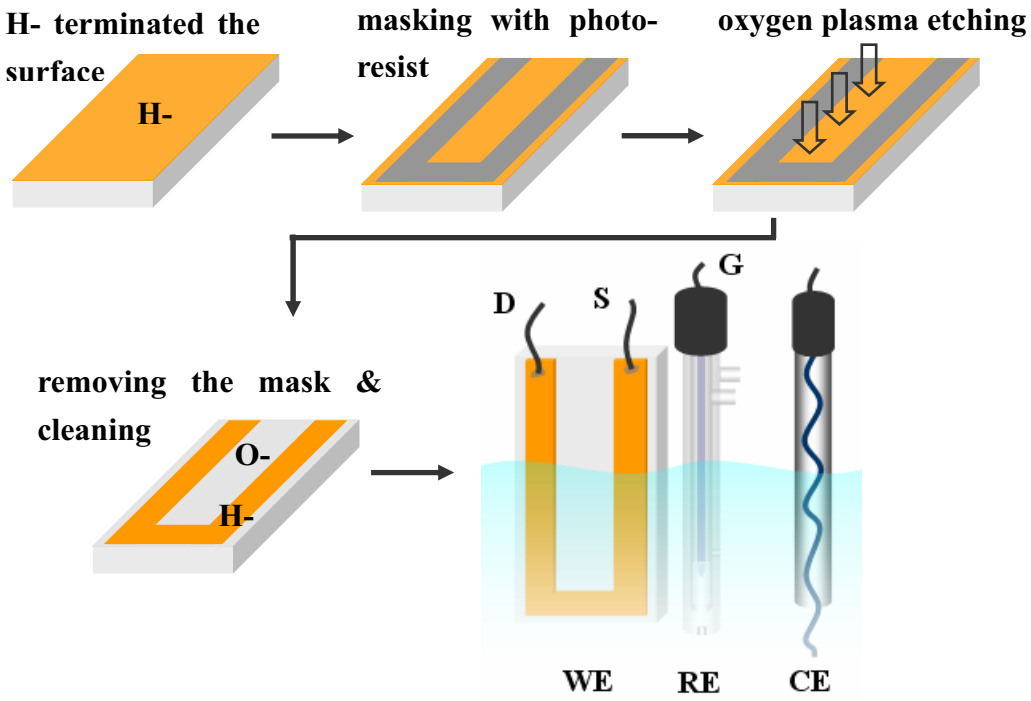

Figure 3.2 *Schematic illustration of the diamond based SGFET fabrication process. The process steps for constructing graphene based SGFET are similar (description is in chapter 8).*

3.3 Preparation of Electrolytes

The electrolyte, titrated with H_3PO_4 and KOH to adjust its pH value, is consisted of 10mM phosphate buffer and 10mM KCl. To produce 1000 ml of 0.01 M Phosphate (pKa=7.2) Buffer at room temperature, with a pH of 7 and an ionic strength of 0.019 M, the recipe is as following [90, 91]:

Step 1 Dissolve 1.2 g of e.g. KH_2PO4 (Mr= 136 g/mol) in approx. 900 ml of pure water, and add 0.746 g KCl (Mr = 74.56).

Step 2 Titrate to pH 7 at the lab temperature of 25°C with KOH (10%) base or H_3PO_4 (10%) acid.

Step 3 Make up volume to 1000 ml with DI water.

Step 4 Recheck the pH value of the buffer.

3.4 Fabrication of Field Effect Devices Based on Carbon Materials

The process of fabricating carbon surface based field effect transistor (FET) is shown schematically in Figure 3.1 (diamond based metal semiconductor field effect transistor, MESFET) and Figure 3.2 (diamond and graphene based solution gated field effect transistor, SGFET). Description of the devices is in part II.

PART II TRANSFER DOPING OF CARBON SURFACES

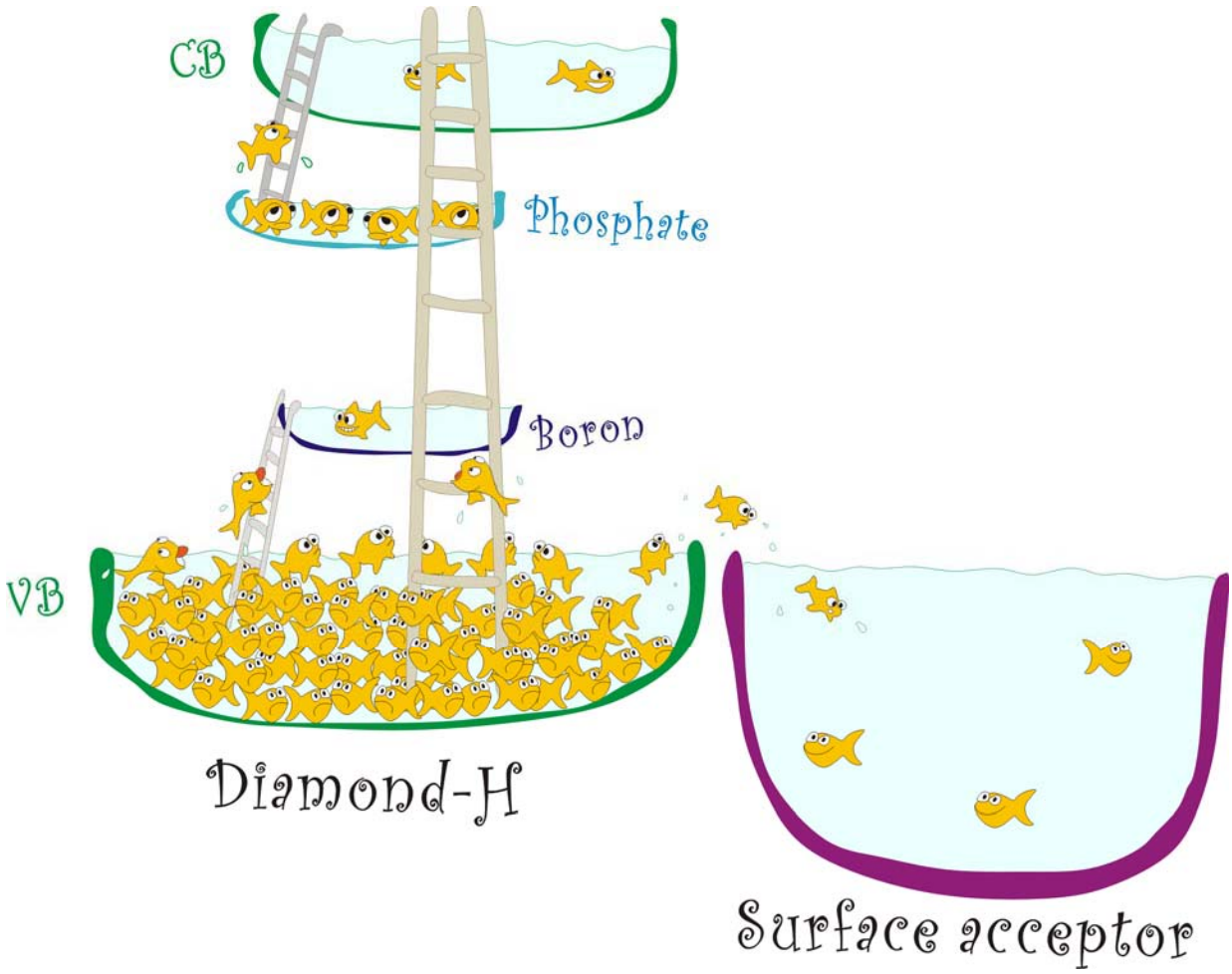

Chapter 4 Surface Transfer Doping of Carbon Surfaces in Controlled Atmosphere

4.1 Transport Characteristics of Hydrogen Terminated Diamond

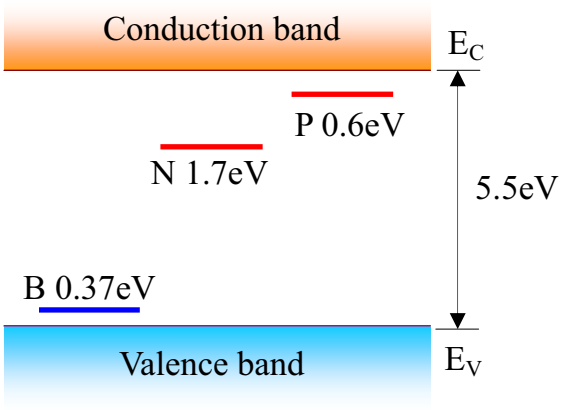

Figure 4.1 *Activation energy for conventional acceptors and donors in bulk diamond, data was taken from [92].*

Thanks to its many outstanding properties (see Table 2.2) like exceptional high thermal conductivity, breakdown field and electron and hole mobility, diamond reveals great potential for realizing high-frequency and high-power devices, specifically for use under adverse conditions and in harsh environment applications. Experimentally, p-type or n-type bulk diamond is achieved via adding dopants like boron or phosphorus during the diamond growing process. However, the doping for such a wide bandgap, atomic dense semiconductor, has turned out to be a tricky task that limits electronic applications of diamond. Donors and acceptors levels are far away from the band edges of diamond, which yields a low degree of ionization at room temperature (see Figure 4.1).

In 1989, Landstrass and Ravi [3, 4] found a novel p-type conductive phenomenon on hydrogenated surfaces of intrinsic diamond. **When exposed to normal atmosphere**, such surfaces exhibit the following features: a p-type 2D conductivity with a sheet resistance of the order of $10-20k\Omega/\square$, a shallow acceptor level with an apparent activation energy of less than 50mV, a high sheet concentration of more than $10^{13} cm^{-2}$ of charge carriers, and a

hole mobility of around $100-150 cm^2/Vs$ [5, 6]. The thickness of the conductive layer is estimated to be less than 10nm [7]. Kazushi Hayashi et al. [5] presented a comparative Hall-effect study of B-doped epitaxially grown diamond films oxidized and hydrogen terminated surfaces. The Hall effect results along with those of secondary ion mass spectroscopy (SIMS) inferred that: 1) although the conduction of both hydrogenated undoped and B-doped samples is **p** type, the carrier density p_s of both hydrogenated samples at room temperature (RT, 297K), however, are around $3\times10^{13}\mathrm{cm}^{-2}$, which is 4~5 orders of magnitude larger than that of the oxidized B-doped sample ($4\times10^{8}\mathrm{cm}^{-2}$) and are nearly constant in the temperature range of 150 to 400 K; in addition, the Hall mobility of the hydrogenated films is 1~2 orders of magnitude smaller than that of the oxidized B-doped film at 297 K and increases with temperature, while that of the oxidized B-doped film decreases. The authors concluded that that most of the free carriers (holes) in the hydrogenated B-doped sample at RT were not due to the B acceptor, but **had another origin!**

The first one was developed on the basic of classical concepts of doping in semiconductors. Landstrass and Ravi [3, 4] assigned the role of hydrogen to the passivation of donor like bulk or surface defects which in turn were held responsible to cooperate a p-type base conductivity of unspecified origin. Later, also this p-type base conductivity was directly assigned to hydrogen by classifying hydrogen-related point defects in the subsurface region of the diamond lattice acting as shallow accepters. These so-called sub-surface hydrogen accepters dominated the discussion of the hydrogen-induced surface conductivity for a number of years and were the basis of even more elaborated models that were developed to explain the electrical characteristics of surface field effect devices based on the hydrogen-induced surface conductivity. They claimed, however, inconclusive positioning the subsurface hydrogen acceptor in a nm-range directly below the surface [8, 9] or even claiming a “separation layer” between them and the surface [10]. In order to substantiate the sub-surface by hydrogen accepter concept, a number of potential hydrogen related point defects were studied theoretically by density functional theory (DFT) calculations in search for a shallow acceptor level. No point defect was found appropriate. The subsurface hydrogen acceptors remained speculative. In this situation, Maier et al. [11] suggested an alterative doping model based on a concept that was novel in solid state and semiconductor physics: the electrochemical surface transfer doping model [11, 13]. This model was based on qualitative results by Ri Sung-Gi et al. [12] who found a significant response of the hole density and mobility associated with the hydrogen-induced surface conductivity when samples are exposed to acidic or alkaline atmosphere. Acidic conditions increase surface conductivity while an

alkaline ambient lead to a decrease (see Figure 4.2).

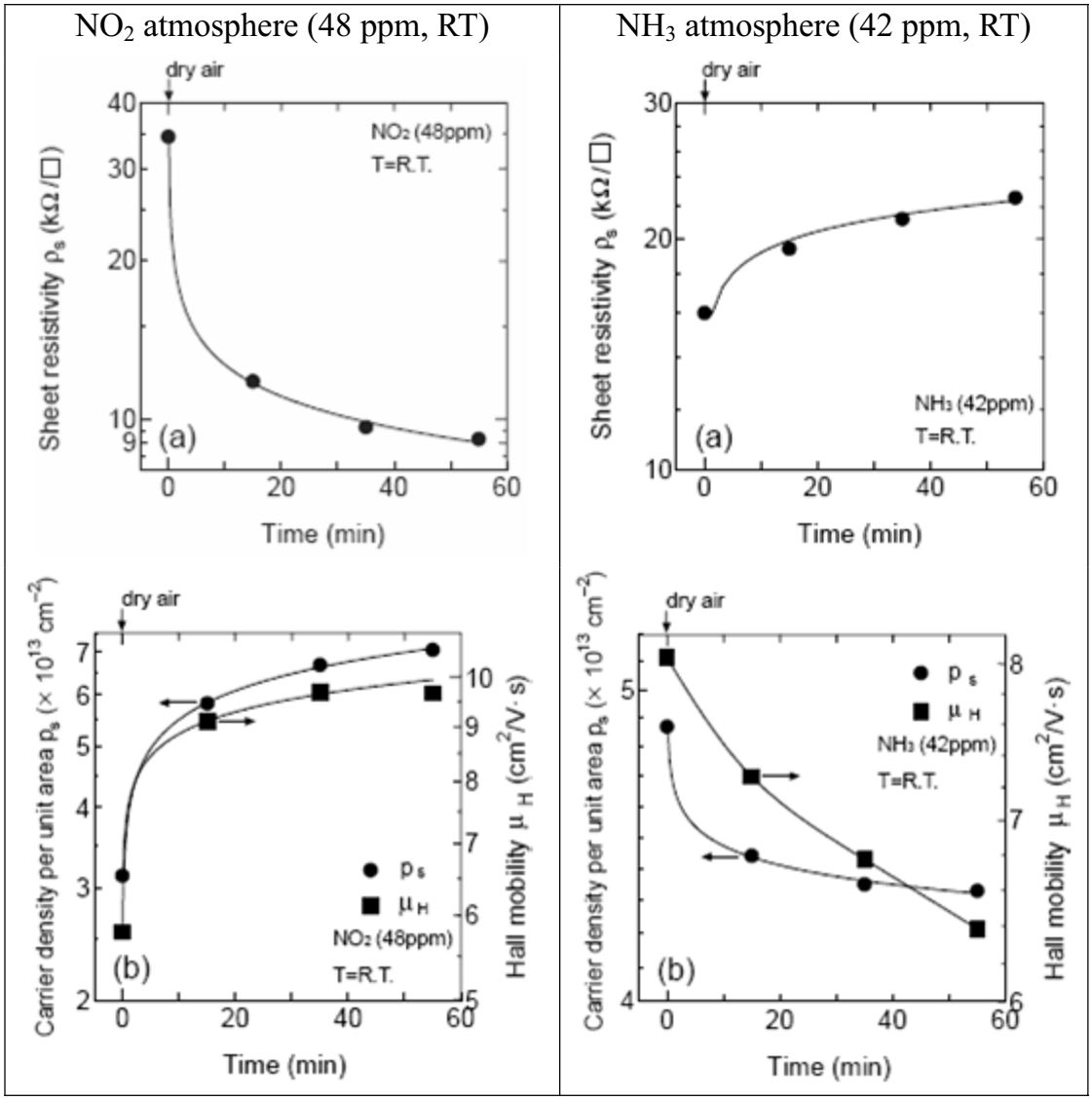

Figure 4.2 *Time dependence of diamond-H in NO_2 (48 ppm) and NH_3 (42 ppm) gas atmospheres at room temperature. Each value at t=0 corresponds to the values in dry air [12].*

In 2000, Maier et al. [11] suggested their doping model mentioned above in which they explained the pH sensitivity and the exceptional role of the hydrogen terminated of the diamond. In their model, doping is not achieved via specific acceptors in the diamond lattice, but by electrochemically active red-ox couples forming on the diamond surface in humid atmospheres. The role of the hydrogen termination is only indirect by lowering the ionization energy of the material sufficiently. This lead to a situation where the valence band maximum (VBM) of the hydrogen terminated diamond surface is just above the chemical potential of the red-ox electrons associated with the water layer from atmosphere that is physisorbed at the surface. Electron transfer form diamond to the $H_3O^+ / (H_2O + H_2)$ redox couple is thus accomplished and accounts for the hole accumulation layer, driving

the redox reaction toward equilibrium:

$$2H_3O^+ + 2e^- \rightleftharpoons 2H_2O + H_2 \tag{4.1}$$

Each electron transfer in this way leaves a hole behind and a negative action that was originally accompanying the ions. The driving force for the electron transfer is the difference in chemical potential of electrons in the liquid phase μ_e and in diamond (Fermi level E_F). In equilibrium μ_e and E_F are equal at the interface (as shown schematically in Figure 4.3), following Nernst's equation (see chapter 2.3.2):

$$\mu_e^{[H_2]} = \mu_0 - \left(\frac{kT}{2}\right)\ln\left[\frac{\left(\left[H_3O^+\right]/\left[H_3O^+\right]_{SHE}\right)^2}{\left(\left[H_2\right]/\left[H_2\right]_{SHE}\right)}\right] \tag{4.2}$$

$\mu_0 = -4.44eV$ is the chemical potential for red-ox electrons associated with (4.1), i.e. concentration (1 mole/liter) standard hydrogen electrode (SHE) conditions; thus, $\left[H_3O^+\right]_{SHE}$ and $\left[H_2\right]_{SHE}$ are the hydronium and the density of dissolved hydrogen of the SHE, respectively. Assuming the latter being proportional to the hydrogen partial pressure in the gas phase (1bar for the SHE) yields:

$$\begin{aligned}\mu_e^{[H_2]} &= -4.44eV + \frac{0.059}{2}eV\left[2pH + \log\left(\frac{p_{H_2}}{bar}\right)\right] \\ &= -4.44eV + 59meV\left[pH + \frac{1}{2}\log\left(\frac{p_{H_2}}{bar}\right)\right]\end{aligned} \tag{4.3}$$

It can be seen from (4.3) that, at constant partial pressure of H_2, μ_e merely depends on pH value of the aqueous layer at the atmospheric conditions. As long as $\mu_e^{[H_2]}$ lies above the Fermi level at the diamond surface, electrons transfer from hydrogenated diamond into the water layer and build up the surface conductivity. This process courses to a halt when $\mu_e^{[H_2]} = E_F$ is achieved.

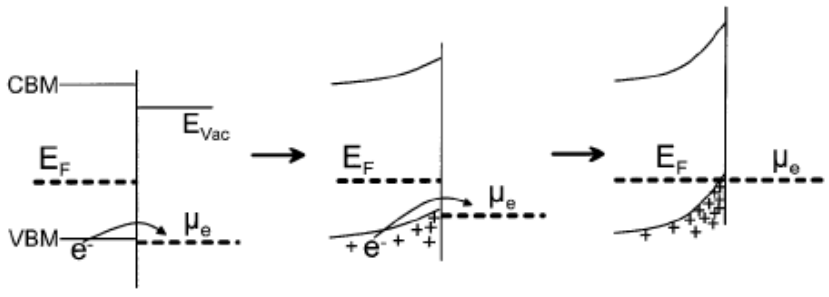

Figure 4.3 *Evolution of band bending during the electron transfer process at the interface between diamond and the water layer [11]. We omit the superscript* $^{[H_2]}$ *in the figure.*

Within the framework of electrochemical transfer surface doping mechanism, J.Foord et al. [14] and J. Angus et al. [13] proposed that the O_2 red-ox couple instead of the H_2

red-ox couple in the absorbed water layer were responsible for the transfer doping process due to the equilibration of:

$$O_2 + 2H_2O + 4e^- \rightleftharpoons 4OH^- \tag{4.4}$$

Their reasoning is that chemical potential $\mu_e^{[O_2]}$ of the O_2 red-ox couple is lower than that of the H_2 red-ox couple. The equilibrium value $\mu_e^{[O_2]}$ of reaction (4.4) can be calculated following a similar procedure as for the H_2 red-ox couple:

$$\begin{aligned}\mu_e^{[O_2]} &= -4.84eV + \frac{0.059}{4}eV\left[4\cdot(14-pH) - \log\left(\frac{p_{O_2}}{bar}\right)\right] \\ &= -5.67eV + 59meV\left[pH - \frac{1}{4}\log\left(\frac{p_{O_2}}{bar}\right)\right]\end{aligned} \tag{4.5}$$

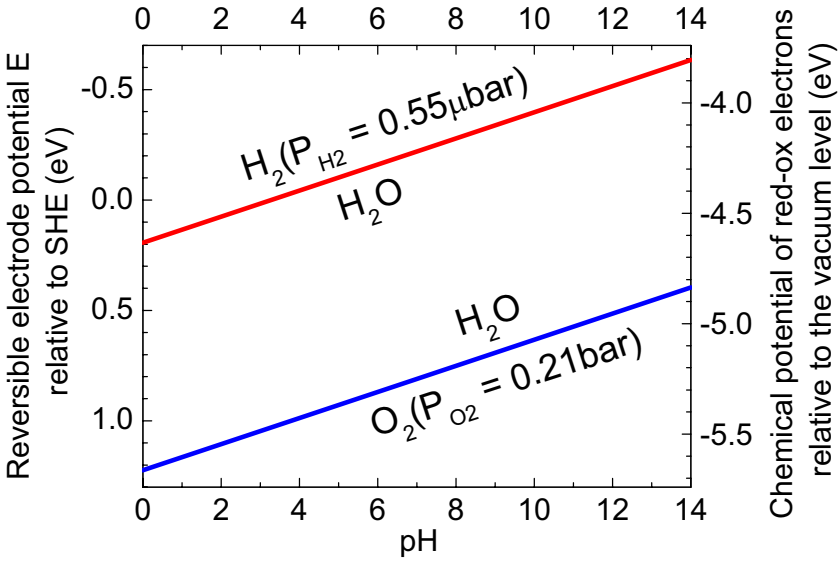

Figure 4.4 *Eh-pH diagram of water. The red line represents the upper limit of water stability and the blue line represents the lower limit of stability. The slop of the two lines are 0.059V/pH. The energy scale, indicated in electron volts, using either the standard hydrogen electrode (SHE, right scale) or the vacuum level (4.44eV relative to SHE, left scale).Detail is in the text.*

Indeed, both of these reactions participate in the transfer doping process, establishing a so-called mix-potential. A more systematic study of this concept will be presented in Chapter 5. Here, as an introduction and simple explanation for the experimental results reported in the early literature on surface conductivity, we briefly describe it qualitatively. Relating the concentration of dissolved hydrogen and oxygen in the aqueous layer to their partial pressure in atmosphere, i.e. $p_{H_2} = 0.55\mu bar$ and $p_{O_2} = 0.21bar$ [93], the chemical potential of the red-ox electrons associated with the H_2 and the O_2 couple are, respectively:

$$\mu_e^{[H_2]} = -4.22eV + 59meV(pH - 7) \quad (4.6)$$

$$\mu_e^{[O_2]} = -5.25eV + 59meV(pH - 7) \quad (4.7)$$

Following our discussion of section 2.3.2, this can be translated to the reversible electrode potentials E for both red-ox couples:

$$E_{H_2} = -0.22 - 0.059V(pH - 7) \quad (4.8)$$

$$E_{O_2} = 0.81V - 0.059V(pH - 7) \quad (4.9)$$

Plotting these electrode potentials as a function of pH is the famous Eh-pH diagram shown in Figure 4.4. In an electrochemical cell operating with an SHE as a reference electrode, the Fermi level at the surface of the working electrode polarized by a voltage U vs. the reference electrode can be directly translated to the left hand scale of Figure 4.4.

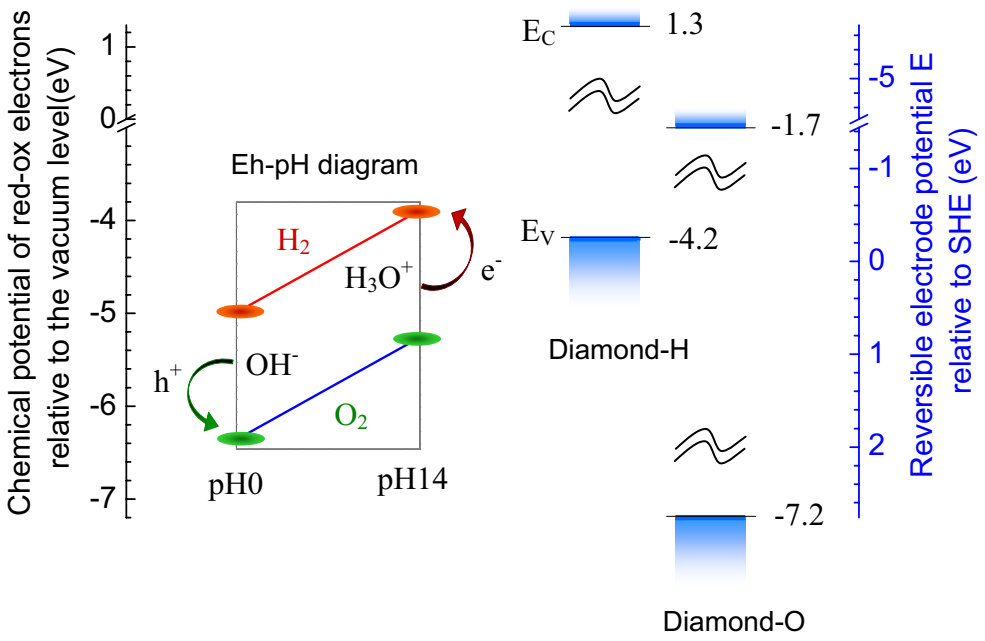

Figure 4.5 *Transfer doping of diamond (hydrogen terminated and oxygen terminated) by two pair of redox couples: the H_2 red-ox couple and the O_2 red-ox couple at pH0 and pH14. Their energy relative to valence band maximum of hydrogen terminated diamond is shown, with a common vacuum/SHE ruler as reference.*

Thus for a given cell voltage and pH the diagram shows directly which of the two electrode reactions is driven catholically or anodically. If, for example, the cell voltage U and the pH are such that the diagram yields a working point between the two reversible potential lines, the hydrogen reaction is anodic, converting H_2 to H_3O^+ and the oxygen reaction is cathodic converting O_2 to OH^-. We will discuss this situation in more detail in chapter 5. The specific cell voltage for which both reactions are at the same rate but with

opposite polarity, i.e. cancel each other in terms of electrical current is an important characteristics of the cell: it is the voltage which the cell establishes itself (without a voltage source) by the equilibration of the working electrode with the ensemble of active red-ox couples. This is the so-called open circuit voltage. The corresponding condition in terms of electrostatic potential and charge density profiles (compare chapter 5) are identical to the ones for the isolated electrode surface in contact with the electrolyte. Thus, also the areal hole density at the diamond surface is defined by the open circuit condition explained above, implying a Fermi level position at the diamond surface (relative to the vacuum level) between the H_2 and the O_2 line in the Eh-pH diagram. This diagram is replotted together with the band diagram for hydrogenated and oxygen-terminated diamond in Figure 4.5.

According to Figure 4.5, as the pH value of the water layer increases, the chemical potential of the H_2 red-ox couple and of the O_2 red-ox both couple move upward relative to VBM of diamond. Let's consider the H_2 red-ox couple for the time being (similar analysis holds for O_2 red-ox couple). Provided that the partitial pressure of H_2 is constant, then as the pH value of absorbed water increases, the chemical potential $\mu_e^{[H_2]}$ of the red-ox electrons of the H_2 red-ox couple as well as the Fermi level E_F of diamond move up since $\mu_e^{[H_2]} = E_F$ in equilibrium, resulting in less holes, i.e. poorer conductivity. Similarly, lowering the pH value enhances the conductivity. Following this theory, the Hall effect results by Ri Sung-Gi et al. [12] are understood in a straight-forward fashion: when introducing HCl (pH decreases), the surface conductivity of hydrogen terminated diamond increases, while introducing NH_3 (pH increases) leads to the opposite result. Similar results that follow this prediction of the charge transfer doping model have been presented by Foord et al. [94] and Kohn et al. [15, 95]. Note that in the work by Kohn et al. [15, 95, 96], measurements were done via a so call "ungated ISFET" geometry. ISFET is the short representative for "ion sensitive field effect transistor", sometimes also referred to as "solution gated field effect transistor", SGFET. For a constant control voltage applied to the electrolytic gate, also the SGFET on the basis of hydrogen-terminated diamond eventually shows a pH dependence of the areal hole concentration in the surface conductive layer: increasing pH leads in this case to an increase of hole concentration and conductivity, i.e. just the opposite of that is expected under open circuit conditions when following the transfer doping model as discussed above. This apparent "contradiction" was misinterpreted as evidence against the transfer-doping model [44, 97-100] for quite some time by a number of researchers. This reasoning was founded on misconception. The transfer doping model based on the chemical equilibrium between the diamond surface and the electrolytic ambient. In the SGFET geometry, this equilibrium is not established; in

general it is even prevented by the gate voltage. Detail discussion of a hydrogenated diamond SGFET is in Chapter 8.

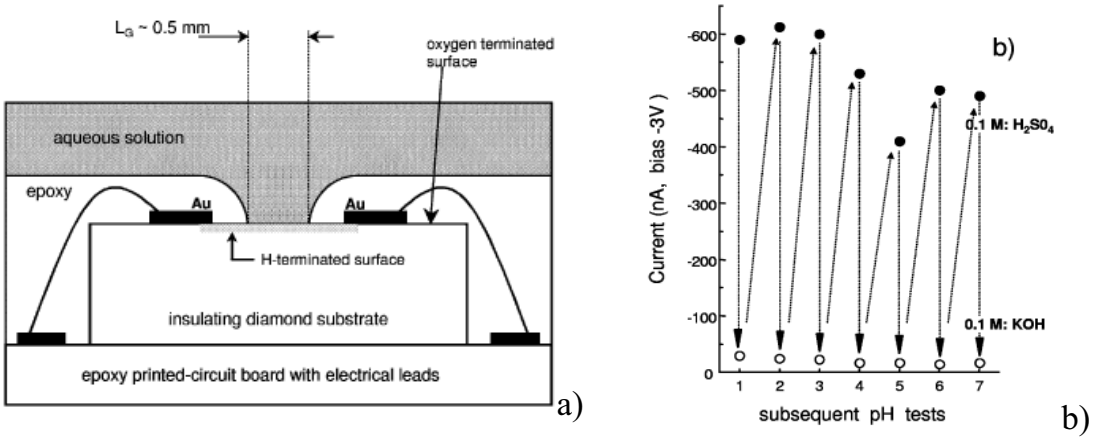

Figure 4.6 *a) Schematic cross-section of an "ungated ISFET" on a hydrogen terminated diamond surface channel by Kohn et al. [15]; b) the "output current" of the "ISFET" in sequential pH tests [15]. Their cycling experiments showed that acidic solution (0.1M H_2SO_4) increases the current (conductivity) while base solution (0.1M KOH) reduces it.*

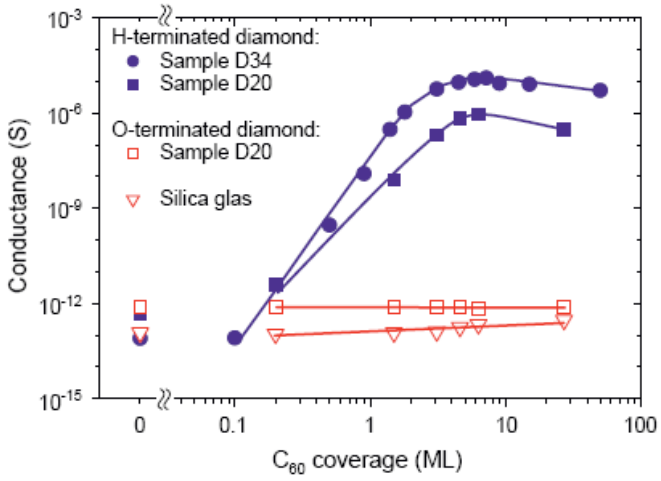

Figure 4.7 *Conductance of different substrates as a function of C60 coverage, by P.Strobel et al. [17]. Full data points: deposition on hydrogenated diamond; open data points: controlled experiments.*

The charge transfer doping mechanism, however, is not limited to hydrogenated diamond in contact with aqueous solution or a humid vapor phase, i.e. in the field of electrochemistry, but also works for matter that lies at the surface of diamond and has potential for acting as a surface acceptor. P. Strobel et al. first established the mechanism outside electrochemistry. They evaporated fullerenes (C_{60}, solid phase) [16, 17] and fluorinated fullerenes ($C_{60}F_{48}$, in molecular form) [17] onto hydrogenated diamond surfaces, and found that both species induce p-type surface conductivity on a level comparable (C_{60}) or even higher ($C_{60}F_{48}$) than that observed under atmospheric conditions. Similarly, Qi et al. [18] demonstrated p-type surface transfer doping of hydrogenated

diamond (100) by the molecular electron acceptor tetrafluoro-tetracyanoquinodimethane (F4-TCNQ).

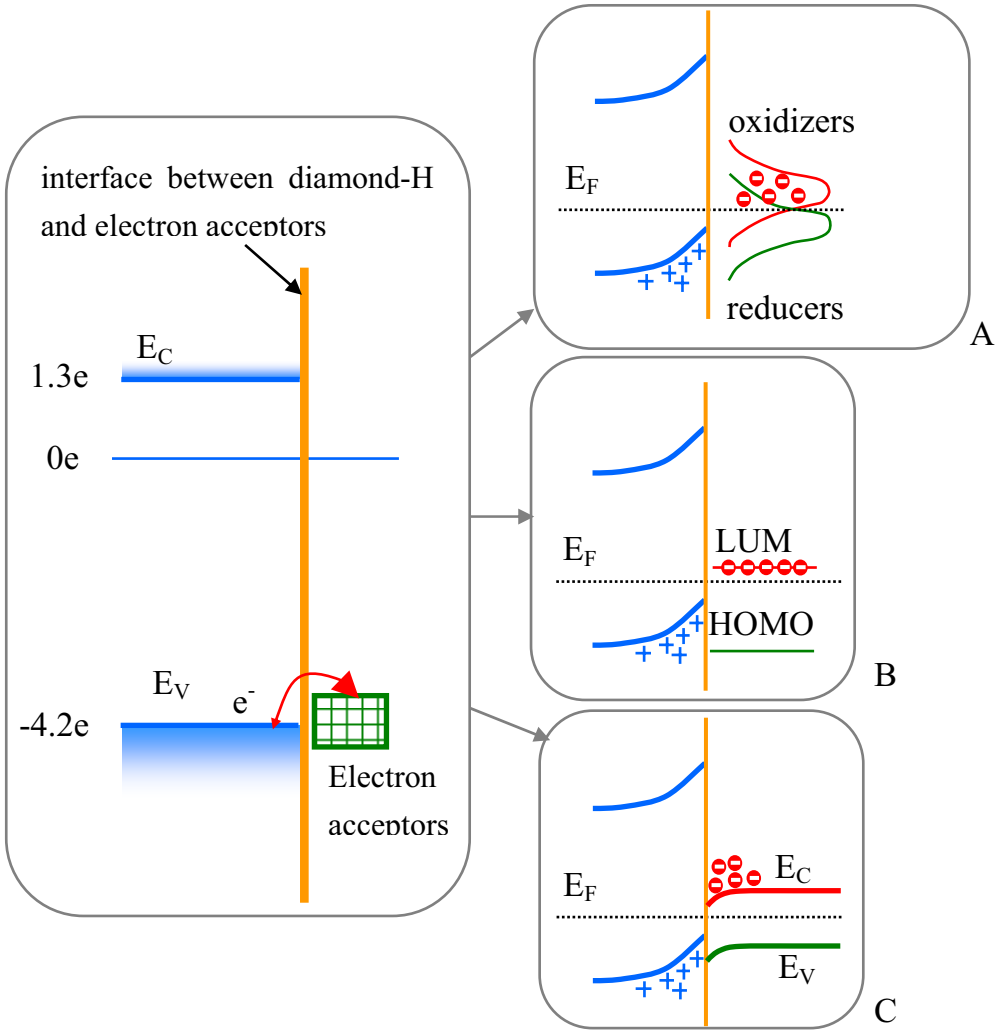

Figure 4.8 *Surface transfer doping of hydrogenated diamond: electrons are transported from the valence band of diamond into the "electron acceptors" that are located on the surface. Examples of "electron acceptors" are: A) oxidizers in an electrochemical reaction [11]; B) molecular adsorbates like flurofullerenes [17]; C) solid fullerite [16, 17]. Explanation is in the text. Note that for oxygen terminated diamond, the valence band maximum energy is -7.23eV relative to vacuum (see Figure 4.5). This value is much below the Fermi energy of any potential electron acceptor and transfer doping for diamond-O has consequently never been observed.*

In summary, surface transfer doping has been proven to take place at hydrogen terminated diamond surfaces. The criterion of a qualified electron acceptor is that the activation energy from the valence band maximum of diamond to the excited electronic states residing on the surface is not too large. Examples of appropriate electron acceptors on hydrogenated diamond are (see Figure 4.8) (A) oxidants that remove electrons from diamond via a redox reaction. The reactions may take place in contact with a bulk electrolyte or an electrochemically active moisture layer in appropriate atmosphere. (B)

Molecular adsorbates with sufficiently high electron affinity that serves as dopants ($C_{60}F_{48}$, F4-TCNQ) [17, 18]. The electrons transfer from the valence band of diamond into the lowest unoccupied molecular orbital (LUMO) of the adsorbate. Note that the HOMO (highest occupied molecular orbital) level is to organic molecules what the valence band is to inorganic semiconductors. The same analogy exists between the LUMO level and the conduction band. The energy difference between the HOMO and LUMO level is regarded as molecular band gap energy; (C) Solid fullerite, which forms a heterojunction with diamond [16, 17]. These variations of surface transfer doping are schematically illustrated in Figure 4.8.

4.2 Transport Characteristics of Graphene

4.2.1 Introduction

The graphene sheet is a two-dimensional electronic system. The band structure of its electronically relevant π and π^* bands is represented by cones in the corners of the hexagonal Brillouin zone that touch at the Fermion energy, making graphene a zero-band-gap semiconductor or a semimetal. Due to the strictly linear dispersion relation, electrons and holes represent massless, relativistic quasi-particles, and the cones are denoted as Dirac cones. However, doping of graphene in the traditional way, i.e. via replacing certain matrix atoms by impurities, seems to be an impossible task. In stead, the doping of graphene is realized by adsorbing atoms and/or molecules on its surface [13, 21, 22]. K. S. Novoselov et al. [19, 101] are the first group that studied the resistivity variation of graphene upon inducing gases. They suggested that gas adsorption can increase the number of the holes if the gas is an acceptor or increase the number of electrons if the gas is a donor. Following their frontier work, researchers found that the induced gas may change the resistivity of graphene, and the sign of the change indicated whether the gas was an electron acceptor (e.g. NO_2 [23, 101-106], H_2O [23, 101, 107, 108], octanoic acid [107], and I_2) or an electron donor (e.g. NH_3 [23, 101, 104, 105, 109], trimethylamine [107], CO [23, 101], NO [23] and ethanol [19]).

To understand the mechanism of the doping process, O. Leenaerts et al. [23] performed first-principles study of the gas molecule absorption on graphene and proposed the so called “chemical doping model”. They suggested two charge transfer mechanisms in the doping process: i) a charge transfer can occur due to the relative position in the density of states (DOS) of the HOMO and LUMO of the adsorbate. If the HOMO is above the

Fermi level of pure graphene (the Dirac point), there is a charge transfer to graphene. If the LUMO is below the Dirac point, charge will transfer to the molecule. ii) The charge transfer between adsorbate and graphene is also partially determined by the mixing of the HOMO and LUMO with the graphene orbitals (hybridization). This mixing scales with the overlap of the interacting orbitals and the inverse of their energy difference.

T. O. Wehling et al. [24, 25], based on their density functional theory (DFT) calculations, presented a quantitative results on the "chemical doping" model. On classifying the adsorbate into two groups, i.e. closed-shell molecules and open-shell molecules, they found that:

i) for closed-shell molecules or atoms, like H_2O, are chemically inert and exhibit gaps between HOMO and LUMO on the order of 5~10eV. In order to have these adsorbates to donate or accepts electrons to/from graphene, a chemical potential mismatch between molecule and graphene of the same order of magnitude is required. However, they may still influence graphene by redistributing charges within graphene or between graphene and its substrate.

ii) For open-shell molecules, like NO_2, alkali and most halogen ad-atoms, are very reactive, since their gaps between HOMO and LUMO are much smaller (of the order of 1eV). Thus, they may come along with additional molecular orbitals close to the Dirac point of graphene and act as direct dopants. They accept or donate one electron, bind ionically to graphene but hybridize weakly with the graphene bands and experience very low migration barriers.

Hwang et al. [25, 110], however, proposed a different physical model for the changes in graphene's conductivity during gas exposure, called the "scattering mechanisms". They assumed that Coulomb scattering is the dominant limit on mobility. And charge impurities created by gas adsorption on graphene partially neutralized the Coulomb scatters that are induced by the substrate, thereby allowing a rapid increase in mobility.

Up to now, most of the experimental works about transfer doping between graphene and gas species are based on two point conductivity measurements or graphene MOSFET devices, few is known about the kinetics of the doping process. The electrochemical surface transfer doping mechanism, although meanwhile established for diamond surfaces, has not yet been considered as a doping mechanism for graphene. In the following, we will study the charge transfer behavior of graphene samples in contact with gas species via in-situ Hall effect measurements. On analyzing the variation of charge carrier type, concentration and mobility in the graphene as a function of exposing time and gas atmosphere, we will show that not only charge transfer follows the electrochemical charge transfer mechanism but also the "scattering mechanism" (by Hwang et al. [25, 110]). Finally, we will show later that the doping process on graphene is equivalent to that

on hydrogen terminated diamond.

4.2.2 Experimental Setup

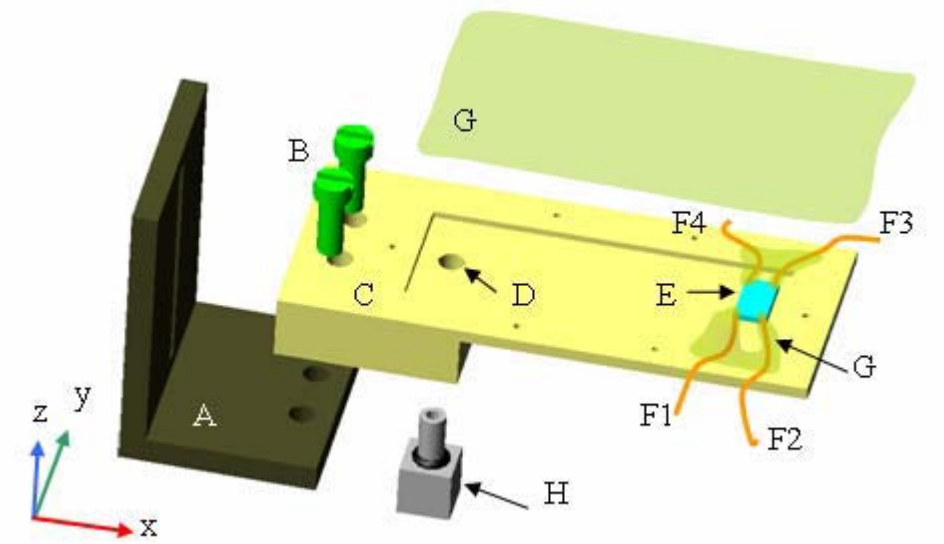

Figure 4.9 *Sketch the specifically designed sample holder used for the Hall effect measurements under controlled atmosphere. A) Aluminum holder, which is movable in x-y-z direction; B) screws that mount the sample holder; C) sample holder, which is fully sealed by epoxy (G) and has a window that open to the chemical atmosphere (H); E) Graphene sample, lied inside the sample holder; F1)~F4) contacts to the sample; G) epoxy cover; H) Teflon container. The magnetic field (varies from 0T to 0.7T) is along the "z" axis, which perpendicularly crosses the 2D plane of graphene sample.*

The samples used in this experiment were graphene sheets produced on the silicon-terminated (0001) face of a semi-insulating, hexagonal 6H-SiC single crystal by high-temperature annealing in an inert gas atmosphere [89] . The average thickness of the graphene layer was 1.05 ± 0.1 monolayer as determined from the x-ray excited photoelectron spectrum of the C1s core level by a procedure described elsewhere [71]. Later, the edge of the SiC plane is polished by sand paper to remove the graphitic contamination on the edge, so that the conductance is confined on the two dimensional graphene plate and fulfills the prerequisite for the van-der-Pauw contact geometry (see section 2.3.2). After following the standard cleaning procedure, the sample is transferred to a self-made setup as shown in Figure 4.9. Next, four gold wires, with their end touching the corners of the square in the Van der Pauw geometry, are connected to the graphene sample via silver paste contacts. Later, the contact area is carefully covered by a chemically resistive epoxy tape to avoid the metal contacts being attacked by the corrosive chemical

gases. Care is taken that the "gap" between any two neighboring contacts is not covered by epoxy and always open to the external atmosphere. Next, the whole chamber is sealed by epoxy except a 4mm diameter hole (called "window"), where optional Teflon container can be attached and thereby close the chamber. On filling the Teflon container with specific solution (before mounting the Teflon container to the sample holder), gas species from the solution corresponding to their specific vapor pressure are introduced into the sample chamber. When the Teflon container is removed, the "window" as well as the sample container, is thereby open to normal atmosphere.

a)

b)

Figure 4.10 *Ex-situ measurement of pH value in the gas experiments by pH dry papers. a) chambers that is filled with NH_3 (25%), KCl(10mM) and HCl (37%), respectively. The pH paper in all case is far beyond the liquid level. The liquid to chamber volume ratio is kept to be the same as the one in the Hall measurement. b) reference color for the pH indicator paper. By comparing the color of the testing pH paper and the reference, one can determine the pH value of the humid vapor: NH_3 (25%) ~ pH10, KCl (10mM) ~ pH7, HCl (37%) <pH1.*

Table 4.1 *Properties of the solutions and their vapor used in the experiments.*

solutions	NH_3 (25%)	HCl (37%)
vapor pressure at 20°C	0.48 bar [111]	0.15 bar [112]
pH value of vapor	10	<1

In the Hall effect measurement, two type of solutions are used: NH_3 (25%) and HCl (37%). The pH value of the vapors from the solution is measured ex-situ by the universal indicator paper (pH 1-14, graduation 1.0 pH, purchased from Carl Roth GmbH, Germany) (Figure 4.10) [9]. We choose the indicator paper rather than the more precise pH electrode

[9] First of all NH_3 (25% in water), HCl (37% in water) and KCl (10mM) solution are kept in three different glass containers. The volume between the solution and the whole glass container (ca. 1:40) is kept to be the same as that of the Hall effect experiment, so that the pH value of the atmosphere inside the container is expected to be the same as the one in the experiment. Later, dry pH paper that is kept above the liquid level by the PE plastic sticks is quickly added to the container. On closing the bottle, the color of the

because the latter one only works properly in solution but not in vapors phase. Properties of the solution are sum up in Table 4.1.

4.2.3 Results

All of the samples tested were n-type, as determined from their negative Hall coefficients. The measurements performed yield the sheet resistivity and sheet carrier concentration, from which carrier mobility values can be determined. The values obtained from each measurement are shown in Figure 4.11 to Figure 4.13. Note that the time scale here (at least a few minutes) is much larger than the one in the exsitu experiments monitoring the color variation of pH paper. In the latter case, the pH paper changes the color and becomes stable in a few seconds. Thereby we can neglect the time that is necessary for generating the homogeneous atmosphere and assume that the pH value of the bulk "vapor atmosphere", i.e. the one that is far away from the graphene-vapor interface, is in steady state during the Hall effect experiments.

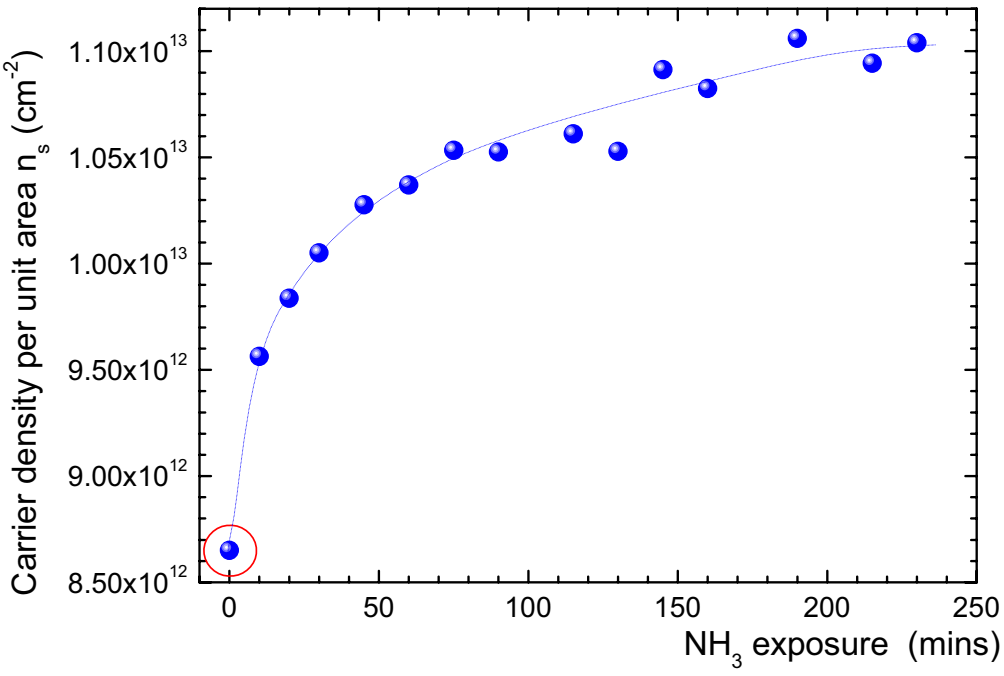

Figure 4.11 *Electron concentration of epitaxial graphene in humid ammonia environment and at room temperature. The data collected at 0 min (in red circle) refers to measurement in normal atmosphere. Shortly after that, the sample is exposed to NH_3 (25%) atmosphere.*

paper changes and becomes stable immediately (in a few seconds). The pH value of the humid atmosphere inside the container and also the one in the Hall effect measurement experiment can be obtained by referring to the color ruler of the pH papers.

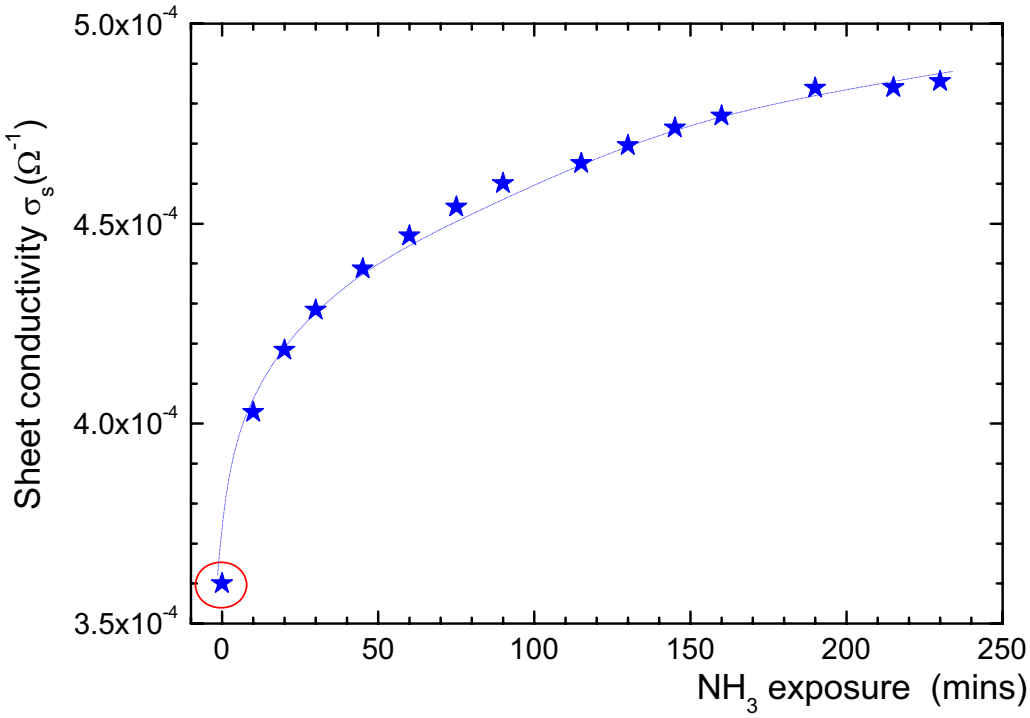

Figure 4.12 *Sheet conductivity of epitaxial graphene in humid ammonia environment and at room temperature. The data collected at 0 min (in red circle) refers to measurement in normal atmosphere. Shortly after that, the sample is exposed to NH_3 (25%) atmosphere.*

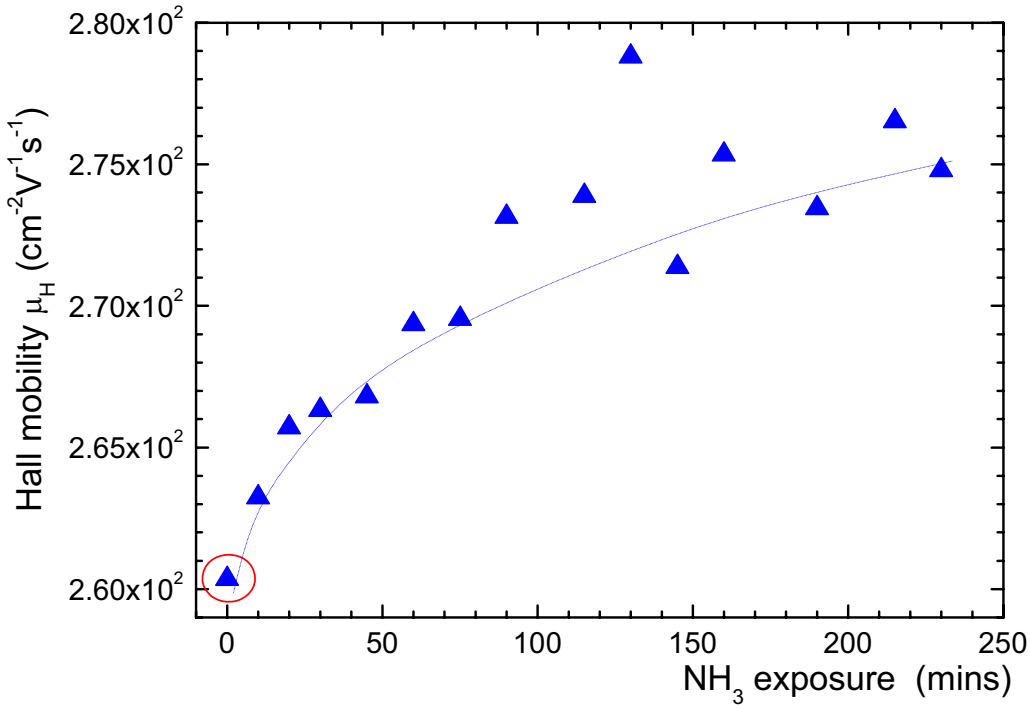

Figure 4.13 *Hall mobility of epitaxial graphene in humid ammonia environment and at room temperature. The data collected at 0 min (in red circle) refers to measurement in normal atmosphere. Shortly after that, the sample is exposed to NH_3 (25%) atmosphere.*

In Figure 4.11, the sheet carrier concentration of graphene n_S at time t=0 is

corresponding to the one at normal atmosphere. Shortly after the humid NH_3 gas is admitted to the chamber, n_S increases from $8.6\times10^{12}cm^{-2}$ to a saturation value of around $10.9\times10^{12}cm^{-2}$ at 200 mins, i.e. n_S raises by 27% relative to the value at t=0. The increase of n_S along with the negative sign of the Hall coefficient proves that, upon contact with the humid NH_3 atmosphere, additional electrons are transferred into graphene. The sheet conductivity σ_S of the graphene raises from $3.60\times10^{-4}\Omega^{-1}$ (at 0 min) to $4.85\times10^{-4}\Omega^{-1}$ (at 200 mins), i.e. by 35%. The Hall mobility $\mu_H=\sigma_s/(en_s)$ extracted from Figure 4.11 and Figure 4.12 varies only slightly (5%) in the experiment (Figure 4.13). Later, the humid NH_3 gas is removed via detaching the Teflon container and then purching the chamber by a fan. On waiting for long enough time (ca. 1~2 days), carrier concentration n_S, Hall mobility μ_H and sheet conductivity σ_S decrease gradually and finally yield values that are more or less identical with the ones at the start of the experiment. Thus charge transfer is reversible, albeit at a very long time scale.

In an equivalent set of experiments, humid hydrogen chloride gases (from 37% HCl solution) is introduced into the sample chamber. The transients determined from each Hall effect and conductivity measurements is plotted in Figure 4.14 to Figure 4.16. In all cases a negative Hall coefficient is detected.

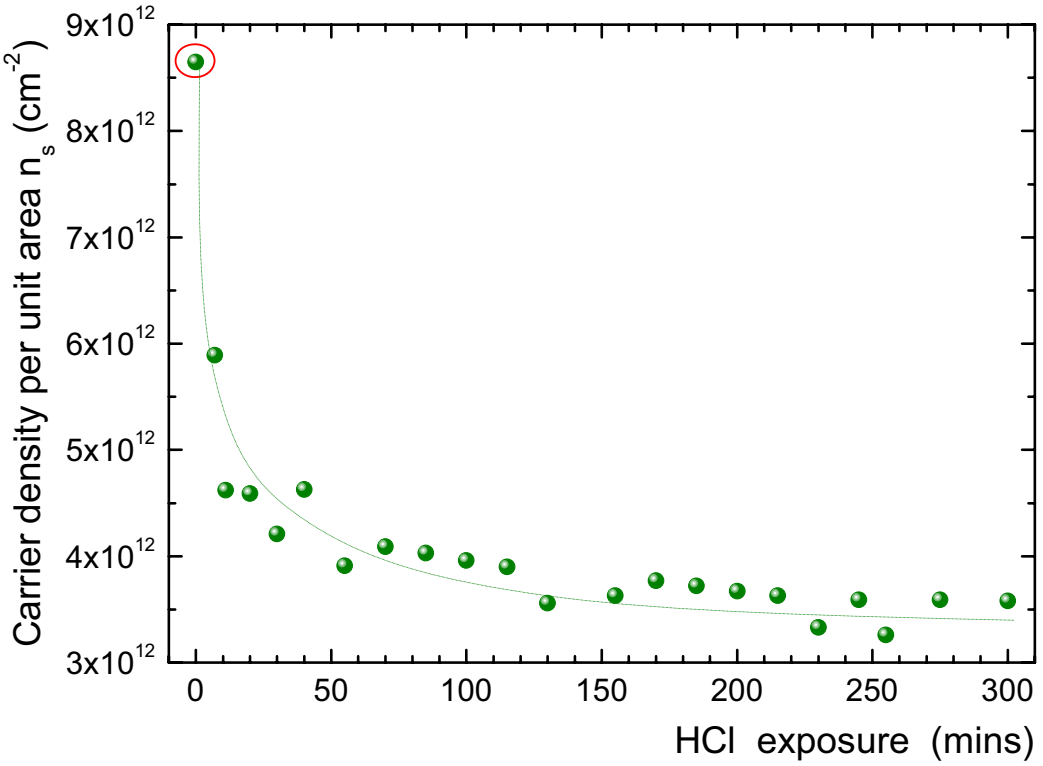

Figure 4.14 *Electron concentration of epitaxial graphene in humid HCl atmosphere and at room temperature. Before introducing to humid HCl gases, experiments are performed in normal atmosphere, as marked by red circle.*

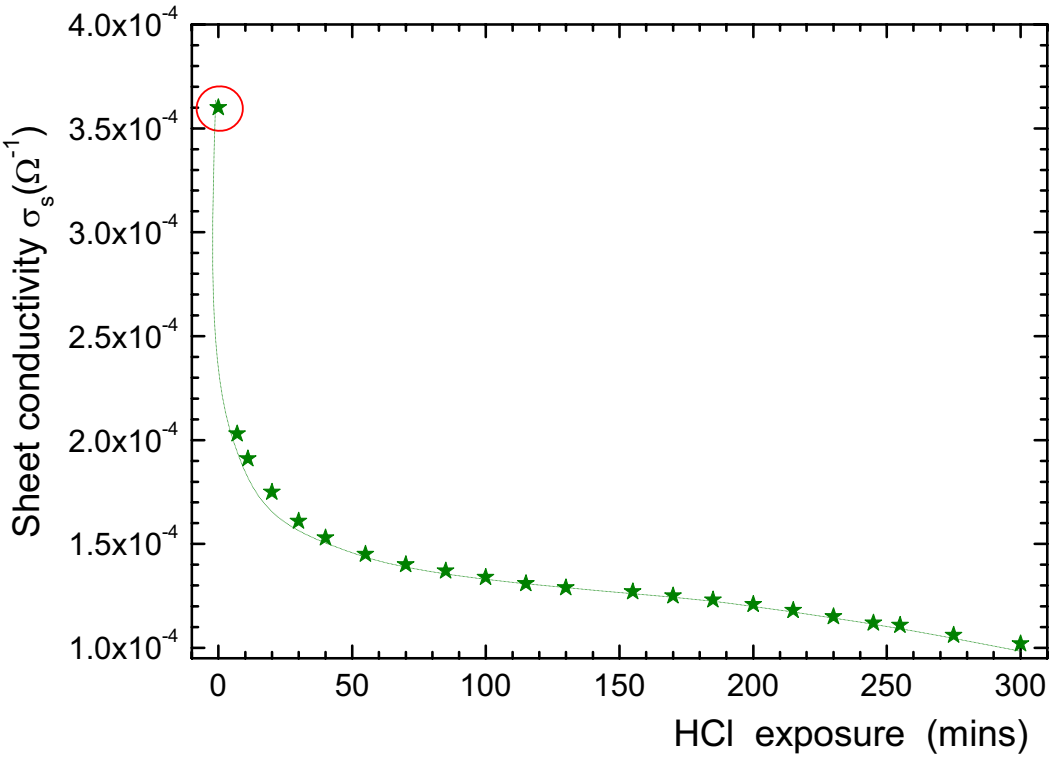

Figure 4.15 *Sheet conductivity of epitaxial graphene in humid HCl atmosphere and at room temperature. Before introducing to humid HCl gases, experiments are performed in normal atmosphere, as marked by red circle.*

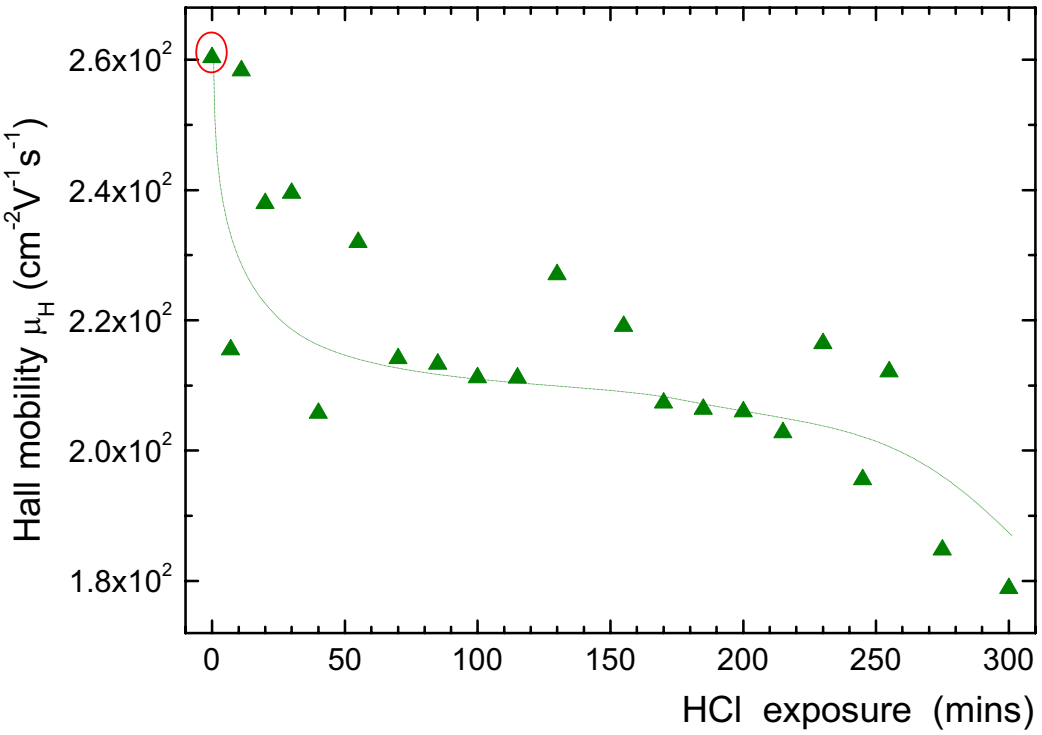

Figure 4.16 *Hall mobility of epitaxial graphene in humid HCl atmosphere and at room temperature. Before introducing to humid HCl gases, experiments are performed in normal atmosphere, as marked by red circle.*

In contrast to the NH_3 experiments, on exposure of graphene to humid HCl, the carrier concentration n_S decreases (Figure 4.14), from $8.6\times10^{12}cm^{-2}$ (at 0 min) to $3.3\times10^{12}cm^{-2}$ (at 230mins), i.e. by 62%. At the same time, the sheet conductivity σ_s shown in Figure 4.15, decreases by 72% to a minimum of $1.0\times10^{-4}\Omega^{-1}$ at 300 mins. The Hall mobility μ_H, which is calculated from sheet conductivity and sheet carrier concentration, reduces by about 31% from $260.5cm^{-2}V^{-1}s^{-1}$ to $178.9cm^{-2}V^{-1}s^{-1}$.

We notice that, in both HCl and both NH_3 experiments, the Hall mobility μ_H of the graphene sample varies slightly (Figure 4.13 and Figure 4.16). The variation of mobility suggests that there is negligible increase in scattering due to impurities [101, 110], the so-called the "scattering mechanisms" by Hwang et al. [25, 110]. Schedin et al. [101] proposed that, for example, the water absorption on graphene, or trapped between the graphene and substrate, provided sufficient dielectric screening of the gas-induced charged impurities to account for the lack of additional scattering with gas adsorption. Similar phenomena are found on diamond-H (see Figure 4.2).

4.2.4 Discussion

1. Charge Transfer Doping: Thermodynamics

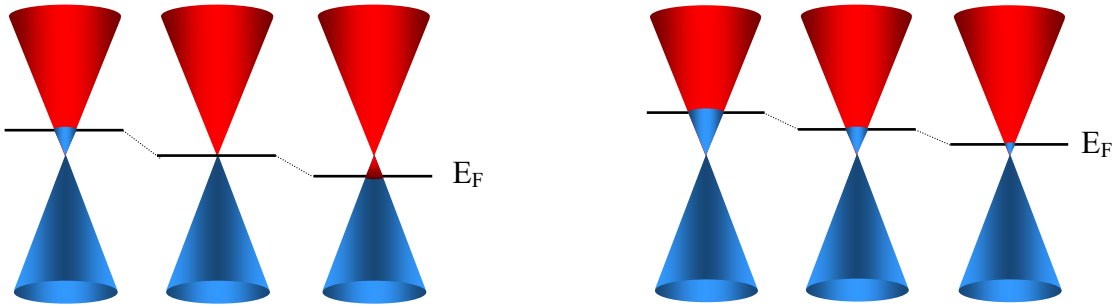

a) Free-standing graphene b) Epitaxial graphene

Figure 4.17 *a) Doping of free standing graphene. The left and right panels correspond to n-type and p-type doping, respectively, while the center panel represents the pure graphene layer; b) Epitaxial graphene on silicon carbide with a natural substrate induced n-type doping shown in the center panel, the Fermi level moves up (left panel) for gaining electrons and moves down (right) for losing electrons.*

By using Hall measurements, one can quantify the mechanism behind the electronic response of graphene to external atmosphere. The results in the former section show that the absorption of gases induces electron transfer to and from the graphene: humid NH_3 gas

increases both the electron concentration and the conductivity of graphene, while humid HCl gas decreases. In this case, humid NH_3 acts as a donor while humid HCl is an acceptor. Recall that the Fermi level is a strict measure for, and thus a monotonous function of, the density of valence electrons in a solid. For an n-type semiconductor, an increase of free charge carriers (electrons) thus corresponds to an up-ward shift of the Fermi level in a two-dimensional band structure representation as the one sketched in Figure 4.17. A down-ward shift, on the other hand, is always connected with a depletion of electron and an increase in hold concentration.

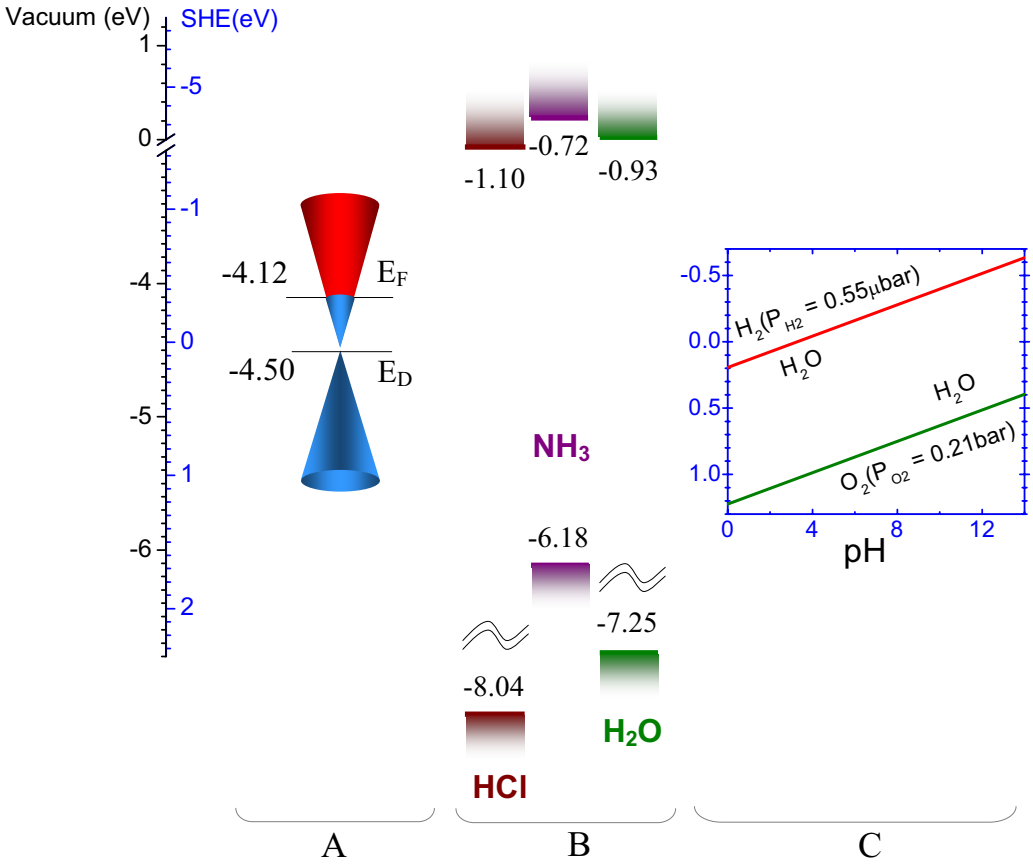

Figure 4.18 *Energy levels of graphene and its potential dopants. A) epitaxial SiC(0001)-graphene , with the Dirac point located at around -4.5eV [113] and the Fermi level of -4.12eV (calculated from (4.20)). B) highest occupied molecular orbital (HOMO) and lowest unoccupied molecular orbital (LUMO) of individual HCl, NH_3 and H_2O [114]. C) the electrochemical potential for the H_2/H_3O^+ and O_2/OH^- redox couples for typical atmospheric hydrogen and oxygen concentration and as a function of pH value calculated from Nernst equation. The energy scale has been linked to both the standard hydrogen electrode and the vacuum level.*

The question next is: is the graphene doped by the action of single gas molecules (NH_3, HCl or H_2O) as suggested by the models so far [23-25] for graphene, or, is due to the collective properties of an electrolytic ensemble of hydrated ions as suggested by the

electrochemical surface transfer doping model [11] [14] [13]? The HOMO and LUMO level of the individual gas molecules, as well as the chemical potential of the redox couples relative to the vacuum level are shown in Figure 4.18. The three types of gases that are used in our experiments, NH_3, HCl and H_2O are known as closed-shell molecules with large HOMO-LUMO gaps [114]. The Dirac point of graphene is separated from all HOMOs by at least 1.5eV and from all LUMOs by more than 3.0eV. Thereby, direct transfer doping of graphene by gas molecules is impossible, which, is as well suggested by T.O.Wehling et al. [24] from their theoretical studies. However, when those closed-shell molecules, NH_3 or HCl forms clusters with H_2O (or in chemists' language, undergo acid/base dissociation in water), the hydronium or hydroxyl ions (the electrochemical redox couples discussed in section 4.1) are generated. This in fact leads to thermodynamically favorable charge transfer reactions:

$$O_2 + 2H_2O + 4e^- \rightleftarrows 4OH^- \tag{4.10}$$

$$H_2 + 2H_2O \rightleftarrows 2H_3O^+ + 2e^- \tag{4.11}$$

Both reactions take place simultaneously, following the mix-potential theory (see chapter 5). In conclusion, the in-situ Hall effect experiments on graphene show that a basic atmosphere (NH_3) increases the number of electrons while an acidic atmosphere (HCl) reduces it. Similar experiments by Ri Sung-Gi et al. [12] on hydrogen terminated diamond found that on exposing such samples to a basic (NO_2) atmosphere the hole density increases, while exposing them to acidic environment (NH_3) resulted in the disappearance of the holes. These results are consistence with the electrochemical charge transfer doping model. In another word, the electrochemical surface transfer doping model is not limited to hydrogenated diamond but can be also applied to other two dimensional conductors like graphene. However, considering thermodynamic equilibrium only tells the tendency of a reaction and gives no information about its development in time. We will discuss the kinetics of the reaction in the following.

2. Charge Transfer Doping: Kinetics

As is discussed previously, the electron concentration of graphene increases/decreases as the sample is exposed to humid NH_3 / HCl gases. These additional charge carriers originate from external donors via electrochemical reactions. Consequently, the transient of the change of carrier concentration in graphene can be related to the kinetics of the (electro)chemical reactions. We adopt a simplified evaluation of the reaction of graphene exposed to humid acidic or basic atmosphere:

$$Graphene + e^- \rightarrow Graphene + R \tag{4.12}$$

$$Graphene - e^- \rightarrow Graphene + O \tag{4.13}$$

Here, graphene acts like an oxidant in equation (4.12) and as a reluctant in equation (4.13). We consider in both cases just the forward direction. They are of first order [115, 116] in the "reactant e^-" and thus depend only on the Fermi level position in the graphene. Consequently, we fit the charge carrier density vs. time as exponential transients (introduction about the reactions order is given in Appendix II). The best simulation results are then (see Figure 4.19):

$$n_s^{NH_3} = -2.2\times10^{12}\,cm^{-2}\cdot\exp\left(-t/40\,\text{min}\right)+1.1\times10^{13}\,cm^{-2} \tag{4.14a}$$

$$n_s^{HCl} = 4.8\times10^{12}\,cm^{-2}\cdot\exp\left(-t/15\,\text{min}\right)+3.6\times10^{12}\,cm^{-2} \tag{4.15b}$$

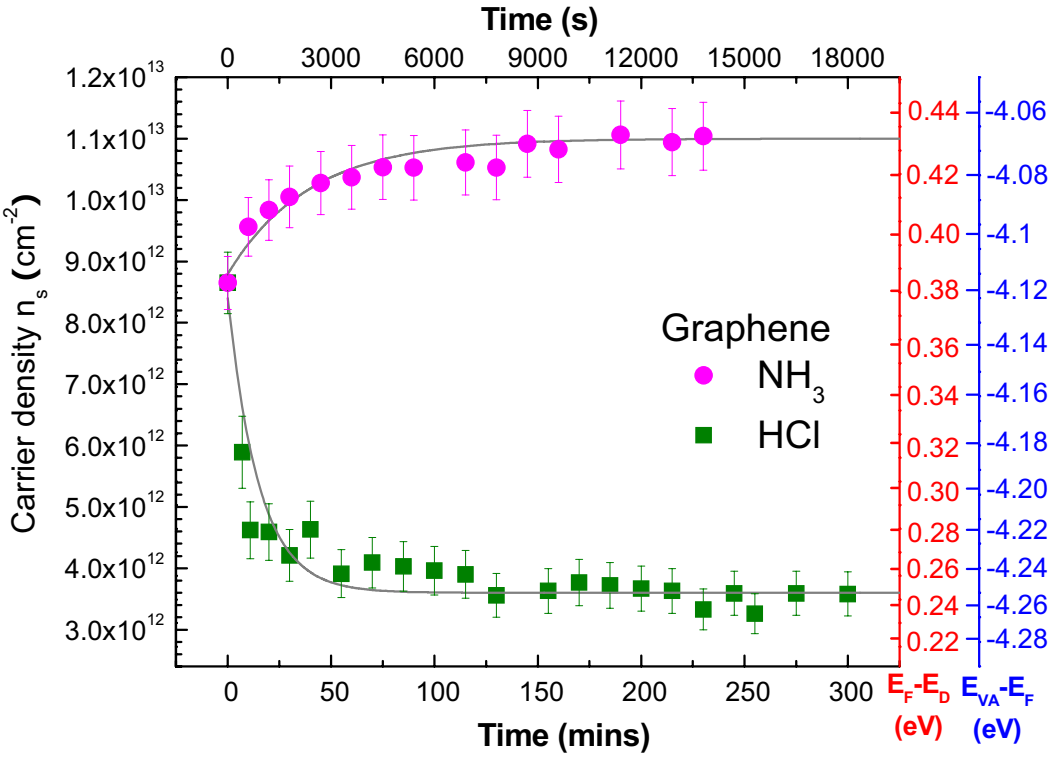

Figure 4.19 *Fit of the carrier concentration as a function of time (Figure 4.11 and Figure 4.14) for humid NH_3 and HCl gases, respectively, by exponential transients (full line). The left scale shows the areal carrier density n_s. The right scales shows the Fermi level relative to Dirac point (in red) and relative to the vacuum level (in blue). Calculation of the Fermi energy is in the text.*

Following the definition of current density, $j = \frac{dQ}{Area\cdot dt} = e\cdot\frac{dn_s}{dt}$, the charge transfer current density for the case of humid NH_3 and HCl is, respectively:

$$j^{NH_3}(t) = e\cdot\frac{dn_s^{NH_3}}{dt} = -1.47\times10^{-10}\,\frac{A}{cm^2}\cdot\exp(-\frac{t}{2400s}) \tag{4.16a}$$

$$j^{HCl}(t) = e\cdot\frac{dn_s^{HCl}}{dt} = 8.53\times10^{-10}\,\frac{A}{cm^2}\cdot\exp(-\frac{t}{900s}) \tag{4.17b}$$

where we count cathodic currents connected with a transfer of electrons from graphene to surface adsorbates as positive.

In graphene, the density of state $D(E)$ around direct point can be expressed as (i. e. the linear dispersion relation for charges close to the Fermi energy):

$$D(E) = \chi \cdot |E - E_D| \tag{4.18}$$

where $\chi = 1.18 \times 10^{14} cm^{-2} (ev)^{-2}$ (see [71] and section 8.4.2). And thus the areal charge density q_s in graphene can be related to $(E - E_D)$ as :

$$q_s = -\frac{1}{2} \chi \cdot (E - E_D)^2 \cdot sign(E - E_D) \tag{4.19}$$

For $E_F > E_D$, the areal density of electrons are:

$$n_s = -q_s = \frac{1}{2} \chi \cdot (E_F - E_D)^2$$
$$\text{or} \quad \sqrt{\frac{2n_s}{\chi}} = |E_F - E_D| \tag{4.20}$$

Thereby, one can relate the areal charge density from Hall effect experiments to the Fermi energy of both graphene, as shown in Figure 4.19 (right scale).

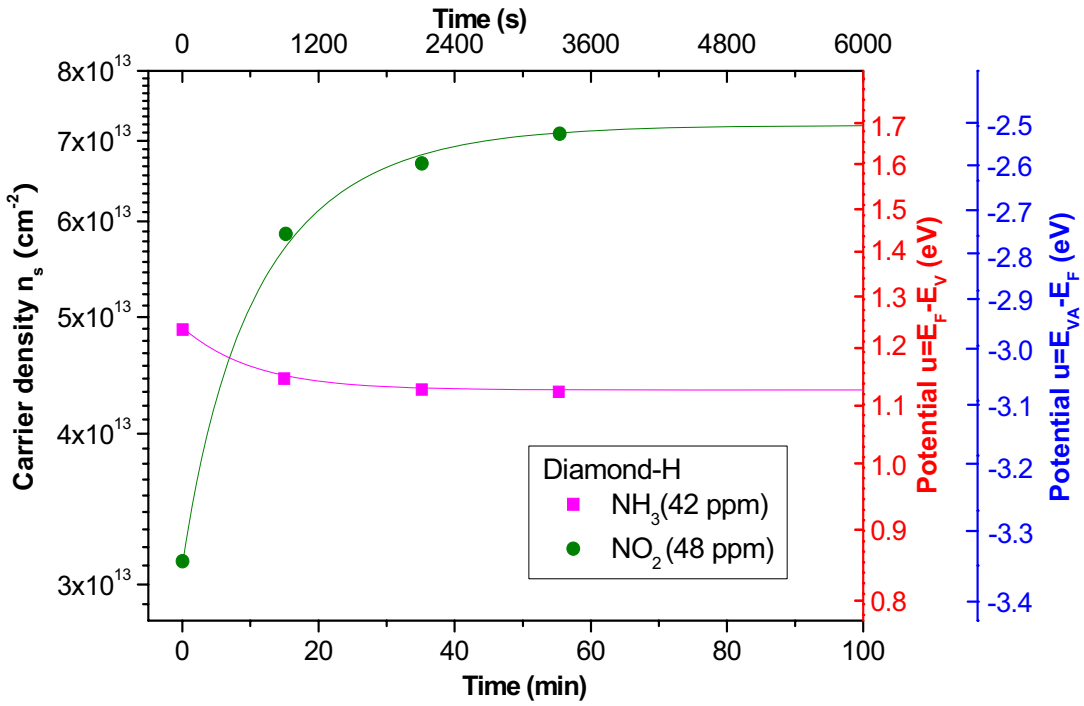

Figure 4.20 *Fit of Figure 4.2 (data is taken from Ri Sung-Gi et al. [12]). The carrier concentration as a function of time for humid NH_3 and HCl gases, respectively.*

At initial time, $t \to 0$, the net current density is dominated by current in one direction,

for humid NH_3, $j^{NH_3}{}_0 = -1.47\times10^{-10}\,Acm^{-2}$, and for humid HCl, $j^{HCl}{}_0 = 8.53\times10^{-10}\,Acm^{-2}$. At infinite time ($t \to +\infty$), the measured current density approaches zero, i.e. the absolute value of forward current is equal to backward current. In this case, thermodynamic equilibrium is achieved. By defining the charge-transfer resistance as: $R_{CT} = \left(E - E_{equ.}\right)\big/ j_0$, where $E_{equ.}$ is the equilibrium potential, then a simple evaluation gives: for humid NH_3, $R_{CT}{}^{NH_3} = -\left(0.38-0.43\right)V\big/1.47\times10^{-10}\,Acm^{-2} = 3.40\times10^{8}\,\Omega cm^2$ and for humid HCl, $R_{CT}{}^{HCl} = \left(0.38-0.25\right)V\big/8.53\times10^{-10}\,Acm^{-2} = 1.52\times10^{8}\,\Omega cm^2$.

Next, we perform a similar fit of the variation of the charge carrier concentration during the charge transfer process of diamond. The best simulation results are (see Figure 4.20):

$$n_s{}^{NH_3} = 5.5\times10^{12}\,cm^{-2}\cdot\exp\left(-t/10\,\mathrm{min}\right) + 4.35\times10^{13}\,cm^{-2} \tag{4.21a}$$

$$n_s{}^{NO_2} = -41\times10^{12}\,cm^{-2}\cdot\exp\left(-t/15\,\mathrm{min}\right) + 7.21\times10^{13}\,cm^{-2} \tag{4.22b}$$

The charge transfer current density for introducing humid NO_2 and HCl to diamond is, respectively:

$$j^{NH_3}(t) = e\cdot\frac{dn_s{}^{NH_3}}{dt} = 1.47\times10^{-9}\,\frac{A}{cm^2}\cdot\exp(-\frac{t}{600s}) \tag{4.23a}$$

$$j^{NO_2}(t) = e\cdot\frac{dn_s{}^{NO_2}}{dt} = -7.29\times10^{-9}\,\frac{A}{cm^2}\cdot\exp(-\frac{t}{900s}) \tag{4.24b}$$

Similar to graphene, the areal hole density n_S defines the Fermi level E_V relative to the valence band maximum E_V at the diamond surface $u_s = E_V - E_F$ (u_s is called surface potential), as described in detail in reference [117]:

for the non-degenerate case ($u_s < 0$): $$n_S(u_S) = \sqrt{\frac{2kT\varepsilon\varepsilon_0 N_V}{e^2}}\cdot\exp\left(\frac{u_S}{2kT}\right) \tag{4.25}$$

and

for the degenerate case ($u_s > 0$): $$n_S(u_S) = \sqrt{\frac{2kT\varepsilon\varepsilon_0 N_V}{e^2}}\cdot\sqrt{1+\frac{u_S}{kT}+\frac{8}{15\sqrt{\pi}}\left(\frac{u_S}{kT}\right)^{5/2}} \tag{4.26}$$

where $\varepsilon = 5.8$ is the dielectric constant of diamond, ε_0 the vacuum permeability, N_V the effective valence band density of states of diamond which amounts to $2.7\times10^{19}\,cm^{-3}$ at room temperature, e is the elementary charge, and kT is the thermal energy. And from these equations, one can relate areal carrier concentration to the surface potential and thus the Fermi level of diamond, as shown in Figure 4.20 (right scale).

At initial time, $t \to 0$, the net current density is dominated by current in one direction, on introducing NH_3, $j^{NH_3}{}_0 = -1.47\times10^{-9}\,Acm^{-2}$, and for NO_2, $j^{HCl}{}_0 = 7.29\times10^{-9}\,Acm^{-2}$. Similarly, the charge-transfer resistance of diamond-humid gas interface can be evaluated:

for humid NH_3, $R_{CT}^{NH_3} = (1.24 - 1.12)V / 1.47 \times 10^{-9} Acm^{-2} = 8.16 \times 10^7 \Omega cm^2$ and for humid NO_2, $R_{CT}^{NO_2} = -(0.86 - 1.70)V / 7.29 \times 10^{-9} Acm^{-2} = 1.15 \times 10^8 \Omega cm^2$.

4.3 Summary: Transfer Doping of Semiconductors

To sum up, in contrast to traditional doping, which requires introducing impurities into a semiconductor host lattices, "surface transfer doping" is a novel doping mechanism by which the dopant, without entering the semiconductor matrix, exchanges charge with the semiconductor across the semiconductor-dopant interface. The surface dopant can be less or more complex, from isolated molecules to thin solid layers up to electrochemical phases with various sorts of solvated ionic species [117], as shown in Figure 4.21. In the electrochemical surface transfer doping, dopants are red-ox couples. They are (in contrast to HOMO/LUMO and CBM/VBM) amphoteric. Each has a characteristic μ_e and all together they establish the "mixed potential equilibrium" for which also the lattice of the electrode reactions is involved.

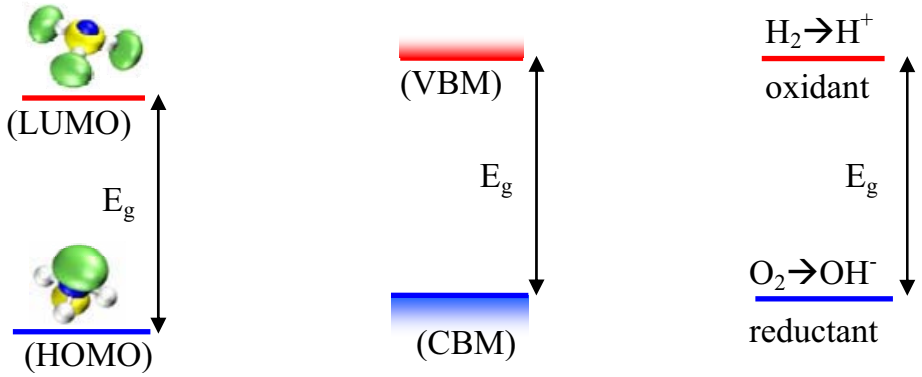

a) NH_3 molecule [23] b) Semiconductor c) Electrolyte [118]

Figure 4.21 *Examples of surface dopant: isolated molecules a), solid layers of semiconductor [119] or metal [120] b), and gaseous or liquid electrochemical red-ox couples c).*

Chapter 5 Red-Ox Processes at Carbon-Electrolyte Interfaces

5.1 The Concept of Polarizable and Nonpolarizable Interfaces

Red-ox processes in electrochemical circuits take place at electrode-electrolyte interfaces. The property of the interface determines the kinetics of the red-ox process. One of the most important properties of the interface is what electrochemists call its polarizability[10]. The definition of polarizable, according to J.O.Bockris et. al [88], is to what extent an interface resists or accepts potential changes. There are two limiting cases of electrode-electrolyte interfaces (or simply called "electrodes" in literatures):

- The ideal polarizable interface: It does not allow a DC current (the so-called faradayic current) to flow across the interface, irrespective of the voltage drop across it. Currents observed in circuit are with an ideal polarizable electrode, therefore, must be displacement currents, charging up capacitive elements;
- The ideal nonpolarizable interface: Even an infinitesimal change in the voltage drop across the interface causes an infinite faradayic DC current, such that changes of total voltages applied to a circuit must be distributed among the other sections of the circuit until new equilibrium concentration are established across the interface. Consequently, there are no overpotentials for this type of electrode. [121]. A comparison of these two terms is listed in Table 5.1.

In practice, neither of these ideal configurations can be produced. A real interface is neither ideally polarizable nor ideally nonpolarizable. Thus, it depends on the level of faradayic current allowed in any electrochemical circuit, if an electrode can be

[10] The term "polarizability" is sometimes confusing to nonchemists. One can make a comparison with the physical term "electric polarizability". In physics, electric polarizability is the tendency of charge distribution, like the electron cloud of an atom or molecule, to be distorted from its normal shape by an external electric field without a DC charge transport being induced. This concept is in electrochemistry extended to describe the electrode-eletrolyte interface as a whole. A polarizable electrode is one at which electric field changes, i.e. voltage drops, can be arranged such that charges are redistributed without DC currents to be induced.

approximated by one or the other limiting cases, or, eventually be none! Thanks to its relative small exchange current density j_0 as compared to other electrodes, e.g. active metal, the hydrogen terminated diamond electrode is generally described in literature as a polarizable electrode. It is even believed that there should be no charge transfer reaction at all across such an interface. However, this is in principle a misconception. Specifically when open circuit conditions are to be understood, the faradaic current density appears to be zero, and thus even the diamond electrode must be treated as a non polarizable one. In order to measure the red-ox process of diamond-electrolyte interface, i.e. its "nonpolarizable" behavior, we will perform two different types of experiments in the following: the open circuit potential measurement and the polarization curve measurements, both of which take relative long time as compared to those in the SGFET experiments (see chapter 8). In addition, we will do the same measurements on graphene samples. A comparison of diamond-H and graphene electrode will be presented finally.

Table 5.1 *Distinction of ideal polarizable and nonpolarizable interface.*

Interface	Ideal Polarizable	Ideal Nonpolarizable
General properties [86, 122]	Hard to pass a current across; NO charge transfer occur	Hard to change the potential; charge transfer take place
Equivalent circuit [88]	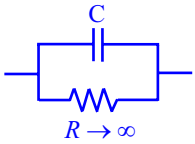	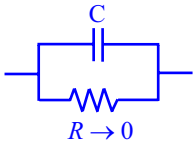
Analogue	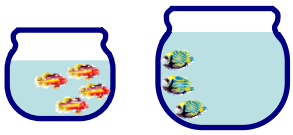 Leak-proof interface	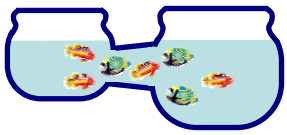 Infinitely-strong leaking interface
Current-potential curves	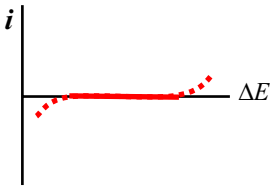	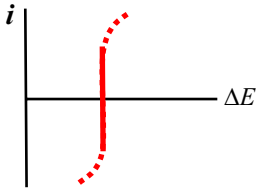
Examples	Mercury electrode, platinum electrode	Good reference electrodes, like Ag/AgCl

5.2 Experimental Setup

Two types of two-dimensional conductive carbon surfaces were used in the experiments: the hydrogen terminated diamond and the graphene sheet surface.

The diamond samples are type IIa (100) intrinsic single crystal diamond plates of 5 mm by 8 mm size. First of all, the diamond plates are treated with hydrogen plasma and kept in normal atmosphere for one day to allow stable conductivity (see section 3.1). Later, the plates are treated in different ways, yielding samples A to C:

● Sample A: fully hydrogen-terminated surface. There is no further patterning or oxidation treatment on the sample.

● Sample B: patterned hydrogen-terminated surface. The surface is patterned into a U-shaped H-terminated conductive channel, which is 16mm in length and 2mm in width. The remaining of the surface is treated by oxygen plasma and rendered insulating.

● Sample C: partially oxidized surface. The sample was exposed to peroxide (30%) for 30 minutes under simultaneous UV illumination by a mercury discharge lamp (254 nm, 20 W, 3 cm distance unfocussed). Such an oxidation process converts some of the C-H bonds into C-OH bonds, which is analyzed by IR spectroscopy as shown in Appendix IV.

The graphene samples are produced on the silicon-terminated (0001) face of a semi-insulating, hexagonal 6H-SiC single crystal by high-temperature annealing in an inert gas atmosphere [89]. The average thickness of the graphene layer was 1.05 ± 0.1 monolayer. Besides the diamond and graphene samples, a platinum wire with 0.5mm in diameter and 2cm in length is used for comparison study in place of the carbon electrodes as electrochemical working electrode.

Finally, silver paste and silver wire were used to fabricate perfectly ohmic contacts to the carbon surfaces. Care was taken that only the electrode surface and not the metal contact was exposed to the electrolyte. This was achieved without any epoxy or sealant, simply by dipping only the hydrogen-terminated diamond or graphene into the electrolyte and keeping the metal contacts out in air. The active electrode areas exposed to the electrolyte were $15 mm^2$ for all the carbon samples except diamond sample B, whose area is $11 mm^2$.

The electrolyte consisted of 10mM phosphate buffer and 10mM KCl which was titrated with H_3PO_4 and KOH to adjust the pH (see section 3.4). The reference electrode was an electrochemical Ag/AgCl electrode (3M KCl solution, Schott B2220). The red-ox potential of that electrode is +0.20 V vs. standard hydrogen electrode (SHE) at room temperature.

For measuring open circuit voltages (OCV), a Keithley 617 electrometer with an

internal resistance larger than $10^{12}\Omega$ is used. The OCV data is automatically recorded as a function of time over a long period until a saturation value is reliably established.

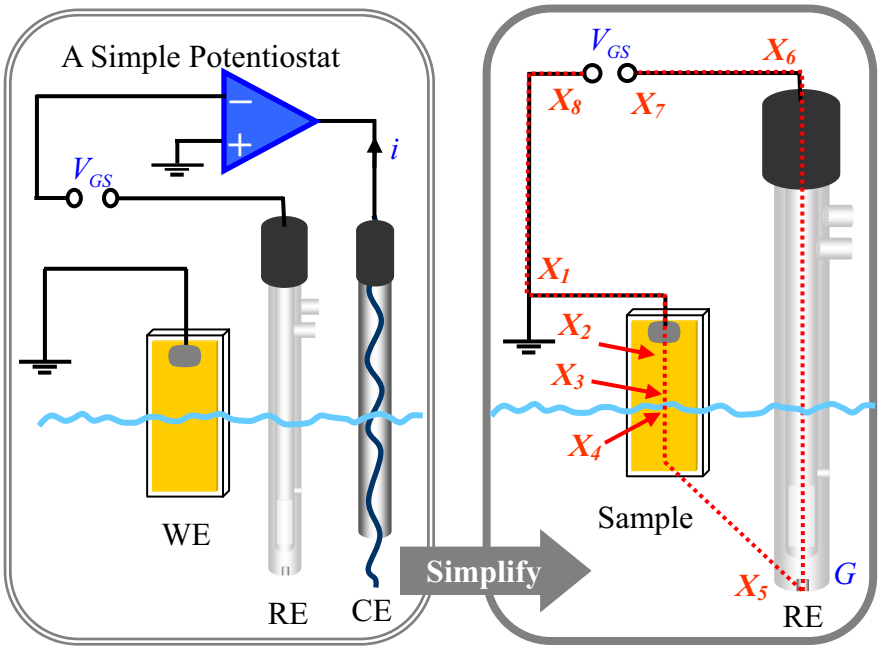

Figure 5.1 *Simple schematics of the electrical circuit adopted in the experiment. "WE" is the working electrode; "RE" is a double junction Ag/AgCl (3M) reference electrode; and "WE" is the working electrode, which is a platinum wire in our case. Voltages are given with respect to the reference electrode, i.e. relative to x6=x7. The path from x1 to x8 is the one for which the band diagram is analyzed in Figure 5.2.*

A UNISCAN Model PG580 potentiostat in three-electrode configuration with a platinum wire as a counter electrode is used in the measurement of polarization curves. For the measurement of the carbon electrodes, i.e. the hydrogen terminated diamond and the graphene sample, the potentiostat is operated in the chronoamperometry mode, in which current is measured with respect to time (at least 20mins) whilst the electrochemical cell is in a controlled potential mode. For the measurement of the platinum electrode, which is expected to allow relatively large Faradiac current compared to the displacement current, a linear scan mode is used. In the linear scan mode, the potential is linearly increased as a function of time (the scan rate is 0.5mV/s), and the current is recorded continuously.

The complete electrical circuit is sketched in Figure 5.1. The characteristic marks along the path from x1 to x8 will be referred to when discussing the experimental results. In the following all voltages will be specified with respect to the reference electrode (x6) and positive sign for the current will be assigned to anodic current of the diamond working electrode, i.e. to a flow of positive charge from the diamond to the electrolyte.

5.3 The Semiconductor-Electrolyte Interface

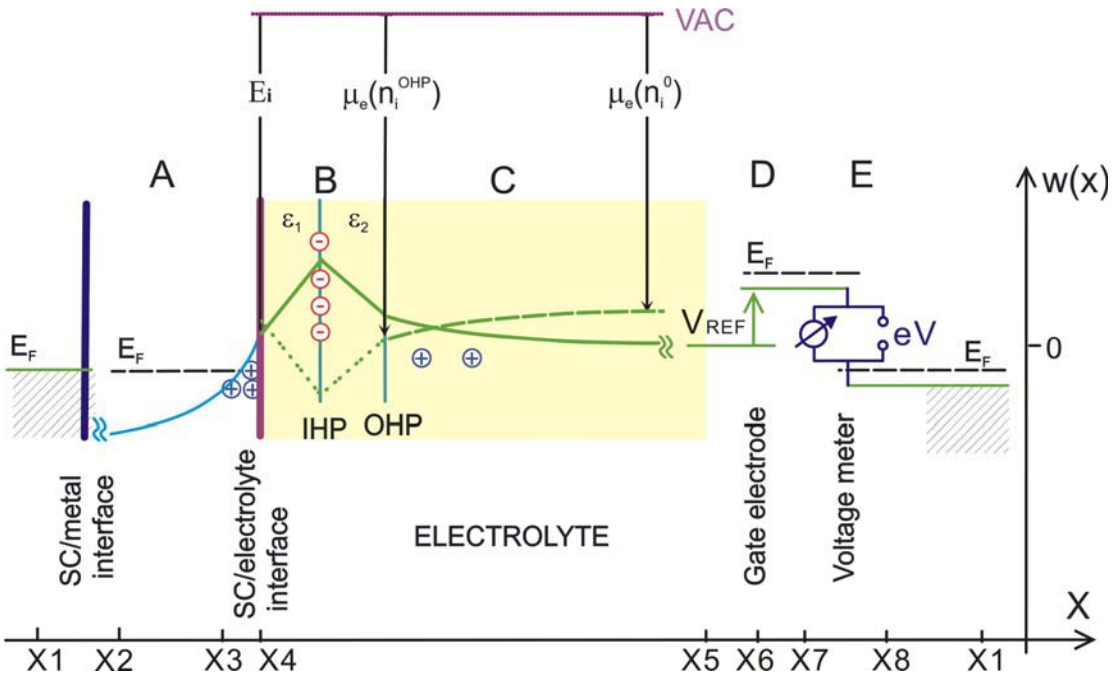

Figure 5.2 *The potential diagram w(x) of the complete galvanic cell used to study the hydrogen-terminated diamond electrode* [11]*. The potential diagram is constructed along the path defined in Figure 5.1 by approximating the electrode as perfectly polarizable. The dashed line shows the construction of an effective chemical potential of the red-ox electrons of a specific red-ox couple. It is extended as an electrochemical potential across the compact layer (double line) to construct a reference level at the semiconductor surface that is valid for the red-ox electrons at the OHP and indicates the direction of electron transfer when compared to the Fermi level in the semiconductor. The potential diagram of graphene is similar (details are referred to Figure 8.8b).*

Before presenting our results we first discuss the semiconductor (diamond and graphene)/electrolyte interface. We adopt the schematic band diagram of the complete electrochemical circuit sketched in Figure 5.1, i.e. we consider the electrostatic energy $w(x)$ for a negative unit charge as a function of position x. As shown in Figure 5.2, the circuit consists of A (x1 to x4) the working electrode from the metal contact to the free surface exposed to the electrolyte; B, the compact layer consisting of range 1 between the semiconductor surface and the inner Helmholtz plane (IHP) and of range 2 between the inner and the outer Helmholtz plane (OHP); C (OHP to x5) the diffuse layer in the electrolyte; D (x5 to x6) the reference electrode including its double layer towards the electrolyte; and E (x7 to x8) the voltmeter and/or the voltage source. The current meter

[11] The construction of band diagram was exclusively based on equilibrium arguments along the electrical circuit with the exeption of the compact layer range. Thus, the electrode has been treated as ideally polarizable.

used for measuring the polarization curves can be assumed to be ideal and has no influence on the charge and potential profile. Therefore it has been omitted in Figure 5.2. We set the potential w(x) deep in the electrolyte where it is asymptotically constant to zero. We assume for simplicity that the wiring of the circuit is completely done with silver. In reality, different metals are used but contact potentials in the circuit cancel and therefore need not be considered explicitly in Figure 5.2.

In section A, the potential profile is shown via the valence band maximum (Ev) of diamond (in blue) and the conduction band minimum (Ec) of graphene (in red). In the solid-state parts where the electrical current is carried by electrons (or holes), the Fermi level is indicated by a dashed line.

In section B, the sheet charge at the inner Helmholtz plane, that has been exemplarily assumed to be negative in the potential diagram, depends on the ionic composition of the electrolyte and the specific ion adsorption susceptibility of the surface. It is this dependence that mainly accounts for the ion sensitivity of the electrode when operated in the SGFET architecture [123-125] (see chapter 8). Note that the choice of negative σ_{ads} is merely for illustration and has no consequences for a principle outline in the following. We have assumed a negative σ_{ads} here.

For a given electrolyte and a given temperature, the total areal (i.e. depth integrated) space charge density in the diffuse layer, σ_{diff}, and with it the electric field at the OHP is a monotonic function of w_{OHP} as expressed by the Grahame equation [126] (see chapter 8); so is consequently the potential at the IHP. Since the sheet charge density of ions affixed at the IHP, σ_{ads}, is again for given temperature and electrolyte composition, a well defined function of this potential only, it is also well defined for a given w_{OHP}. To first approximation, we assume σ_{ads} is independent of w_{OHP} and thus a constant for given electrolyte.

The reference electrode in section D creates a Galvani potential drop eV_{REF} due to the equilibration of its characteristic red-ox couple with the electron reservoir of the solid. In the case of the Ag/AgCl reference electrode this is the equilibration of silver ions in the metallic and electrolytic phase, and V_{REF} is the half cell potential of the electrode.

The voltage source or the voltage meter in section E results in discontinuity $eV = w(x_7) - w(x_8)$ in both the electrostatic potential and the Fermi level. For the open circuit voltage measurement (without a voltage source), $w(x_7) - w(x_8)$ is the open circuit voltage of the galvanic cell. The measurement of open circuit voltage (OCV) is conceptually equivalent to choosing the voltage applied by a voltage source such that the current across the electrode/electrolyte interface is zero. If only one red-ox couple, say the

hydrogen red-ox couple, were active at the diamond/electrolyte interface, the open circuit voltage would be the difference in the reversible potential of that red-ox couple and the reference electrode (See [127] for a detailed explanation).

Finally, Charge neutrality requires that the areal charge density $\sum_{SC}$ in the semiconductor side of the interface balances the sum of σ_{diff} and σ_{ads}, and thus p is well defined for a given w_{OHP} as well. For the diamond electrode with a negligible concentration of interface states, $\sum_{SC} = e \cdot p$ is made up exclusively by the holes in the diamond valence band. For graphene, as already mentioned above, $\sum_{SC}$ includes all charges in the graphene, the interface states and the SiC space charge layer. $\sum_{SC}$ in turn defines the Fermi level at the semiconductor/electrolyte interface (x4) (see chapter 4). Kirchoff's loop rule of electrostatics requires the sum of the applied voltage V and the (constant) half cell potential V_{REF} to be identical to $-(1/e)w(x_1)$, i.e. $w(x_1) = w(x_8) = -eV - eV_{REF}$. This fixes the voltage V that belongs to the given w_{OHP}. Summarizing, the parameter w_{OHP} allows us to construct the total potential profile in the electrolyte and the semiconductor part of the circuit.

In the following, we will consider the electron exchange across the electrode/electrolyte interface. In general, more than one red-ox couple will be present in the electrolyte and thus the total electric current is the sum of partial currents, each assigned to an individual red-ox couple. For aqueous electrolytes in contact with atmosphere, at least the hydrogen/hydronium and the oxygen/hydroxyl couples already mentioned must be considered. The driving force of the partial currents is the difference in the electrochemical potential of electrons and red-ox electrons on either side of the compact layer [12]. On the electrode side, the electrochemical potential of the electrons is the Fermi level E_F, which is determined by $\sum_{SC}$ which involves the charge carrier concentration (see chapter 4). And on the electrolytic side, the electrochemical potential $\bar{\mu}$ needs to be evaluated for each red-ox couple separately. Let us exemplarily consider the contribution I_{H_2} of the hydrogen/hydronium couple to the total faradaic current *I*. At equilibrium, the chemical potential μ^{OHP} relative to E_{VAC} at the OHP of the red-ox electrons in the electrolyte corresponding to this red-ox couple is determined via Nernst equation by the concentrations of the red-ox active species at the OHP:

[12] Note that for technical reasons, the current is not measured between the diamond-H and reference electrode, but instead, between the diamond-H and the counter electrode (a platinum wire).

$$\mu^{OHP} = \mu\left(n_{H_3O^+}^{OHP}\right) = \mu_{SHE} - kT \cdot \ln\left(\frac{n_{H_3O^+}^{OHP}}{1mol/liter}\right) + \frac{kT}{2}\ln\left(\frac{\left[H_2\right]^{OHP}}{\left[H_2\right]_{SHE}}\right) \tag{5.1}$$

$\mu_{SHE} = -4.44eV$ is the chemical potential of the standard hydrogen electrode with respect to the vacuum energy. $n_{H_3O^+}^{OHP}$ is the molar proton concentration at the OHP, and $\left[H_2\right]^{OHP}$ and $\left[H_2\right]_{SHE}$ are the concentrations of dissolved hydrogen in the electrolyte and in the standard hydrogen electrode, respectively. Similar analysis can be done for the oxygen/hydroxyl red-ox couple, following the Nernst's equation (see chapter 4).

Across the diffuse layer the concentration of the red-ox active ions is exponentially increasing or decreasing with w(x) for positive or negative valency, respectively. This holds as long as mass transport is not the limiting step for the electrode reaction under consideration. Specifically, we have

$$n_{H_3O^+}^{OHP} = n_{H_3O^+}^{0} \cdot \exp\left(\frac{w_{OHP}}{kT}\right) \tag{5.2}$$

for the hydronium profile. $n_{H_3O^+}^{0}$ is the H_3O^+ concentration in the bulk of the electrolyte where w(x)=0. Inserting (5.2) into (5.1) shows that the chemical potential $\mu\left(n_i^{OHP}\right)$ can also be calculated by using the asymptotic bulk concentrations n_i^0 of the red-ox ions to obtain $\mu\left(n_i^0\right)$ and by subtracting the potential w_{OHP}. We use the general index i instead of H_3O^+ here to indicate that in principle all charged constituents of the red-ox couple change their concentration across the diffuse layer. Finally, in order to calculate the electrochemical potential of the red-ox electrons at the OHP relevant for charge exchange across the compact layer, the influence of the electrostatic potential difference between the electrode surface and the OHP has to be considered. This is done by adding $w_{OHP} - w(x_4)$ to μ^{OHP} giving the result $\overline{\mu}^{OHP} = \mu\left(n_i^0\right) - w(x_4)$ for the electrochemical potential of the red-ox electrons (see Figure 5.2).

5.4 Open Circuit Potential: Steady State

Figure 5.3 to Figure 5.7 shows the open circuit voltage transients of the electrodes vs. the Ag/AgCl electrode (left hand scale) as a function of pH. On the right hand scale the measured voltages are translated to the SHE as a reference. Equilibration times, i.e. times necessary to have a stable reading of the open circuit potential (OCP), are at least 1000s for all the electrodes after a change of electrolyte pH. Note that this time transient is much

longer as compared to the experimental time in the SGFET experiments (see chapter 8). The equilibration times for the diamond electrodes (Figure 5.3 to Figure 5.5) are longer than for the graphene electrode (Figure 5.6) and much longer than for the platinum electrode (Figure 5.7). For diamond electrodes, the U-shape patterned (sample B) and the partially oxidized electrode (sample C) equilibrate significantly faster than the untreated sample A. We cannot exclude an unintentional slight oxidation of sample B due to imperfect masking during the structuring of the electrode that would explain comparable equilibration times as observed for the intentionally oxidized sample C. We will discuss the transient time in OCP measurement in section 5.6.

In all experiments a non-zero cell voltage V_{OC} can clearly be measured that decreases with pH. Also note that this pH dependence is opposite to the pH dependence seen in an SGFET configuration when the voltage of constant channel conductivity is monitored (see chapter 8)[13].

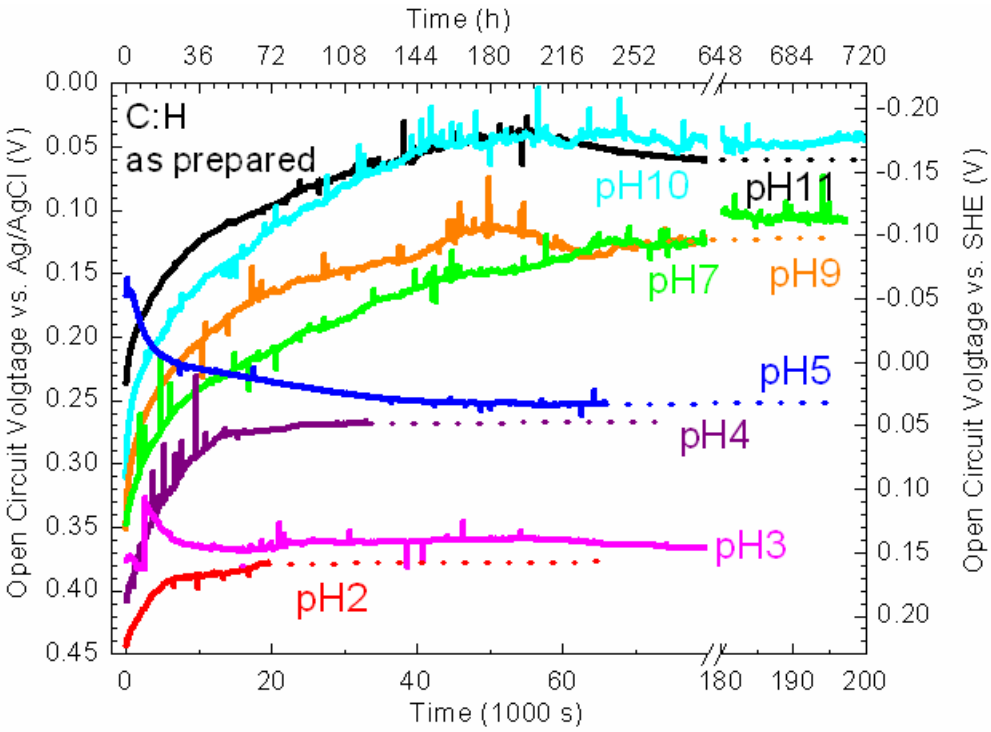

Figure 5.3 *Open circuit voltage transients of a fully hydrogen-terminated diamond electrode (sample A).*

[13] The fact that the plot of the gate-source voltage response of the SGFET vs. pH in Figure 8.4 and Figure 8.7 appears also increasing like the OCP in Figure 5.8 is simply due to the fact that electrode potentials in this chapter and gate-source voltages in chapter 8 are defined with opposite sign.

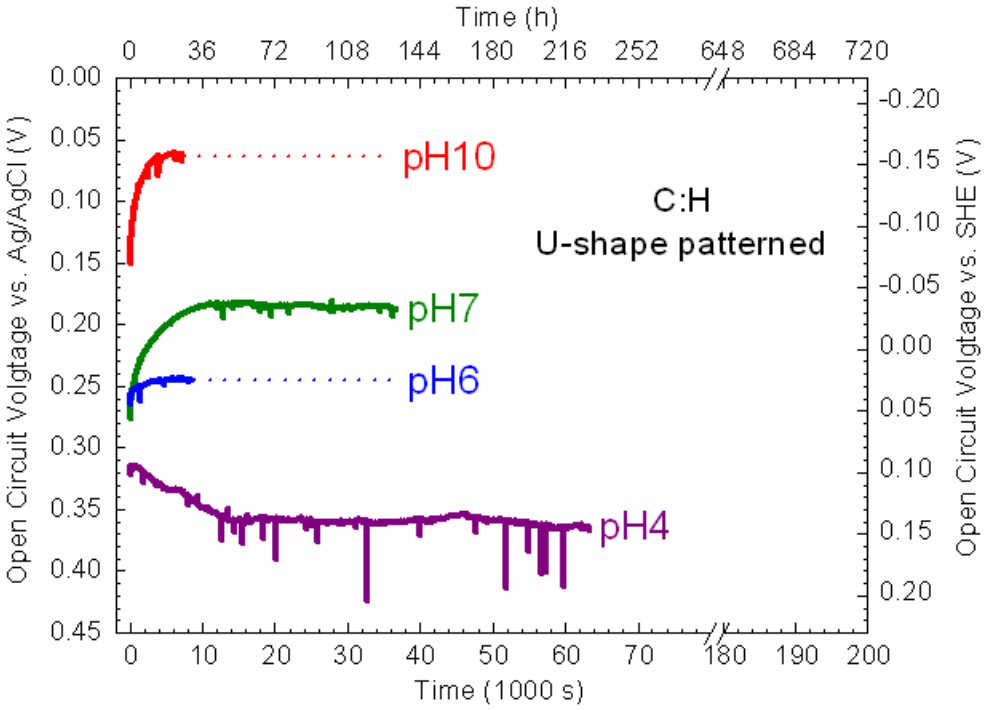

Figure 5.4 *Open circuit voltage transients of a hydrogen-terminated diamond electrode which is patterned into a u-shaped conductive channel (sample B).*

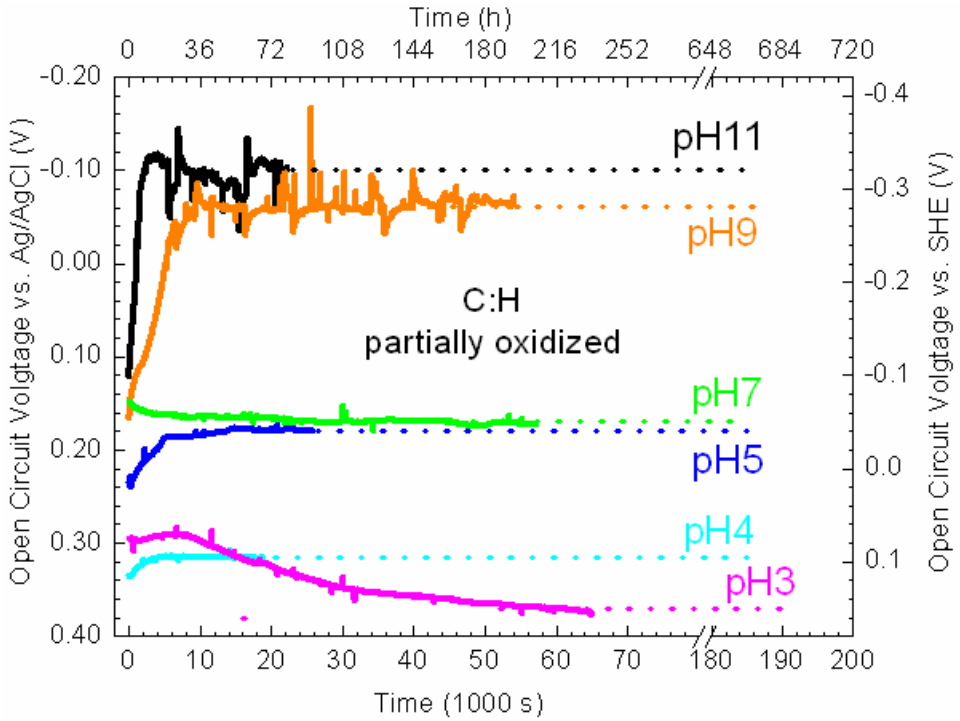

Figure 5.5 *Open circuit voltage transients of a hydrogen-terminated electrode after partial oxidation (sample C).*

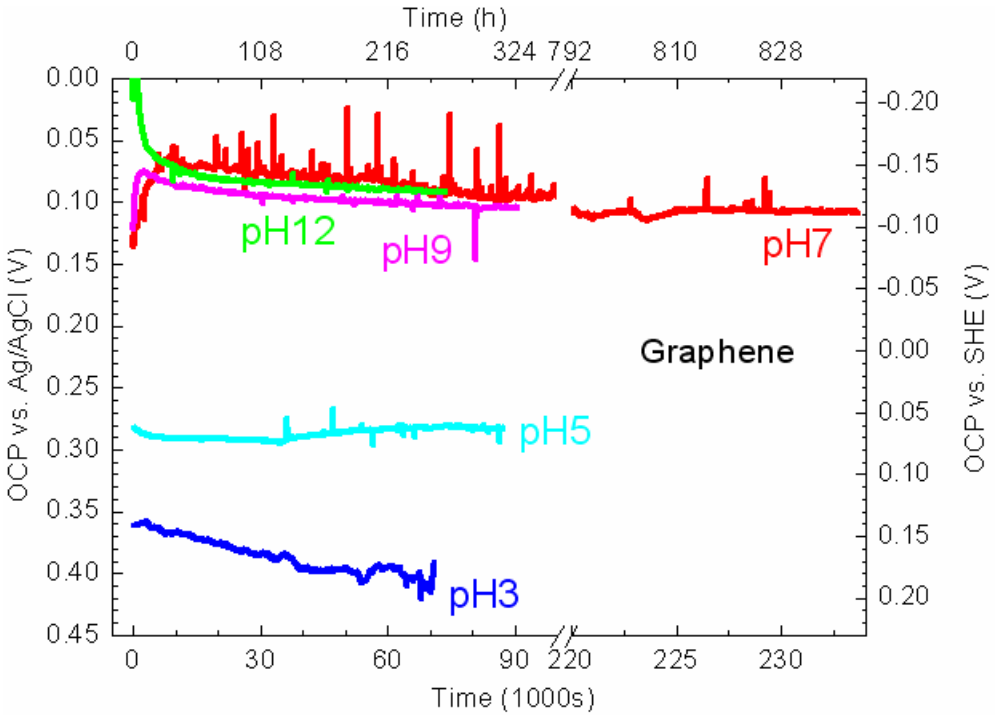

Figure 5.6 *Open circuit voltage (OCP) transients of a graphene electrode.*

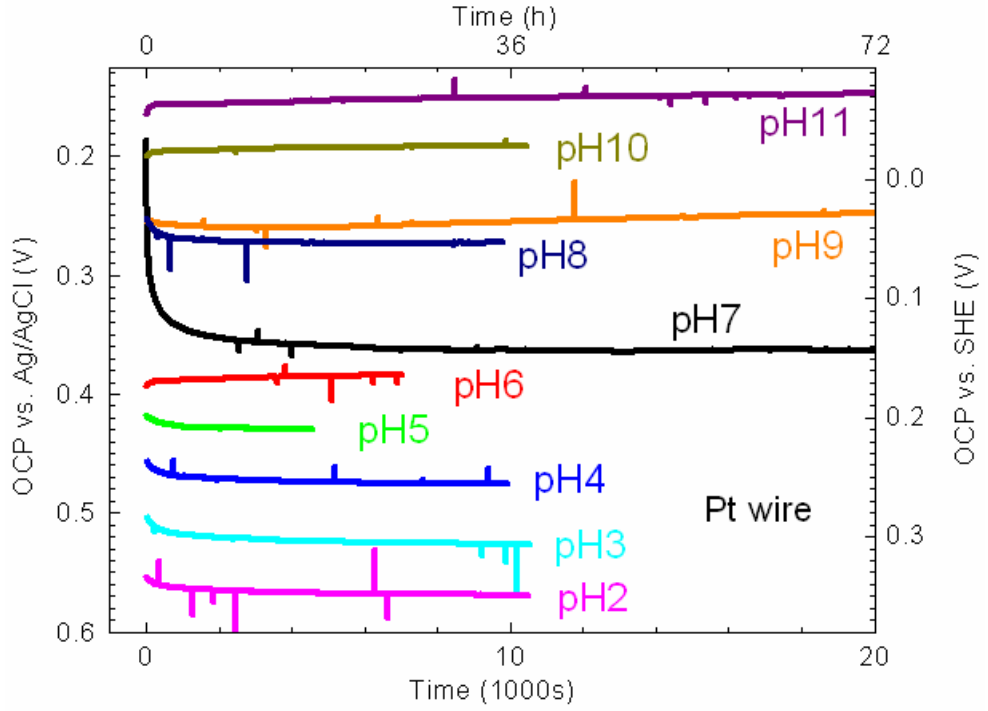

Figure 5.7 *Open circuit voltage (OCP) transients of a platinum electrode (for comparison).*

In Figure 5.8 we summarize the saturated open circuit voltages as a function of pH. We see in all cases a negative pH sensitivity which is approximately linear within the scatter of the data. Sensitivity factors range from -40mV/pH for the hydrogen-terminated diamond (sample A and B) to a value apparently constant with a Nernstian response of -59mV/pH for the partially oxidized diamond electrode (Sample C). The sensitivity factor

of graphene and platinum electrode are nearly the same, i.e. -43mV/pH. The pH dependence of the reversible potentials of the hydrogen/hydronium (in red) and of the oxygen/hydroxyl (in blue) red-ox couples follow Nernst's equation and are indicated in Figure 5.8 as well.

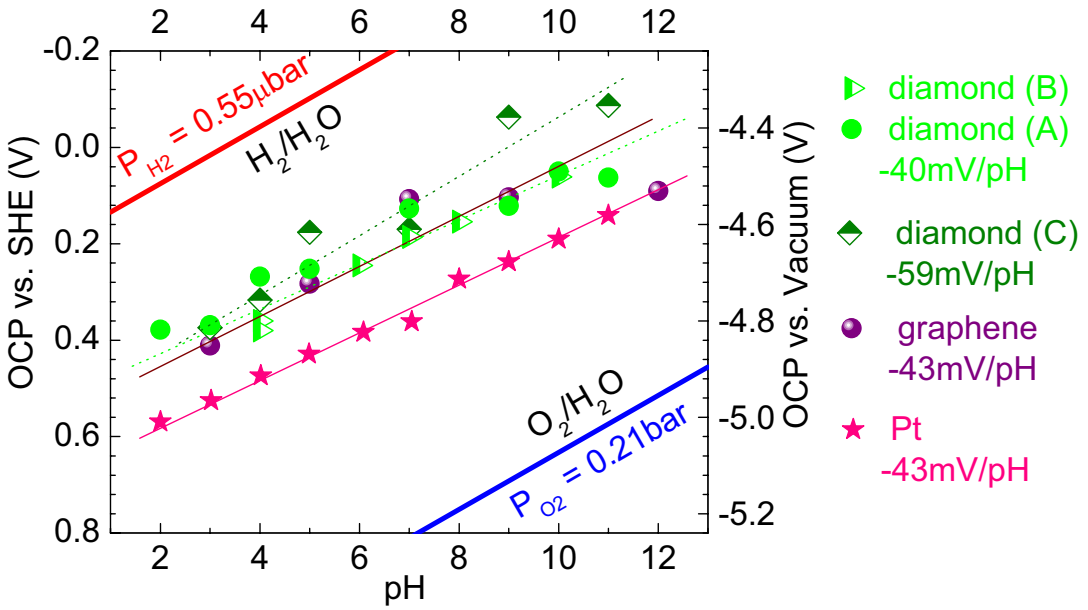

Figure 5.8 *The pH dependence of the saturated open circuit voltage for hydrogen-terminated, partially oxidized diamond, graphene and platinum wire electrode. The red and blue lines correspond to the electrochemical potentials of the hydrogen/hydronium and the oxygen/hydroxyl red-ox couples under atmospheric conditions, respectively. Setting* $0.55\mu bar$ *for the partial pressure of* H_2 *and* $0.21bar$ *for the partial pressure of* O_2 *in atmosphere, the potential (relative to the SHE electrode) of the hydrogen/hydronium red-ox couple and the oxygen/hydroxyl red-ox couple in aqueous solution are* $P_{H_2} = -0.22V - 0.059V \cdot (pH - 7)$ *and* $P_{O_2} = 0.81V - 0.059V \cdot (pH - 7)$.

5.5 Polarization Curves and the Mixed Potential Theory

Both the hydrogen/hydronium and the oxygen/hydroxyl red-ox couple obviously determine the charge transfer equilibrium at the electrode/electrolyte interface, and the open circuit potential measured is a mixed potential. This situation is typically found in the electrochemistry of corrosion where one of the two red-ox couples involves the electrode material itself, and the mixed potential is also called corrosion potential [128].

In Figure 5.9 we have schematically constructed for pH 7 a so-called Evans diagram usually adopted for the discussion of corrosion potentials [129],[130]. On the logarithmic

scale the Faradaic current densities $j_{H_2} = I_{H_2} / A$ and $j_{O_2} = I_{O_2} / A$ are shown with their respective anodic (j^+, blue) and cathodic (j^-, red) contributions as a function of the applied voltage. For a given red-ox couple, j^+ and j^- cancel exactly when the voltage applied to the working electrode is identical to the red-ox potential P of the corresponding red-ox couple (-0.22V vs. SHE for the H_2 and +0.81V vs. SHE for the O_2 couple). Obviously, these conditions can be fulfilled for the hydrogen/hydronium or for the oxygen/hydroxyl red-ox couples separately, but never for both simultaneously. The functional form of the partial current densities in Figure 5.9 has been schematically assumed to follow the Butler-Volmer relation [131].

$$j_k = j_{0,k} \cdot \left[\exp\left(\frac{\alpha_k \left(V - P_k\right) F}{RT} \right) - \exp\left(-\frac{(1-\alpha_k)\left(V - P_k\right) F}{RT} \right) \right] \tag{5.3}$$

with the transfer coefficient α_k, the reversible potential P_k and the reversible exchange current density $j_{0,k}$. Each of these quantities is specific for the red-ox couple under consideration denoted here by the index *k*, and $j_{0,k}$ and α depend on the electrode material as well. This relation is usually valid as long as the 'overpotential' $\left|V - P_k\right|$ is low enough to guarantee that the electron exchange across the electrode/electrolyte interface is the limiting step for the Faradaic current. For higher overpotentials, the diffusive transport of red-ox particles to the electrode interface in general becomes the limiting process, and the polarization curves $j_k(V)$ saturate. In Figure 5.9 we have neglected this effect. Following the Butler-Volmer relation (5.3), the anodic and cathodic partial current densities thus give straight lines in the Evans diagram. Inside the voltage range defined by $-\eta_{O_2} = P_{O_2} - V \gg kT / \alpha_{O_2}$ and $\eta_{H_2} = V - P_{H_2} \gg kT / (1 - \alpha_{H_2})$ only the anodic current corresponding to the oxygen/hydroxyl red-ox couple and the cathodic current of the hydronium/hydrogen red-ox couple need to be considered. This voltage range will be denoted as the corrosion window in the following. In Figure 5.9 it extends from about -0.15V to 0.75V vs. SHE. Open circuit conditions require that the cathodic and the anodic current densities cancel, and thus the intersection of the current curves in the corrosion window defines the open circuit voltage V_{OC}. For the schematic of Figure 5.9 we have set $\alpha_{H_2} = \alpha_{O_2} = 0.5$ and $j_{0,H_2} = j_{0,O_2}$, and thus $V_{OC} = \left(P_{H_2} + P_{O_2}\right) / 2$, i.e. the corrosion potential is the average of the two reversible potentials of the two red-ox couples involved. This specific result, of course, depends on our simplifying assumption of identical reversible exchange current densities and of transfer coefficients adding to one. It is thus coincidental that the experimental range of OCV's measured at pH 7 is almost consistent with

$V_{OC} = \left(P_{H_2} + P_{O_2}\right)/2 = 0.3V$ vs. SHE ($0.36 \pm 0.03V$ vs. SHE, compare Figure 5.8).

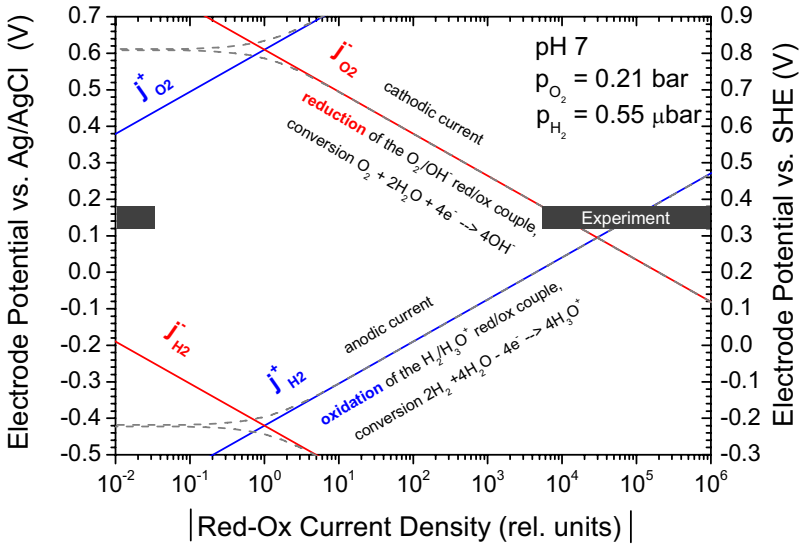

Figure 5.9 *Schematic Evans diagram for simultaneous redox activity of the hydrogen-hydronium and the oxygenhydroxyl redox couples in an electrolyte at pH7 and in contact with atmosphere.*

Within the corrosion window, the total current density is easily evaluated from (5.3) as

$$j = j_0 \cdot \left[\exp\left(\frac{\alpha \eta F}{RT}\right) - \exp\left(-\frac{\beta \eta F}{RT}\right) \right] \tag{5.4}$$

i.e. again a Butler-Volmer like relation with the overpotential $\eta = V - V_{OC}$ now referenced to the mixed potential VOC and the reaction current density j_0 replacing the reversible exchange current densities (see also Figure 5.9). $\alpha = \alpha_{H_2}$ stands for the transfer coefficient of the hydrogen reaction and $\beta = 1 - \alpha_{O_2}$ for the complement of the transfer coefficient of the oxygen reaction. Note, that in general the pre factors in the exponent do no longer add up to one, i.e. $\alpha + \beta \neq 1$. Evaluating (5.3) for both the hydrogen and the oxygen reaction inside the corrosion window, and demanding $j_{H_2}(V_{OC}) = -j_{O_2}(V_{OC})$, gives by straight forward calculus

$$V_{OC} = \left[\frac{\alpha}{\alpha + \beta} P_{H_2} + \frac{\beta}{\alpha + \beta} P_{O_2} \right] - \frac{kT}{e} \times \frac{\ln\left(j_{0,H_2} / j_{0,O_2}\right)}{\alpha + \beta} \tag{5.5}$$

The first term on the right hand side is a weighted average of the reversible potentials of the two red-ox couples involved, where the weighing factors are the relative transfer coefficients. The second term takes the generally different reversible exchange current densities into account. We would like to comment on the mixed potential observed here in the framework of real corrosion phenomena. The reader may, for example, replace the oxygen red-ox couple by one that corresponds to the corrosion of an ignoble metal

electrode, say $Fe \rightleftharpoons Fe^{2+} + 2e^-$ with $\left[Fe^{2+}\right] = 5 \cdot 10^{-6} mol / liter$ which has a reversible potential $P_{Fe} = -0.60V$ vs. SHE. In an Evans diagram this red-ox couple lies below the hydrogen/hydronium one (and even outside the frame of Figure 5.9). At the corrosion potential, i.e. under open circuit conditions, the zero electrical current thus implies a cathodic partial current of the hydrogen/ hydronium red-ox couple balancing an anodic partial current of same magnitude of the iron couple. The consequence is the corrosion reaction of iron under hydrogen evolution with the reaction rate corresponding to the reaction current density read from the Evans diagram. Going back to our case of the mixed potential of the hydrogen/hydronium and the oxygen/hydroxyl couple, we see that the 'corrosion' reaction in this case is not involving the electrode, but is **the water synthesis from oxygen and hydrogen**. In fact, it does not even require an electrical circuit but just an electrode surface providing and consuming electrons at the rate of the exchange current. Under the open circuit conditions studied, i.e. for an innert electrode in an aqueous solution in contact with atmosphere, we thus observe a charge transfer equilibrium witnessed by the non-zero cell potential vs. our reference electrode that corresponds to a persistent production of water from the oxygen and hydrogen reservoir of the atmosphere. Electrons are exchanged with the hydrogen/hydronium and the oxygen/hydroxyl red-ox couples at the same rate. This amazing result will be elaborated on further below.

In the following, we will discuss the pH dependence of the mixed potential on the basis of (5.5). If we assume, as the simplest approximation, that the reaction kinetics of the hydrogen and the oxygen reaction are independent of pH, the reversible exchange current densities and the transfer coefficients in (5.5) are constant. A variation of the proton concentration is then taken into account by the pH dependence of P_{H_2} and P_{O_2} as given by Nernst's equation and as already discussed above. The open circuit voltage, i.e. the corrosion potential, is then to follow the same pH shift of $-59mV / pH$. Assuming pH independent kinetics is, however, a rather crude assumption, and it comes not as a surprise that the experimental pH dependence of Figure 5.8 is deviating from the Nernstian expectation. This deviation can be due to a pH dependence of either one of the reversible exchange current densities and transfer coefficients or to a combination of several of them. For a further analysis, the polarization curves, i.e. the I-V curves of the cell, for both red-ox couples would have to be measured independently. We stress explicitly here, however, that the Nernst value for the pH dependence of the mixed potential is not a canonical one, and not even a limit. Depending on the sign and magnitude of pH shifts of j_{H_2} / j_{O_2} and of the transfer coefficients α and β, the slope of the pH curves in Figure 5.8 can be smaller, but also larger than $-59mV / pH$.

So far we have described both the hydrogen and the oxygen reaction by the Butler-Volmer equation (5.3) within the corrosion window, implicitly assuming that the reaction rate is controlled by the charge transfer of red-ox electrons across the electrode/electrolyte interface. The polarization curve, i.e. the I-V characteristics of the galvanic cell formed by the hydrogen and the oxygen red-ox couples active at the electrode side and of the Ag/AgCl red-ox couple of the reference electrode, is thus expected to follow (5.4).

The polarization curves (Tafel plot) of the diamond electrode are shown in Figure 5.10. On the cathodic side (lower voltages) of all the electrodes, the current is preferentially due to the oxygen reaction $O_2 + 2H_2O + 4e^- \rightarrow 4OH^-$. The cathodic part of the polarization curve may even be extrapolated to the reversible potential of the oxygen reaction at $P = +0.81V$ vs. SHE. The result is shown in Figure 5.10 in an Evans diagram similar to the schematic one of Figure 5.9. The back extrapolation of the cathodic current with a transfer factor of $\beta = 0.5$ yields a reversible exchange current density of $j_{0,O_2} \approx 1 \cdot 10^{-15}\, A/cm^2$ for the oxygen/hydroxyl red-ox couple at the hydrogen-terminated diamond surface. As explained above, the anodic current due to the hydrogen/hydronium couple is apparently not reaction controlled, and a back extrapolation can only be interpreted with great caution. The corresponding current density for the open circuit voltage can, however, be taken from the reaction current density. Extrapolating back from that value ($0.11V$ and $3 \cdot 10^{-11}\, A/cm^2$) with $\alpha = 0.5$ would give a reversible exchange current density of $j_{0,H_2} \approx 7 \cdot 10^{-16}\, A/cm^2$. Although this value should only be taken as a very rough estimate it is yet interesting to note that it is within a factor two identical with j_{0,O_2}. From literature [132, 133], we know that the oxygen reaction is generally a slow process as compared to the hydrogen process. Thereby, for carbon electrodes in standard buffer, the oxygen reaction is charge-transfer limited in the entire range from its reversible potential up to the corrosion potential. By extrapolating the cathodic current density to the voltage of zero current V_{OC}, the reaction current density under open circuit conditions is given. For the hydrogen terminated diamond electrode $j_0 = 3.0 \times 10^{-11}\, A/cm^2$. To illustrate this result, consider a diamond-H surface in contact with water under atmospheric conditions. A reaction current density of $3.0 \times 10^{-11}\, A/cm^2$ means that it catalytically mediates the water synthesis reaction $O_2 + 2H_2 \rightarrow 2H_2O$ with an areal rate of $j_0/(2e) = 9.4 \times 10^7\, cm^{-2}s^{-2}$, corresponding to $j_0/(2F) = 1.6 \times 10^{-16}\, moles \cdot cm^{-2}s^{-2}$. Although this reaction rate can clearly be measured electrochemically and proves the red-ox activity of the diamond surface under atmospheric conditions, it is minute in terms material transformation. Using

the molar density of water ($0.055 moles/cm^3$) one may translate this reaction rate to the growth rate of a water layer, the result being $2.9\times10^{-15} cm/s \approx 1nm/year$. Despite this ridiculously low reaction rate the electron transfer associated with it is in perfect agreement with the kinetics of surface transfer doping under atmospheric conditions. Taking j_0 as an estimate for an electron exchange current density across the diamond surface driven with a chemical potential difference of $0.5eV$ gives a generation rate of $2\times10^8 holes\cdot cm^{-2}\cdot s^{-1}$. It will thus take about three hours to induce a typical hole density of $2\times10^{12} holes\cdot cm^{-2}$. **Such transients, sometimes even with longer saturation times, are in fact observed for the appearance of surface conductivity of hydrogen-terminated diamond under atmospheric conditions** [11, 14]**!** We explicitly stress here that the exchange current densities measured in this experiment correspond to a solid/liquid interface and can thus only serve as a rough estimate for the time scale. The real charge exchange of the surface transfer doping mechanism involves only a thin water layer, and reaction kinetics can be substantially different, probably faster, under those conditions.

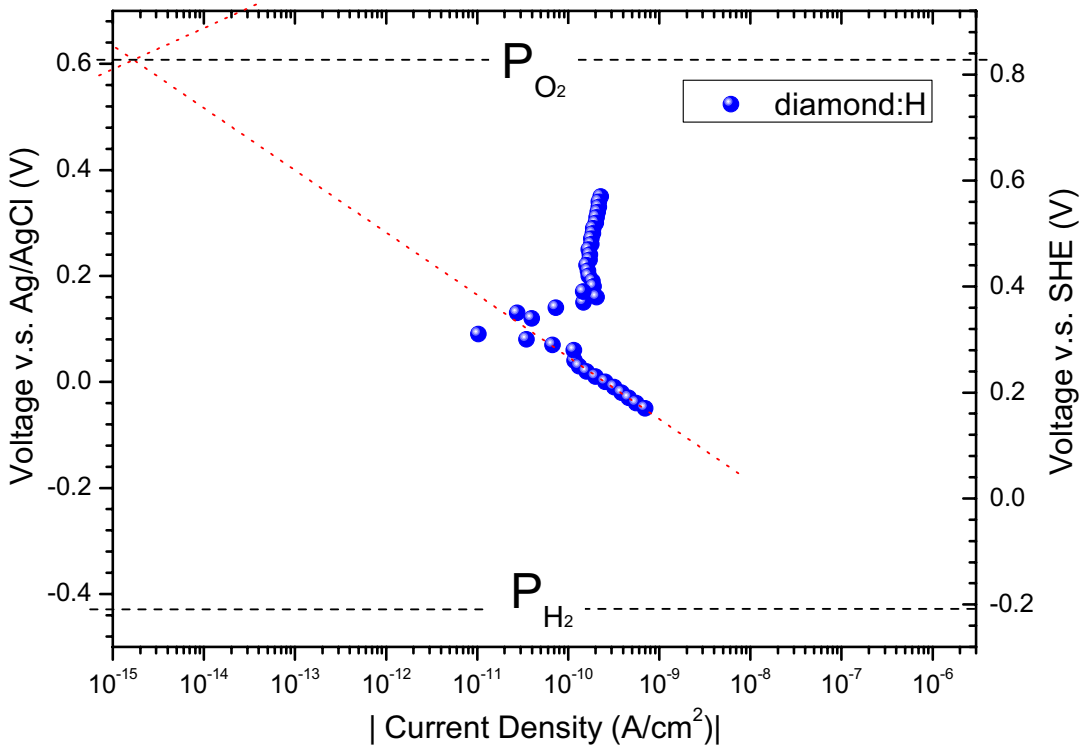

Figure 5.10 *Quasi static polarization curves of the hydrogenated diamond electrode in standard electrolyte (pH7) within the complete corrosion window between the oxygen and the hydrogen reaction. Using equation (2.31), the transfer coefficient α_{O_2} can be calculated as 0.51.*

On the anodic side ($V > V_{OC}$) the Faradaic current is predominantly carried by the hydrogen reaction $H_2 + 2H_2O \rightarrow 2H_3O^+ + 2e^-$. The polarization curves of both electrodes

are clearly deviating here from the Butler-Volmer behavior, indicating a saturation of the current. Such saturation is expected when the reaction becomes mass transport limited, and the data here obviously are mainly diffusion limited. For the case at hand, the diffusion of hydrogen to the electrode surface has to be considered. The hydrogen partial pressure in atmosphere equals $5.5 \cdot 10^{-7} bar$ [93], which corresponds to a molecular density of dissolved hydrogen $n_{H_2} = 2.9 \cdot 10^{11} cm^{-3}$ [134]. With a room temperature diffusion constant of $D_{H_2} = 5 \cdot 10^{-5} cm^2/s$ [135] and a typical extension of the diffusion layer between $l = 10^{-3} cm$ and $l = 10^{-2} cm$ [136], the maximum diffusion current density $r_{H_2} = n_{H_2} D_{H_2} / l$ for H_2 molecules lies between $1.5 \cdot 10^9$ and $1.5 \cdot 10^{10} cm^{-2} s^{-1}$. This corresponds to electrical current densities $j_{H_2} = 2e \cdot r_{H_2}$ between $5 \cdot 10^{-10}$ and $5 \cdot 10^{-9} A/cm^2$. This rough estimate is consistent with the data of Figure 5.10. An extrapolation of the anodic current density corresponding to (5.3) is no longer possible in this case. Note that, due to the ~100 times higher partial pressure of oxygen in air and thus of dissolved oxygen in the electrolyte, the diffusion limited current density on the cathodic side is never reached in the experiment.

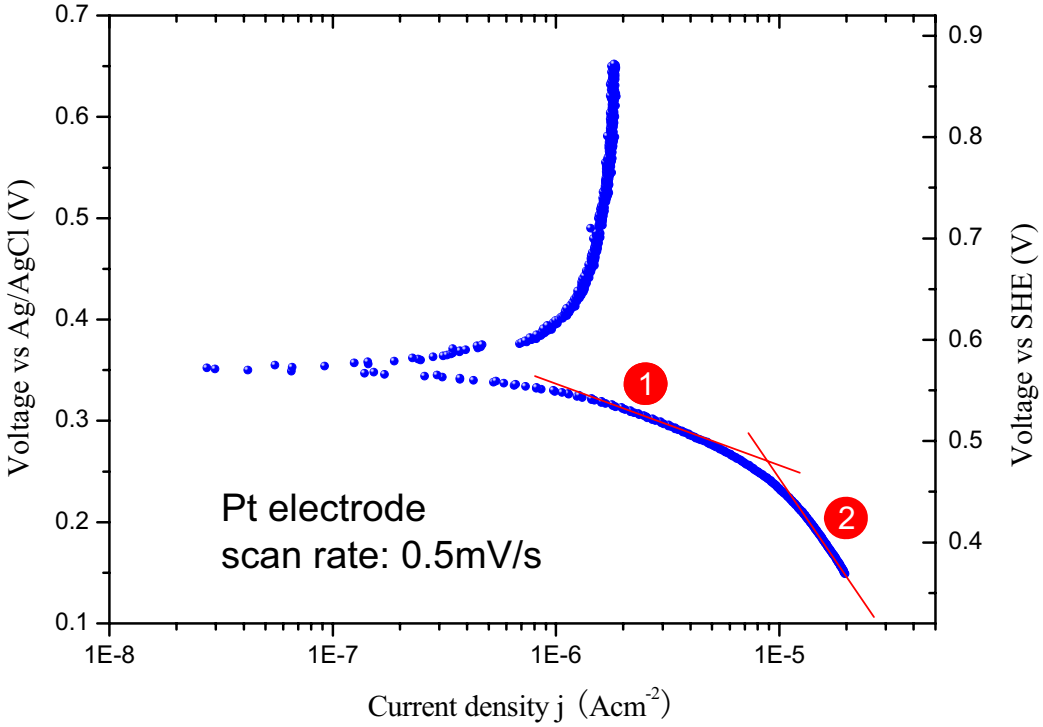

Figure 5.11 *Linear scan polarization curves of platinum electrode in standard electrolyte (pH7) within the complete corrosion window between the oxygen and the hydrogen reaction. Using equation (2.31), the transfer coefficient α_{O_2} in region 1 and region 2 (in red) are 0.77 and 0.17, respectively.*

Figure 5.11 shows the linear scan polarization plot of platinum electrode. Similar to

carbon electrodes, on the anodic side ($V > V_{OC}$) the polarization curves is dominated by a saturation of the current as a result of mass transport limitation. On the cathodic side ($V < V_{OC}$) and the data here possibly are not only diffusion limited but also charge transfer limited, yielding a "bending" of the curve rather than a straight line. The similarity of the characteristic as compared to diamond and graphene electrode verifies our discussion above, i.e. diamond and graphene behaves like noble metal (platinum), in which hydrogen process and oxygen process takes place simultaneously and contribute a mix potential (corrosion potential) at equilibrium.

5.6 Open Circuit Potential: Transient

The equilibration times (transient) of the open circuit voltage $V(t)$ reflect the kinetics of the charge transport across the electrode-electrolyte interface. If we denote the total charge transfer rate of all red-ox reactions across the compact layer as $j(V)$, the open circuit voltage has be fulfill [137]:

$$-C(V)\left(\frac{dV}{dt}\right) = j(V) \tag{5.6}$$

$-1/C(V)$ is in general given by the response $dV/(dQ/A)$ of the total electrostatic potential sweep V across the open circuit with respect to a transfer of positive unit charge from the semiconductor side to the electrolyte side of the compact layer. Applying the Butler-Volmer equation (2.28) to equation (5.4), yields:

$$-C\left(\frac{dV}{dt}\right) = j_0\left[\exp\left(\frac{\alpha(V-V_{OC})F}{RT}\right) - \exp\left(-\frac{\beta(V-V_{OC})F}{RT}\right)\right] \tag{5.7}$$

As can be seen from Figure 5.10, the assumption of transfer limited currents is only fulfilled for negative overpotentials $\eta = V - V_{OC} < 0$. We will thus evaluated the differential equation (5.7) only for those negative overpotentials. For those, the total current density can be rewritten as

$$j(V) = -j_0 \exp\left(-\frac{\beta(V-V_{OC})F}{RT}\right) = -j_{0,O_2} \cdot \exp\left(-\frac{(1-\alpha_{O_2})(V-P_{O_2})F}{RT}\right) \tag{5.8}$$

In this equation we have written the cathodic current explicitly as the red-ox current of the oxygen reaction again which defines also the relationship between the reaction current density j_0 and the reversible exchange current density j_{0,O_2} of the oxygen reaction. With this, we can write (5.8) also as a differential equation for the overpotential $\eta_{O_2} = V - P_{O_2}$

relative to the reversible oxygen potential and obtain

$$\frac{d\eta_{O_2}}{dt} = \frac{j_{0,O_2}}{C\left(\eta_{O_2}\right)} \cdot \exp\left(-\frac{\left(1-\alpha_{O_2}\right)\eta_{O_2} F}{RT} \right) \tag{5.9}$$

Since we are evaluating the open circuit voltage transients for charge transfer limitation, and the voltage drop across the diffuse layer can be neglected, $C\left(\eta_{O_2}\right)$ can be taken as a constant C specific for the different electrodes, and the solution to (5.9) can be given by

$$\frac{j_{0,O_2}}{C}\left(t-t_0\right) = \frac{RT}{F} \cdot \frac{1}{\left(1-\alpha_{O_2}\right)} \cdot \exp\left(\frac{\left(1-\alpha_{O_2}\right)\eta_{O_2} F}{RT} \right) \tag{5.10}$$

where t_0 is a constant. At room temperature (25 °C), RT/F may be treated like a constant and replaced by 25mV.

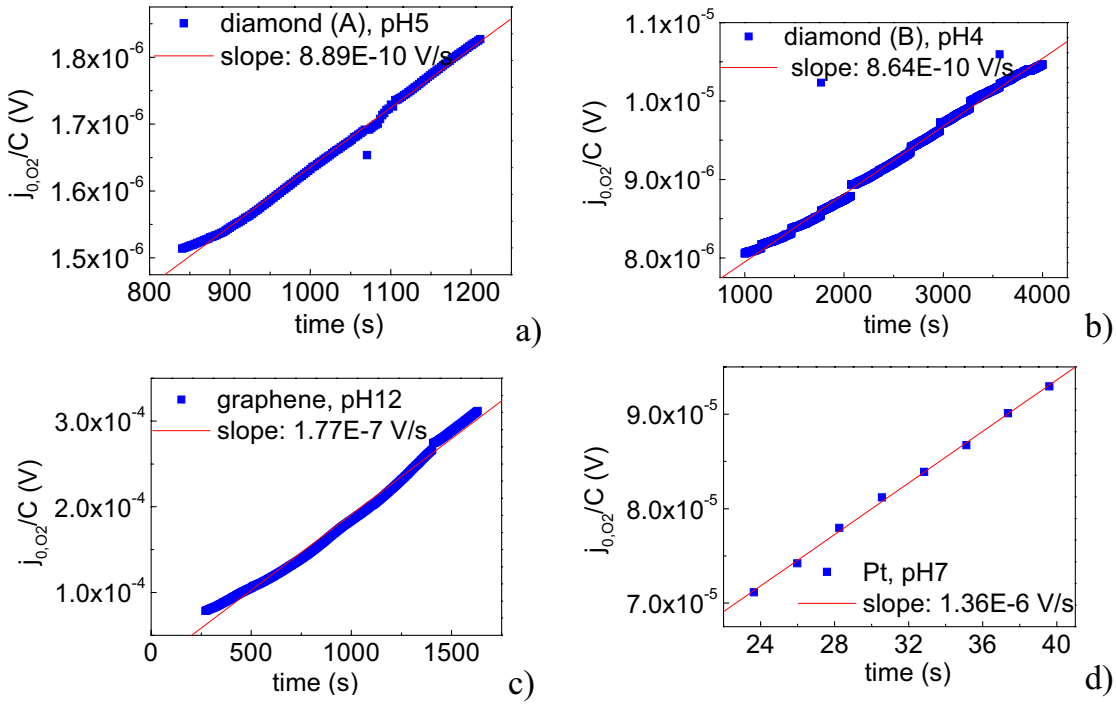

Figure 5.12 *Plots of* $(RT/F)\cdot\left(1-\alpha_{O_2}\right)^{-1}\cdot\exp\left[\left(1-\alpha_{O_2}\right)\cdot\eta_{O_2}\cdot(F/RT)\right]$ *vs. t for the initial time periods, selected of open circuit voltage transients. Only transients which approach equilibrium with negative slope in Figure 5.3 to Figure 5.7, i.e. with increasing* $V(t)$*, are dominated by the cathodic transfer limited current of the oxygen reaction and can be analyzed in this way.*

We have re-plotted the open circuit transients $V(t)$ in form of equation (5.10) in Figure 5.12a)-d) for the carbon electrodes and for the platinum wire electrode. The transfer coefficient α_{O_2} can be calculated using equation (2.31). The slope j_{O_2}/C of the straight line fits to the data in Figure 5.12 allows us to extract the reversible exchange current

density j_{0,O_2} when the double layer capacitance is known. And the resulting j_{0,O_2} is plotted as a function of pH for the different samples in Figure 5.13.

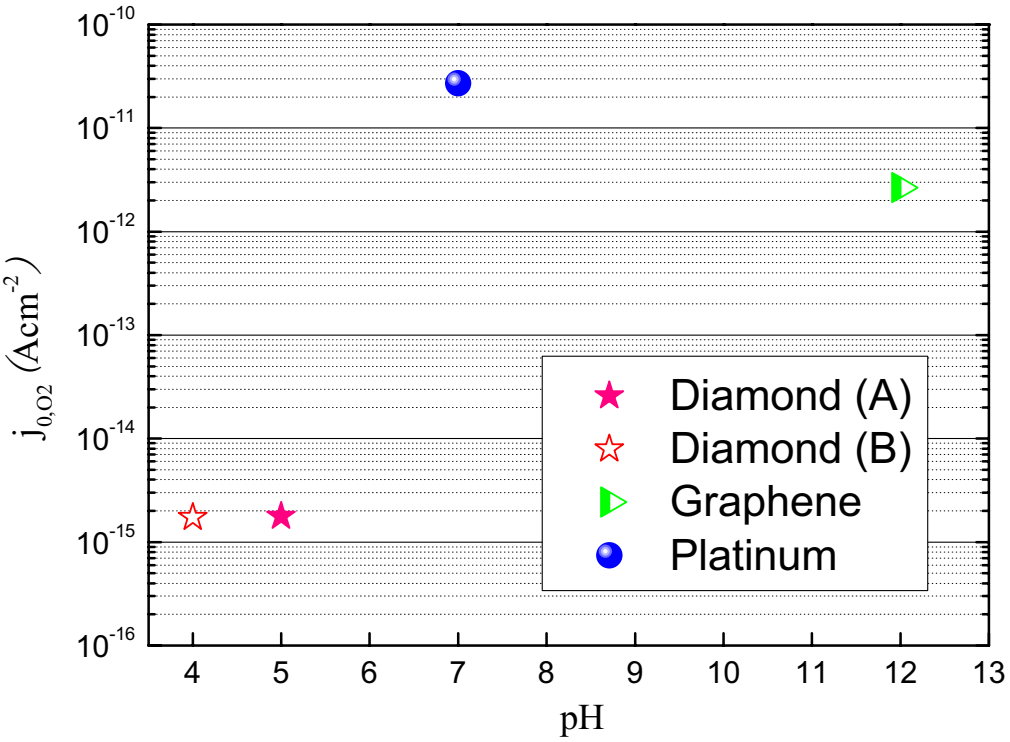

Figure 5.13 *Values of equilibrium current density of the oxygen reaction of different electrodes and for various pH value of electrolyte. For the calculation of* j_0*, the double layer capacitances C for all the electrodes are assumed to be constant* [14]*, and the value of C for diamond-H, graphene and platinum electrodes are* $2\mu Fcm^{-2}$, $15\mu Fcm^{-2}$ *and* $20\mu Fcm^{-2}$ *[138] respectively. The transfer coefficient* α_{O_2} *for diamond-H and platinum electrode, taken from Figure 5.10 and Figure 5.11, are 0.51 and 0.47 (average the value from range 1 and range 2 in the polarization curve), respectively. Thus, we assume* $\alpha_{O_2} = 0.5$ *for all electrodes.*

This double layer capacitance C is taken from literature [123, 138] (also see chapter 8). It can be seen that for the oxygen process, the diamond electrodes have the lowest equilibrium current density, ca. $10^{-15}\,Acm^{-2}$, and j_{0,O_2} for graphene and platinum are of the order of $10^{-12}\,Acm^{-2}$ and $10^{-11}\,Acm^{-2}$, respectively. In chapter 4, we found that the reaction current density j_0 in atmosphere for graphene and diamond is of the order of $10^{-10}\,Acm^{-2}$

[14] In the simulation, we neglect the capacitance in the electrode side and consider only the differential capacitance in the Hemholz layer. The real value of double layer capacitance of diamond and graphene electrodes, in principle, should be larger than this value that we used for simulation.

and $10^{-9}\,Acm^{-2}$. The deviation of j_0 may origin from the fact that the hydration of ions in gas atmosphere (chapter 4) and in liquid are different. In gas atmosphere, charge transfer is more efficient than in liquid phase.

For high concentrations of Chlorine ions in our electrolytes we observe a significant change in the charge transfer kinetics of diamond electrodes. We give these data in Appendix VI but will not present this relationship further within this thesis.

PART III FIELD EFFECT DEVICES BASED ON CARBON SURFACES

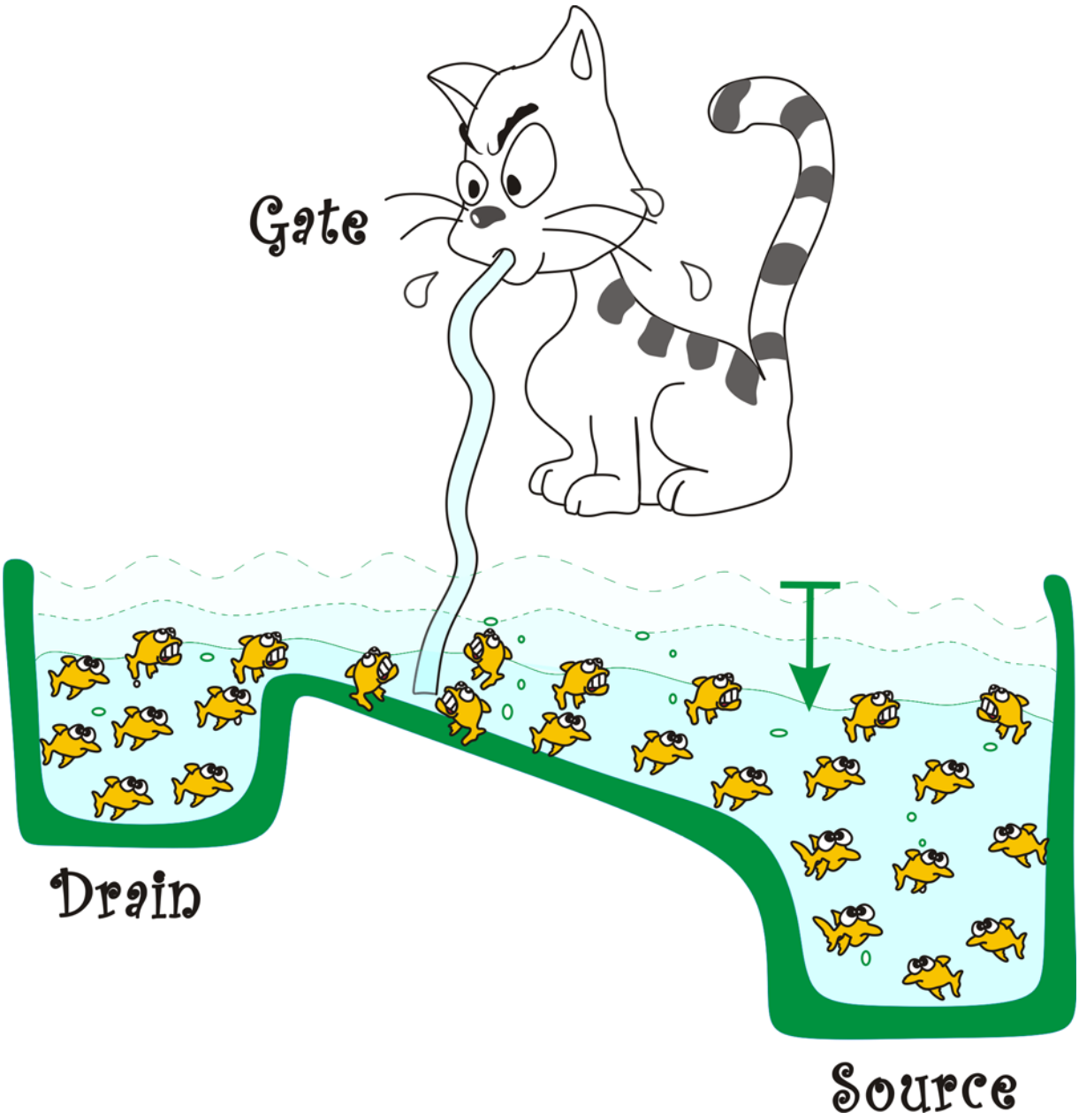

Chapter 6 The Field Effect Concept

A substantial part of this thesis deals with novel field effect devices based on diamond and graphene surfaces. In this chapter we therefore give an introduction to this concept in general.

6.1 Building Blocks of Semiconductor Devices

In reality, a semiconductor surface, as usual, may see vacuum, air, a metal, another semiconductor, an electrolyte or any other conductive/nonconductive medium. In another word, an **interface** is formed once the semiconductor is in contact with a neighboring material. The interface and the neighboring participating regions are called a **junction**. It is not exaggerated to say that **junctions are the building blocks of all semiconductor devices.** The performance of the devices is controlled by a combination of junctions. Figure 6.1 shows the most important building blocks in semiconductor devices.

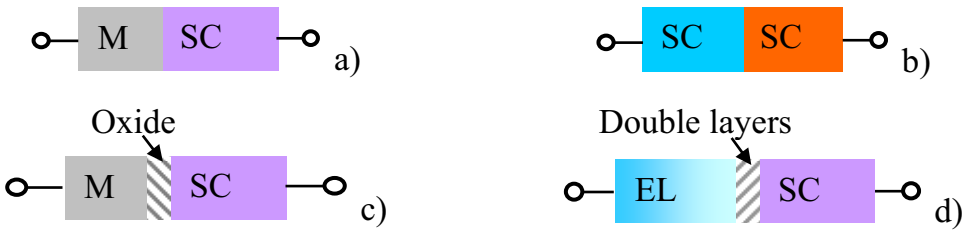

Figure 6.1 *Building blocks in semiconductor devices. a) metal-semiconductor junction that forms an Ohmic or a Schottky contact depending among other features, on the relative workfunction difference. Metal semiconductor field effect transistor (MESFET) and Schottky diodes are constructed from this building block; b) semiconductor-semiconductor heterostructure. In specific case, i.e. when the bandgap of both are the same, a pn junction may form; c) metal-oxide-semiconductor structure, which is the heart of the metal oxide semiconductor field effect transistor (MOSFET); d) electrolyte semiconductor interface, the so-called double layer is form on the electrolyte side. Such an interface is used for fabricating the solution gate field effect transistor (SGFET) with hydrogen terminated diamond or graphene (see Chapter 8)*

In the following, we will use p type semiconductor as an example to demonstrate in brief the most important building blocks that are relevant to this thesis: the metal-semiconductor interface and the metal-oxide-semiconductor structure. In addition to

these classical building blocks, we will discuss the semiconductor electrolyte interface as a more unusual junction.

■ Metal-semiconductor Junction

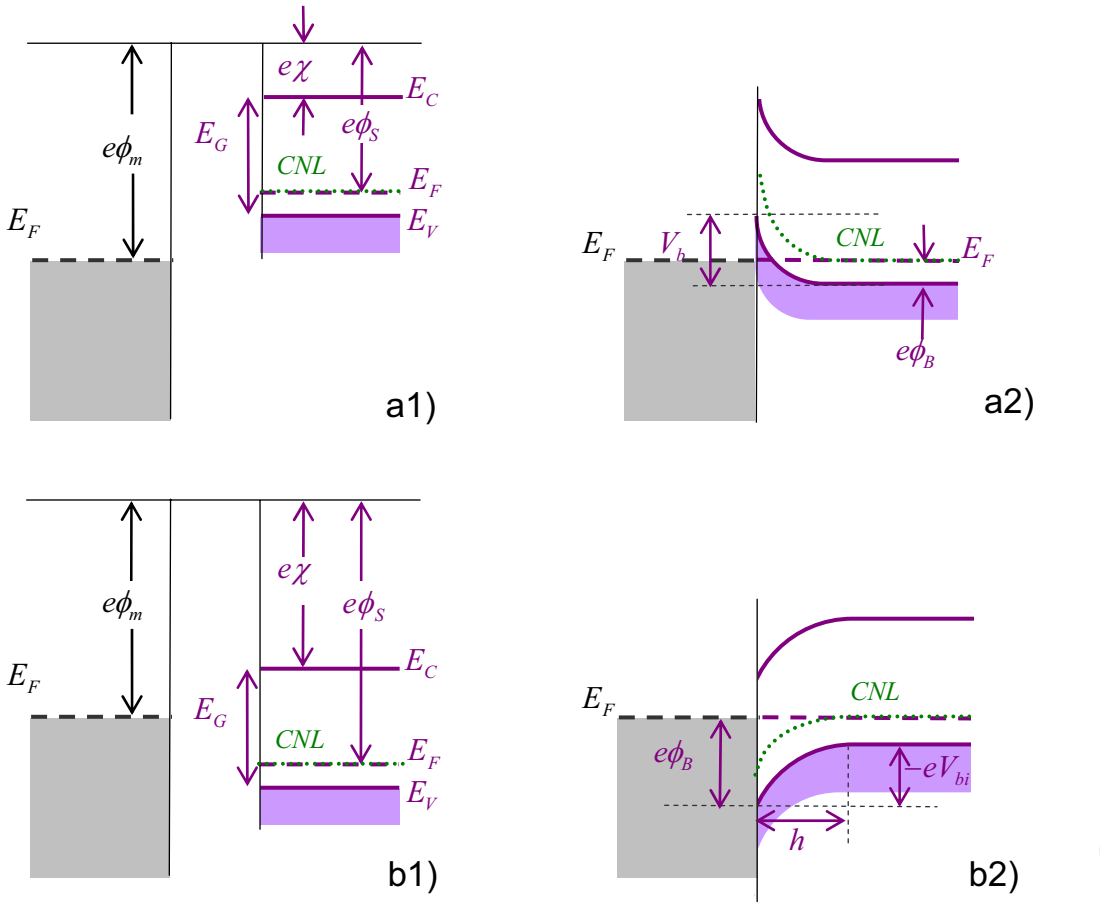

Figure 6.2 *Energy band diagram of a p-type semiconductor in contact with metal. Left column: Before contact; right column: After contact. a)* $\phi_m > \phi_s$, *the metal semiconductor (p-type) contact shows ohmic contact characteristics; b)* $\phi_m < \phi_s$, *a Schottky contact is formed. Due to the depletion layer at the interface, the contact shows rectifying behavior, i.e. a diode characteristics with the barrier height* $e\phi_B$ *as the central parameter. CNL stands for the charge neutrality level that coincides with the Fermi level in the bulk of the semiconductor when no voltages are applied to the device [139].*

Let's consider a metal and a p-type semiconductor which are not in contact and are in separate systems. The work functions $e\phi_m$ and $e\phi_S$ of both materials are defined as the energy differences between their Fermi-levels and the vacuum level as a common reference (Figure 6.2). The energy difference $e\chi$, measured from the bottom of the conduction band E_C to the vacuum level, is the electron affinity of the semiconductor. If the

two materials are brought together, electrons will flow from the material with the higher Fermi-level to that with the lower one until thermal equilibrium is established across the interface. This is achieved by an electronic potential that counteracts on the electron flow. In equilibrium, its total sweep V_{bi} will be the same in magnitude as the original discontinuity of the Fermi-levels has been, i.e. $V_{bi} = \phi_m - \phi_S$ and the Fermi levels will move up. In solid state physics V_{bi} is known as contact potential, specifically when semiconductors are involves as built-in potential. In electrochemistry notation, the term galvanic potential is used in stead.

When $\phi_m < \phi_s$, the built-in potential corresponds to a downward band bending (Figure 6.2 b2), accompanied by a full depletion of holes over a range h towards the semiconductor bulk. The quantity $e\phi_B = (E_G + e\chi) - e\phi_m$ is called the Schottky barrier height. The space charge density $\rho(x)$ in this depletion range is consequently constant and equal to $\rho = -eN_A$ with the acceptor concentration N_A. Solving Poisson's equation, $d^2V/dx^2 = -\rho(x)/\varepsilon\varepsilon_0$, is a trivial task then giving $V(x) = \left[(eN_A)/(2\varepsilon\varepsilon_0)\right]x^2$ for the potential profile in the depletion layer, where x is now counted from the start of the depletion layer towards the interface. The depletion width h is then obviously related to the built-in potential by:

$$h = \sqrt{\frac{2\varepsilon\varepsilon_0}{eN_A} \cdot V_{bi}} \tag{6.1}$$

When an external voltage V is applied in forward direction (+ to the semiconductor; - to the metal), it will drop across the depletion layer meaning it will modify it such that V_{bi} is replaced by $(V_{bi} - V)$. Equation (6.1) can still be applied giving

$$h = \sqrt{\frac{2\varepsilon\varepsilon_0}{eN_A} \cdot (V_{bi} - V)} \tag{6.2}$$

for the depletion layer width as a function of applied forward voltage. Due to the shrinking of the depletion layer, a current density exponentially increasing with forward voltage is observed, contributing the diode characteristics of the Schottky contact.

We address a final remark to the charge neutrality level in the semiconductor. It is a characteristic (though in general temperature dependent) energy of the band structure like the valence or the conduction band edges and defined by the condition that it coincides with the Fermi level asymptotically in the bulk of the semiconductor for the case of chemical equilibrium, i.e. without voltages applied to the device. Thus choosing the CNL for following the electrostatic potential in a semiconductor device directly illustrate voltage drops when reference to contact Fermi levels. Further discussion of Schottky

contact on hydrogen terminated diamond surface is in section 7.2.

■ Metal-oxide-semiconductor Junction

When the charge flow across the metal semiconductor interface is prevented, for example, by inserting an oxide layer in between, then, the metal semiconductor contact is converted to be a metal-oxide-semiconductor structure (also called MOS capacitor, the metal is generally used as a gate contact to apply a bias voltage between the metal and the semiconductor bulk). In reality, charges exist in the oxide layer. These oxide charges are independent of bias voltage and are in most cases positive. In equilibrium and without a bias voltage, the surface of the p-type semiconductor near the oxide usually becomes weakly depleted (downward band bending), as shown in Figure 6.3 (a). The total areal charge density $\sum_{SC}$ in the semiconductor depletion layer and the metal sheet charge density σ_m adjust to the (fixed) oxide charge density such that charge neutrality is fulfilled and the total built-in potential sweep equals the back-circuit galvanic potential $(\phi_S - \phi_m)/e$. When this MOS capacitor is biased, four different cases may exist at the semiconductor surface: When a small negative voltage (V < 0) is applied to the metal gate, the valence-band edge of the p-type semiconductor bends up, and at certain voltage (called flat band voltage), the valence band edge may become flat (Figure 6.3b, **flat band**). As the voltage become more negative, the valence band near the edge may even get upward bended. This band bending causes an **accumulation** of majority carriers (holes) near the semiconductor surface (Figure 6.3c). When a small positive voltage (V> 0) is applied to the gate, the bands bend down more than for V=0, which causes a further **depletion** (Figure 6.3d) of the majority carriers. However, as the voltage increases, the bands may bend even more downward so that the number of electrons (minority carriers) at the surface is larger than that of the holes. This is the case of **inversion** (Figure 6.3e) since the surface is inverted from p-type to n-type.

In all cases, the discontinuity of the Fermi levels is identical to the gate voltage applied, i.e. $E_{F,SC} - E_{F,m} = e \cdot V_G$. As a general consequence of Poisson's equation, a change $\Delta\sum_{SC}$ of the total (deplete integrated) areal charge density in the semiconductor is given by the product of the areal gate capacitance $C_{ox} = (\varepsilon\varepsilon_{ox})/d$ and the change of the electrostatic potential $V(x_s)$ at the channel surface, i.e. $\Delta\sum_{SC} = C_{ox} \cdot \Delta V(x_s)$.

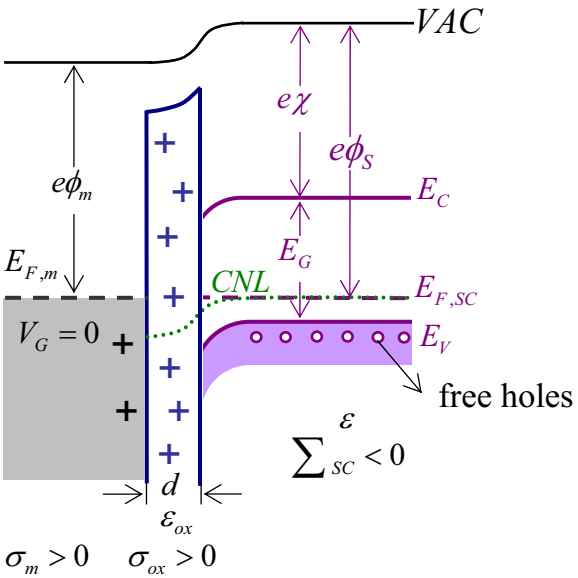

(a) Band diagram of an MOS junction in equilibrium, with positive oxide charges and work function difference $(e\phi_S)-(e\phi_m)>0$.

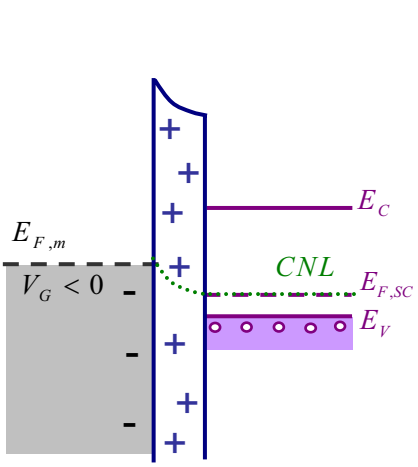

(b) flat band

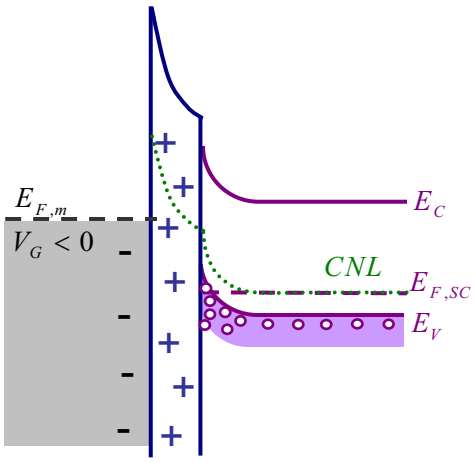

(c)accumulation

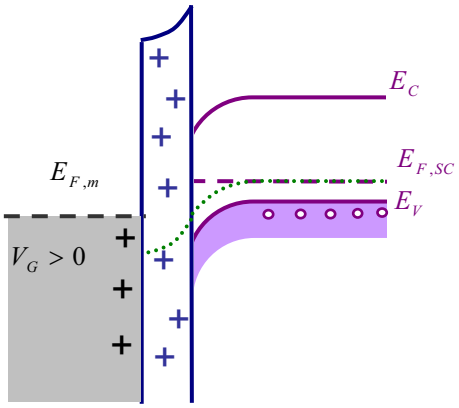

(d) depletion

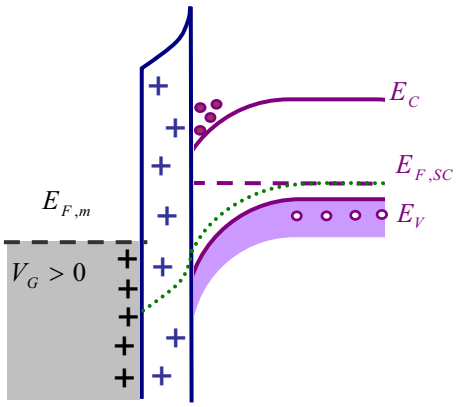

(e) inversion

Figure 6.3 *Energy band diagrams for the metal oxide p-semiconductor structure, for the conditions of equilibrium (a), flat band (b), accumulation (c), depletion (d) and inversion (d). Further description is in the text.*

■ **Electrolyte-semiconductor Interface**

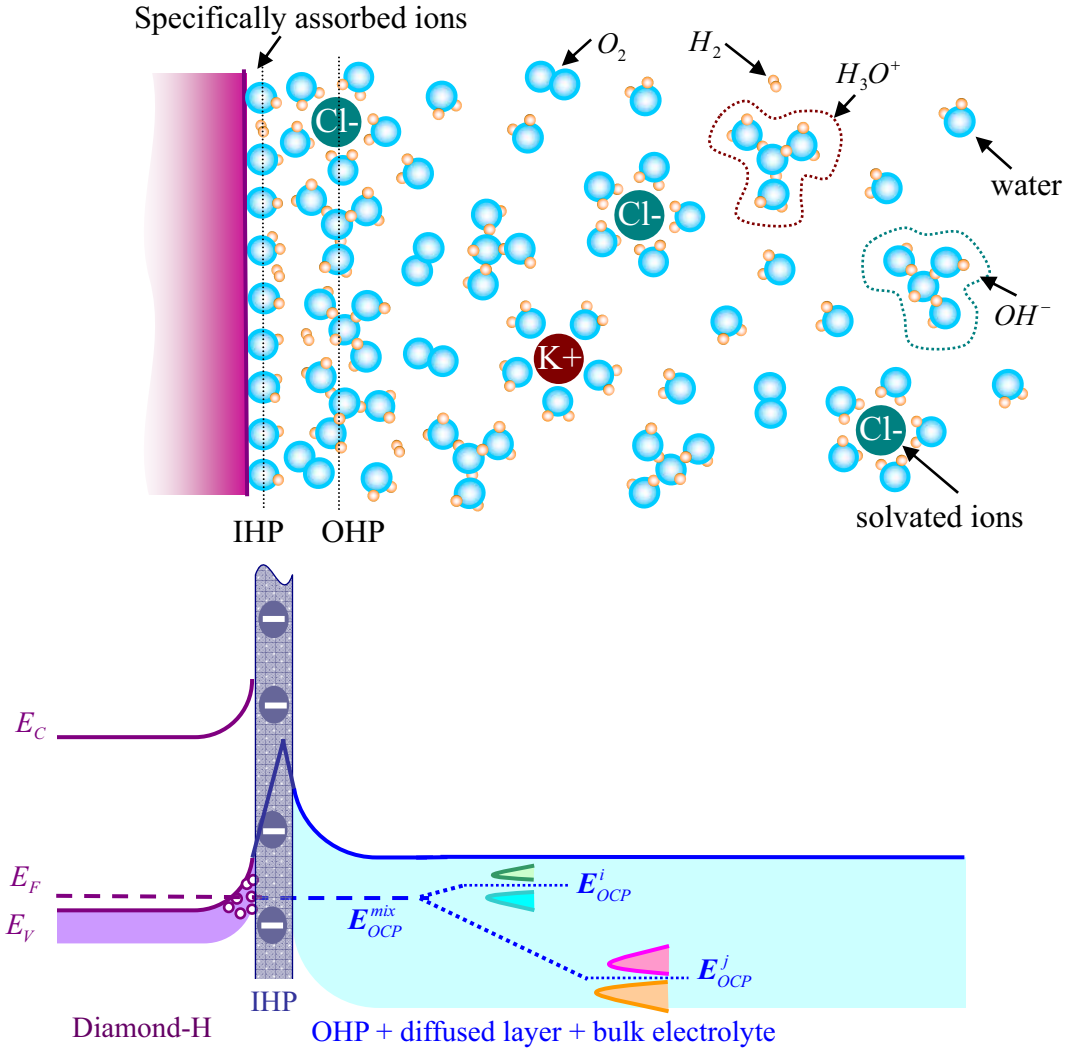

Figure 6.4 *Structure (upper part) and energy band diagrams (lower part) for the electrolyte-semiconductor (p type) structure for the condition of equilibrium, using the mix-potential theory.*

In contrast to metals or semiconductors, the analog of the Fermi level of a electrolyte, i.e. the chemical potential of electrons, is controlled by the red-ox couples inside. And the weight of each red-ox couple to that Fermi level is affected by factors like the electrode-electrolyte interfacial structure via the kinetics of electron exchange. Practically, this can be determined by open-circuit potential measurements (see chapter 5).

6.2 Field Effect Transistors (FETs)

Transistors are the most important semiconductor devices. A transistor is a three-terminal device where the resistance between two of the contacts is controlled by the

third. For the so-called field effect transistor (FET) the three terminals are called source, drain and gate as shown in Figure 6.5. According to the way that the gate capacitor is formed, FETs can be further classified into three different branches,: The first branch is called IGFET (insulated-gate FET), in which the gate capacitor is an insulator. The commonly used MOSFETs (metal insulator semiconductor FET) and newly born SGFETs (solution gated FET) belong to the IGFET branch. The other two branches are the JFET (junction FET) and MESFET (metal semiconductor FET). In a JFET, the gate capacitor is formed by the depletion layer of a p-n junction (JFET), while in a MESFET, this is achieved by a Schottky barrier [139]. For further details, the readers is referred to standard text book on semiconductor such as [139, 140].

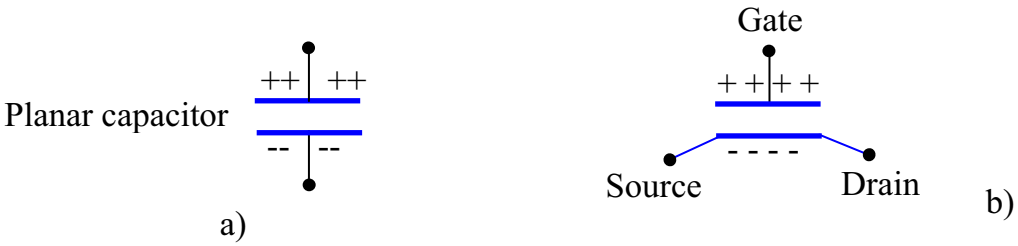

Figure 6.5 *Field effect in a planner capacitor (a) and in a transistor (b).*

The members of the FET family have much in common. The drain-source current that passes through the channel follows a general characteristics. Consider a field effect transistor with a p-type conductive channel as shown in Figure 6.6. Define the direction from source to drain as *y* axis, and the *x* coordinate to be downward, perpendicular to the channel. Now consider the current flowing across the channel (in yellow). Assuming the current flow is one dimensional (the gradual channel approximation) [141]. Then in an incremental length *dy* at position *y* in the channel, the total mobile channel charge is [142]:

$$\left(\int_0^\infty \rho_{ch}(x,y)\,dx\right)\cdot W dy = \sigma_{ch}(y) W dy \tag{6.3}$$

where $\rho_{ch}(x,y)$ is the charge per unit area in the channel at position (x,y). Recall that current is defined as the amount of charge passing through a given area per unit time. The channel current I_{DS} at a given *y* is:

$$I_{DS} = W Q_{ch}(y)\frac{dy}{dt} = W Q_{ch}(y) v(y) \tag{6.4}$$

with *v(y)* as the average channel hole velocity at position *y*.

Consider first $V_{DS} = 0$, i.e. chemical equilibrium within the channel. In this situation, an electrostatic potential $V(x,y)$ is established which we want to understand, such that $eV(x,y)$ is the energy of the semiconductor CNL with reference to the gate electrode

Fermi level as an equipotential plane. This potential establishes a detailed balance of drift and diffusion currents leading to vanishing total current density everywhere. When a finite drain source voltage is applied, the potential profile changes such that the sum of the modified diffusion and drift currents leads to identical and non zero current through every channel cross section.

In most field effect devices this sum can be approximated by the drift current itself. Then the velocity in (6.4) can be replaced by the drift velocity:

$$v(y) = \mu(y)\varepsilon_L(y) \tag{6.5}$$

Here $\mu(y)$ is the average channel mobility and $\varepsilon_L(y)$ is the longitudinal electric field dV/dy. With this, the current density can be written as

$$I_{DS} = W\sigma_{ch}(y)\mu(y)\cdot\left(-\frac{dV}{dy}\right) \tag{6.6}$$

and is independent of y. In field effect devices, the **mobile** channel charge density $\sigma_{ch}(y)$ depends only implicitly via $V(y) = V(y, x_{ch})$ on the position coordinate y where x_{ch} is the locus of the mobile charges in the channel. $V(y)$ is in general a monotouious function of y so that integration of equation (6.6) over the channel length L from source to drain can be transformed to an integration over voltage and yields

$$\boxed{I_{DS}\cdot L = -W\int_0^L \mu(y)\cdot\sigma(y)\frac{dV}{dy}dy = -W\mu\int_{V(0)}^{V(L)}\sigma(V)dV} \tag{6.7}$$

where in the last step μ has been extracted from the integral as an average mobility. With $V(0) = -V_{GS}$ and $V(L) = -V_{GS} + V_{DS}$, this gives

$$\frac{I_{DS}\cdot L}{W\cdot\mu} = -\int_{-V_{GS}}^{-V_{GS}+V_{DS}}\sigma_{ch}(V)dV = S(V_{GS}, V_{DS}) \tag{6.8}$$

S (in unit of Jcm^{-2}) yields the output characteristics $I_{DS}(V_{DS})$ with V_{GS} as a constant parameter, and the transfer characteristics $I_{DS}(V_{GS})$ with V_{DS} as a constant parameter. Note that in the limit of small source drain voltage, the integral in (6.8) yields $S(V_{GS}, V_{DS}) = -\sigma_{ch}(-V_{GS})\cdot V_{DS}$, In the ohmic range, the output characteristic

$$I_{DS} = -\frac{W\cdot\mu}{L}\cdot\sigma_{ch}(-V_{GS})\cdot V_{DS} \tag{6.9}$$

is thus linear and the transfer characteristics follows the function $-\sigma_{ch}(-V_{GS})$. Equation (6.8) is the central relation for all types of field effect devices. as a simple example we illustrate it for the classical MOSFET device based on the MOS structure of Figure 6.3. An n-type source and drain region completes it to from the transistor, and it is operated in the inversion region of the channel. In that region, the two built-in p-n junctions at the channel

ends are removed by the gate voltage turning the channel n-type as well, and the longitudinal voltage V_{DS} drops exclusively along the channel length. Further more, the space charge within the channel is in this regime dominated by the electrons in the conduction band, i.e. mobile $\sigma_{ch}(y)$ and total space charge density $\sum_{SC}(y)$ can be set equal to each other. Thus, with V_T being a channel threshold potential where inversion sets in (more electrons than holes!), $\sum_{SC} = \sigma_{ch}(y) = C_{ox} \cdot (V - V_T)$. With this, (6.8) yields

$$I_{DS} = \frac{W}{L} C_{ox} \mu \left[(V_{GS} + V_T) V_{DS} - \frac{V_{DS}^2}{2} \right] \tag{6.10}$$

Note that following one sign convection (Figure 6.3 and Figure 6.6) V_T is positive and the inversion region corresponds to negative V_{GS} with $V_{GS} < -|V_T|$. Consequently, negative V_{DS} drives positive current in $+y$ direction from source to drain. Further more, for inversion and accumulation layers, the potential $V(x_{ch})$ at the depth coordinate of the locus of the mobile charges can be set equal to the potential $V(x_s)$ at the channel surface.

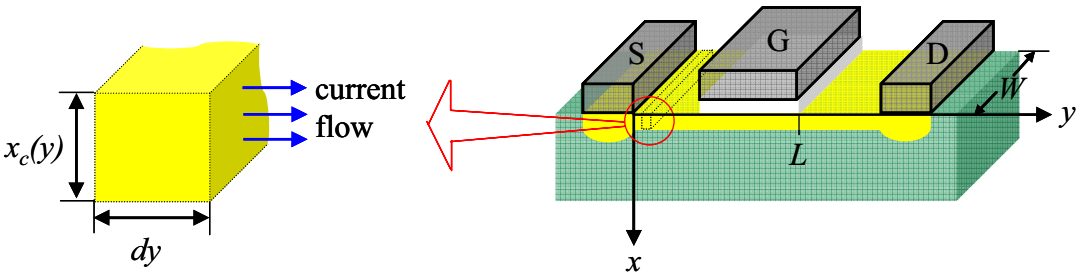

Figure 6.6 *Geometry of a general field effect transistor. The block in yellow is a p-type conductive channel on the substrate (green). Holes carry the current by moving in the positive y direction. A small strip of dy in length and $x_c(y)$ in depth is shown on the left hand side. Total charge under the strip is $\sigma_{ch}(y)Wdy$. "S", "D" and "G" represent for "source", "drain" and "gate" respectively.*

A I_{DS} - V_{DS} plot with V_{GS} as parameter is called output characteristics, while a I_{DS} - V_{GS} plot at constant V_{DS} value is called transfer characteristics. There are three distinct regions in the output characteristic of the FET family: linear region, saturation region and pinch-off region.

6.3 Introduction to Metal Semiconductor FETs

A metal semiconductor field effect transistor (MESFET) is a special FET, in which a

Schottky junction serves as gate that modulates the depletion region between the gate electrode and the conductive channel underneath and thereby the current [143-145]. Obviously, such a device is constructed from three metal-semiconductor building blocks with one being a Schottky contact and the other two ohmic contacts.

In the following, we will derivative an analytical model for long channel p-type MESFETs, using the results from the discussion of metal semiconductor contact in section 6.1. As for all FETs, the mathematical treatment of MESFETs starts with equation (6.8). Express the charge per unit area in the channel at position *y*, $\sigma_{ch}(y)$, as:

$$\sigma_{ch}(y) = e \cdot N_A \cdot t(y) \tag{6.11}$$

where N_A is the acceptor concentration of the p-type semiconductor, and $t(y)$ is the effective channel thickness at position *y*. It is given by:

$$t(y) = a - h(y) \tag{6.12}$$

With *a* as the thickness of the channel. The depletion width, $h(y)$, is controlled locally by the bias $V(y)$ which varies from $V(0) = -V_{GS}$ to $V(L) = -V_{GS} - V_{DS}$ across the Schottky junction:

$$h(y) = h\left(V(y)\right)\sqrt{\frac{2\varepsilon\varepsilon_0}{eN_A}\left(V_{bi} - V(y)\right)} \tag{6.13}$$

As discussed in section 6.1. with this the mobile channel charge density $\sigma_{ch}(y) = \sigma(V)$ can be written as

$$\sigma_{ch}(V) = eN_A \cdot a - \sqrt{2eN_A\varepsilon\varepsilon_0\left(V_{bi} - V\right)} \tag{6.14}$$

And according to (6.8), $S(V_{GS}, V_{DS})$ can be evaluated:

$$\begin{aligned} S(V_{GS}, V_{DS}) &= -\int_{-V_{GS}}^{-V_{GS}+V_{DS}} \sigma_{ch}(V)dV \\ &= -eN_A \cdot aV_{DS} + \frac{2}{3}\sqrt{2eN_A\varepsilon\varepsilon_0}\left[\left(V_{bi} + V_{GS} - V_{DS}\right)^{3/2} - \left(V_{bi} + V_{GS}\right)^{3/2}\right] \end{aligned} \tag{6.15}$$

Using the pinch-off voltage V_T, defined by the condition $a = h(V_T) = \sqrt{\frac{2\varepsilon\varepsilon_0}{eN_A}} \cdot \sqrt{V_{bi} - V_T}$ to express the layer thickness a, (6.15) can be rewritten as:

$$\begin{aligned} S(V_{GS}, V_{DS}) &= -\sqrt{2\varepsilon\varepsilon_0 eN_A}\sqrt{V_{bi} - V_T} \cdot V_{DS} \\ &+ \frac{1}{3}\sqrt{2eN_A\varepsilon\varepsilon_0}\left[2\left(V_{bi} + V_{GS} - V_{DS}\right)^{3/2} - \left(V_{bi} + V_{GS}\right)^{3/2}\right] \\ &= -\frac{1}{3}\sqrt{2\varepsilon\varepsilon_0 eN_A}\left(V_{bi} - V_T\right)^{3/2}\left[\frac{3V_{DS}}{V_{bi} - V_T} - \frac{2\left(V_{bi} + V_{GS} - V_{DS}\right)^{3/2} - \left(V_{bi} + V_{GS}\right)^{3/2}}{\left(V_{bi} - V_T\right)^{3/2}}\right] \end{aligned} \tag{6.16}$$

With this, the characteristic is found from (6.8) as

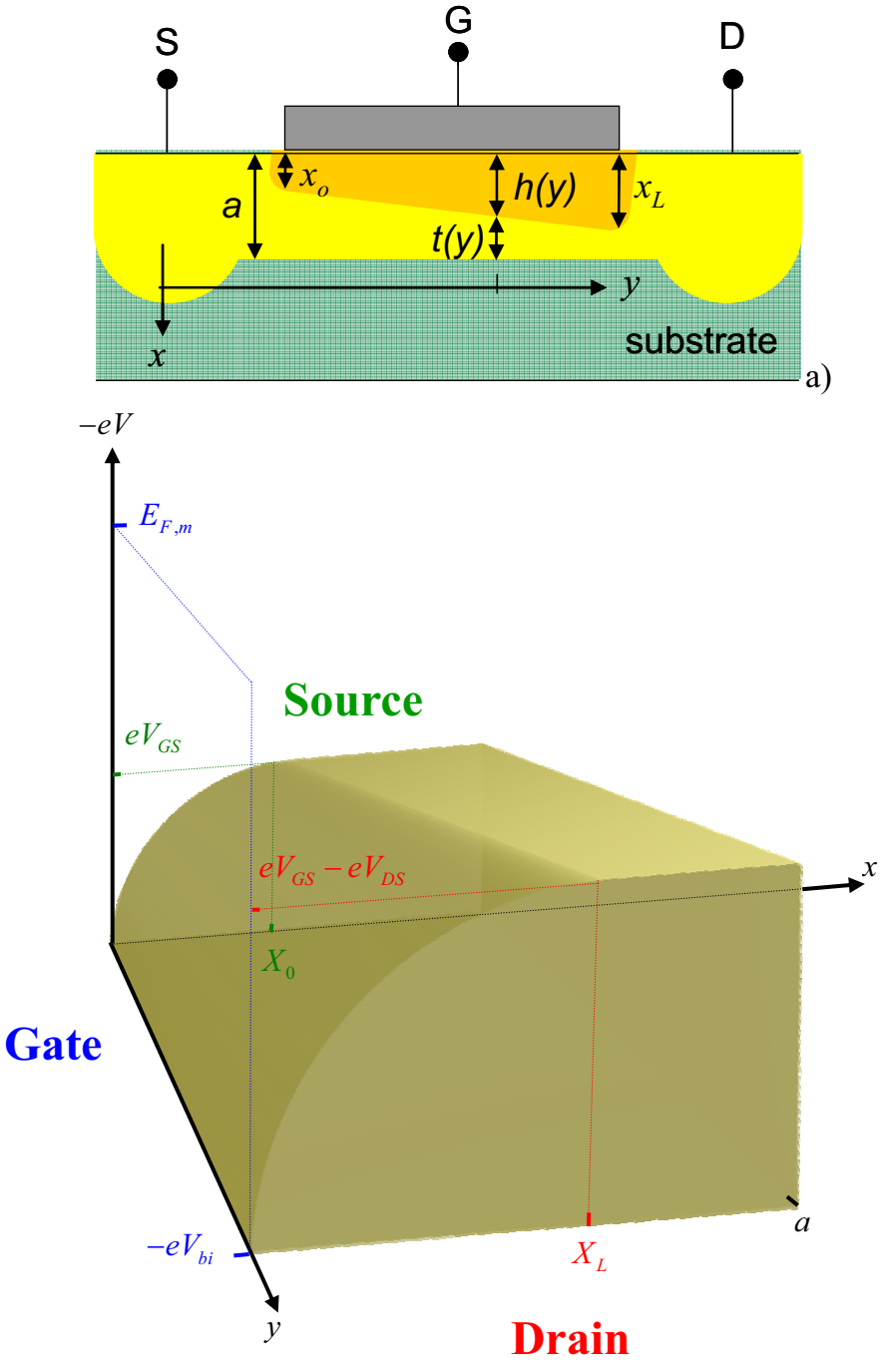

Figure 6.7 *a) Cross section of a p-channel MESFET. The gate (in blue) forming Schottky contact with the conductive channel (in yellow). The thickness of the channel is a. At position y, the depletion width is h(y) and the effect thickness of the remaining channel is t(y). b) Profile of CNL of the conductive channel as a result of applied drain-source voltage* V_{DS} *and gate-source voltage* V_{GS}*, respectively. The electrostatic potential* $V(x,y)$ *in the surface interface plane along the channel, visualized as the energy* $E_{F,m} - eV(x_s,y)$ *of the valence band maximum relative to the Fermi level in the gate metal (compare Figure 6.2-b2).*

$$I_{DS} = -\frac{e^2 N_A{}^2 a^3 W \mu}{6 L \varepsilon \varepsilon_0}\left[\frac{3V_{DS}}{V_{bi}-V_T} - \frac{2\left(V_{bi}+V_{GS}-V_{DS}\right)^{3/2} - \left(V_{bi}+V_{GS}\right)^{3/2}}{\left(V_{bi}-V_T\right)^{3/2}}\right] \tag{6.17}$$

μ is the mobility of holes, V_T is the threshold voltage: for this depletion-type p-channel MESFET, V_T is positive while for enhancement-type, V_T is negative. Equation (6.17) is the drain source current in the linear mode of operation. Note again that negative V_{DS} drives positive current in our sign convention, i.e. it is valid up to the maximum of $I_{DS}\left(-V_{DS}\right)$. Saturation due to pinch-off is not covered by (6.17). As a good approximation $I_{DS} = I_{DS}\left(-V_P\right)$ can be expressed for $-V > -V_P$, and the pinch-off voltage V_P can be found by $dI_{DS}/dV_{DS} = 0$ for each gate source voltage.

Thanks to the complexity of the analytical models for MESFETs (the discussion above is one example. Another popular model proposed by Khatibzadeh et al. [146]), people explored other models like the so-called finite element methods [147], and the empirical Curtice model [141]. In chapter 7, we will use the analytical models (6.17), and the Curtice model to simulate the output characteristic of hydrogen terminated diamond MESFETs.

6.4 Introduction to Solution Gated FETs

A traditional Solution Gate Field Effect Transistor (SGFET) [52, 148, 149] is a device that is “modified” form the classical Metal Oxide Semiconductor Field Effect Transistor (MOSFET) by removing the metal gate from a MOSFET and replacing it with a reference electrode and an electrolyte, whose concentration of certain ions is for example to be determined from the characteristics fo the transistor (Figure 6.8). Another popular used name for the SGFET is therefore ISFET (Ion Sensitive Field Effect Transistor) when the SGFET is used for sensing the concentration of ions. However, the insulating oxide in a SGFET is not always necessary. As long as the solution semiconductor interface is polarizable enough (see the discussion in section 5.1), SGFETs work properly without intentional insulation gate. The hydrogen terminated diamond SGFETs or graphene SGFETs are of this type, which in the following will be called novel SGFETs. Figure 6.8 shows a representative sketch of MOSFET and SGFET. It can be seen that in MOSFET, metal oxide semiconductor structure is applied for constructing the “field effect”, while in SGFET; this is achieved by the solution semiconductor building block, with or without insulator. Both of these building blocks served as planner capacitor to generate the “field

effect". Thanks to the similarities of these building blocks, the current-voltage characteristic of them has much in common. In the following text, we will start with a simple comparison of MOSFETs and traditional SGFETs.

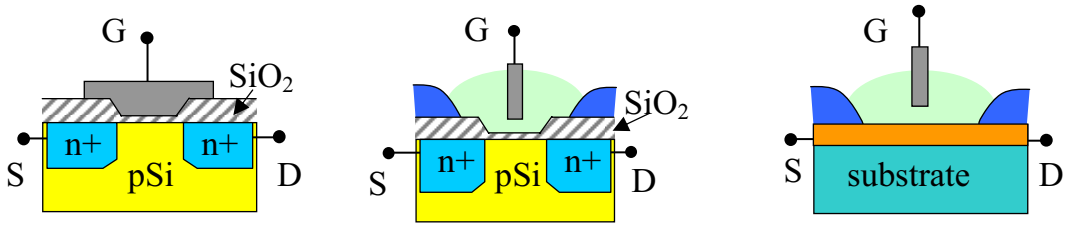

a) b) c)

Figure 6.8 *Schematic representation of MOSFET and SGFET. a) MOSFET, b) traditional SGFET with p-type silicon. In which gate ("G") is composed by a reference electrode and electrolyte. c) novel SGFET with hydrogen terminated diamond or graphene (in orange), in which the gate oxide is removed due the polarizable nature of the electrolyte-semiconductor interface. For both of the two SGFETs, every part has to be encapsulated except the gate area, which is open to the electrolyte.*

For a MOSFET and an SGFET, we can express $\sigma_{ch}(V)$ in equation (6.8) in form of oxide capacitance per unit area C_{OX}. Hence, equation (6.10) is valid for both devices [148]. Rewrite (6.10) as:

$$I_{DS} = \beta(V_{GS} - V_T - \frac{1}{2}V_{DS}) \cdot V_{DS} \tag{6.18}$$

where β is a geometric sensitivity parameter, $\beta = \mu C_{OX} W/L$, with C_{ox} as the gate insulator capacitance per unit area and *W/L* as the width to length ratio of the channel. V_{GS}, V_{DS} and V_T are the gate-source voltage, drain-source voltage and threshold voltage, respectively. The threshold voltage V_T is always offset by a characteristic value from flat band potential $(\phi_{SC} - \phi_m)/e$. This offset contains a contribution $\delta V_{ox} = \sigma_{ox}/C_{ox}$ depending on the oxide layer, thickness and dielectric constant (see Figure 6.3). Thus

$$V_T = \phi_{SC} - \phi_m + \frac{\sigma_{ox}}{C_{ox}} + V_0 \tag{6.19}$$

For SGFETs, the compact layer between to solid and the electrolyte acts in a similar way as the oxide layer: it can host a fixed areal charge density σ_{ads} that is due to adsorbed ions from the electrolyte (i.e. voltage independent), and it can separate the mobile (ionic) charge of the gate electrolyte from the solid. As a consequence, a term $\sigma_{ox}/C_{cl} + \sigma_{ads}/C_{ocl}$ has to be added to the threshold voltage where C_{cl} and C_{ocl} are the capacitances of the total and the outer compact layer, respectively (see section 2.3).

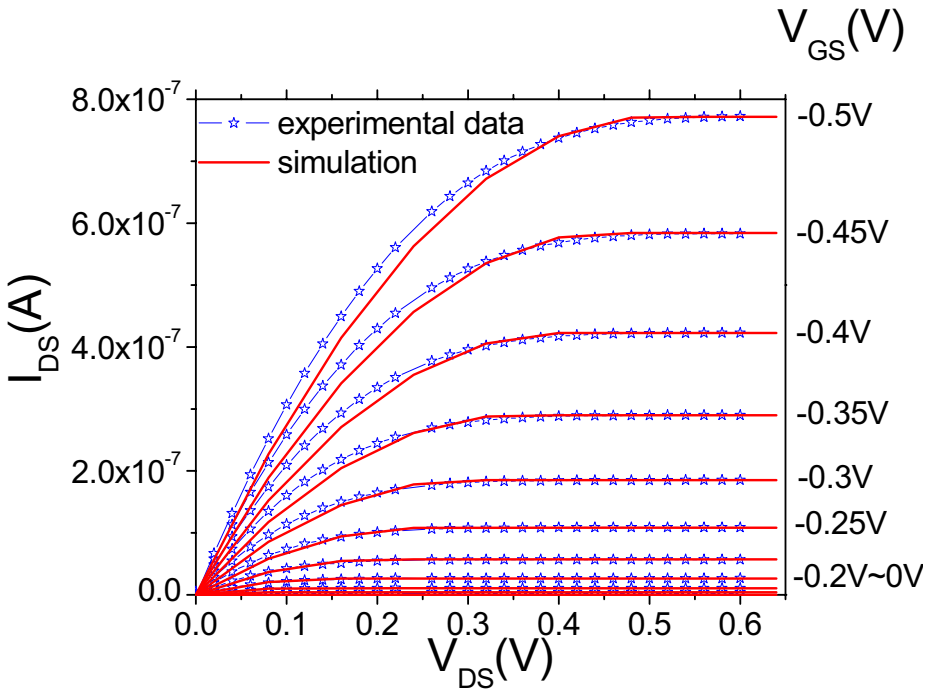

V_{GS} (V)	-0.05	-0.1	-0.15	-0.2	-0.25	-0.3	-0.35	-0.4	-0.45	-0.5
simu. C_{dl} ($\mu F/cm^2$)	1.00	0.67	0.74	0.93	1.09	1.31	1.50	1.68	1.83	1.96

Figure 6.9 *Simulation of hydrogen terminated diamond SGFETs with the long-channel analytical model of MOSFET (equation (6.10)). The conductive channel is* $W = 0.1cm$ *in width and* $L = 1.3cm$ *in length. The electrolyte is a phosphate buffer (pH7) and the reference electrode is Ag/AgCl (3M). More experimental description of this SGFET is in chapter 8. For the simulation, the oxide capacitance* C_{OX} *in (6.10) is replaced by electrochemical double layer capacitance* C_{dl}*, the value of which is listed in the table, varying by a factor of 2 with gate-source voltage* V_{GS}*. The other parameters for modeling are:* $\mu = 41cm^2/Vs$*,* $V_T = 0V$*. Note that the specific threshold voltage depends on the kind of reference electrode used in the experiment. The value of zero is thus coincidental in this case!*

The SGFET on the basis of hydrogenated diamond works in the accumulation region (for holes) for which the characteristic function $\sigma_{ch}(V)$ is in fact similar to the inversion region for the MOSFET. It will be discussed in detail in chapter 8. Experimentally, only the role of the dielectric is taken by the compact Helmholtz layer. For negative ions adsorption in the compact layer and when neglecting the voltage drop in the diamond and the diffuse layer in the electrolyte, on can in fact show that the same $\sigma(V)$ characteristics as for the MOSFET is expected with

$$V_T = \Phi_{SC} + \mu_{Ag^+} + \frac{\sigma_{ads}}{C_{ocl}} + \frac{1}{e}U\left(-\frac{\sigma_{ads}}{e}\right) \tag{6.20}$$

The function U is nearly constant replacing V_0. C_{ocl} is the capacitance of the outer compact layer and μ_{Ag^+} is the chemical potential of the red-ox electrons of the reference electrode used in the experiment (Ag/AgCl in our case) that replace the metal work function for the electrolytic gate.

For an SGFET, ion sensitivity is provided by specific adsorption at the inner Helmholtz plane, i.e. by the term σ_{ads} in threshold voltage of the transistors. It is usually governed by the dissociation of surface oxide groups. Hence, it is specific proton adsorption that makes an SGFET sensitive to the pH of an electrolyte! For traditional SGFETs, for example those with siliconoxide as insulators, the oxide surface charge can be described by the site-binding model, which is based on an equilibrium between the amphoteric SiOH surface sites and the H^+- ions in the solution [148, 149]. For novel type SGFETs, there is no oxide layer between the electrode and the sample surface, since nonoxide semiconductor surfaces (hydrogen terminated diamond or epitaxial graphene) are directly touching the electrolyte. Thereby nearly no hydroxyl groups bind on the solid side of the interface. As a result, the "site-binding model" does not work for novel SGFETs devices. The mechanism of novel SGFET will be discussed in chapter 8.

In conclusion, MOSFETs and novel SGFETs share much in common. For both, the long-channel approximation is fulfilled, and both work on similar charge control mechanisms. As a consequence, the output characteristic of novel SGFETs can be perfectly simulated like for MOSFETs (equation (6.10)), only the oxide capacitance must be replaced by the compact layer capacitance C_{cl}. An example is presented in Figure 6.9.

Chapter 7 The Diamond based Metal Semiconductor Field Effect Transistor (MESFET): Experiments and Modeling

7.1 Literature Results

Thanks to the excellent properties of diamond, like wide bandgap, high electron mobility, high electron saturation velocity and high breakdown voltage, the utilization of diamond for electronic devices has been of significant interest in the recent decades [150, 151]. Semiconducting diamond has been proposed for the application as radiation detector, power and microwave devices, green and UV LED's, thermistors and various switching and sensing devices [151]. Among them, the diamond MESFET is of particular interest because the performance of a MESFET is controlled by the Schottky gate, and the breakdown voltage of diamond Schottky diodes has been demonstrated be much higher than for other semiconductors like silicon and SiC at the same doping level [152]. The first diamond based MESFET (on boron doped diamond) is reported by Shiomi et al. [153] in 1989. However, no pinch-off performance has been observed in the output characteristics despite of much effort, probably due to the limited accuracy of doping technique adopted. In the same year and shortly after, Landstrass and Ravi [3, 4] reported on surface conductivity on hydrogen terminated intrinsic diamond. Such specimens, when exposed to normal atmosphere, exhibit: a p-type two-dimensional conductivity with a sheet resistance of the order of $10-20k\Omega/\square$, a hole concentration around $10^{13}cm^{-2}$, and a hole mobility of about $100-150cm^{-2}/Vs$ [5, 6]. The thickness of the conductive layer is estimated to be less than 10nm [7]. Several years later, Kawarada et al. [8, 154] made the first attempt on fabricating hydrogen terminated intrinsic diamond MESFETs of both enhancement and depletion type [155]. Their success was based on the capability of producing gate lengths in the micrometer range and below [156, 157].

Although diamond MESFETs has been fabricated and demonstrated, yet, the

physical/chemical nature of the gate metal/diamond interface is still under discussion. Device physicists are puzzled by the mechanism behind the hydrogen terminated diamond MESFET. Main issues that under debate are, for example:

1) "Two-dimensional surface acceptor model" [8, 158] or " diffused acceptor model" [5, 159]: whether acceptors caused by hydrogen are distributed two-dimensionally on the surface or three-dimensionally from the surface down into the subsurface region via diffusion of hydrogen atom;

2) "Complete contact model" [8] or "incomplete contact model" [8-10]: whether the gate metals and the diamond surface are in direct contact or indirect contact where "separation layer" is inserted between the metal and the diamond.

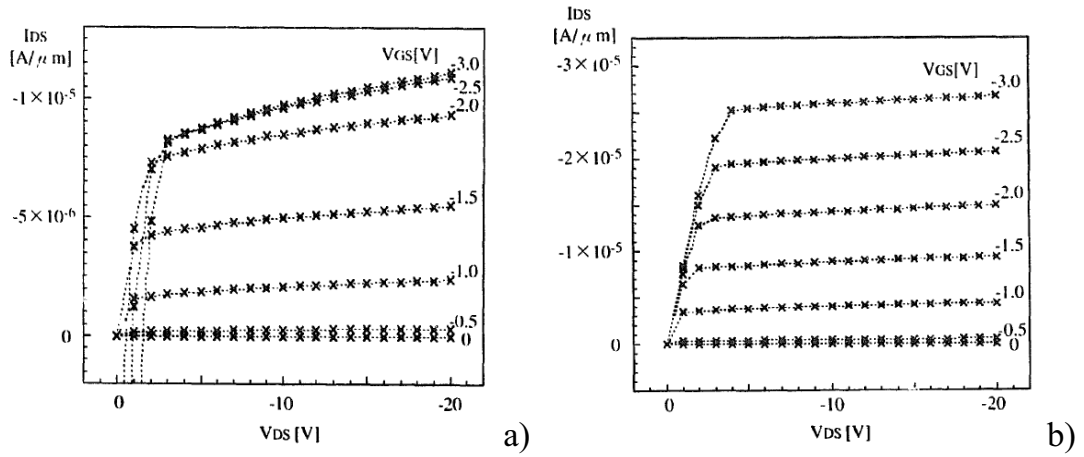

Figure 7.1 *Output characteristics of simulated diamond-H MESFETs, with the gate length* $L_g = 7\mu m$ *and an areal acceptor concentration of* $1\times10^{13} cm^{-2}$ *[8]: a) Following the "complete contact model", with the Schottky barrier height of 2.0eV; b) Following the "incomplete contact model". The gate metal has a Schottky barrier height of 0.8eV. The dielectric constant of the insulator is 2. Note that there is large leaking current in the "complete" case.*

On verifying the truth of those models, devices physicists applied commercial computer simulation, which, however, is based on the model on classical semiconductor MESFETs, especially the GaAs MESFETs [146, 147]. Rather than using the Shockley's analytical models that is developed on the physical picture of the classical semiconducting channel [141, 160] (see chapter 5), those computer programs like SPICE use empirical models, which are based on the equivalent circuits for the devices to be modeled [139, 141]. However, they are still founded on the assumption of classically doped channels which extend to a certain depth below the interface and which are depleted from the surface into the bulk of the semiconductor. This assumption is a fundamental misconception for the 2D hold gas associated with the surface conductivity of intrinsic diamond. Without realizing this physical difference between hydrogen terminated diamond and the classical doped

semiconductor, for which the simulation programs are built, the effort of directly applying such a computer program for interpreting the physical picture of diamond-H MESFETs can highly misleading. For example, such comparative simulations of diamond-H MESFETs and MOSFETs showed that, the MESFETs are always accompanied with large gate leakage currents, since there is no gate oxide [9]. Since much lower leaking currents are measured, some researchers conclude that the diamond FET devices should rather be a MOSFET type (see Figure 7.1) and they claim the existence of a "gap" between gate metal and diamond that serves as a natured insulator. Upon device modeling, the "gap material" believed to be around 0.3nm thick and have a dielectric constant of $\varepsilon \sim 2$ by H.Kawarada et al. [8], while following A.Denisenko et al. [10] it is 30~50nm in thick and has a dielectric constant of $\varepsilon \sim 50$.

In the following, we will present our experimental work of diamond-H MESFETs. Our results will show that the leaking gate-source current decreases systematically with the shrinkage of the gate which causes transition from a double-diode to a transistor characteristics. The suppression of gate currents to a tolerable level is thus a gate length effect and not due to some hypothetical insulator under the gate. Computer assisted simulation based on analytical models as well as empirical modeling is performed.

7.2 The Metal-Diamond Schottky Diode

The Schottky diode is the key element in a classical MESFET. Before studying MESFET characteristics, let's first look how this diode works. In this section, we will present the experimental results of diamond Schottky diodes fabricated with aluminum or chromium contacts.

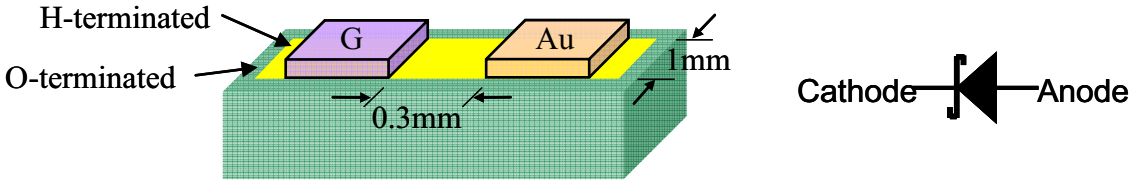

Figure 7.2 *Schematic of diamond Schottky diode and its symbol. The surface conductive channel is sketched in yellow. The Ohmic contact is formed by Au, and the Schottky contact (G in the figure) is constructed by Cr or Al.*

Diamond Schottky diodes are fabricated on intrinsic single crystalline (100) diamonds, either of type IIa bulk crystals or microwave plasma CVD epitaxially grown diamond films on type Ib substrates. First, the diamond surfaces are wet-chemically

cleaned and subsequently terminated with hydrogen by hydrogen plasma, following the receipt in Chapter 3. Next, the samples are kept in normal atmosphere for one day to allow stable p-type surface conductivity. Later, the conductive channel is confined to be 1mm in width via isolating the surrounding surface area by oxygen plasma. Positive photo-resist paint is used as mask during this process. The masking process is described in Chapter 3.

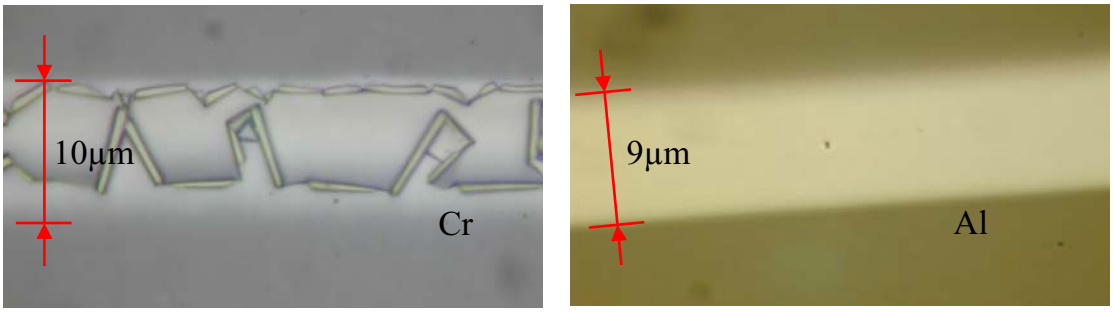

Figure 7.3 *Optical picture of chromium (Cr) and aluminum (Al) gate on a single crystal diamond (100) surface that is hydrogen terminated. Chromium is partially peeled off from the hydrogen terminated diamond. The origin of such poor adhesion is unclear. It is probably related to the hydrophobic nature of hydrogen terminated diamond, because the same material (Al) sticks well on oxygen terminated diamond.*

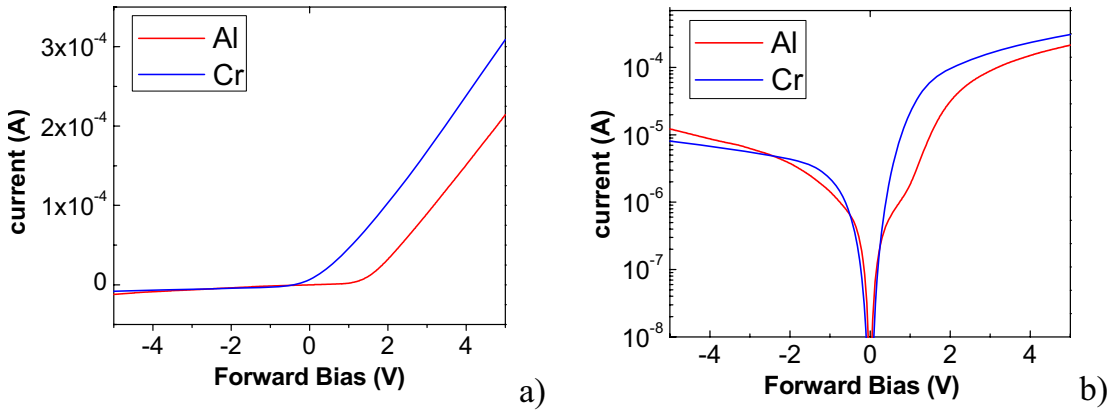

Figure 7.4 *Current-voltage characteristic of the aluminum Schottky diode and the chromium Schottky diode on hydrogen terminated diamond surface in linear scale a), and logarithm scale b). Au forms ohmic contact with diamond-H, and Cr or Al forms Schottky contact on diamond-H. Neglecting the contact resistance between Au and diamond-H, the plots is I-V curve for the diamond-Cr or diamond-Al Schottky diode.*

Finally, the ohmic contacts are fabricated by thermal evaporation. Ohmic contacts are formed by gold (Au) and Schottky contacts are fabricated by using chromium (Cr) and aluminum (Al). The morphology of Schottky contacts on diamond is studied by optical microscopy, as shown in Figure 7.3. After evaporation, Cr is found to be is partially broken, probably due to the poor adhesion between and Cr and the hydrophobic diamond surface.

However, such problem does not exist in the case for aluminum. The picture shows that, upon deposition, aluminum appears to be more stable than chromium on diamond-H surface.

Table 7.1 *Properties of materials relevant to our experiments*

Materials	Au	Al	Cr	diamond-H
Electronegativity (in Pauling unit)	2.54	1.61	1.66	H: 2.20 C: 2.55
Work function (eV)	5.1	4.28	4.5	5.10 ± 0.2
ϕ_B from literatures (V)	0	0.59 [161]	NA	NA
ϕ_B calculated from Figure 7.4 (V) [15]	NA	0.54	0.47	NA

The contacting metal is chosen following the Schottky rule of metal-semiconductor contacts (see section 6.1). Following this, the Schottky barrier for a p-type semiconductor is predicted to be: $\varphi_B = \left(E_g + \chi\right) - \phi_m$. For surface conductive diamond, the Fermi level of the surface is even pushed into the valence band by up to 0.9eV [162] so that $E_g + \chi = 4.2eV$ has to be replaced by the workfunction $\varphi_{diamond-H} \le 5.1eV$. The workfunction ϕ_m of Au is much larger than that of Al and Cr (Table 7.1), and the Schottky barrier expected for Au is (close to zero and unclear) smaller than Al and Cr. In addition, H.Kawarada et al. [9, 154, 161] proposed an empirical "selection rule" for hydrogen terminated diamond, based on their experimental results. They suggested that ohmic contacts ($\chi \ge 1.8$, in Pauling unit) or Schottky contact ($\chi < 1.8$, in Pauling unit) are formed by selecting the metal electronegativity in the periodic table. Thereby following their "selection rule", Au forms ohmic contact while Al and Cr form Schottky contacts on hydrogen terminated diamond. In addition, from Table 7.1, it can be seen that the electronegativity as well as the workfunction of aluminum is slightly smaller than chromium. Thereby the barrier height for chromium is expected to be slightly smaller than that of aluminum.

[15] The calculation is based on "thermionic-emission theory". Due to the complexity of the theory, the derivative of the theory, however, is beyond the scope of the thesis . For detail discussion, readers may refer to *Physics of Semiconductor Devices (3rd edition)* by Sze, S.M. and K.K. Ng, Wiley-Interscience (2006).

7.3 Diamond Based MESFETs: Experiments

The processes for constructing MESFETs on hydrogen terminated diamond surfaces Schottky diodes are similar and described in section 7.2. The differences are: first, in case of MESFETs, there are two Au contacts that serve as drain and source (Figure 7.5); second, the gate length has to be modified to be small enough such that the drain-source current is not dominated by the leaking current from gate-source (see reasoning below). To do so, two razor blades with adjustable gap-distance are used as shadow masks in the metal gate evaporation process.

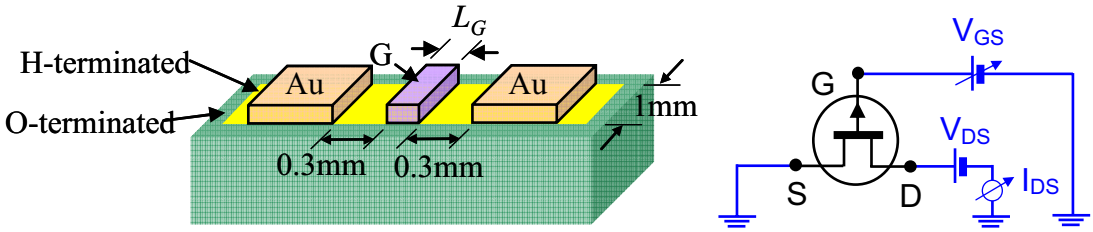

Figure 7.5 *Schematic of a diamond (p channel) MESFET and its symbol in electric circuit. The surface conductive channel is refined to be the hydrogen terminated area (H-terminated). Ohmic contacts (drain and source) are formed by Au, and the Schottky contact ("G" in the figure) is constructed by Cr or Al. Different gate length from* $9\mu m$ *to* $1000\mu m$ *is used in the experiment (see the text).*

The output characteristic of Al gate MESFETs, with various gate length from $L_G = 9\mu m$ (a) to $L_G = 1000\mu m$ (d) are shown in Figure 7.6. In contrast to common representation in literature we show both polarities of source drain voltage. The voltages specified are in all cases vs. the grounded source electrode.

A qualitative transition is observed with increasing gate length for Figure 7.6 a) to c) the current-voltage output follows the working principle of a MESFET. However, the situation in a)-c) to d) is rather that of a pair of half-cut back-to-back Schottky diodes that are simply operated with different voltages vs. the gas as a common contact and of which only one is included in the current measurement (see Figure 7.7). Even for Figure 7.6a) to Figure 7.6c) the classical MESFET model fails. As L_G increases from $9\mu m$, $16\mu m$ to $40\mu m$, I_{DS} decreases from $\sim 10^{-4} A$, $\sim 10^{-5} A$, $\sim 10^{-6} A$, i.e. by two orders of magnitude.

Recall equation (6.17):

$$I_{DS} = \frac{e^2 N_a^{\,2} a^3 W \mu_p}{6 L_G \varepsilon_s} \left[\frac{3V_{DS}}{V_{bi} - V_T} - \frac{2\left(V_{DS} + V_{bi} - V_{GS}\right)^{3/2} - 2\left(V_{bi} - V_{GS}\right)^{3/2}}{\left(V_{bi} - V_T\right)^{3/2}} \right] \qquad (6.17)$$

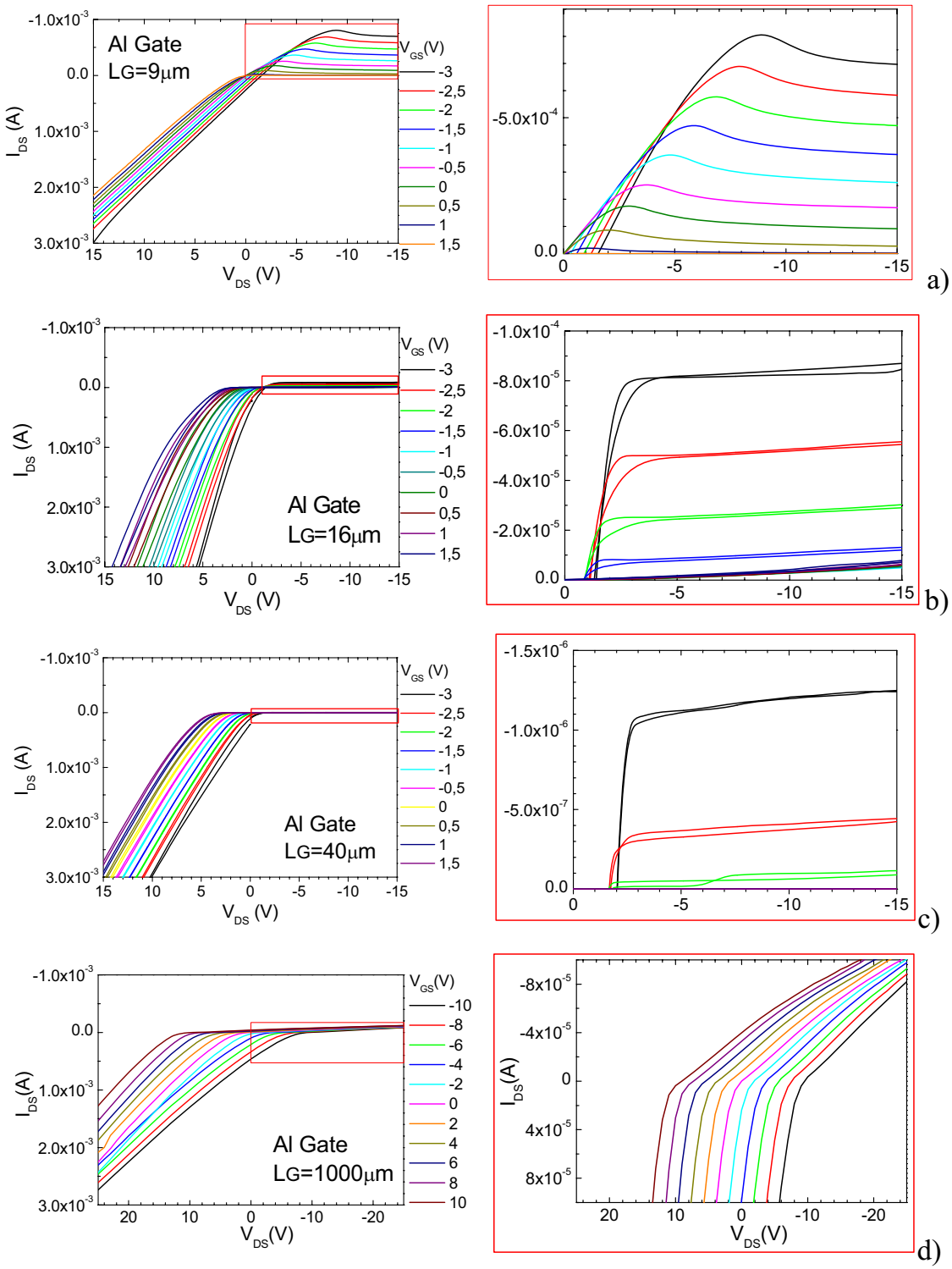

Figure 7.6 *Output characteristic of Al gate MESFET with various gate length: a)* $L_G = 9\,\mu m$, *b)* $L_G = 16\,\mu m$, *c)* $L_G = 40\,\mu m$, *d)* $L_G = 1000\,\mu m$. *The drain-source distance of a), b) and c) is 0.6mm, and of d) is 2mm. The width of the conductive channel is 1mm. right column is the corresponding enlargement of the red region in left column. Similar data are measured for chromium gate MESFETs.*

which predicting a current characteristics varying proportional to the inverse gate length, i.e. change by only a factor 4.4. As the other parameters remain constant (explanation of parameters is in section 6.3), I_{DS} is controlled by gate length L_G and the threshold voltage V_T.

For gate length L_G variation from tens of micrometer to thousand micrometer, we may qualitatively explain the phenomena observed according to the sketch in Figure 7.7 which is a cross-section view of the "MESFET" structure in Figure 7.5. Suppose a group of holes feel the electric field and travel from drain to source (in the figure, only one hole is plotted for simple representation). In case of a short gate (Figure 7.7a), holes may in fact be transferred through the conductive channel that is modulated by the Schottky gate. However, when the gate length is getting proceedingly large (Figure 7.7b), competing currents to the gate take over and the transfer current finally vanishes. The device is no longer a MESFET but instead a pair of back-to-back Schottky diodes that is being half-cut in between[16]! Since in the experiments, the current meter is placed between drain and gate. The recorded "drain-source current" I_{DS} is actually the current for the Schottky "half" diode between gate and source driven by a forward voltage of $V_{DS} - V_{GD}$ (see Figure 7.7b). This is exactly what we observed in Figure 7.6d).

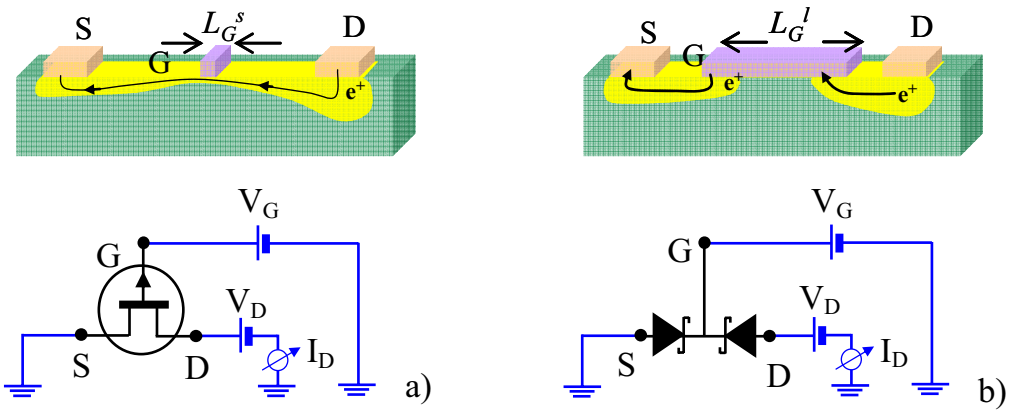

Figure 7.7 *Cross-section of the "MESFET" structure (up) and its corresponding equivalent circuit (down): a) with small gate length L_G^s, b) with large gate length L_G^l. Description is in the text.*

To sum up the discussion above, the aluminum/chromium gate MESFET experiments

[16] Note that, in traditional back-to-back Schottky diodes (called a BARITT diode), there is no "gate" in between. For a detailled discussion of current voltage characteristic of BARITT diode, readers may refer to *Physics of Semiconductor Devices (3 edition)*, by Simon M. Sze and Kwok K. Ng, Wiley-Interscience (2006).

show that the output characteristic of these devices is essntially controlled by gate length. As gate length increases further more into the thens of micrometer range, the gate itself becomes a huge sink or source of charges, and prohibits any charge transfer between drain and source. The recorded drain-source current I_{DS}, in the latter situation, is actually the current of the Schottky diode between gate and drain. This behavior that a MESFET converts to a Schottky diode device as a result of gate length enlargement, is a distinguishable feature of junction type FETs (MESFETs and JFETs) as compared to MOSFETs. In case of MOSFETs, however, the oxide works as insulator that prohibits any charges being collected by the gate and hence a situation like in Figure 7.7b) could not take place[17]. The scaling of the output characteristic with gate length thus clearly directly proofs that the hydrogen terminated diamond MESFET is a transistor in which metal and semiconductor are in direct contact (a real MESFET). It is not an effective MOSFET, i.e. an FET in which a "separation layer" is inserted between metal and the conductive channel, as described as usually suggested in literature [8-10]. The immeasurable leaking current for sub-micron gate length is simply achieved by a suppression of the gate-source leaking current (Figure 7.8b) due to the geometric reduction of the gate contact and a take over by the transfer current between source and drain (Figure 7.8a).

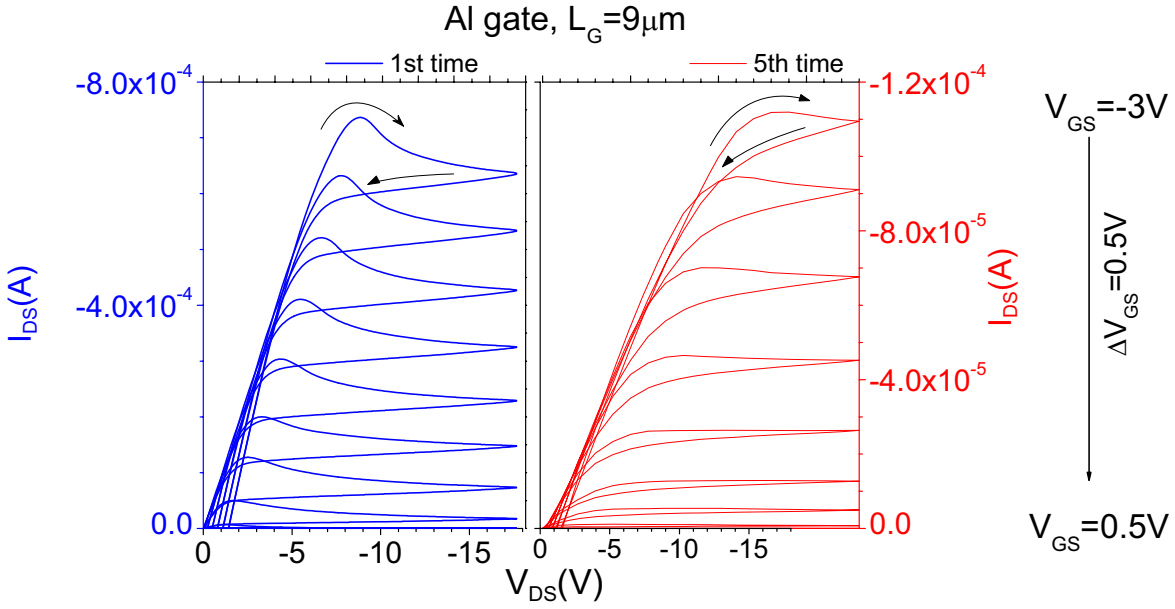

Figure 7.8 *Output characteristic of Al gate MESFET, with gate length of ~9µm, and the drain-source distance of 0.6mm. The width of the hydrogen terminated conductive channel is around 1mm. Left hand side: first run measurements; right hand side: the fifth run transients swing over and hysteresis of the characteristics are due to capacitive effects and are slightly reduced with time.* V_{DS} *was varied with a scan rate of ~3V/s in this experiment .*

[17] We assume here that the oxide is an ideal insulator and tunneling of charges is negligible.

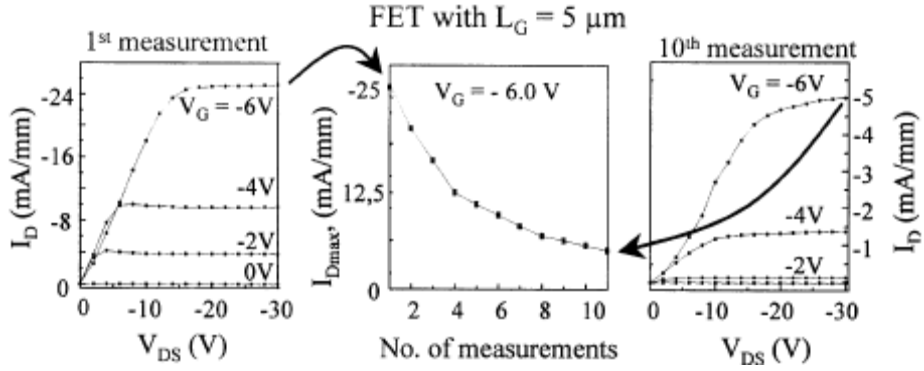

Figure 7.9 *Current degradation of an aluminum gate MESFET during successive measurements by Denisenko et al. [10].*

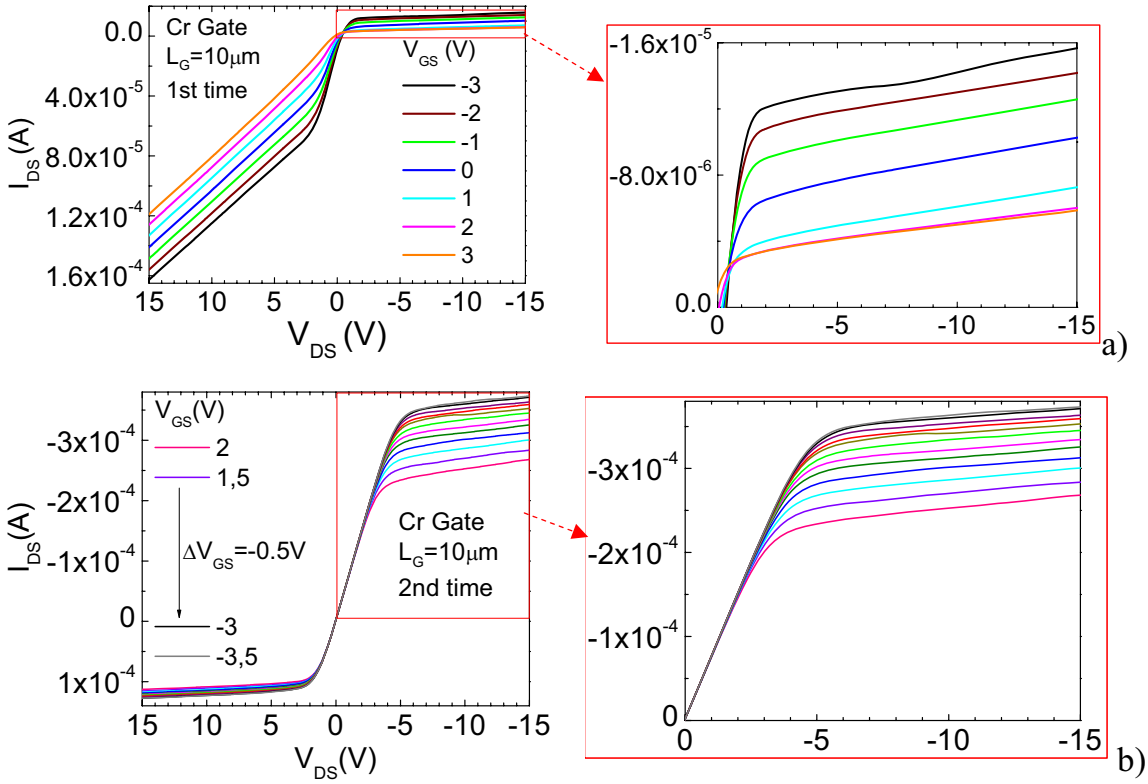

Figure 7.10 *Output characteristic of Cr gate MESFET, a) for measurement in the first time and b) for the second time. The gate length is* $\sim 10\mu m$*, and the drain-source distance is 0.6mm. The width of the hydrogen terminated conductive channel is around 1mm.*

Finally, we present data on the stability of diamond MESFETs. For aluminum gate MESFETs, the drain-source current I_{DS} decreases with repeating V_{DS} cycles. A comparison of output characteristic for the first and the fifth run is shown in Figure 7.8. A.Denisenko et al. [10] report similar phenomena on aluminum gate MESFETs (Figure 7.9). The origin of this current degradation is yet unclear. Possible explanations are thermally induced oxidation between the gate and the diamond, or the hydrogen terminated channel itself may be partially oxidized resulting in lower conductance. Hence, To improve

the performance of the device further, sealing and packing of the whole MESFET chip is necessary.

Even more dramatic instability phenomena are found for Cr gate MESFETs that is operated in air. However, the drain-source current, instead of degrading like in the case of the Al gate, increases more than twenty-fold on the negative drain-source voltage side (Figure 7.10) between the first and the second run. The Cr gate that is evaporated onto hydrogen terminated diamond (Figure 7.3) is partially peeled off. At this point, we may only speculate that Ohmic heating of the weak regions of the contact area may cause proceeding changes of the device characteristics.

7.4 Diamond Based MESFETs: Simulations

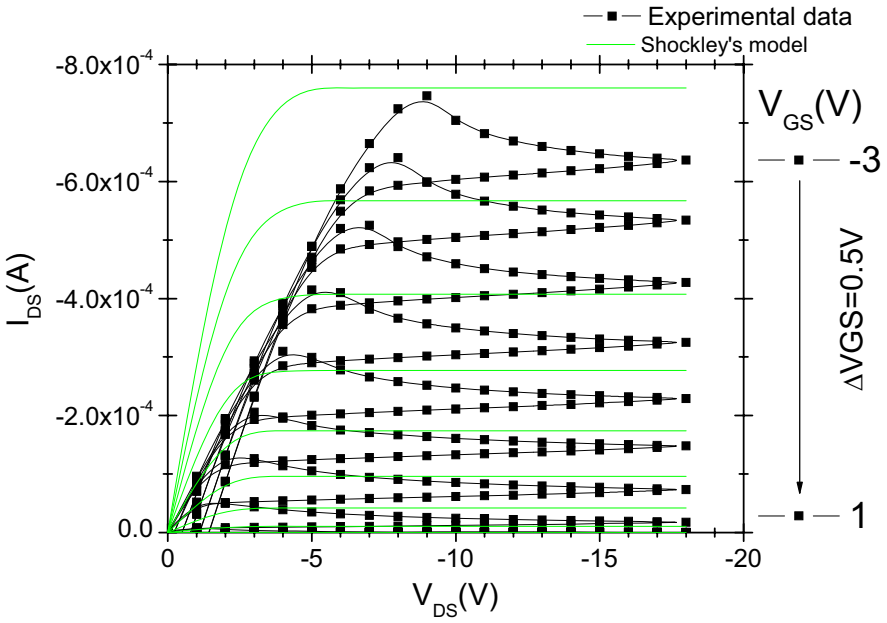

Figure 7.11 *Simulation of Figure 7.6a), using Shockley's analytical model that is expressed as equation (6.17). Parameters for simulation are:* $L_G = 9\mu m$, $W = 1mm$, $N_a = 3\times10^{16} cm^{-3}$, $a = 0.35\mu m$, $\mu = 50 cm^2/Vs$, $V_T = 1V$, $\varepsilon_s = 5.133\times10^{-13} F/cm$.

Analytical models for FETs as discussed in section 6.2-6.4, were first presented by W.Shockley in 1952 and are based on the long-channel approximation (also called gradual channel approximation) [141, 160]. The basis of this is that the potential profile fulfils the relation $|\partial V/\partial y| \ll |\partial V/\partial x|$ and the channel is not large enough to cause velocity saturation. In this regime, the carrier velocity is under constant mobility. The drain-source current of the classical MESFET can be expressed as (derivative of this equation is in section 6.3):

$$I_D = I_T\left[\frac{3V_{DS}}{V_{bi}-V_T} - \frac{2\left(V_{DS}+V_{bi}-V_{GS}\right)^{3/2} - 2\left(V_{bi}-V_{GS}\right)^{3/2}}{\left(V_{bi}-V_T\right)^{3/2}}\right]$$
$$with \quad I_T = \frac{e^2 N_a{}^2 a^3 W \mu_p}{6L\varepsilon_s} \tag{6.17}$$

We may use this formula to show the difference between a classical MESFET and the diamond-H MESFET. Even with optimized parameter device, the model fails to fit the experiment!

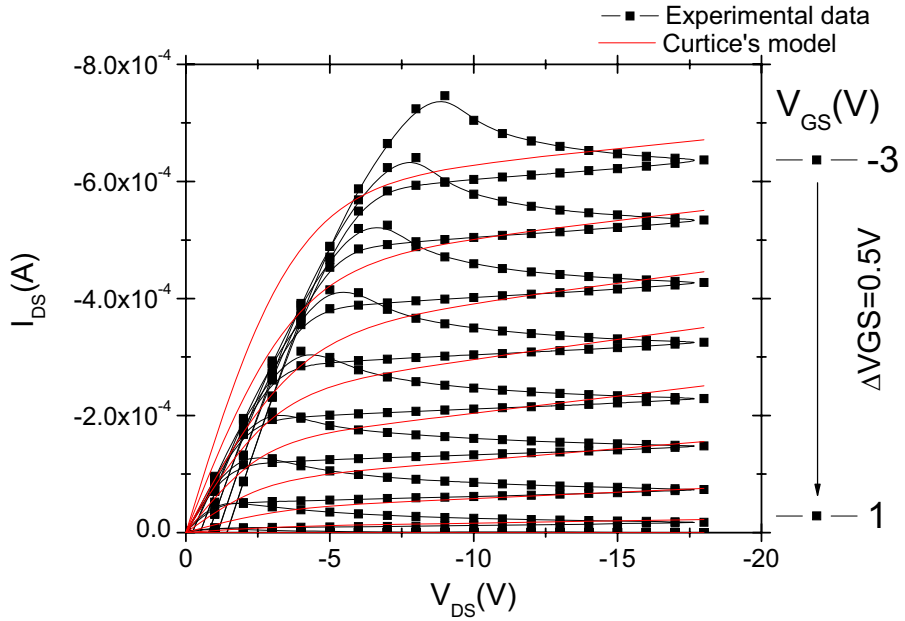

Figure 7.12 *Simulation of Figure 7.6a), using Curtice Model. The parameter for simulation are:* $\lambda = 0.008 \sim 0.08$, $\alpha = 0.2 \sim 0.5$, $a = 0.35\mu m$, $\mu = 50 cm^2/Vs$, $V_T = 1V$, $L_G = 9\mu m$, $W = 1mm$, $N_a = 3\times10^{16} cm^{-3}$, *and* $\varepsilon_s = 5.133\times10^{-13} F/cm$.

As a consequence, the charge carrier and potential profiles can be evaluated by solving Poisson's equation and the charge carrier statistics for each channel position *y* as a on-dimensional problem (for fixed *y*), taking a local channel potential *V(y)* as boundary value. With this, we may alternatively use the empirical Curtice model that is adopted by the SPICE software [145]. This model uses a single equation given by:

$$I_{DS} = \beta\left(V_{GS}-V_T\right)^2\left(1+\lambda V_{DS}\right)\tanh\left(\alpha V_{DS}\right) \quad \text{for} \quad \left(V_{GS} \geq V_T\right)$$
$$\text{with} \quad \beta = \frac{\mu\varepsilon_s}{2a}\cdot\frac{W}{L} \tag{7. 1}$$

β is the so-called device transconductance parameter, L is the channel length, λ and α are the channel modulation parameters, scaling with the drain-source voltage. These two parameters and the threshold voltage V_T are usually determined empirically. The

meanings of the other parameters are the same as Shockley's model (see section 6.3).

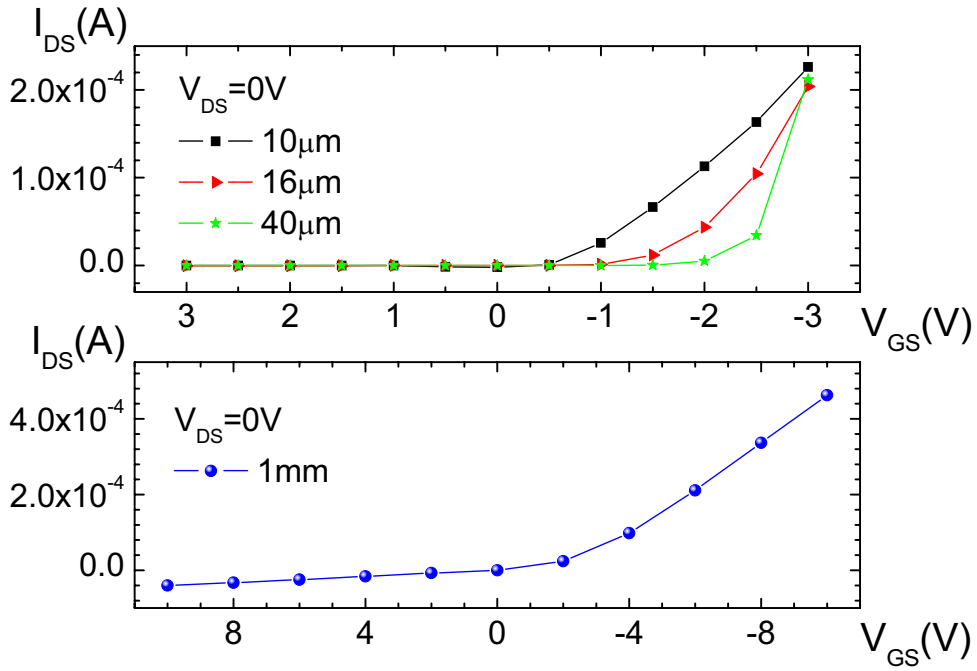

Figure 7.13 *Drain-source current as a function of gate-source voltage, at drain-source voltage equal to zero.*

The comparison of the simulations and the experiment is far from being satisfactory. In fact, this does not come as a surprise since in all cases the modeling relies on the long channel approximation and neglectable gate currents as a transistor. The diamond-H device, however, only works for short channels as demonstrated above, with the edges of the gate contact playing the decisive role. This is clearly demonstrated as well by the scaling of the gate current with gate length. $I_{DS}\left(V_{GS}, V_{DS}=0\right)$ corresponding to a symmetric arrangement of source and drain, obviously contributes the I-V characteristics of the drain gate Schottky "half" diode which is identical by symmetry to the other "half" diode (source-gate, see Figure 7.7b). This IV-characteristic is shown for different gate lengths in Figure 7.13. For a classical MESFET device it should vary propotional to the gate length, i.e. an increase by a factors of 100 is expected when going from $L=10\mu m$ to $L=1mm$. In fact experiment shows no increase at all but on the contrary, a slight decrease by a factor of 2 (at $V_{GS}=-3V$). The current being essentially independent of gate length clearly proofs that the device operates via the two edge regions of the gate contact towards source and towards drain. Modeling such a device requires solving two-dimensional Poisson's equation and the transport equations fully, i.e. simultaneously for the depth coordinate x and the channel coordinately y.

Chapter 8 Solution Gated Field Effect Transistors (SGFETs) on Diamond and Graphene

8.1 Introduction

In 1970 Bergveld introduced the so-call ion sensitive field effect transistor (ISFET). It is based on the concept of a solution gate field effect transistor (SGFET) [52], which refers to a device that is similar to a silicon MOSFET, except that the metal gate ("M") is replaced by an electrolyte and a reference electrode, and the oxide ("O") is modified to achieve certain ion sensing properties. A general introduction to the mechanism of SGFETs is given in section 6.4. In contrast to classical MOSFETs, the "oxide" in SGFETs is not always necessary. For instance, the insulation can be done by the Hemholz layer at the semiconductor/electrolyte interface. For perfect performance, the interface should allow Faradaic current flow across, i.e. should be polarizable (see section 5.1). The hydrophobic surfaces of hydrogen terminated diamond (diamond-H) and graphene, when in contact with aquatic electrolyte, form in deed polarizable interfaces with most electrolytes and thus can be adopted without any further gate insulation processes for SGFET's.

The first application of diamond-H as sensing element in the "oxide free" SGFETs was demonstrated by Kawarada et al. [44]. Due to the exceptional chemical properties of diamond, like the wide electrochemical potential window (3.0~3.5eV, more than 1eV wider than for graphite or platinum electrodes) [162], high chemical inertness and excellent biocompability [163, 164], diamond-H based chemical sensors as well as biosensors have been realized by a number of research groups in the years that followed [45-47].

A SGFET on the basis of graphene as sensing element was first constructed by Das et al. [165] in 2008. Later, the performance of such a device was studied by Ang et al. [166] and Ohno et al. [167]. Due to the fact that the electrical characteristics of graphene is sensitive to surface conditions, also gas sensors using graphene field effect transistors (FET) have been realized.

The electrical characteristics of diamond-H and graphene SGFETs have been

measured by several researchers yet the mechanism behind these graphene chemical sensors is not well understood. Different models all based on the concept of a perfect polarizable electrode, lack of agreement about this mechanism [44, 168-171], which is one of the motivations for us: we analyze and model the devices, by taking into account the specific semiconductive and surface properties of diamond-H and graphene. In addition, we will evaluate the performance of both devices via measuring the output and transfer characteristics for different pH of the electrolyte. For graphene, the influence of substrate space charges and especially the interface states between graphene and the SiC substrate have been taken into account. These defects are shown to have a decisive influence on the transfer characteristics for epitaxial graphene on SiC and can therefore not be neglected.

Last but not least, diamond-H SGFETs are often linked to the charge transfer doping mechanism in literature [99], which is, however, a misconception. A perfectly polarizable or nonpolarizable electrode does not exist. In reality, depending on the overpotential, always a faradayic current is allowed and any electrodes can behave more or less polarizable [86]. The same is true for diamond-H and graphene electrodes! Both electrodes can be understood as polarizable when discussing their role in the SGFET concept, but must be treated as unpolarizable in order to understand the charge transfer doping (see chapter 5). We will readdress this issue and examine the polarizability of those electrodes in this chapter.

8.2 Experimental Setup

8.2.1 Patterning of a Conductive Channel

For the diamond-H SGFET, a natural intrinsic type IIa single crystal diamond that is hydrogen terminated on its (100) surfaces of 5 mm by 8 mm size is used. The hydrogenation termination process followed the recipe of sections 3.1. The samples used for the graphene SGFETs are graphene sheets produced on the silicon-terminated (0001) face of a semi-insulating, hexagonal 6H-SiC single crystal by high-temperature annealing in an inert gas atmosphere [89]. The average thickness of the graphene layer was 1.05 ± 0.1 monolayer as determined from the x-ray excited photoelectron spectrum of the C1s core level by a procedure described elsewhere [71] with the inelastic mean free path adjusted such that consistency was reached with data obtained from low-energy electron microscopy [89]. Later, both diamond-H and graphene samples are patented into U-shaped conductive channels, which is defined by masking the channel area with a positive

photolithographic resist and removing the remainder of the graphene in an oxygen plasma. For diamond-H, the semiconductive channel is of about 16 mm in length (source-drain distance) and 2 mm in width. For graphene, the conductive channel is of dimension $14\,mm \times 1.4\,mm$. Finally, both channels are contacted at their ends respectively by silver paste and gold wire, which yields perfectly Ohmic contacts that serve as source and drain (see Figure 8.1).

8.2.2 The Electrolyte

The background electrolyte consists of 10mM phosphate buffer (pH7) and 10mM KCl, following recipe 3.4. For buffer of different pH, H_3PO_4 and KOH are used for the titrating. All the chemical products are purchased from Carl-Roth (Germany) without further purification.

8.2.3 Electrochemical Electrodes

Gate Electrode: The gate electrode is provided by an electrochemical Ag/AgCl reference electrode (3M KCl solution, Schott B2220) that was placed at a distance of 10 mm in front of the sample [18]. The red-ox potential of that electrode is +0.20 V vs. standard hydrogen electrode (SHE) at room temperature.

Working electrode: Working electrodes are the U-shaped conductive channels of diamond-H or graphene as we described previously. Care is taken that only the conductive channel of the electrode but not the metal contacts are in contact with the electrolyte. This is achieved without any epoxy or sealant simply by dipping only the bottom of the "U" shape conductive channel into the electrolyte and keeping the metal contacts out in air. For diamond-H (Figure 8.1a), about 11 mm of the channel length are dipped into liquid and thus controlled over the whole cross section by the electrolytic gate, which, as a consequence, yields the full pinch off of the channel in the output characteristics of the FET. For graphene (Figure 8.1b), by dipping the bottom part of the sample into solution the graphene channel is controlled over an effective length of 7.5 mm by the electrolytic gate.

[18] Potential drop between gate electrode and working electrode can be neglect, due to the relative short distance in between and the high conductivity of the solution.

8.2.4 Electrical Circuitry

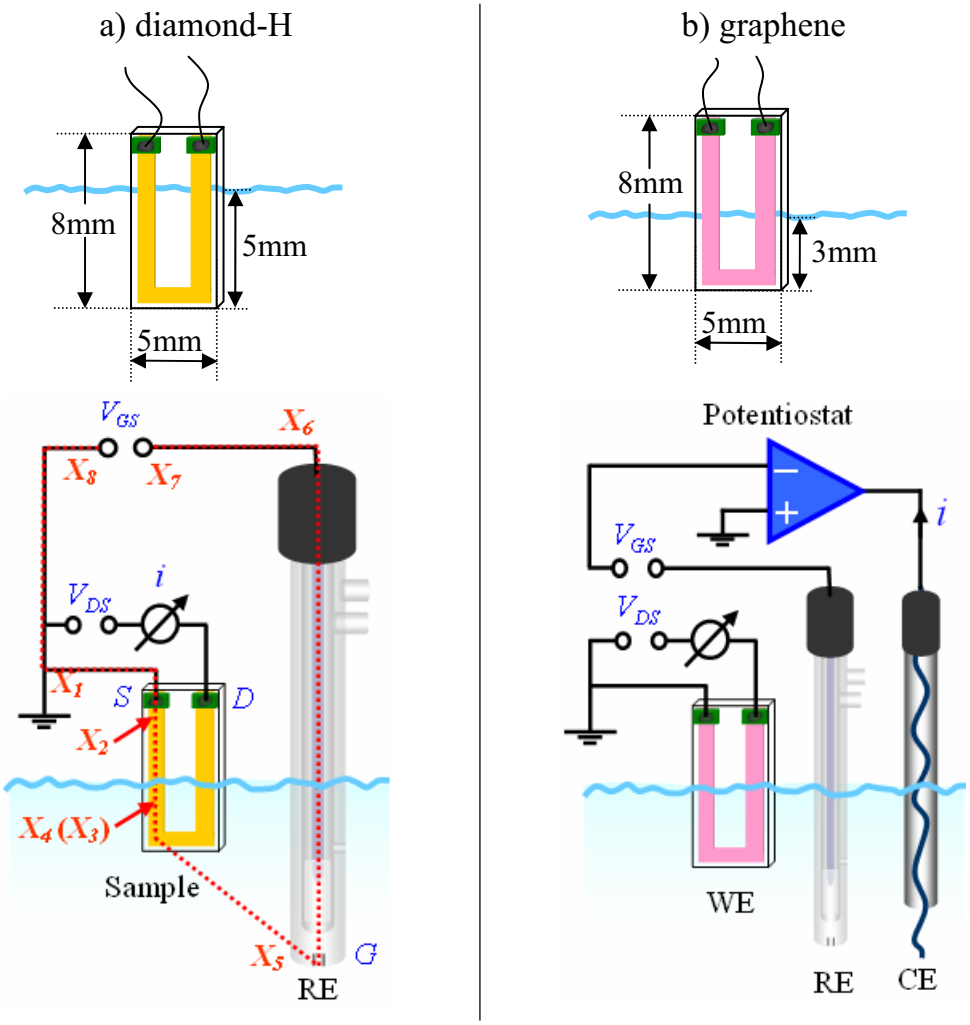

Figure 8.1 *Schematics of the Solution Gate FET based on a U-shaped surface conductive channel of a) diamond-H and b) graphene. In the graphene case the faradaic current load of the reference electrode (RE) was suppressed by the use of a counter electrode (CE) and a potentialstat. For the diamond based device this purely technical provision was not necessary. "WE", "RE" and "CE" represents for "working electrode", "reference electrode" and "counter electrode". "S", "D" and "G" stand for "source", "drain" and "gate" contacts. X_4 and X_3 are one spot laterally but different in depth: X_4 is at the surface graphene layer while X_3 is deep in the substrate.*

Both diamond and graphene electrodes were grounded at the source contact and drain-source voltage is applied via a programmable voltage source. For the measurement of the graphene SGFETs, a UNISCAN Model PG580 potentiostat operated in three-electrode configuration is used to apply the gate-source voltage [19]. For the

[19] The source contact serves as a working electrode. A platinum wire serves as a counter electrode and the gate itself (Ag/AgCl) as the reference electrode.

measurement of the diamond-H SGFETs, as the current between the diamond working electrode and the gate electrode is lower than 3nA throughout the whole experiment [20], it is unnecessary to use a three-electrode configuration. Instead by a DC voltage source is used for the gate-source voltage as well. In both cases, the source-drain current was measured with a Keithley 617 electrometer. The faradayic gate current due to the red-ox activity of the electrodes was dealt with in detail in chapter 5. For the SGFET characteristics, it is irrelevant and needs not to be considered in this chapter. The setup to measure the SGFET characteristics is shown in Figure 8.1.

8.3 Performance of SGFETs Based on Hydrogen Terminated Diamond and Graphene

8.3.1 The pH Response of the Diamond-H SGFET

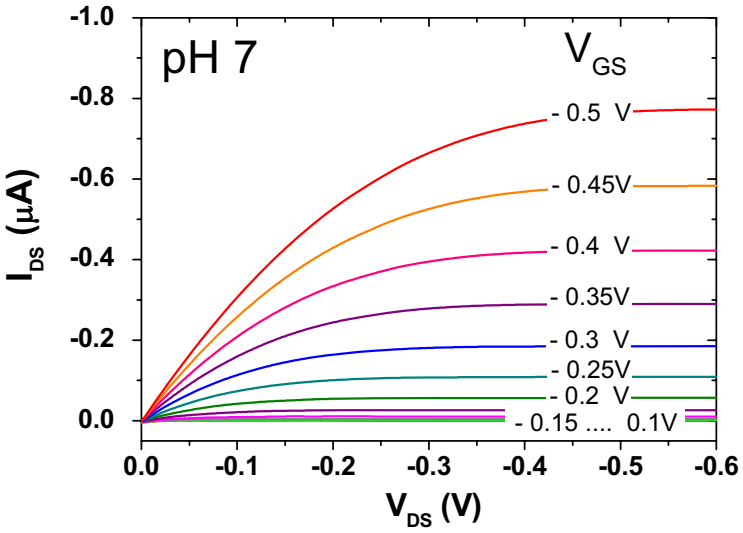

Figure 8.2 *Field effect output characteristics of the surface conductive diamond SGFET at a pH of 7.*

The pH response of the SGFET is monitored as a change in the output characteristics when the proton concentration in the electrolyte is varied. In Figure 8.2 the field effect output characteristics of the hydrogen terminated diamond SGFETs are shown for pH 7. Keeping the drain-source voltage V_{DS} at a value small compared to the pinch-off voltage, the drain-source current is proportional to the hole concentration in the FET channel. The transfer characteristics for a fixed drain-source voltage of $-0.05V$ and pH values between

[20] The gate current of the order of a few nA is due to the same red-ox reactions that are responsible for the generation of the hole accumulation layer according to the surface transfer doping model (see chapter 5).

2.4 and 7 are shown in Figure 8.3. Data points are represented by open symbols and the full lines are guides to the eye. For a constant source gate voltage, increasing pH enhances the channel conductance. For a constant source drain current, a change in pH results in a shift of the transfer characteristics on average by $19mV / pH$.

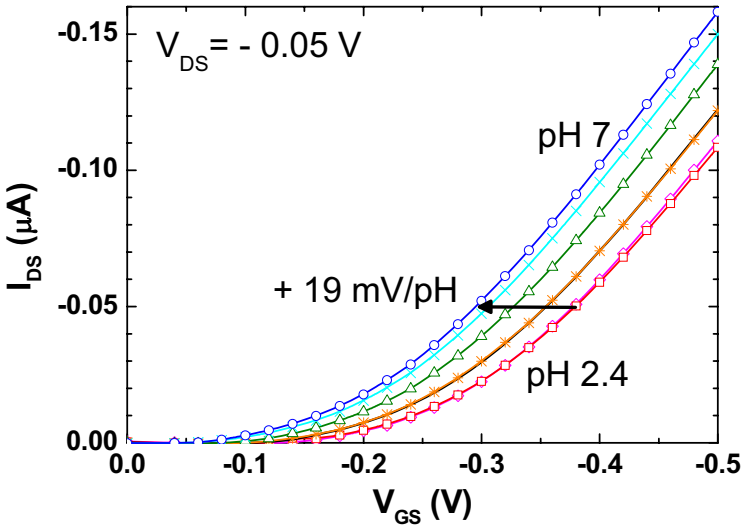

Figure 8.3 *Transfer characteristics of the SGFET for a constant source-drain voltage of -0.05V, i.e. in the linear I_{DS}-V_{DS} range. pH values are between 7 and 3 in steps of 1; the most acidic electrolyte has pH 2.4.*

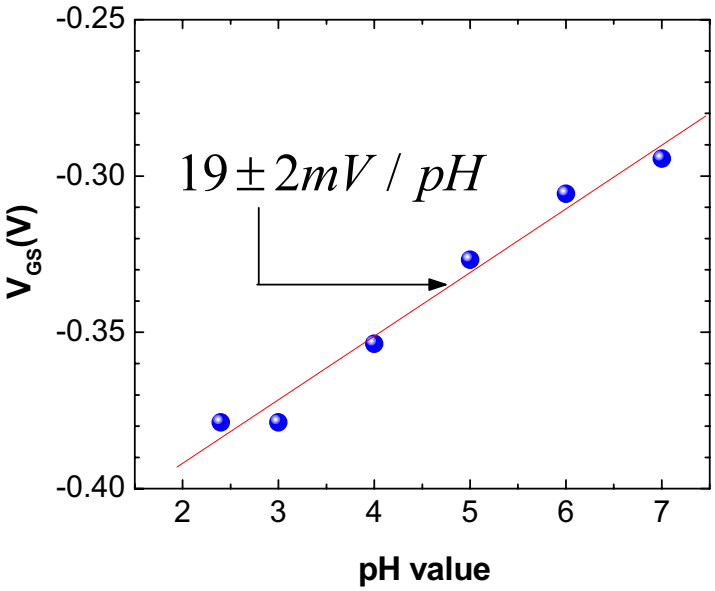

Figure 8.4 *The pH sensitivity of the SGFET in the limit of small source-drain current ($V_{DS} = -0.05V$, $I_{DS} = -0.05\mu A$) with the Ag/AgCl electrode used as gate electrode.*

For a set point of the ISFET of $I_{DS} = -0.05\mu A$ we have extracted the pH sensitivity from Figure 8.3 as shown in Figure 8.4. The straight line from a linear regression is the average pH sensitivity stated above. The value of $19 \pm 2mV / pH$ is in good agreement with the one of $15mV / pH$ recently reported by Dankerl et al. [172].

8.3.2 The pH Response of the Graphene SGFET

In Figure 8.5 the field effect output characteristics of the graphene SGFET are shown exemplary for pH 7. No saturation of current on graphene SGFET is observed up to drain-source voltage V_{ds} equal to 0.5V. To avoid hydrogenation or oxidation of the graphene electrode at high overpotential, we thereby limit the amplitude of V_{ds} to be smaller than 0.1V. For each gate-source voltage, which was varied between -1.1 V and +0.2 V in steps of 0.1 V, we measure perfectly linear I-V characteristics up to the maximum drain-source voltage of $|V_{ds}| = 0.1$ V. For a gate-source voltage of -0.5 V a minimum in the channel conductance is observed, consistent with ambipolar transport of electrons and holes in the graphene channel.

Fixing the drain-source voltage at V_{DS} = -50 mV, we have measured the transfer characteristics of the graphene SGFET, i.e. the drain-source current I_{DS} as a function of gate-source voltage V_{GS}, for different pH of the electrolyte as it is shown in Figure 8.6.

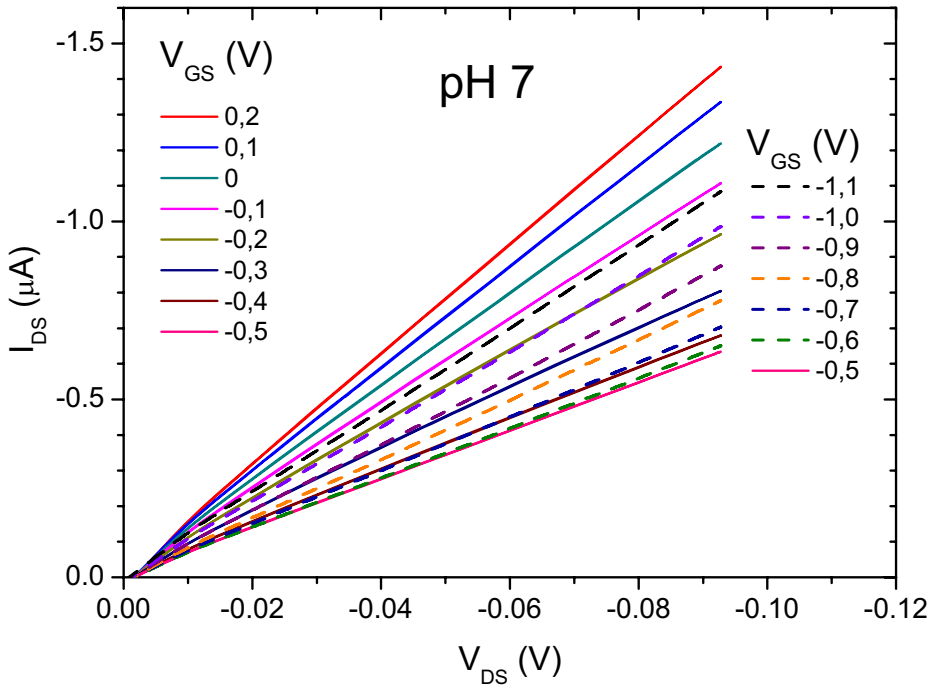

Figure 8.5 *Field effect output characteristics of the graphene based SGFET at a pH of 7.*

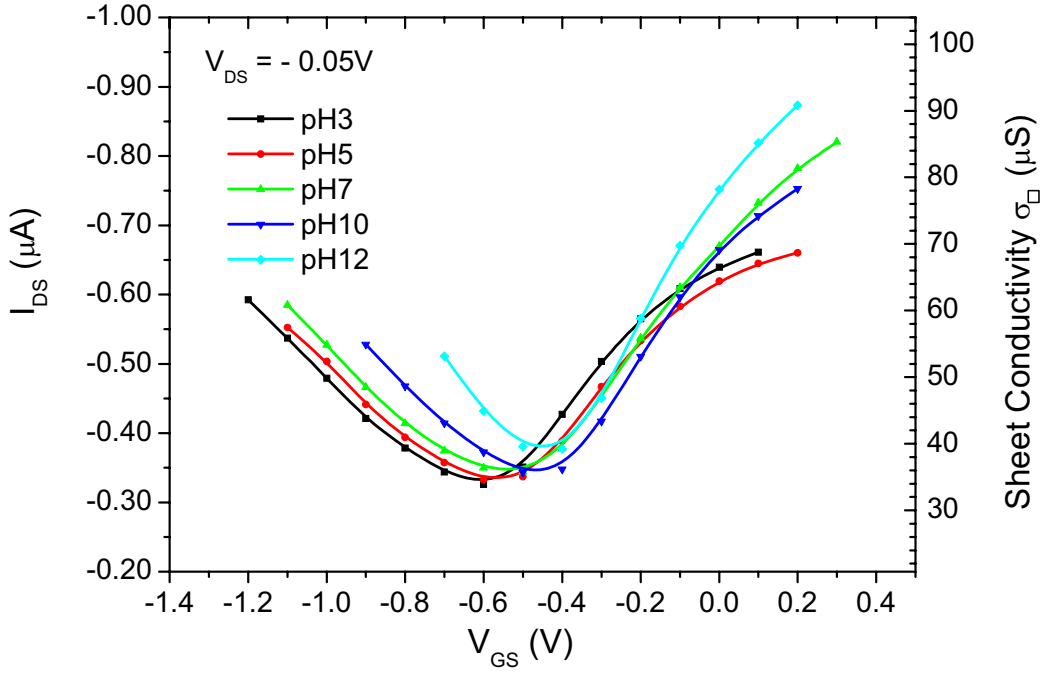

Figure 8.6 *Transfer characteristics of the graphene based SGFET for a constant drain-source voltage of* $-0.05\,V$ *for different pH of the electrolyte.*

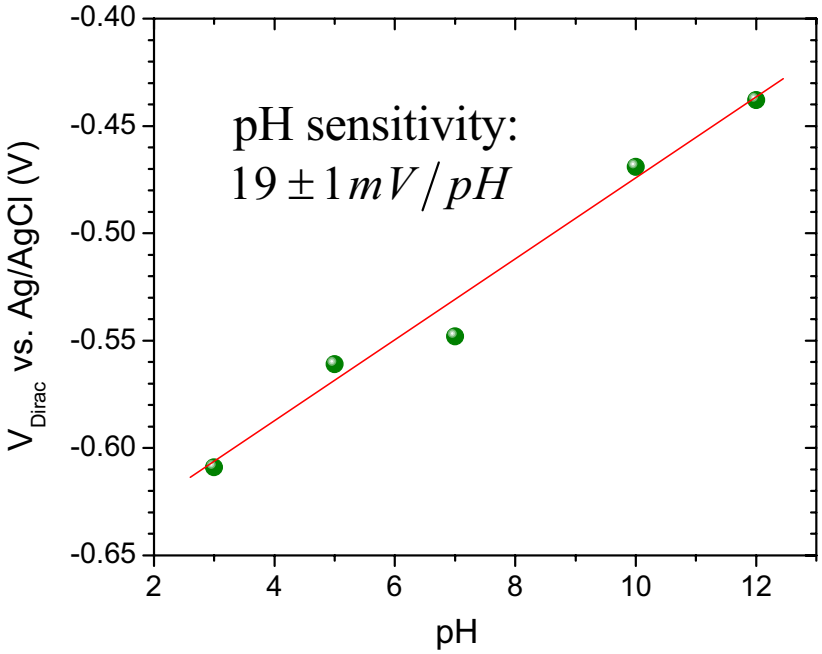

Figure 8.7 *The pH sensitivity of the SGFET in the limit of small drain-source voltage* ($V_{DS} = -0.05\,V$) *displayed as the Dirac voltage vs. pH.*

Except for extreme alkaline conditions (pH 12), we find a universal minimum conductance of $6.8\,\mu S$ with a scatter of 3%. Taking the aspect ratio of 5.2 (length over width) of the graphene channel into account this value corresponds to a minimum sheet conductivity of $(35 \pm 1)\,\mu S$ which will be further discussed below. The transfer characteristics of Figure 8.6 is systematically shifted with increasing pH to increasing

gate-source voltages. On the anodic side (increasingly negative V_{GS}) this shift is almost ideally rigid, again with the exception of the most alkaline electrolyte, whereas on the cathodic side the I-V curves indicate a saturation that tends to be more pronounced for acidic electrolytes. We extract the pH sensitivity of the graphene SGFET and plot it in Figure 8.7 as the voltage V_{Dirac} that belongs to minimum channel conductivity vs. pH. We find a sensitivity factor of $19 \pm 1\, mV / pH$ that is within the experimental uncertainty identical to the pH sensitivity that was found for SGFET's based on hydrogen-terminated and surface conductive diamond! More systematic studies on graphene are mandatory to identify the mechanism behind the pH sensitivity of the surface potential in the present case. At this point we may just note the striking similarity between the two carbon surfaces, despite their different electronic and structural properties.

8.4 The Potential Diagram of the SGFET Circuit

8.4.1 General Discussion

The potential diagram w(x) of the full gate-source circuit is sketched in Figure 8.8 along a path x defined in Figure 8.1c). The upper diagram (a) refers to the diamond electrode; the lower one (b) to the more complicated device on epitaxial graphene on SiC. It consists of (A, x_1 to x_4) the semiconductor (SC) electrode from source contact to the free surface exposed to the electrolyte; (B) the compact layer consisting of the inner Helmholtz plane (IHP) and the outer Helmholtz plane (OHP); (C, OHP to x_5) the diffuse layer in the electrolyte as well as the field free bulk electrolyte; (D, x_5 to x_6) the gate electrode (Ag/AgCl) including its double layer towards the electrolyte and (E, x_7 to x_8) the gate voltage source. Figure 8.8 is drawn like an electron band diagram and hence the potential w(x) drawn as a bold line refers to the electrostatic energy of a negative unit charge and has a sign opposite to that conventionally adopted in electrochemistry. In section A we choose the valence band maximum E_V to show the potential profile in the diamond-H and the Dirac energy to show it for the graphene electrode. In the solid-state parts where the electrical current is carried by electrons (or holes), the Fermi level is indicated by a dashed line. The potential drop between the semiconductor/metal interface and the source contact (X_1 to X_2) is linked to the constant galvanic potential between the source contact metal with work function ϕ_{Me} and the semiconductor. The connection between potential and Fermi level is fixed at x_4. The gate voltage source results in the same discontinuity in both the electrostatic potential and the Fermi-level between x_7 and x_8.

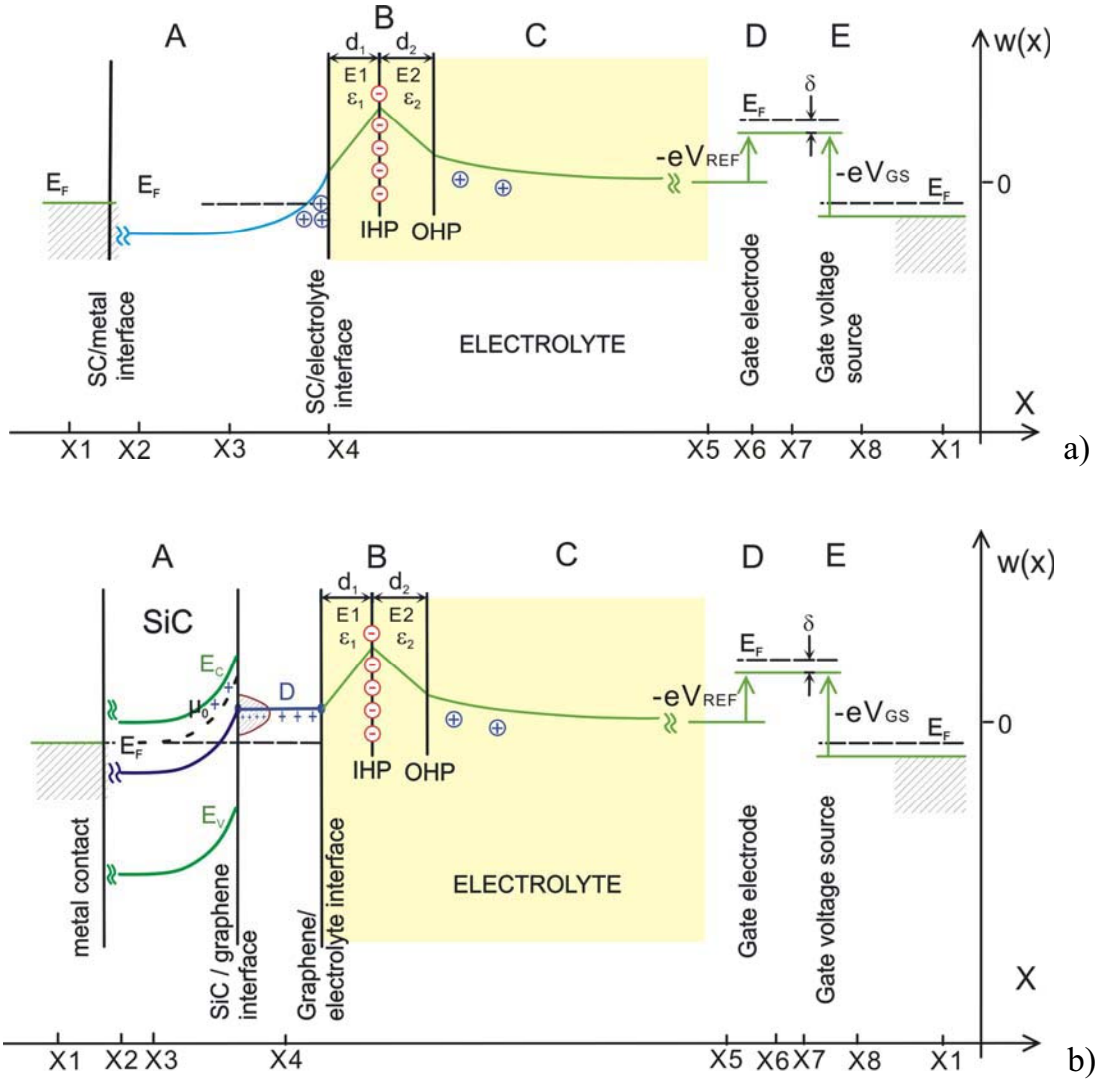

Figure 8.8 *The potential diagram w(x) of the complete electrical source-gate circuit of the diamond (a) and graphene (b) SGFETs along the path depicted in Figure 8.1. Scale in the diagram is not refers to real dimension. Ionic charges are indicated as circles, electrons and holes just as – and + signs, respectively. Since slightly doping of the SiC substrate does not affect the performance of the graphene layer, for simplicity and to be consistent with the potential diagram of diamond, we assume a n-type SiC here in the illustration. For further details see text.*

The reference electrode creates a Galvani potential drop G_{REF} due to the equilibration of its characteristic red-ox couple with the electron reservoir of the solid. For simplicity we assume for the schematic of Figure 8.8 that the metallic parts of the whole circuit are formed by only one material (i.e. silver). Different metals used in practice induce only contact potentials that cancel and need therefore not to be considered explicitly. The sheet charge σ_{ads} at the inner Helmholtz plane, that has been exemplary assumed to be negative in the potential diagram, is made up by preferentially absorbed ions from the electrolyte. They are usually held responsible for the ion sensitivity of the SGFET [125]. For reasons

which will become obvious later, the potential is chosen to be zero asymptotically in the bulk electrolyte. Corresponding to Kirchhoffs loop rule of electrostatics the total potential drop across the circuit must be zero.

The Fermi level in the reference electrode contact is by a characteristic constant δ offset from the electrostatic potential at that contact. If we define a surface potential u_s as the potential at the semiconductor surface x_4 relative to the Fermi level of that position, i.e. $u_s = w(x_4) - E_F$, we may substitute the galvanic potential to the source contact within the total potential drop $w(x_4) - w(x_1)$ between the semiconductor surface and the gate metal. The result is:

$$w(x_4) - w(x_1) = u_s + E_i - \phi_{Me} \tag{8.1}$$

with the ionization energy E_i of the semiconductor. For the graphene/SiC system as semiconductor $E_i = E_{VAC} - E_{Dirac}$, i.e. the ionization energy is defined as the energy of the vacuum level relative to the Dirac energy for the free surface. For a more detailed explanation the reader is referred to [173].

The potential profile is composed of the solid state sections (A and E) and the liquid electrolytic sections (B, C and D). Since the electrolytic part of both diamond and graphene SGFETs are similar, we take the simpler case of the diamond SGFET to analyze the potential profile across the electrolytic sections of the circuit. As starting point, consider an areal (i.e. depth integrated) hole density p in section A of the circuit. The sheet conductivity of the SGFET channel is then proportional to p with the mobility and the elecmentrary charge as proportionality constants. We will use p as a parameter to construct the potential profile.

Potential drop through the compact layer (section B)

Assume the dielectric constant of between x_4 and the IHP and between the IHP and the OHP is ε_1 and ε_2, respectively. The electric field E_1 in the inner part of the compact layer, i.e. between x_4 and the IHP, is directly linked to the areal hole density p by Gauss law of electrostatics yielding $E_1 = ep/(\varepsilon_0\varepsilon_1)$, and it is modified by the adsorbed ion charge density σ_{ads} at the IHP to give $E_2 = (ep + \sigma_{ads})/(\varepsilon_0\varepsilon_2)$ for the outer part of the compact layer, i.e. between IHP and OHP. The dielectric constants ε_1 and ε_2 will in general deviate from that of the bulk electrolyte ($\varepsilon_{el} \approx 80$) on account of the restricted orientational freedom of the water molecules in the compact layer. The potential drop across the compact layer is given by multiplying the electrical field with the respective spacing d_1 between x_4 and the IHP and d_2 between the IHP and the OHP:

$$w_{OHP} - w(x_4) = \frac{ep}{\varepsilon_0 \varepsilon_1} d_1 + \frac{ep + \sigma_{ads}}{\varepsilon_0 \varepsilon_2} d_2 \qquad (8.2)$$

Potential drop within the diffuse layer (section C)

The overall charge neutrality condition for the complete diamond/electrolyte interface (including the hole accumulation layer) requires that depth-integrated areal ionic charge density in the diffuse layer is $\sigma_{\text{diff}} = -\text{ep} - \sigma_{\text{ads}}$. It is related to the potential drop w_{OHP} across the diffuse layer the by the Grahame equation [126]:

$$\sigma_{diff} = -ep - \sigma_{ads} = \pm\sqrt{2\varepsilon_{EL}\varepsilon_0 RT}\sqrt{\left|\sum_{i=1}^{N} n_i^0 \cdot \left(\exp\left(\frac{z_i w_{OHP}}{kT}\right) - 1\right)\right|} \qquad (8.3)$$

where the n_i^0 and the z_i are the asymptotic molar bulk concentrations and valencies, respectively, of the complete ensemble of ions in the electrolyte, and RT is the molar thermal energy [126]. The sign of σ_{diff} in equation (8.3) has to be chosen identical to that of w_{OHP}. In accordance with the approach taken by Härtl et al. [123] and others before, we assume that the sheet charge density σ_{ads} of ions affixed at the IHP depends on the electrolyte composition only (specifically on pH), but not on the potential w_{OHP}. Although the Grahame equation looks quite complicated at first glance, it is easily seen that $\left|\sigma_{diff}\left(|w_{OHP}|, n_i^0\right)\right|$ is zero for $w_{OHP} = 0$ and is monoton increasing with all arguments. It can thus be inverted to yield $w_{OHP}(p, \sigma_{ads}) = w_{OHP} - w(x_5)$, i.e. a characteristic function of p for each electrolyte characterized by the n_i^0.

Potential across the reference electrode and the gate voltage source (sections D and E)

The product of the elematrary charge and the Galvani potential of the reference electrode $-e \cdot V_{REF} = w(x_6) - w(x_5)$ is the difference between the chemical potential μ_{Ag^+} of the red-ox electrons of the silver ions of the reference electrode and of the electrons in the metal phase of the reference electrode $\mu_{Ag} = -\Phi_{Ag}$, where we have alternatively expressed the chemical potential of the electrons in the solid silver phase relative to the vacuum level by the negative of the work function Φ_{Ag} of silver. Thus, $-eV_{REF} = \mu_{Ag^+} + \Phi_{Ag}$. Potential drop in the gate voltage source is obvious: $w(x_8) - w(x_7) = e \cdot V_{GS}$, which is identical to the discontinuity of the Fermi level as well.

Potential drop though the solid part of the circuit

Kirchhoff's loop rule of electrostatics requires that all potential differences in the whole circuit add to zero. Hence, the last term that is unknown so far, the potential drop across the solid part of the circuit $w(x_1)-w(x_4)$ must be identical to $w(x_8)-w(x_4)$ giving:

$$w(x_1)-w(x_4)=\frac{ep}{\varepsilon_0\varepsilon_1}d_1+\frac{ep+\sigma_{ads}}{\varepsilon_0\varepsilon_2}d_2-w_{OHP}(p)+\mu_{Ag^+}+\Phi_{Ag}+eV_{GS} \tag{8.4}$$

For the graphene/SiC SGFET, $e\cdot p$ in equation (8.4) has to be replaced by the total areal charge density in the semiconductor section A of the circuit, including the graphene potential SiC/potential interface states and the space charge layer in the SiC. $w(x_4)-w(x_1)$ is therefore different for the diamond SGFET and the graphene SGFET. We will discuss them separately in the following.

8.4.2 Potential Drop across the Semiconductor Part in Diamond-H SGFETs

The areal hole density p defines the Fermi level at the diamond/electrolyte interface (x4) relative to the valence band maximum E_V as described in detail in reference [117]. With the surface potential u_s at the diamond/electrolyte interface, $u_s=E_V-E_F$, the areal hole density p can be written as

$$p(u_S)=\sqrt{\frac{2kT\varepsilon\varepsilon_0N_V}{e^2}}\cdot\exp\left(\frac{u_S}{2kT}\right) \tag{8.5}$$

for the non-degenerate case ($u_s<0$) and

$$p(u_S)=\sqrt{\frac{2kT\varepsilon\varepsilon_0N_V}{e^2}}\cdot\sqrt{1+\frac{u_S}{kT}+\frac{8}{15\sqrt{\pi}}\left(\frac{u_S}{kT}\right)^{5/2}} \tag{8.6}$$

for the degenerate case ($u_s>0$).

$\varepsilon=5.8$ is the dielectric constant of diamond, ε_0 the vacuum permeability, N_V the effective valence band density of states of diamond which amounts to $2.7\times10^{19}cm^{-3}$ at room temperature, e is the elementary charge, and kT is the thermal energy. Note that $p(u_s)$ is obviously a purely intrinsic and monotone relationship for the material that can thus be inverted to give $u_s(p)$. Inserting $u_s(p)$ into equation (8.1) yields:

$$w(x_4)-w(x_1)=u_s(p)-u_{me}=u_s(p)+E_i-\Phi_{me} \tag{8.7}$$

The term $(E_i-\Phi_{me})$ is independent of the ionic composition of the electrolyte and it is

also independent of the applied voltage. Finally, inserting (8.7) into (8.4) yields:

$$-eV_{GS} = \frac{ep}{\varepsilon_0 \varepsilon_1} d_1 + \frac{e(p+\sigma_{ads})}{\varepsilon_0 \varepsilon_2} d_2 - w_{OHP}(p) + \mu_{Ag^+} + \Phi_{Ag} - \Phi_{me} + E_i + u_s(p) \qquad (8.8)$$

The difference between the two metal work functions ($\Phi_{Ag} - \Phi_{me}$) is zero when Ag is used for the wiring of the circuit exclusively (assumed for the schematic of Figure 8.8, or compensates with further contact potentials otherwise). The chemical potential of the red-ox electrons associated with the silver ions of the reference electrode is $\mu_{Ag^+} = -4.44eV - 0.2eV = -4.64eV$ where we have used the energy of the standard hydrogen electrode (SHE) on the vacuum energy scale (-4.44 eV) and the red-ox potential of the reference electrode vs. SHE (+0.20 eV). Thus, we finally have

$$-eV_{GS} = (4.64\,eV - E_i) - u_s(p) - \frac{ep}{\varepsilon_0 \varepsilon_1} d_1 - \frac{ep+\sigma_{ads}}{\varepsilon_0 \varepsilon_2} d_2 + w_{OHP}(p, \sigma_{ads}) \qquad (8.9)$$

8.4.3 Potential Drop across the Semiconductor Part in Graphene SGFETs

The contact potential $w(x_1) - w(x_4)$ between the metal contact and the graphene/electrolyte interface is not shown explicitly in Figure 8.8b) but can be expressed by the surface potential $u_s = w(x_4) - w(x_1) + \phi_{Me} - E_i$. The choice of semi-insulating SiC with the upward band bending corresponds to the situation in our experiment but has no influence on our data analysis. Also the voltage drop across graphene (x_4) can be neglected compared to the voltage drops across the Helmholtz layer and the space charge region in SiC. Consequently, we have assigned a constant potential across the graphene layer as indicated by the horizontal lines.

We will use the abbreviation ϕ for the surface potential u_s of the graphene in the following, i.e. for the energy of the Dirac point (D) relative to the Fermi level (E_F) at position x_4. We further define $x = \Phi / (kT)$ as the surface potential in units of the thermal energy kT. The Dirac energy D is experimentally found to be 0.7 eV below the conduction band minimum E_C of SiC [174, 175] which fixes the band edges E_C and E_V of the substrate in Figure 8.8b). The potential across the SiC space charge layer plus the graphene layer (x_3 to x_4) corresponds to the integrated areal charge density $\Sigma(\Phi)$ that is composed of three contributions: $\Sigma(\Phi) = \Sigma_{def} + \Sigma_{SiC} + \Sigma_g$ (compare Figure 8.8b). The first term takes defect states due to the reconstructed interface layer between graphene and the SiC substrate into

account. This interface layer is the (6√3×6√3)R30° reconstruction of the SiC(0001) surface which has been shown to create a surface state band with little dispersion and considerable density of states [176]. If we specify the two-dimensional density of states of that band as $D_{def}(E)$ with E taken relative to the Dirac energy of the graphene layer, the areal space charge accommodated in the interface defects can be written as

$$\Sigma_{def}(\Phi) = -e \cdot \int_{-\infty}^{\infty} \frac{D_{def}(E)}{1+\exp\left(\frac{E+\Phi}{kT}\right)}\, dE + e \cdot N_{+} \tag{8.10}$$

where eN_+ is the hypothetical areal charge density if the defect band were completely unoccupied. The second contribution Σ_{SiC} represents the charge in the space charge layer of the SiC substrate. Since semi-insulating SiC material has been used, it can easily be shown that Σ_{SiC} is negligible when compared to Σ_g and Σ_{def} for all possible scenarios of band bending. The last term Σ_g corresponds to the areal charge density in the graphene layer. We will specify Σ_g in the following.

Assuming identical mobilities of electrons and holes, the voltage of minimum conductivity obviously belongs to surface potential zero, and the corresponding gate-source voltage shall be denoted as the Dirac voltage V_{Dirac} (vs. Ag/AgCl) in the following. The areal excess charge density in the π* band above and the π band below the Dirac energy is $e \cdot (p-n)$ with the areal hole density p and the areal electron density n. Then the areal charge density Σ_g in the graphene layer can be expressed as a function of surface potential as (see Appendix VII):

$$\frac{\Sigma_g(x)}{e \cdot \kappa \cdot (kT)^2} = \left[\tfrac{1}{2}x^2 + 2\int_0^{|x|} R(t)\, dt \right] \cdot sign(x) \tag{8.11}$$

and the areal charge carrier concentration $c = n + p$ in the graphene layer can be expressed as (see Appendix VII):

$$\frac{c(x)}{\kappa \cdot (kT)^2} = 2\alpha + \tfrac{1}{2}x^2 \tag{8.12}$$

$x = 2/\left(\pi\hbar^2 {v_F}^2\right)$ is related to the Fermi velocity v_F of the graphene. The value of x can be measured from photoelectron spectroscopy, $x = (1.18 \pm 0.06) \cdot 10^{14}\, cm^{-2}\, (eV)^{-2}$ [71]. The quantity $\kappa \cdot (kT)^2$ is a natural unit for the areal charge carrier concentration of a single graphene layer which amounts to $7.4 \cdot 10^{10}\, cm^{-2}$ at room temperature and $\alpha = \int_0^{\infty} \frac{u}{1+\exp(u)}\, du = \frac{\pi^2}{12} = 0{,}8225$. $R(t) = \int_t^{\infty} \frac{1}{1+\exp(u)}\, du = \ln\left[1+\exp(-t)\right]$ is the Fermi

residuum. Note that $\Sigma_g(x)$ and $c(x)$ are odd and even functions, respectively.

Finally, We take the surface potential as a variable and construct the corresponding relative gate-source voltage. One contribution to this is obviously ϕ itself, the other is the voltage drop across the Helmholtz layer which is proportional to the charge modulation $\Sigma(\Phi)$ in the SiC space charge layer (x_3 to x_4) plus the graphene layer (x_4), divided by the (areal) Helmholtz capacitance C_{HH}:

$$-e\cdot V_{GS} = \Phi + \frac{e}{C_{HH}}\cdot\Sigma(\Phi) + \sigma_{ads}\cdot\frac{e}{C_{ocl}} - eV_{REF} - \delta \tag{8.13}$$

Here we neglect the voltage drop across the diffuse layer in the electrolyte, i.e. we approximate the excess ionic charge in the diffuse layer of the electrolyte by a sheet charge at the OHP compare Figure 8.8. For the areal capacitance of the compact layer we use $15\,\mu F/cm^2$. This value corresponds to nominal thicknesses of $d_1 = 0.25nm$ and $d_2 = 0.40nm$ and dielectric constants of $\varepsilon_1 = 6$ and $\varepsilon_2 = 25$ for the inner (surface to IHP) and outer (IHP to OHP) part of the compact layer, respectively, and was found appropriate for the compact layer capacitance of graphite in previous work [177]. C_{ocl} is the outer compact layer capacitance already introduced in chapter 5. Since the adsorbed ionic charge density can be to first order be assumed to be independent of the surface potential, the last three terms of equation (8.12) can be subsummized in a constant V_0 independent of ϕ. Inserting equations (8.11) and (8.10) into (8.13):

$$-e\cdot V_{GS} = \Phi + \frac{e}{C_{HH}}\left[\frac{1}{2}\mathrm{K}\phi^2 + 2xkT\int_0^{\phi/kT} R(t)\,dt - \int_{-\infty}^{\infty}\frac{D(E)}{1+\mathrm{e}^{\frac{\phi+E}{kT}}}dE + N_+ + eV_0\right] \tag{8.14}$$

and forming the derivative yields

$$-\frac{d(eV_{GS})}{d\Phi} = 1 + \frac{e^2}{C_{HH}}\left[\,\kappa|\Phi| + 2\kappa(kT)\cdot R\left(\left|\tfrac{\Phi}{kT}\right|\right) + \left\{D_{def} * g\right\}(-\Phi)\right] \tag{8.15}$$

The last term in the brackets on the right hand side is the convolution of the defect density of states with the negative derivative of the Fermi Dirac function, taken at energy -Φ (relative to the Dirac energy), i.e. $g(E) = -\frac{d}{dE}\left[\frac{1}{1+\exp\left(\frac{E}{k_BT}\right)}\right] = \frac{1}{kT}\frac{\exp\left(\frac{E}{kT}\right)}{\left(1+\exp\left(\frac{E}{kT}\right)\right)^2}$, which is an even function in its argument with area 1.

8.5 Discussion of Diamond-Based SGFETs

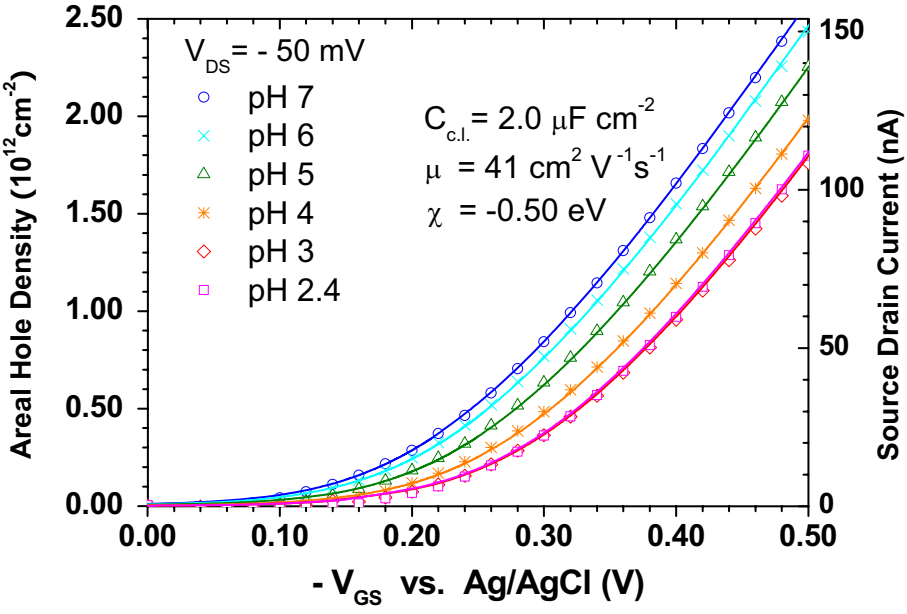

Figure 8.9 *Fits of the transfer characteristics of Figure 8.3 (symbols, right hand scale) according to the model of Figure 8.8a) (hole densities on the left ordinate). The parameter distinguishing the different pH cases is the adsorbed ionic charge density at the inner Helmholtz plane (IHP). Global parameters used in the model are the hole mobility ($\mu = 41 cm^2 V^{-1} s^{-1}$), the nominal areal capacitance of the compact layer ($2.0 \mu F / cm^2$), and the electron affinity of the hydrogen-terminated diamond surface in contact with the aqueous electrolyte ($\chi = -0.50\ eV$).*

In the following, we will further evaluate (8.8) and (8.9) with the experimental data. Equation (8.8) is essentially the inverse of the transfer characteristics shown in Figure 8.3 and can directly be compared to the experimental values after using the geometry of the surface conductive channel, the hole mobility and the source-drain voltage to convert the source drain current to the areal hole density. In Figure 8.9 we have re-plotted the experimental data of Figure 8.3 (symbols) and compare them with (8.8) and (8.9) (solid lines). For each pH the correct ionic composition has been used to evaluate w_{OHP} for a given hole concentration according to (8.3). The ionic composition comprises monovalent and divalent positive and negative ions as it results from the buffer curves of the phosphate buffer, the titration, and the background salt concentration.

The model describes the data with excellent agreement in the super-linear threshold range and above. Following the work of Härtl et al. [123], we have set the inner and outer Helmholtz planes identical for this first scenario ($d_2 = 0$). That leaves $d_1 / (\varepsilon_0 \varepsilon_1)$ as the nominal inverse areal capacitance $1 / C_{c.l.}$ of the compact layer as free parameter in (8.8)

and (8.9). For the fits of Figure 8.9 a value of $2.0\ \mu F / cm^2$ was chosen. This value is the average of experimental values published in [178] and [179]. Once the compact layer capacitance is fixed, the hole mobility of the carriers results with a small error margin from the fits of Figure 8.9. This is demonstrated in Figure 8.10 where we compare the transfer characteristics for pH 7 with the fit for the optimum mobility $\mu = 41\ cm^2V^{-1}s^{-1}$ and for values deviating by $\pm 10\%$. All other parameters in (8.8) and (8.9), namely E_i (or equivalently, $x = E_i - E_G = E_i - 5.5eV$) and σ_{ads}, only shift the transfer characteristics on the voltage axes. It is thus obvious from Figure 8.10 that the mobility is determined with an accuracy better than $\pm 10\%$ (once the compact layer capacitance is fixed).

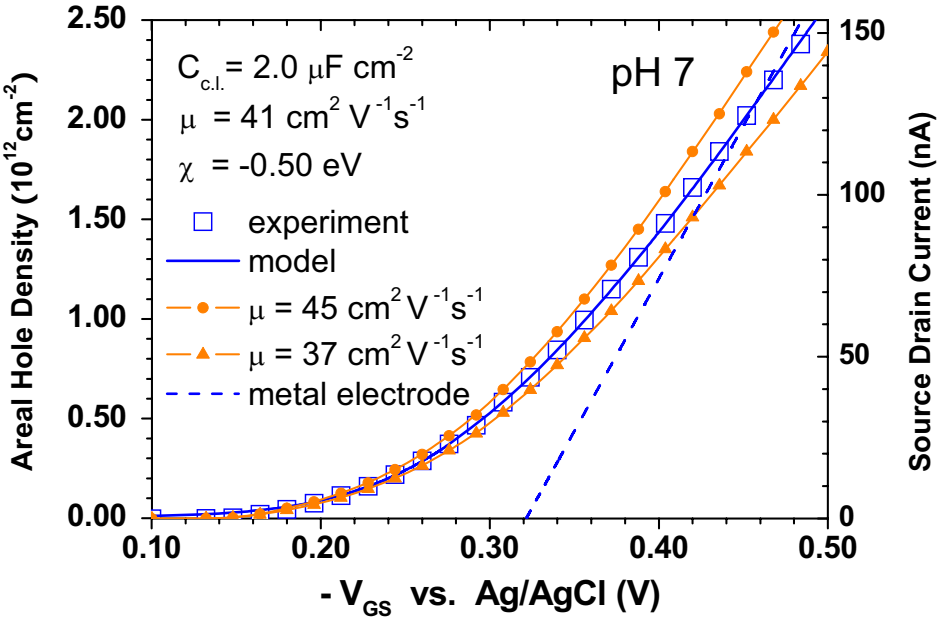

Figure 8.10 *Fit of the transfer characteristics for pH 7 with a variation of the mobility by* $\pm 10\%$ *around the optimum value of* $41\ cm^2V^{-1}s^{-1}$.

The dashed line in Figure 8.10 is the corresponding fit when the voltage drop across the diamond part of the electrical circuit is neglected, i.e. when Grahame's model for metal electrodes is adopted. It is obvious that the non-linear transfer characteristics in the threshold range cannot be reproduced by the metallic model. The slope of the straight line is in that case (up to the elementary charge) identical to the areal capacitance of the compact layer as it is used as a fixed parameter in the model. However, it is apparent that the straight line does not follow the linear part of the transfer characteristics (source-drain current >100nA). That means, an analysis of the transfer characteristics by the 'metallic' model will underestimate the compact layer capacitance by 20%, all other parameters being equal.

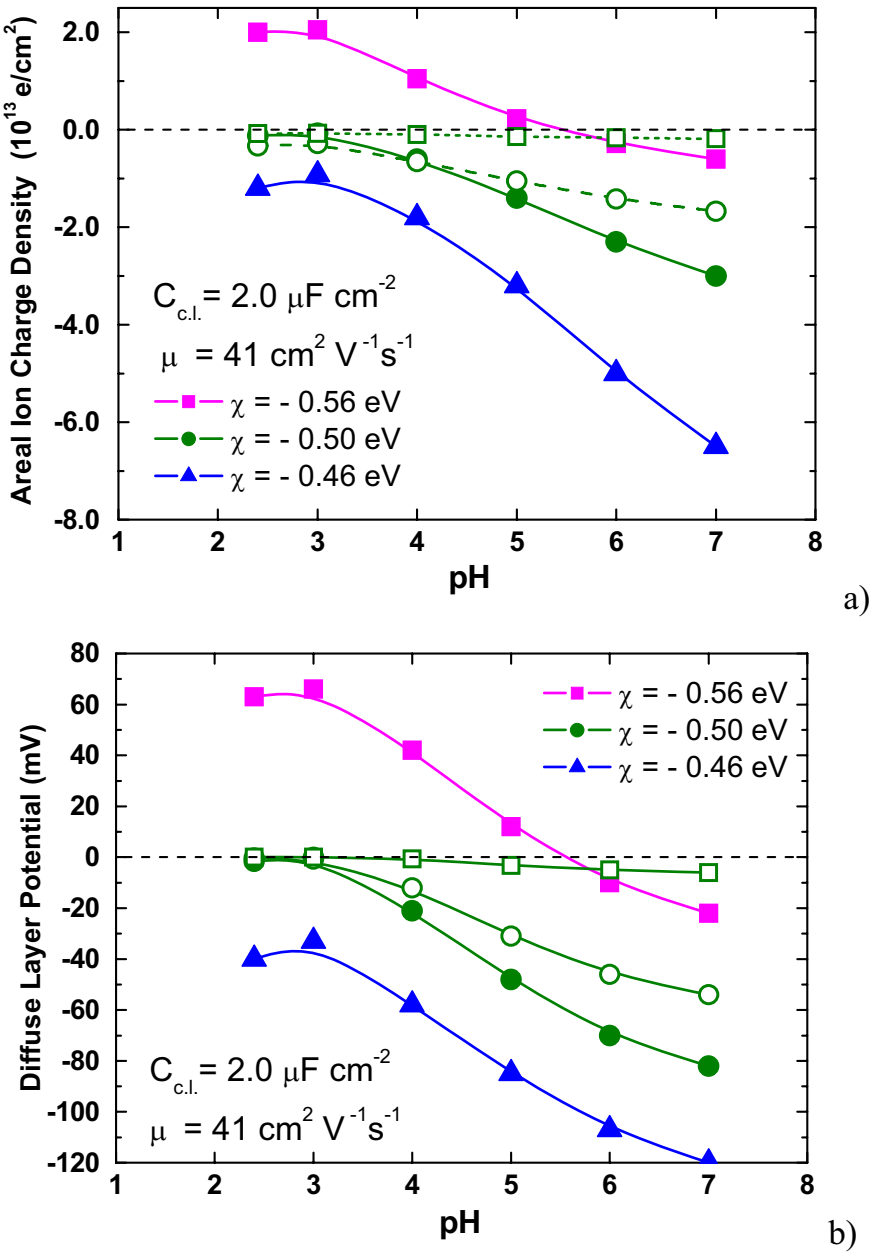

Figure 8.11 *Areal ion charge density affixed at the IHP (a) and open circuit diffuse layer potential (b) as a function of pH as obtained from the fits of Figure 8.9 (full circles) and from fits of the same accuracy but with different electron affinities* χ *(full squares and triangles). The open circuit diffuse layer potential can be identified with the zeta potential which is experimentally accessible by streaming potential measurements and which is found to be zero for* $pH \approx 2$ *to* 3.5*. The open circles and open squares are scenario two and three, respectively. For details on that see text.*

Let us return to Figure 8.9 for the discussion of the further parameters of the model. The shift of the transfer characteristics on the gate voltage axis is brought about by changes of the affixed ion charge density σ_{ads} which decreases with pH. The specific areal ion charge densities that are required for the fits in Figure 8.9 are shown as a function of pH in Figure 8.11a) (full circles). They are essentially zero for pH 2.4 and 3 and become negative

with increasing pH, reaching $\sigma_{ads}/e = -3\cdot10^{13} cm^{-2}$ for pH 7. Experimentally this charge density is inaccessible, but rather is the mobile ionic charge in the diffuse layer σ_{diff}. The latter is related to the potential w_{OHP} at the OHP by the Grahame equation (8.3). σ_{diff} changes complementary with the areal hole charge density and thus depends on the gate voltage. Under open circuit conditions w_{OHP} can be identified as the so-called zeta potential and extracted from streaming potential measurements. Open circuit conditions in an SGFET correspond to a situation where the source-gate voltage V_{GS} is equal to the open circuit voltage V_{OC} at the same diamond electrode measured versus Ag/AgCl under identical electrolyte conditions (see chapter 5). From a fit of the experimental transfer characteristics to (8.8) and (8.9) a value of w_{OHP} for $V_{GS} = V_{OC}$ can be extracted which corresponds to the zeta potential. We have measured V_{OC} for pH between 2 and 10 and the corresponding diffuse layer potential $-(1/e)\cdot w_{OHP}^{OC}$ vs. pH is shown in Figure 8.11b) by the full circles.

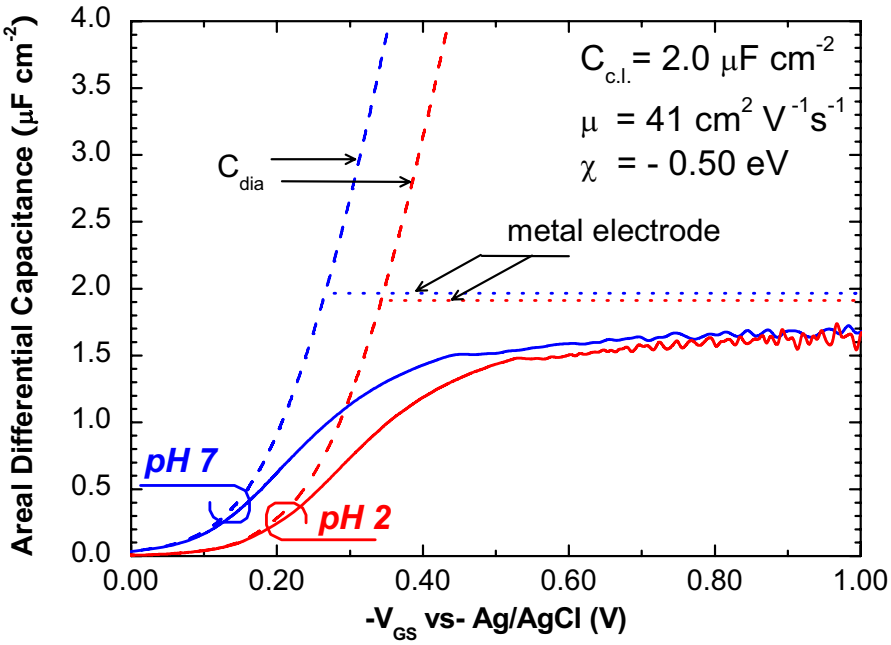

Figure 8.12 *Areal differential capacitance of the complete circuit of Figure 8.8 as extracted from the fits of Figure 8.9 for pH 2 and pH 7. The 'noise' on the curves is due to the numerical inversion of (8.6).*

Data on the zeta potential to be compared with w_{OHP}^{OC} are so far only reported for a polycrystalline hydrogen-terminated diamond surface in contact with electrolytes comparable with the ones used here [13],[123]. Since the sample used in that experiment was a of high quality material with presumably large grain sizes we consider the zeta

potentials reported with some caveat also as representative for the case at hand. For a background salt concentration of 10mM KCl comparable as in our case, the zeta potential varies from $\approx 0mV$ at pH 3 (the so-called iso-electric point) to $\approx -60mV$ for pH 7 which is in very good agreement with the data in Figure 8.11b) (zero to $-80mV$).

From the comparison of the open circuit diffuse layer potentials $-(1/e)w_{OHP}^{OC}$ with the published zeta potentials we can extract an important microscopic parameter of the hydrogen-terminated diamond surface in contact with aqueous electrolytes. To this end, we focus once more on (8.8) and (8.9) that links the gate voltage to the hole density. It contains the difference between the diamond ionization energy E_i and 4.64 eV as an offset for the voltage axis. Thus, a change in the ionization energy (or -equivalently- of the electron affinity $\chi = E_i - 5.5eV$) of the diamond surface causes a rigid shift of the transfer characteristics on the gate voltage axis. Such a shift can be compensated by appropriate changes in adsorbed ion densities σ_{ads} so that a fit as perfect as demonstrated in Figure 8.9 is maintained. We have illustrated this compensation with three different assumptions for the electron affinity of the diamond surface. $\chi = -0.50\,eV$ is the case of Figure 8.9 as discussed so far; $\chi = -0.56\,eV$ and $\chi = -0.46\,eV$ allow to fit the transfer characteristics with the same accuracy (not shown). However, the corresponding open circuit diffuse layer potentials are far off the measured zeta potentials in those cases (Figure 8.11b). From this analysis we can thus determine the electron affinity of the hydrogen-terminated diamond (100) surface in contact with an aqueous electrolyte as $\chi = -0.50 \pm 0.02eV$.

The derivative of the transfer characteristics of Figure 8.3 constitutes the static differential capacitance for the total electrical circuit. We have extracted the areal differential capacitance from the fit curves to the data and show them for pH 7 and pH 2 in Figure 8.12 (full lines). In the spirit of the model presented in Figure 8.8 it is tempting to define $C_{dia}(V_{GS}) = e^2\, dp(u_S)/du_s$ as the differential areal capacitance of the diamond accumulation layer alone (dashed lines in Figure 8.12). This is so because $(1/e)u_s(p)$ mimics the modulation of the gate voltage dependent potential drop across the hole accumulation layer (8.5). The total capacitance is then a serial combination of C_{dia} and the double layer capacitance on the electrolyte side. In the threshold range of the transfer characteristics ($-V_{GS} < 0.15V$), the total areal capacitance is in fact dominated by C_{dia}, and it approaches a constant value in the linear range $-V_{GS} > 0.5V$. Note that this constant is, however, 20% lower than the nominal areal differential capacitance of the compact layer ($2.0\ \mu F\ cm^{-2}$). Only when a metal electrode is modelled (horizontal dotted lines in Figure 8.12), the capacitance of the whole circuit approaches that of the compact layer. The potential drop between the metal source contact and the diamond/electrolyte interface is

thus the dominating effect for the static differential capacitance of the SGFET in the threshold range.

8.6 Discussion of Graphene-Based SGFETs

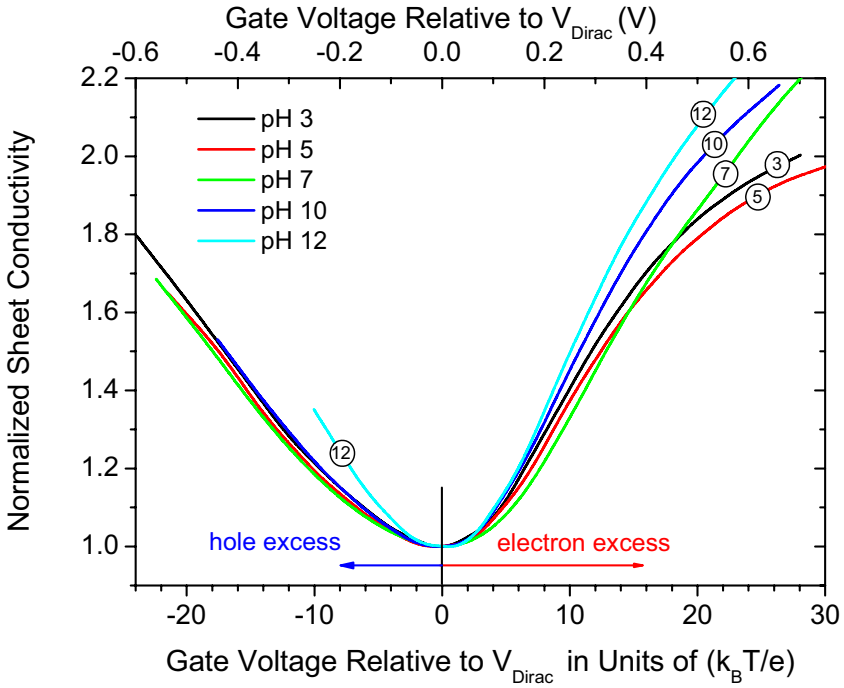

Figure 8.13 *Normalized plot of the transfer characteristics of the SGFET. For negative relative voltage the sheet conductivity falls on a master curve for all pH. For the positive branch pronounced scatter of the data is observed.*

For further evaluating our data in the spirit of equation (8.15), we have re-plotted Figure 8.6 in Figure 8.13 with the gate voltage relative to the Dirac voltage and with the ordinate normalized to the minimum sheet conductivity. The master curve obtained in this way is nearly independent on pH on the anodic side (except for pH 12) and shall be discussed in the following. Assuming the same mobility μ for electrons and holes in graphene, equation (8.12) yields directly the sheet conductivity $\sigma_{\square}(x) = e \cdot \mu \cdot c(x)$ as a function of surface potential with e being the elementary charge. Specifically, we find $\sigma_{\square,\min} = 2\alpha \cdot \kappa (kT)^2 \cdot e \cdot \mu$ for the minimum sheet conductivity (x=0). From our experiment we extract $\sigma_{\square,\min} = 35 \pm 1\,\mu S$. This yields $\mu = 1800 \pm 100\, cm^2 V^{-1} s^{-1}$ for the mobility of electrons and holes in the graphene layer of our graphene SGFET when the Fermi level coincides with the Dirac energy. With the further assumption of equal and constant electron and hole mobility we can infer from (8.13):

$$\frac{\sigma_{\square}(x)}{\sigma_{\square,\min}} = 1 + \frac{x^2}{4\alpha} \tag{8.16}$$

for the normalized sheet conductivity that is plotted in Figure 8.13. Note that the channel conductivity varies in our experiment by less than a factor of 2.2 which certainly justifies the assumption of a mobility independent of charge carrier concentration.

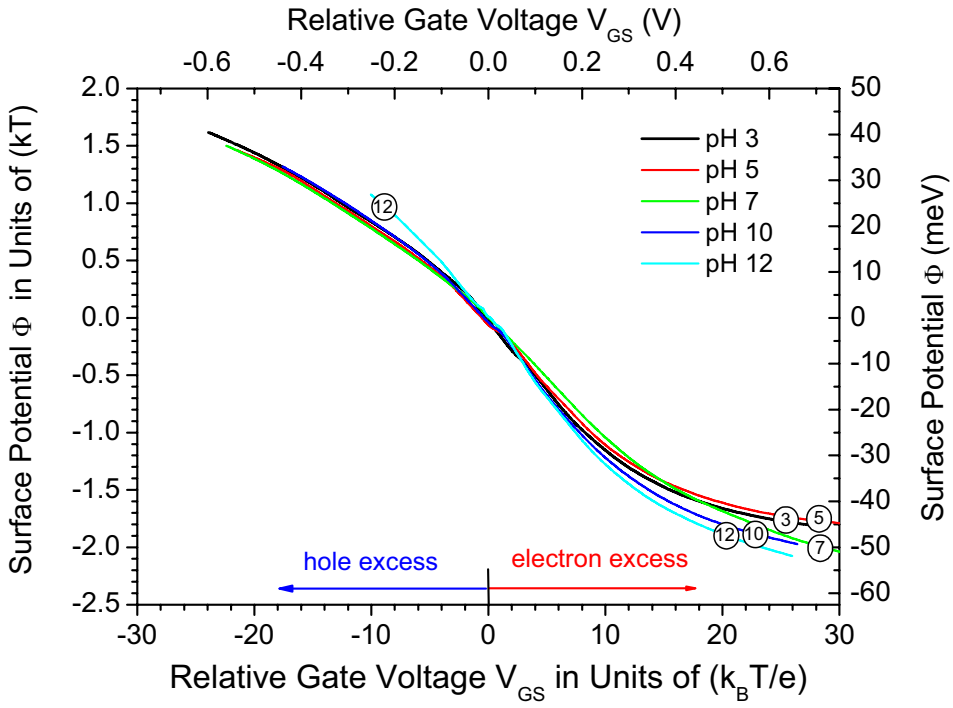

Figure 8.14 *Surface potential vs. relative gate voltage as extracted from Figure 8.13 and discussed in the text.*

Equation (8.16) is easily inverted and thus allows calculating the surface potential from the normalized sheet conductivity:

$$x = \frac{\Phi}{kT} = \pm\sqrt{4\alpha \cdot \left(\frac{\sigma_{\square}(x)}{\sigma_{\square,\min}} - 1\right)} \tag{8.17}$$

where the positive sign refers to the branch with negative relative gate voltage in Figure 8.13 (hole excess) and vice versa. Using equation (8.17) we can transform the transfer characteristics to evaluate the surface potential in the graphene layer as a function of the relative gate-source voltage. This is plotted in Figure 8.14.

For further evaluating (8.15), we introduce spectroscopic defect density of states function for the SiC/graphene interface $S(E) = \{D_{def} * g\}(E)$, which is the real defect density probed with $g(E)$ as resolution function. S(Φ) is easily obtained from inverting (8.15):

$$S(-\Phi) = D_0 \cdot \left\{ \left[-\frac{d(eV_{GS})}{d\Phi} - 1 \right] \cdot \frac{C_{HH}}{C_0} - \left| \frac{\Phi}{kT} \right| - 2 \cdot R\left(\left| \frac{\Phi}{kT} \right| \right) \right\} \qquad (8.18)$$

where $D_0 = \kappa\, kT = 2.9 \cdot 10^{12}\, cm^{-2}\,(eV)^{-1}$ at room temperature. $C_0 = e^2 \kappa\, kT$ is a constant that amounts to $0.47\ \mu F\ cm^{-2}$ at room temperature and is thus small compared to the Helmholtz capacitance of $C_{HH} = 15\ \mu F\ cm^{-2}$ that has been introduced before. In fact, the second and third terms in the bracket on the right hand side of (8.18) are smaller than 2 within the variation of the surface potential Φ in our experiment and thus constitute only a minor correction to the first term which is essentially the derivative of the gate control voltage w.r.t. the surface potential. Nevertheless, we have taken them into account when transforming the data of Figure 8.14 via (8.15) into the spectroscopic defect density of states shown in Figure 8.15.

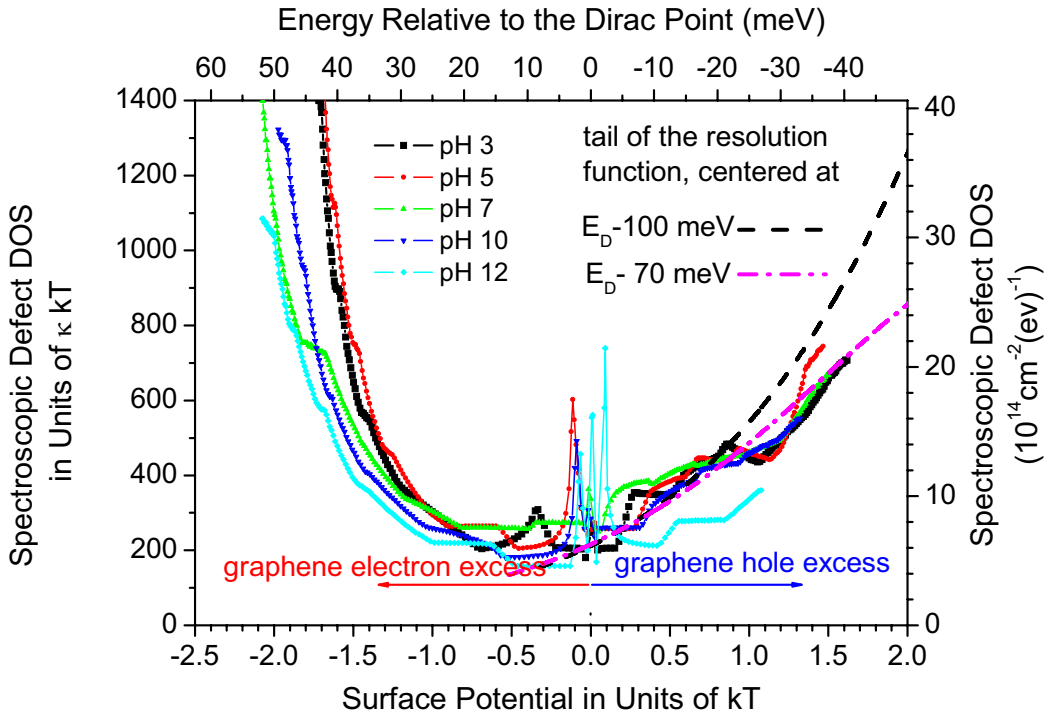

Figure 8.15 *Spectroscopic defect density of states for the SiC/graphene interface as evaluated from the data. The dashed and the dash-dotted lines are the tail of the resolution function for two different assumptions for the energy of interface defects relative to the Dirac energy.*

The spectrum shows a minimum around the Dirac energy with steep increase towards higher energies (i.e. towards the SiC conduction band minimum) and lower energies (i.e. towards the SiC mid gap energy). We have also plotted the resolution function $g(E)$ for two cases, centred at -100 meV (dashed line) and centred at -70 meV (dash-dotted line) relative to the Dirac energy, respectively. In both cases, the tail of the resolution function

fits the spectroscopic DOS reasonably well. Thus, the data are consistent with a narrow (in fact δ-function type) band of defect states whose areal density n_{def} is identical with the scaling factor of the resolution function fitted to the data. For case 1, this scaling factor is $11000\,\kappa(kT)^2 = 8.1\cdot10^{14}\,cm^{-2}$ and for case 2 it is $4000\kappa(kT)^2 = 3.2\cdot10^{14}\,cm^{-2}$. The data are thus consistent with a band of defect states between 70 and 100 meV below the Dirac energy and with concentration between 3.2 and $8.1\cdot10^{14}\,cm^{-2}$. This latter upper limit is, however, not unique due to the exponential character of the resolution function for sufficiently large argument. The data are thus equally consistent with any larger concentration of defects shifted by $kT\cdot\ln(A)$ further towards lower energies into the band gap of SiC. However, $8.1\cdot10^{14}\,cm^{-2}$ corresponds already to 65% of the surface atom density of the SiC (0001) surface ($1.22\cdot10^{15}\,cm^{-2}$), and to about 20% of the graphene atom density. Thus, two out of three Si interface atoms would be expected to give rise to a dangling bond-like defect in case 1. A substantially larger defect density than that is hard to imagine. We may therefore consider the range of energies and concentrations specified above as a reasonable estimate for the defect DOS.

On the high energy side of Figure 8.15 the data show a strong scatter and the spectrum increases even stronger than the resolution function allows. We may speculate that here already disorder induced tail states of the conduction band of the SiC become visible whose density of states is expected to increase exponentially to higher energies. We have to admit at this point, that the data allow no further conclusions.

Finally, we would like to reconsider equations (8.11) and (8.12) for the areal charge and charge carrier density, respectively, of graphene as a function of temperature and surface potential. They constitute fundamental relationships for the analysis of conductivity and capacitance experiments on graphene based devices. In fact, in the absence of interface defects and when neglecting the space charge in the substrate onto which the graphene layer is prepared, equation (8.12) directly yields the temperature dependent charge carrier concentration and thus the sheet conductivity with the charge carrier mobility as the connecting parameter. For small variation of the surface potential around zero as in our experiment, the assumption of a mobility independent of the charge carrier density in graphene is certainly justified. Equation (8.12) is, however, generally valid as long as the dispersion relation of the π and the π^* bands remain linear and the occupation of the σ and σ^* bands with holes and electrons, respectively, can be neglected. Moreover, equation (8.11) yields the temperature dependent areal differential capacitance C_g of a graphene layer as

$$C_g(\Phi,T) = e\frac{d\,\Sigma_g}{d\,\Phi} = e^2\kappa\cdot kT\cdot\left[2\,R\left(\frac{\Phi}{kT}\right)+\frac{\Phi}{kT}\right] \tag{8.19}$$

The prefactor $C_0 = e^2\kappa\cdot kT$ was already defined above. For $\Phi = 0$, equation (8.19) gives a minimum areal differential capacitance $C_{\min}(T) = 2\ln(2)\cdot C_0(T)$ that amounts to $0{,}66\ \mu F\ cm^{-2}$ at room temperature. This value is in excellent agreement with experimental data [180]. We note in passing that this finite minimum areal capacitance is an intrinsic property of graphene and does not require charge inhomogeneities as suggested in [177].

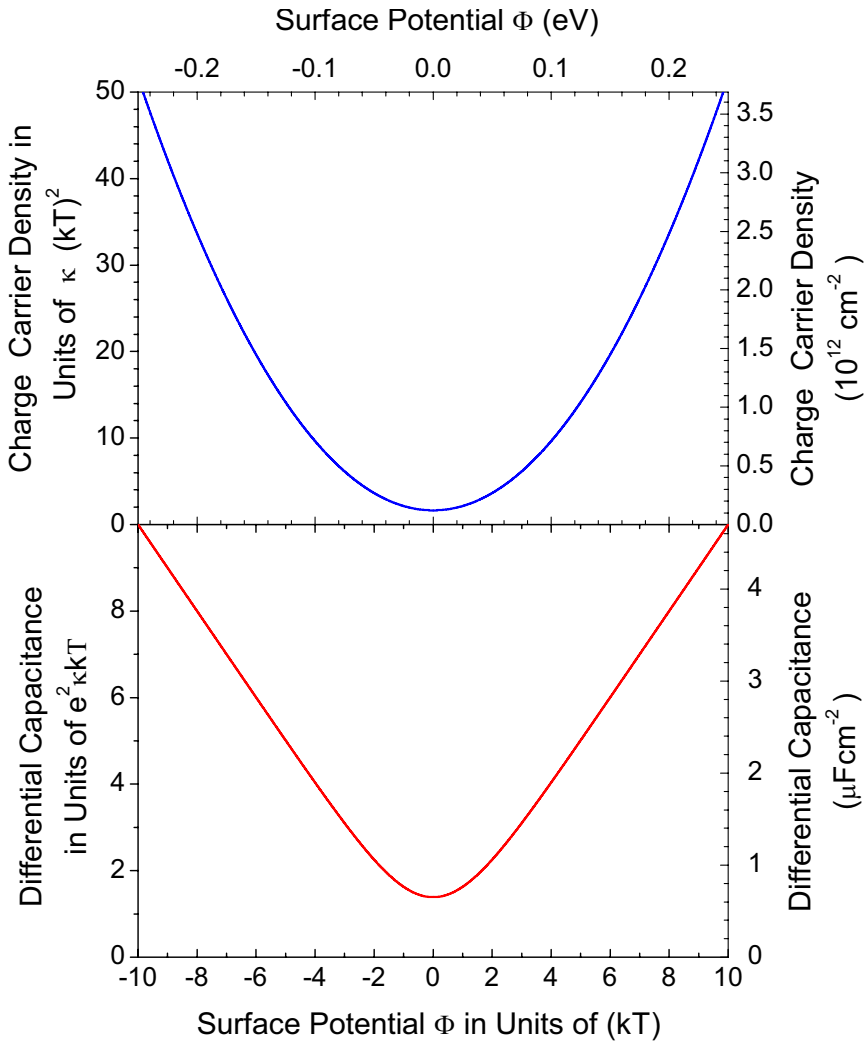

Figure 8.16 *Temperature dependent areal charge carrier density (upper panel) and areal differential capacitance (lower panel) as a function of surface potential, i.e. of the energy difference between the Dirac energy and the Fermi level in graphene.*

We have plotted the areal charge carrier concentration $c(\Phi,T)$ corresponding to (8.11) and the areal differential capacitance $C_g(\Phi,T)$ corresponding to (8.19) in Figure 8.16. The temperature dependence is in both cases taken into account in form of the natural

units adopted for the left hand side ordinates and the lower abscissa. The right hand scale and the upper abscissa refer to the specific quantities for room temperature.

8.7 Summary: Carbon-Based Solution Gated Field Effect Transistors

We have demonstrated the pH sensitivity of diamond-H SGFFETs and of graphene SGFETs. The transfer characteristics of both devices show amazingly similar pH dependent shifts of 19 ±1 mV/pH. To study the working principle of the devices, we analyze the charge and the potential profiles in the semiconductors (diamond-H or graphene) as well as in the whole circuit. From this analysis we derive expressions for the transfer characteristics of both SGFETs that faithfully describe experimental data. From corresponding fits to our experimental data, characteristic parameters and defect densities (for the graphene case) are determined.

Appendix

Appendix I Derivation of the Nernst's Equation

Consider an electrochemical cell, where electrons released in one electrode by oxidation of an electrode flow through a conducting wire to another electrode and are used for reduction reaction, as illustrated in Figure a1. Following IUPAC (International Union Pure and Applied Chemistry) convention [181], in general case, we have the electromotive force, E, of the cell: $E = E$ (reduction electrode: right) – E (oxidation electrode: left). The E of many half-cell reactions is generally measured via being paired with a standard hydrogen electrode (SHE). In literature, this is written as *Eh*.

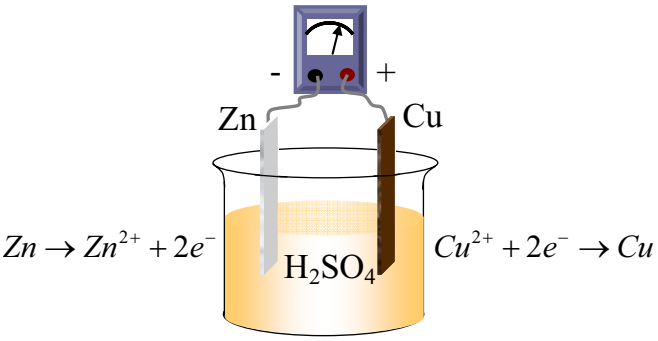

Figure a1 *Schematic illustration of an electrochemical cell consisting of two half cells. Electrons are released in the left half-cell by the oxidation of a Zn electrode, and are transferred to the right half cell where these react with the solution to cause deposition of Cu onto the Cu electrode. The net reaction in the cell is* $Zn + Cu^{2+} \rightarrow Zn^{2+} + Cu$.

We will calculate the value of E in two different methods: the kinetic treatment and the thermodynamic treatment. Both of the two treatment yield the same result [88]:

1. Derivation of Nernst's equation from the kinetic treatment

According to the concept of the exchange-current density j_0 ((2.25) and (2.26)), under equilibrium conditions fulfills:

$$F \cdot \vec{k} \cdot c_A \cdot \exp\left((1-\alpha) \frac{F\phi_{ml}}{RT} \right) = j_0 = F \cdot \overleftarrow{k} \cdot c_D \cdot \exp\left(-\alpha \frac{F\phi_{ml}}{RT} \right) \qquad \text{(a.1)}$$

where c_A is the concentration of an electron-acceptor ion, while c_D is that of an electron donor. Hence,

$$\phi_{ml} = \frac{RT}{F}\ln\frac{\overleftarrow{k}}{\vec{k}} + \frac{RT}{F}\ln\frac{C_D}{C_A} \tag{a.2}$$

Since $\left((RT/F)\ln\left(\overleftarrow{k}/\vec{k}\right)\right)$ is not a function of concentration, we can rewrite it as a constant $\phi_{ml}^{\ominus}$. In addition, replace the ϕ_{ml} (electrode potentials relative to the electrolyte) by E, and consider the activity instead of concentration (derivative the equation for current density is in section 2.3; here we assumed the activity was 1), the Nernst equation comes up:

$$E = E^{\ominus} + \frac{RT}{F}\ln\frac{a_D}{a_A} \tag{a.3}$$

2. Derivation of Nernst's equation from the thermodynamic treatment

Let's consider the half cell reaction on Cu electrode, $Cu^{2+} + 2e^- \rightleftharpoons Cu$ and rewrite it in a more general form: $M^{Z+} + Ze \rightleftharpoons M$. Assume electrochemical equilibrium is achieved. Then the general thermodynamic condition for **equilibrium** is (since for neutral metal, the electrochemical potential is equal to the chemical potential):

$$\mu_M = \overline{\mu}_M = \overline{\mu}_{M^{Z+}} + Z\overline{\mu}_e \tag{a.4}$$

Recall the definition of electrochemical potential and rewrite the terms:

$$\begin{aligned} &\overline{\mu}_{M^{Z+}} = \mu_{M^{Z+}} + ZF\phi_s \\ &\overline{\mu}_e = \mu_e - F\phi_M \text{ (since the charge of electron is negative)} \end{aligned} \tag{a.5}$$

Insert (a.4) into (a.5):

$$\mu_M = \mu_{M^{Z+}} + Z\mu_e + ZF\left(\phi_s - \phi_M\right) \tag{a.6}$$

Then, the electrode potentials relative to electrolyte is:

$$\begin{aligned} &\Delta\phi_e = \phi_M - \phi_S = \frac{\mu_{M^{Z+}} + Z\mu_e - \mu_M}{ZF} = -\frac{\Delta G}{ZF} \\ &\text{in standard state,} \quad \Delta\phi_e^{\ominus} = \frac{\mu_{M^{Z+}}^{\ominus} + Z\mu_e^{\ominus} - \mu_M^{\ominus}}{ZF} = -\frac{\Delta G^{\ominus}}{ZF} \end{aligned} \tag{a.7}$$

Recall the expression of chemical potential that are related to standard electrochemical potential and the activities:

$$\mu_i = \mu_i^{\ominus} + RT\ln a_i \tag{a.8}$$

a_i (i represent the general case) is 1 for metal and electrons in their standard state. Then (a.7) becomes:

$$\Delta\phi_e = \frac{\mu_{M^{Z+}}^{\ominus} + Z\mu_e^{\ominus} - \mu_M^{\ominus}}{ZF} + \frac{RT}{ZF}\ln a_{M^{Z+}} \tag{a.9}$$

Combine (a.7) and (a.9), and use the general representative "E" instead of $\Delta\phi_e$. Finally, the Nernst equation is yielded:

$$E = E^{\Theta} + \frac{RT}{ZF}\ln a_{M^{Z+}} \quad \text{(a.10)}$$

And in general case, $$E = E^{\Theta} + \frac{RT}{ZF}\ln\frac{a_{A^{Z+}}}{a_D} \quad \text{(a.11)}$$

Appendix II Order of Chemical Reactions

In kinetics chemistry, the rate of a chemical reaction, *v*, is related to the molar concentrations of reactants A, B, following the so-called **rate law** as $v = k[A]^a[B]^b$, where k is a reaction constant [116]. The sum of the exponents on the concentration terms is called the **order** of the reaction. For example, a reaction having the rate law as $v = k[A][B]^2$, is a third order (since 1+2=3) reaction. Reactions of different orders accompany with corresponding rate law. A simple first-order reaction $A \to Z$, which depends on the concentration of only one reactant A, has the following rate law: $v = -d[A]/dt = k[A]$. The integrate rate law is: $\ln[A] = -kt + \ln[A]_0$. Certain reactions can be considered as first-order reaction as long as the **pseudo-first-order conditions** can be established, either: 1) $A + B \to Z$, and $[A] \gg [B]$, i.e. reactant is in great excess with respect to the other reactant B; or 2) $A \xrightarrow{B} Z$, where B is a catalyst.

Reversible reactions are more complicated. For a first-order reversible reaction: $A \underset{k_b}{\overset{k_f}{\rightleftharpoons}} Z$, where rate constant symbolism denoting the forward (k_f) and backward (k_b) steps. Define $[X]_0, [X]_e$ and $[X]_t$ as concentration of "X" (A or Z) at time *0* mins, equilibrium and at time *t* mins, respectively. Then the concentration of A at equilibrium is equal to the concentration of at time zero minus the conversion in moles to Z (defined as y), given: $[A]_e = [A]_0 - y = \frac{k_b}{k_f - k_b}[A]_0$, and $[Z]_e = y = \frac{k_f}{k_f + k_b}[A]_0$. Thus the integral rate law is modified as: $\ln(\frac{[A]_0 - [A]_e}{[A]_t - [A]_e}) = (k_f + k_b)t \equiv k \cdot t$, where the sum of k_f and k_b is defined as k, the overall reaction constant.

Appendix III The Effect of Cl-Ions on the Red-Ox Kinetics of Diamond-H electrode

The data set in Figure a2 (open diamonds) has been measured on hydrogen terminated diamond electrode in an electrolyte with a twenty-fold higher concentration of KCl than the standard electrolyte as discussed in chapter 5. We were motivated to study the effect of increasing halogen ion concentration by experiments on SGFETs by us and others showing a pronounced increase of Faradaic currents with increasing iodine and chlorine ion concentrations. (See, for example, $I_{ds}vs.V_{gs}$ for $V_{ds}=0$ in Fig. 2 of reference [125]; this current is in fact a Faradaic (gate) current such as we discuss here! See Appendix VI as well for a comparison). We thus expect a major change in the red-ox kinetics with halogen concentration that is confirmed in Figure a2. Kanazawa et el.[125] ascribe the effect of chloride ions on their ISFET characteristics as due to a specific adsorption of Cl- in the Helmholtz layer. The open circuit voltage shifts by $0.1V$, and the cathodic and anodic current densities are clearly higher than before. Both the cathodic and the anodic current densities moreover do no longer follow the Butler-Volmer relation, all indicating that chlorine ions have a major impact on the charge transfer of electrons at the diamond/electrolyte interface. This issue is subject of on-going research work.

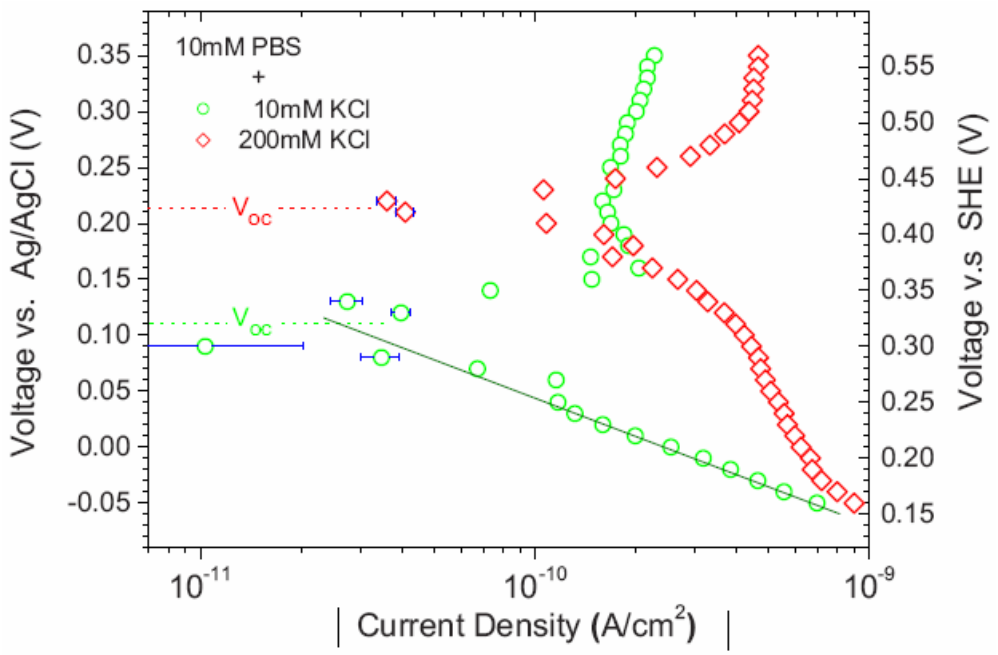

Figure a2 *Quasi static polarization curves for diamond (A) in standard electrolyte at pH7 and the other one with a high concentration of KCl 0.2 M.*

Appendix IV Partial Oxidation of Diamond Surfaces

Attenuated total reflection infrared spectroscopy (ATR-IR) is used to identify the chemical oxidation on diamond surface. In this experiment, an ATR diamond sample (with the edge of 45 degree) is used as waveguide prism. The sample is of intrinsic type IIa (100). First of all, the sample is hydrogen terminated and studied by ATR-IR in both *p*-polarization and *s*-polarization mode. Later, the sample is dipped into a quartz tube that is filled with peroxide (30%). The sample as well as the tube is under simultaneous UV illumination by a mercury discharge lamp (254 nm, 20 W, 3 cm distance) for 30 minutes. Followed the standard cleaning procedure, FTIR-ATR is again used to measured the surface termination of the sample (as compared to the one that is freshly hydrogen terminated). On background correction, a peak located at around 3587 cm^{-1} is identified to be the OH-group that is attached on diamond surface. The possible chemical reaction route is sketched in Figure a3a).

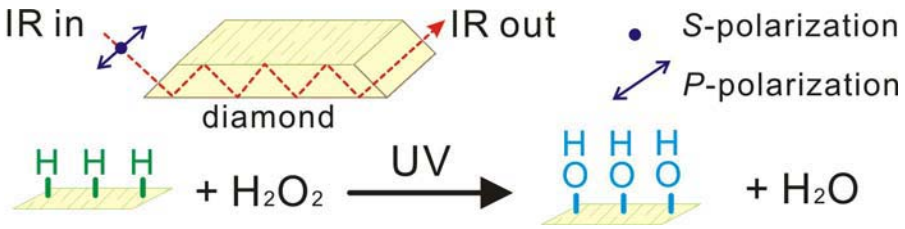

a)

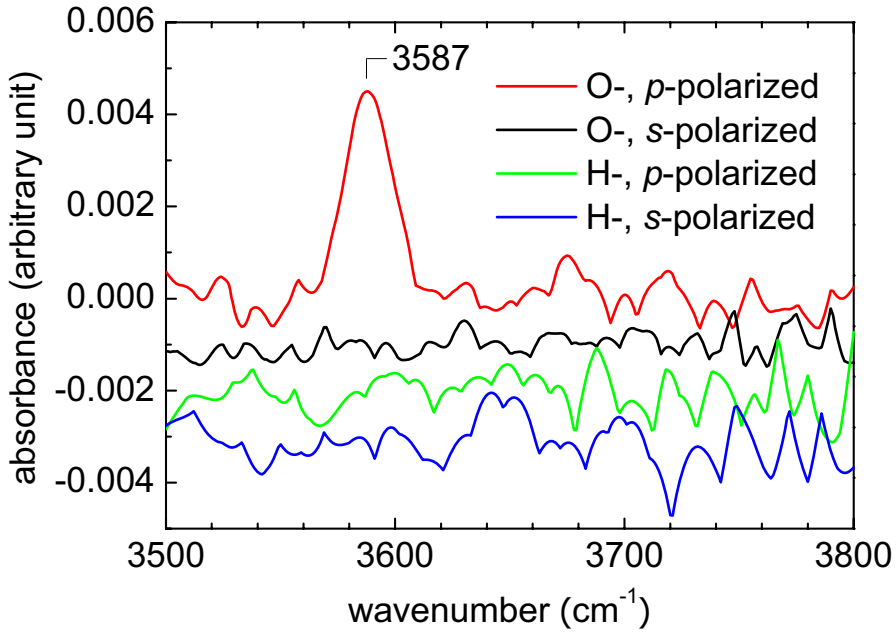

b)

Figure a3 *The FTIR-ATR setup a) and spectrum b) of hydrogen terminated diamond and partially oxidized diamond. We adopts s and p polarization modes in the experiment: s-polarization is coming out of page and p-polarization is parallel to page. The OH-termination on the partially oxide sample is identified.*

Appendix V SGFETs with Platinum Reference Electrodes

In some literature, platinum electrode is used as a reference electrode in the SGFET measurements. However, platinum electrode (or standard hydrogen electrode) is not suitable for the application as a gate electrode in a pH SGFET, because platinum electrode itself is pH sensitive. For diamond based SGFET, when a platinum gate electrode is used, the pH sensitivity factor (-22mV/pH) deviates from the one measured by a Ag/AgCl reference electrode (+19mV/pH) by 41mV/pH, which is just the pH respond of platinum electrode under open circuit condition relative to the Ag/AgCl reference electrode (see the discussion in section 5.4 and Figure 5.8)!

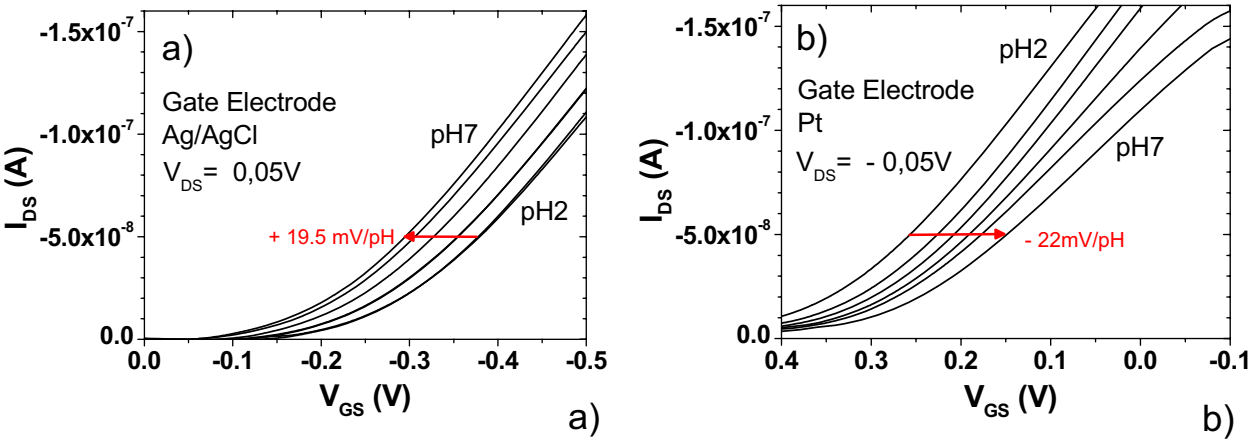

Figure a4 *Transconductance curves of the SGFET in the linear I_{DS}-V_{DS}. pH values between 7 and 2 are varied in steps of one for (a) the Ag/AgCl reference electrode and (b) the Pt wire electrode used as gate.*

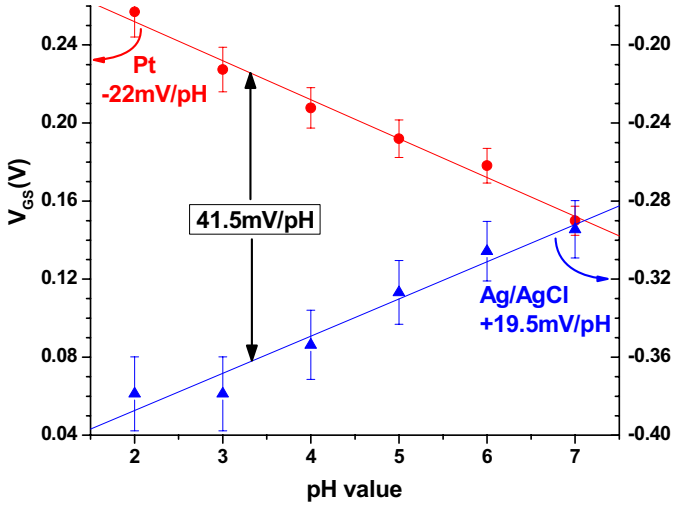

Figure a5 *Comparison of the pH sensitivities of diamond-H SGFET of the same electrolyte (Buffer: 10mM PBS, 10mM KCl) but different gate electrode. The drain-source current for both case are the same, i.e.* $I_{DS} = 0.05\mu A$.

Appendix VI Chlorine Sensitivity of Diamond-H SGFETs

Without further analysis, here we present the output characteristic and transfer character of diamond-H SGFETs with various KCl concentrations, which shows a sensitivity to Cl^- ions. Also see for example, $I_{ds}vs.V_{gs}$ for $V_{ds}=0$ in Fig. 2 of reference [125]; this current is in fact a Faradaic (gate) current such as we discuss here!

However, the diamond-H SGFET is not stable in in high concentrated KCl solution. After a few runs, the device is broken with the conductive channel to be oxidized and yields no measurable conductance.

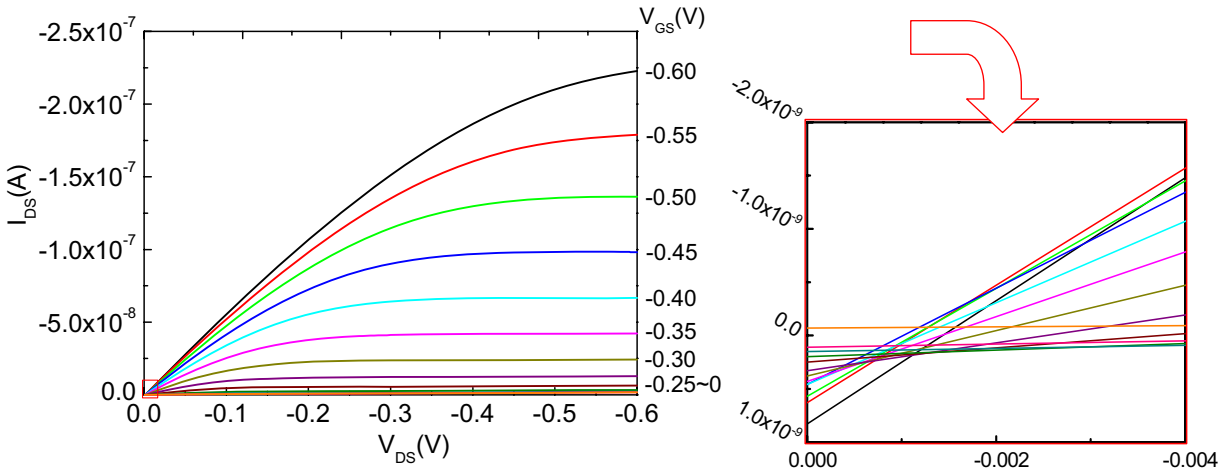

Figure a6 *Output characteristic of diamond-H SGFET with high concentrated KCl. (Buffer: pH7, 200mM KCl, 10mM PBS). There exist none-zero Drain-source current at* $V_{DS}=0$*, due to the leaking current from gate-source (shown in red square).*

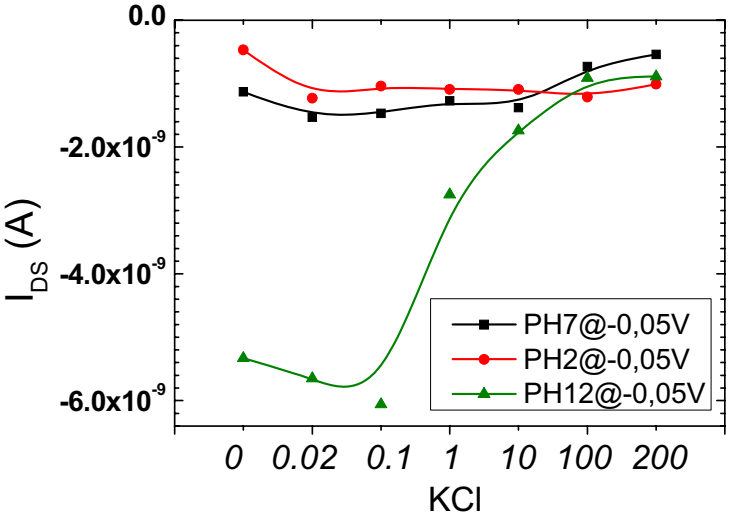

Figure a7 *Transfer characteristic of diamond-H SGFET with different KCl concentration and at buffer of different pH value. The drain-source voltage was fixed to be -0.05V.*

Appendix VII Evaluation of Electron and Hole Densities for Monolayer Graphene

The areal excess electron density n in the graphene, i.e. in the π* band above the Dirac energy, is found as a function of surface potential by integrating the Fermi-Dirac distribution function over the linearly increasing two-dimensional density of states:

$$n(\phi) = \int_0^\infty \frac{\kappa \cdot E}{1+\exp\left(\frac{E+\Phi}{kT}\right)}\,dE = \int_\Phi^\infty \kappa \cdot \frac{E-\phi}{1+\exp\left(\frac{E}{kT}\right)}\,dE \qquad \text{(a.12)}$$

where $\kappa = (1.18 \pm 0.06)\cdot 10^{14} cm^{-2} (eV)^{-2}$ is the slope of the two-dimensional density of states $D_G(E) = \kappa \cdot |E|$ of grapheme [175]. κ is linked via Planck's constant to the Fermi velocity v_F by $\kappa = 2/(\pi \hbar^2 {v_F}^2)$.

Following an approach taken before by Gerischer et al. for the analysis of capacitance data on graphite [177] , we evaluate (a.12) as follows:

The general expression for the areal or volume density of electrons in a system with two or three dimensional density of states $D(E)$ can be separated in three parts due to the symmetry of the Fermi-Dirac function $f(E) = [1+\exp(\beta E)]^{-1}$:

$$\int_{-\infty}^{\infty} D(E)\cdot f(E-E_F)\,dE = \int_{-\infty}^{E_F} D(E)\,dE + \int_{E_F}^{\infty} D(E)\cdot f(E-E_F)\,dE - \int_{-\infty}^{E_F} D(E)\cdot f(E_F-E)\,dE \quad .$$

(A1)

We will evaluate this for the areal electron density $n(\Phi, T)$ in graphene by choosing the origin of the energy axis to be the Fermi energy and by substituting $D(\mathrm{E}) = \kappa \cdot (E-\Phi)\cdot \Theta(E-\Phi)$ with the surface potential Φ as defined in the text and the Heavyside function $\Theta(E)$. We will separately discuss negative and positive sign of Φ.

Case 1, $\Phi \le 0$:

The first term on the left hand side of (A1) gives the trivial, temperature independent result $n_1 = \frac{1}{2}\kappa\,\Phi^2$. The second term gives

$$n_2 = \int_0^\infty \kappa \cdot (E-\Phi)\cdot [1+\exp(\beta E)]^{-1}\,dE \ ,$$

and the third term on the right hand side can be written as

$$n_3 = -\int_{\Phi}^{0} \kappa \cdot (E-\Phi) \cdot \left[1+\exp(-\beta E)\right]^{-1} dE = \int_{-\Phi}^{0} \kappa \cdot (-E-\Phi) \cdot \left[1+\exp(\beta E)\right]^{-1} dE$$

$$= \int_{0}^{-\Phi} \kappa \cdot (E+\Phi) \cdot \left[1+\exp(\beta E)\right]^{-1} dE$$

$$= \int_{0}^{\infty} \kappa \cdot (E+\Phi) \cdot \left[1+\exp(\beta E)\right]^{-1} dE - \int_{-\Phi}^{\infty} \kappa \cdot (E+\Phi) \cdot \left[1+\exp(\beta E)\right]^{-1} dE$$

Summing up n_2 and n_3 gives

$$n_2 + n_3 = 2\kappa \cdot \int_{0}^{\infty} E \cdot \left[1+\exp(-\beta E)\right]^{-1} dE$$

$$-\frac{\kappa}{\beta^2} \cdot \left\{ \int_{-\beta\Phi}^{\infty} t \cdot \left[1+\exp(t)\right]^{-1} dt + \beta\Phi \cdot \int_{-\beta\Phi}^{\infty} \left[1+\exp(t)\right]^{-1} dt \right\}$$

The first term on the right-hand-side is simply evaluated giving $2\alpha \cdot \kappa \cdot (kT)^2$ where the constant $\alpha = \pi^2/12$ and $kT = 1/\beta$ for the thermal energy have been inserted. The second term on the r.h.s. is further evaluated by discussing the expression in brackets as a function $h(y) = h(-\beta\Phi)$. Forming the derivative of h gives

$$\frac{dh}{dy} = -\frac{y}{1+\exp(y)} - \left\{ \int_{y}^{\infty} \left[1+\exp(t)\right]^{-1} dt - y \cdot \left[1+\exp(y)\right]^{-1} \right\}$$

$$= -\int_{y}^{\infty} \left[1+\exp(t)\right]^{-1} dt = -R(y)$$

From the definition of $h(y)$, the value for zero follows as $h(0) = \alpha$ so that $h(y) = \alpha - \int_{0}^{y} R(t)\, dt$, and the electron density $n_1 + n_2 + n_3$ can be summed up to give

$$\frac{n(\Phi,T)}{\kappa \cdot (kT^2)} = \alpha + \frac{1}{2}\left(\frac{\Phi}{kT}\right)^2 + \int_{0}^{-\frac{\Phi}{kT}} R(t)\, dt\,.$$

Case 2, $\Phi \geq 0$:

without using the separation of equation (A1), n can directly be written as

$$n = \int_{\Phi}^{\infty} \kappa \cdot (E-\Phi) \cdot \left[1+\exp(-\beta E)\right]^{-1} dE =$$

$$= \frac{\kappa}{\beta^2} \left\{ \int_{\beta\Phi}^{\infty} \beta E \cdot \left[1+\exp(-\beta E)\right]^{-1} d(\beta E) - \beta\phi \cdot \int_{\beta\Phi}^{\infty} \left[1+\exp(-\beta E)\right]^{-1} d(\beta E) \right\}$$

which is immediately recognized as $\kappa (kT)^2 \cdot h(\beta\Phi)$ so that

$$n = \kappa (kT)^2 \cdot h(\beta\Phi) = \kappa (kT)^2 \cdot \left[\alpha - \int_0^{\beta\Phi} R(t)\, dt \right].$$

Finally, the following expression can be obtained:

$$\frac{n(x)}{\kappa \cdot (kT)^2} = \alpha + \begin{cases} \frac{1}{2}x^2 + \int_0^{-x} R(t)\, dt & for\ x \le 0 \\ -\int_0^{x} R(t)\, dt & for\ x \ge 0 \end{cases} \qquad \text{(a.13)}$$

Here, $x = \Phi / (kT)$ is the surface potential in units of the thermal energy kT, $n_0 = \kappa \cdot (kT)^2$ is a natural unit for the areal charge carrier concentration of a single graphene layer which amounts to $7.4 \cdot 10^{10}\, cm^{-2}$ at room temperature, and $\alpha = \int_0^{\infty} \frac{u}{1+\exp(u)}\, du = \frac{\pi^2}{12} = 0{,}8225$.

$R(t) = \int_t^{\infty} \frac{1}{1+\exp(u)}\, du = \ln\left[1+\exp(-t)\right]$ is the Fermi residuum, for which $\exp(-t)$ is a strict upper limit that is approached asymptotically for positive argument. From the asymptotic limit required for equation (a.13), $\lim_{x\to\infty} n(x) = 0$, it is obvious that α can alternatively be expressed as the complete integral of the Fermi residuum, i.e. $\alpha = \int_0^{\infty}\int_t^{\infty} \frac{1}{1+\exp(u)}\, du\, dt = \int_0^{\infty} \frac{x}{1+\exp(x)}\, dx$. Note that the zero-temperature limit for the electron statistics would just give the parabolic term in equation (a.13), specifically it would yield a zero conductivity contribution of the electrons with the Fermi level at the Dirac point.

From the symmetry of the graphene density of states and the Fermi function it is straight forward to conclude $p(x) = n(-x)$ for the hole concentration as a function of (normalized) surface potential. Combining this with equation (a.13) yields

$$\frac{\Sigma_g(x)}{e \cdot \kappa \cdot (kT)^2} = \left[\frac{1}{2}x^2 + 2\int_0^{|x|} R(t)\, dt \right] \cdot sign(x) \qquad \text{(a.14)}$$

for the areal charge density Σ_g in the graphene layer, and

$$\frac{c(x)}{\kappa \cdot (kT)^2} = 2\alpha + \frac{1}{2}x^2 \qquad \text{(a.15)}$$

for the areal charge carrier concentration c=n+p in the graphene layer. Note that $\Sigma_g(x)$ and $c(x)$ are odd and even functions, respectively.

Appendix VIII In-Situ Electrochemistry-IR Study of Diamond Electrolyte Interface

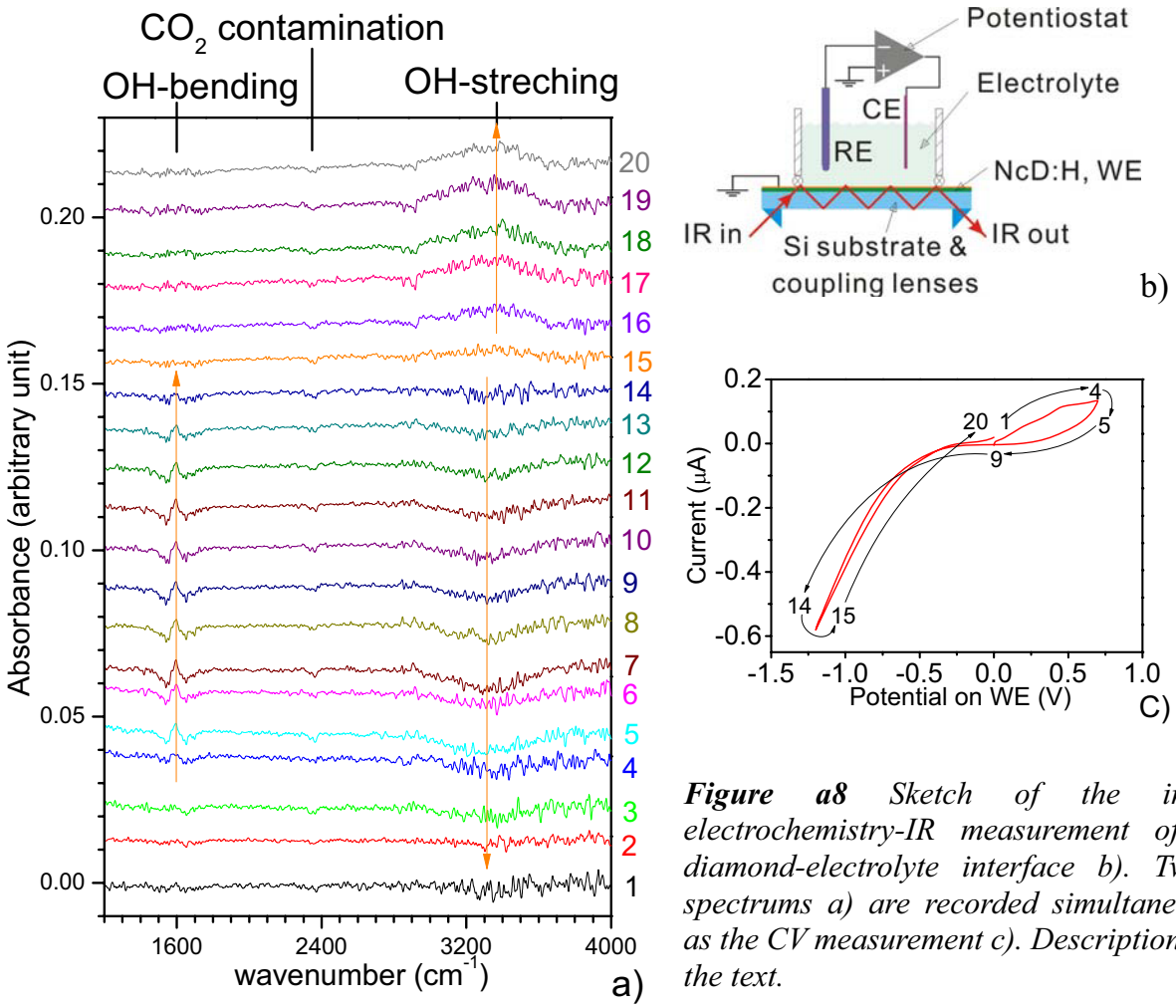

Figure a8 *Sketch of the in-situ electrochemistry-IR measurement of the diamond-electrolyte interface b). Twenty spectrums a) are recorded simultaneously as the CV measurement c). Description is in the text.*

A nanocrystal diamond film (ncD, ca. 200nm thick) on silicon substrate (0.5mm thick and 6mm in diameter) is used as the waveguide disk. The surface of the ncD is hydrogen terminated and served as working electrode (WE) (see Figure a8b, area of WE is 3.14mm^2). The electrolyte is standard buffer of pH 7, as described in section 3.3. The reference electrode (RE) and counter electrode (CE) are Ag/AgCl and platinum, respectively. The experiment is done inside a Teflon container, sealed by O-rings. Cyclic voltammetry (CV, Figure a8c) at a scan rate of 5mV/s is performed simultaneously as the attenuated total reflection infrared (ATR-IR) spectrum is collected. A mercury cadmium telluride (MCT, cooled by liquid nitrogen) detector is used in the ATR-IR measurement, at 4cm^{-1} resolution using at least 100 scans for averaging. Each of the spectrum shown in Figure a8a) is divided by the background, which is collected previously to CV measurements, i.e. without applying any potential on the working electrode.

References

1. JC Angus, N.G., DJ Poferl, SP Chauhan, TJ Dyble, P Sung. , Sin Almazy 3:38, presented at the International Conference on Applications of Synthetic Diamonds in Industry, Kiev, 1971.
2. Angus, J.C., et al., *Chemical Vapour Deposition of Diamond.* Philosophical Transactions: Physical Sciences and Engineering, 1993. **342**(1664): p. 195-208.
3. Landstrass, M.I. and K.V. Ravi, *Resistivity of chemical vapor deposited diamond films.* Applied Physics Letters, 1989. **55**(10): p. 975-977.
4. Landstrass, M.I. and K.V. Ravi, *Hydrogen passivation of electrically active defects in diamond.* Applied Physics Letters, 1989. **55**(14): p. 1391-1393.
5. Hayashi, K., et al., *Study of the effect of hydrogen on transport properties in chemical vapor deposited diamond films by Hall measurements.* Applied Physics Letters, 1996. **68**(3): p. 376-378.
6. Nebel, C.E., et al., *Hydrogen-induced transport properties of holes in diamond surface layers.* Applied Physics Letters, 2001. **79**(27): p. 4541-4543.
7. Kasap, S.O. and P. Capper, *Springer handbook of electronic and photonic materials*. 2006, Springer: New York. p. 551-557.
8. Noda, H., A. Hokazono, and H. Kawarada, *Device modeling of high performance diamond MESFETs using p-type surface semiconductive layers.* Diamond and Related Materials, 1997. **6**(5-7): p. 865-868.
9. Tsugawa, K., et al., *Application and device modeling of diamond FET using surface semiconductive layers*. 1998. p. 19-27.
10. Denisenko, A., et al., *Hypothesis on the conductivity mechanism in hydrogen terminated diamond films.* Diamond and Related Materials. **9**(3-6): p. 1138-1142.
11. Maier, F., et al., *Origin of surface conductivity in diamond.* Physical Review Letters, 2000. **85**(16): p. 3472-3475.
12. Gi, R.S., et al., *Hall Effect Measurements of Surface Conductive Layer on Undoped Diamond Films in NO2 and NH3 Atmospheres.* Jpn. J. Appl. Phys., 1999. **38**: p. 3492–3496.
13. Chakrapani, V., et al., *Charge transfer equilibria between diamond and an aqueous oxygen electrochemical redox couple.* Science, 2007. **318**(5855): p. 1424-1430.
14. Foord, J.S., et al., *Influence of material properties on the performance of diamond photocathodes.* Diamond and Related Materials, 2002. **11**(3-6): p. 437-441.
15. Mueller, R., A. Denisenko, and E. Kohn, *Effect of surface quality on ion sensitivity of H-terminated diamond.* Diamond and Related Materials. **12**(3-7): p. 554-559.
16. Strobel, P., et al., *Surface transfer doping of diamond.* Nature, 2004. **430**(6998): p. 439-441.
17. Strobel, P., et al., *Surface transfer doping of diamond by fullerene.* Diamond and Related Materials, 2005. **14**(3-7): p. 451-458.
18. Qi, D., et al., *Surface Transfer Doping of Diamond (100) by Tetrafluoro-tetracyanoquinodimethane.* Journal of the American Chemical Society,

2007. **129**(26): p. 8084-8085.
19. Novoselov, K.S., et al., *Electric Field Effect in Atomically Thin Carbon Films.* Science, 2004. **306**(5696): p. 666-669.
20. http://www.azonano.com/details.asp?ArticleID=2456.
21. Maier, F., et al., *Origin of Surface Conductivity in Diamond.* Physical Review Letters, 2000. **85**(16): p. 3472.
22. Gierz, I., et al., *Atomic Hole Doping of Graphene.* Nano Letters, 2008. **8**(12): p. 4603-4607.
23. Leenaerts, O., B. Partoens, and F.M. Peeters, *Adsorption of H2 O , N H3 , CO, N O2 , and NO on graphene: A first-principles study.* Physical Review B, 2008. **77**(12): p. 125416.
24. Wehling, T.O., et al., *Molecular Doping of Graphene.* Nano Letters, 2007. **8**(1): p. 173-177.
25. Wehling, T.O., M.I. Katsnelson, and A.I. Lichtenstein, *Adsorbates on graphene: Impurity states and electron scattering.* Chemical Physics Letters, 2009. **476**(4-6): p. 125-134.
26. Geim, A.K. and K.S. Novoselov, *The rise of graphene.* Nat Mater, 2007. **6**(3): p. 183-191.
27. Iijima, S., *Helical microtubules of graphitic carbon.* Nature, 1991. **354**(6348): p. 56-58.
28. Kroto, H.W., et al., *C60: Buckminsterfullerene.* Nature, 1985. **318**(6042): p. 162-163.
29. http://www.h-square.com.
30. Hart, H., L.E. Craine, and D.J. Hart, *Organic Chemistry: A Short Course*. 10th ed. 1999: Houghton Mifflin Harcourt (HMH).
31. Morgan, P., *Carbon fibers and their composites*. 2005: CRC.
32. Locher, M.W.a.R., *Growth and application of undoped and doped diamond films*. 1998. p. 1665.
33. Tarun Sharda, S.B., *Diamond Nanocrystals*, in *Encyclopedia of Nanoscience and Nanotechnology*, H.S.Nalwa, Editor. 2004, American Scientific Publishers. p. 337-370.
34. Adachi, S., *Properties of Group-IV, III-V and II-VI Semiconductors*. Materials for Electronic & Optoelectronic Applications. 2005: Wiley.
35. Lawrence S. Pan (Editor), D.R.K.E., *Diamond: Electronic Properties and Applications* Electronic Materials: Science & Technology. 1994: Springer.
36. Maier, F., J. Ristein, and L. Ley, *Electron affinity of plasma-hydrogenated and chemically oxidized diamond (100) surfaces.* Physical Review B, 2001. **64**(16): p. 165411.
37. http://www.siliconfareast.com/sigegaas.htm.
38. A.K.Ramdas, *Raman, Brillouin and infrared spectroscopy of phonons in conventional diamond*, in *Properties, Growth and Applications of Diamond (Emis Datareviews Series, 26)*, M.H. Nazare and A.J. Neves, Editors. 2000, The Institution of Engineering and Technology. p. 4.
39. Pan, L.S. and D.R. Kania, *Diamond: Electronic Properties and Applications* 1994, Springer.
40. Yu.V.Pleskov, et al., J.Electroanal.Chem., 1987. **228**: p. 19.
41. Fujishima, A., Y. Einaga, and T.N. Rao, *Diamond electrochemistry*. 2005: Elsevier

Science.
42. J.C.Angus, Y.V.Pleskov, and S.C.Eaton, *Chapter 3 Electrochemistry of Diamond*, in *Thin-film diamond II* C.E. Nebel and J. Ristein, Editors. 2004, Academic Press
43. Martin, H.B., et al., *Hydrogen and Oxygen Evolution on Boron-Doped Diamond Electrodes.* Journal of The Electrochemical Society, 1996. **143**(6): p. L133-L136.
44. Kawarada, H., et al., *Electrolyte-solution-gate FETs using diamond surface for biocompatible ion sensors.* Physica Status Solidi a-Applied Research, 2001. **185**(1): p. 79-83.
45. Nebel, C.E., et al., *Diamond for bio-sensor applications.* Journal of Physics D: Applied Physics, 2007. **40**(20): p. 6443-6466.
46. Yang, W., et al., *DNA-modified nanocrystalline diamond thin-films as stable, biologically active substrates.* Nat Mater, 2002. **1**(4): p. 253-257.
47. Hartl, A., et al., *Protein-modified nanocrystalline diamond thin films for biosensor applications.* Nat Mater, 2004. **3**(10): p. 736-742.
48. Davies, G., *Basic Properties of Diamond:Phonon Spectra, Thermal Properties, Band Structure*, in *CVD Diamond for Electronic Devices and Sensors*, R.S. Sussmann, Editor. 2009, John Wiley & Sons, Ltd. p. 3-28.
49. Saravia, L.R. and D. Brust, *Band Structure and Interband Optical Absorption in Diamond.* Physical Review, 1968. **170**(3): p. 683.
50. Nebel, C.E., B. Rezek, and A. Zrenner, *Electronic properties of the 2D-hole accumulation layer on hydrogen terminated diamond.* Diamond and Related Materials. **13**(11-12): p. 2031-2036.
51. Looi, H.J., R.B. Jackman, and J.S. Foord, *High carrier mobility in polycrystalline thin film diamond.* Applied Physics Letters, 1998. **72**(3): p. 353-355.
52. Bergveld, P., *Development of an Ion-Sensitive Solid State Device for Neurophysiological Measurements.* IEEE Transactions on Biomedical Engineering, 1970. **BME-17**: p. 70.
53. Kawarada, H., et al., *Electrolyte-Solution-Gate FETs Using Diamond Surface for Biocompatible Ion Sensors*. 2001. p. 79-83.
54. Song, K.-S., et al., *Label-free DNA sensors using ultrasensitive diamond field-effect transistors in solution.* Physical Review E, 2006. **74**(4): p. 041919.
55. Nebel, et al., *Diamond for bio-sensor applications*. 2007, Bristol, ROYAUME-UNI: Institute of Physics. 24.
56. Rezek, B., et al., *Intrinsic hydrogen-terminated diamond as ion-sensitive field effect transistor.* Sensors and Actuators B: Chemical, 2007. **122**(2): p. 596-599.
57. Garrido, J.A., et al., *pH sensors based on hydrogenated diamond surfaces.* Applied Physics Letters, 2005. **86**(7): p. 073504-3.
58. Kanazawa, H., et al., *Effect of iodide ions on the hydrogen-terminated and partially oxygen-terminated diamond surface.* Diamond and Related Materials. **12**(3-7): p. 618-622.
59. Garrido, J.A., et al., *The Surface Conductivity at the Diamond/Aqueous Electrolyte Interface.* Journal of the American Chemical Society, 2008. **130**(12): p. 4177-4181.
60. Haertl, A., et al., *The Ion Sensitivity of Surface Conductive Single Crystalline Diamond.* Journal of the American Chemical Society, 2007. **129**(5): p. 1287-1292.
61. Novoselov, K., *Graphene: Mind the gap.* Nat Mater, 2007. **6**(10): p. 720-721.
62. Berger, C., et al., *Ultrathin Epitaxial Graphite: 2D Electron Gas Properties and a Route toward Graphene-based Nanoelectronics.* The Journal of Physical Chemistry

B, 2004. **108**(52): p. 19912-19916.
63. Sutter, P.W., J.-I. Flege, and E.A. Sutter, *Epitaxial graphene on ruthenium.* Nat Mater, 2008. **7**(5): p. 406-411.
64. Pletikosic, I., et al., *Dirac Cones and Minigaps for Graphene on Ir(111).* Physical Review Letters, 2009. **102**(5): p. 056808-4.
65. Kim, K.S., et al., *Large-scale pattern growth of graphene films for stretchable transparent electrodes.* Nature, 2009. **457**(7230): p. 706-710.
66. Li, X., et al., *Large-Area Synthesis of High-Quality and Uniform Graphene Films on Copper Foils*. 2009. p. 1312-1314.
67. Choucair, M., P. Thordarson, and J.A. Stride, *Gram-scale production of graphene based on solvothermal synthesis and sonication.* Nat Nano, 2009. **4**(1): p. 30-33.
68. Kosynkin, D.V., et al., *Longitudinal unzipping of carbon nanotubes to form graphene nanoribbons.* Nature, 2009. **458**(7240): p. 872-876.
69. Jiao, L., et al., *Narrow graphene nanoribbons from carbon nanotubes.* Nature, 2009. **458**(7240): p. 877-880.
70. Meyer, J.C., et al., *Direct Imaging of Lattice Atoms and Topological Defects in Graphene Membranes.* Nano Letters, 2008. **8**(11): p. 3582-3586.
71. Seyller, T., et al., *Structural and electronic properties of graphite layers grown on SiC(0???).* Surface Science, 2006. **600**(18): p. 3906-3911.
72. Lauffer, P., et al., *Atomic and electronic structure of few-layer graphene on SiC(0001) studied with scanning tunneling microscopy and spectroscopy.* Physical Review B (Condensed Matter and Materials Physics), 2008. **77**(15): p. 155426-10.
73. Romero, H.E., et al., *n-Type Behavior of Graphene Supported on Si/SiO2 Substrates.* ACS Nano, 2008. **2**(10): p. 2037-2044.
74. Shishir, R.S. and D.K. Ferry, *Intrinsic mobility in graphene.* Journal of Physics-Condensed Matter, 2009. **21**(23): p. 4.
75. Castro Neto, A.H., et al., *The electronic properties of graphene.* Reviews of Modern Physics, 2009. **81**(1): p. 109-162.
76. Novoselov, K.S., et al. *Electronic properties of graphene*. 2007: Wiley-V C H Verlag Gmbh.
77. Czichos, H., T. Saito, and L. Smith, *Springer Handbook of Materials Measurement Methods*. 2006: Springer.
78. Pauw, L.J.v.d., *A method of measuring specific resistivity and Hall effect of discs of arbitrary shape*: Philips Res. Rep. 13, 1–9 (1958).
79. Popović, R.S., *Hall effect devices (2ed edition)*. 2003: Taylor & Francis.
80. Bertt, C.M.A. and A.M.O. Bertt, *Electrochemistry, principles, methods, and applications*. 1994: Oxford University Press. page 53.
81. Scholz, F., *Electroanalytical Methods, guid to experiments and applications*. 2002: Springer. page 5.
82. Grahame, D.C., *Electrode Processes and the Electrical Double Layer*. 1955. p. 337-358.
83. Bockris, J.O.M., M.A.V. Devanathan, and K. Muller, *On the Structure of Charged Interfaces.* Proceedings of the Royal Society of London. Series A, Mathematical and Physical Sciences, 1963. **274**(1356): p. 55-79.
84. Wieckowski, A., *Interfacial electrochemistry: theory, experiment, and applications* 1999: CRC. page 269.
85. www.chemistry.uoguelph.ca/educmat/chem7234.

86. Bard, A.J. and L.R. Faulkner, *Electrochemical Methods, Fundamentals and Applications*. 2001: John Wiley & Sons, Inc.
87. Kaesche, H., *Corrosion of Metals, Physicochemical Principles and Current Problems*. 2003: Springer.
88. John O'M. Bockris, Amulya K. N. Reddy, and M. Gamboa-Aldeco, *Modern electrochemistry, Volume 2*, Springer. p. 815-1057.
89. Emtsev, K.V., et al., *Towards wafer-size graphene layers by atmospheric pressure graphitization of silicon carbide.* Nat Mater, 2009. **8**(3): p. 203-207.
90. Rob Beynon & John Easterby, *Buffer solutions*. 2003: Taylor & Francis.
91. http://www.liv.ac.uk/buffers.
92. Kumashiro, Y., *Electric refractory materials*. 2000, CRC. p. 370.
93. NASA Earth Fact Sheet. (updated 19 April-19-2007) [cited; Available from: http://nssdc.gsfc.nasa.gov/planetary/factsheet/earthfact.html.
94. Foord, J.S., et al., *Influence of the environment on the surface conductivity of chemical vapor deposition diamond.* Diamond and Related Materials. **11**(3-6): p. 856-860.
95. Mueller, R., et al., *On the ion-sensitivity of H-terminated surface channel devices on diamond.* Diamond and Related Materials. **11**(3-6): p. 651-656.
96. Denisenko, A., A. Aleksov, and E. Kohn, *pH sensing by surface-doped diamond and effect of the diamond surface termination.* Diamond and Related Materials. **10**(3-7): p. 667-672.
97. Song, K.-S., et al., *pH-sensitive diamond field-effect transistors (FETs) with directly aminated channel surface.* Analytica Chimica Acta, 2006. **573-574**: p. 3-8.
98. B. Rezek, H.W., D. Shin, T. Yamamoto, C.E. Nebel, , Diam. Rel. Mat., 2006. **15**: p. 673.
99. Nebel, C.E., et al., *Surface electronic properties of H-terminated diamond in contact with adsorbates and electrolytes*. 2006. p. 3273-3298.
100. Kubovic, A., et al., *Electronic surface barrier characteristics of H-terminated and surface conductive diamond.* Diamond and Related Materials. **13**(4-8): p. 755-760.
101. Schedin, F., et al., *Detection of individual gas molecules adsorbed on graphene.* Nat Mater, 2007. **6**(9): p. 652-655.
102. Leenaerts, O., B. Partoens, and F.M. Peeters, *Paramagnetic adsorbates on graphene: A charge transfer analysis.* Applied Physics Letters, 2008. **92**(24): p. 243125-3.
103. Qazi, M., T. Vogt, and G. Koley, *Trace gas detection using nanostructured graphite layers.* Applied Physics Letters, 2007. **91**(23): p. 233101-3.
104. Fowler, J.D., et al., *Practical Chemical Sensors from Chemically Derived Graphene.* ACS Nano, 2009. **3**(2): p. 301-306.
105. Ganhua, L. and et al., *Reduced graphene oxide for room-temperature gas sensors.* Nanotechnology, 2009. **20**(44): p. 445502.
106. Lu, G., L.E. Ocola, and J. Chen, *Gas detection using low-temperature reduced graphene oxide sheets.* Applied Physics Letters, 2009. **94**(8): p. 083111-3.
107. Dan, Y., et al., *Intrinsic Response of Graphene Vapor Sensors.* Nano Letters, 2009. **9**(4): p. 1472-1475.
108. Jung, I., et al., *Effect of Water Vapor on Electrical Properties of Individual Reduced Graphene Oxide Sheets.* The Journal of Physical Chemistry C, 2008. **112**(51): p. 20264-20268.

109. Hugo, E.R. and et al., *Adsorption of ammonia on graphene.* Nanotechnology, 2009. **20**(24): p. 245501.
110. Hwang, E.H., S. Adam, and S. Das Sarma, *Transport in chemically doped graphene in the presence of adsorbed molecules.* Physical Review B, 2007. **76**(19): p. 195421.
111. http://www.inchem.org/documents/icsc/icsc/eics0215.htm.
112. http://www.solvaychlorinatedinorganics.com/.
113. Lee, E.J.H., et al., *Contact and edge effects in graphene devices.* Nature Nanotechnology, 2008. **3**(8): p. 486-490.
114. Chattaraj, P.K., in *Chemical Reactivity Theory: A Density Functional View*. 2009, CRC Press. p. 546-547.
115. Peter Atkins and J.d. Paula, *ATKINS' Physical Chemistry, Seventh Edition*. 2002: Oxford university press.
116. Connors, K.A., *Chemical Kinetics: The Study of Reaction Rates in Solution*. 1990: Wiley-VCH.
117. Ristein, J., *Surface transfer doping of diamond.* Journal of Physics D-Applied Physics, 2006. **39**(4): p. R71-R81.
118. Wakihara, M. and O. Yamamoto, *Lithium ion batteries: fundamentals and performance*. 1999: Wiley-VCH
119. Pinto, H., et al., *p-type doping of graphene with F4-TCNQ.* Journal of Physics-Condensed Matter, 2009. **21**(40): p. 3.
120. Giovannetti, G., et al., *Doping Graphene with Metal Contacts.* Physical Review Letters, 2008. **101**(2): p. 026803.
121. Rubinstein, I., *chapter 1*, in *Physical electrochemistry: principles, methods, and applications*. 1995, CRC.
122. Gileadi, E., *Electrode Kinetics for Chemists, Chemical Engineers and Materials Scientists*. 1993, Wiley-VCH p. 9.
123. A. Härtl, J.A.G., S. Nowy, R. Zimmermann, C. Werner, D. Horinek, R. Netz, and M. Stutzmann, , J. Am. Chem. Soc. , 2007. **129**: p. 1287.
124. T. Sakai, K.-S.S., H. Kanazawa, Y. Nakamura, H. Umezawa, M. Tachiki, H. Kawarada, , Diam. Rel. Mat., 2003. **12**: p. 1971.
125. H. Kanazawa , K.-S.S., T. Sakai, Y. Nakamura, H. Umezawa, M. Tachiki and H. Kawarada, , Diam. Rel. Mat., 2003. **12**: p. 618.
126. D.C. Grahame, Chem. Rev. , 1947. **41**: p. 441.
127. Zhang, W.Y., J. Ristein, and L. Ley, *Hydrogen-terminated diamond electrodes. II. Redox activity.* Physical Review E, 2008. **78**(4): p. 11.
128. L.L. Shreir, R.A.J., G.T. Burstein, *Corrosion (3rd ed.), Volume 1: Metal/Environment Reactions,*. 1994, Butterworth-Heinemann. p. 1:92 - 1:113.
129. U. R. Evans and T. P. Hoar, Trans. Faraday Soc., 1934. **30**: p. 424.
130. M. Stern and A. L. Geary, J. Electrochem. Soc., 1957. **104**: p. 56.
131. R. Memming, *Semiconductor Electrochemistry*. 2001, Wiley VCH, Weinheim. p. 155.
132. K. Kinoshita, *Electrochemical Oxygen Technology,*. 1992, Wiley-Interscience p. 36-38
133. H.Kaesche, *Corrosion of Metals: Physicochemical Principles and Current Problems*. 2003, Springer, Berlin. p. 92.
134. jr., D.A.W.a.N.L.G., J. Chem. Eng. Data, (1979). **24**: p. 356.

135. D.A. Wiesenburg , N.L.G.j., J. Chem. Eng. Data (1979). **24**: p. 356.
136. D.M. Himmelblau, Chem. Rev. , 1964. **64**: p. 527
137. Vijayamohanan, K., A.K. Shukla, and S. Sathyanarayana, *Open-circuit potential-time transients of alkaline porous iron electrodes at various states-of-charge.* Electrochimica Acta, 1991. **36**(2): p. 369-380.
138. Formaro, L. and S. Trasatti, *Capacitance measurements on platinum electrodes for the estimation of organic impurities in water.* Analytical Chemistry, 1968. **40**(7): p. 1060-1067.
139. Sze, S.M. and K.K. Ng, *Physics of Semiconductor Devices , 3 edition*. 2006: Wiley-Interscience.
140. Ellinger, F., *Radio Frequency Integrated Circuits and Technologies*. 2007, Springer. p. 119-164.
141. Ayers, J.E., *Digital integrated circuits analysis and design*. 2005: CRC press.
142. Anderson, B.L. and R. L.Anderson, *Fundamentals of Semiconductor Devices*. 2005: McGraw-Hill Companies, Inc.
143. Zeghbroeck, B.V., *Pinciples of Semiconductor Devices*. 2007: http://ecee.colorado.edu/~bart/book.
144. Pierret, R.F., *Field Effect Devices (2nd Edition)* 1990: Prentice Hall.
145. Carey, E. and S. Lidholm, *Millimeter-Wave Integrated Circuits*. 2004: Springer.
146. Khatibzadeh, M.A. and R.J. Trew, *A large-signal, analytic model for the GaAs MESFET.* Microwave Theory and Techniques, IEEE Transactions on, 1988. **36**(2): p. 231-238.
147. Feng, Y.K. and K. Schemann, *Two-dimensional simulation of sub-[mu]m GaAs MESFETs with ion-implanted doping.* Solid-State Electronics, 1989. **32**(12): p. 1719-1722.
148. Bergveld, P., *Thirty years of ISFETOLOGY: What happened in the past 30 years and what may happen in the next 30 years.* Sensors and Actuators B: Chemical, 2003. **88**(1): p. 1-20.
149. Bergveld, P., *ISFET, Theory and Practice*. 2003: IEEE Sensor Conference in Toronto
150. Tsai, W., et al., *Diamond MESFET using ultrashallow RTP boron doping.* Electron Device Letters, IEEE, 1991. **12**(4): p. 157-159.
151. Trew, R.J., J.B. Yan, and P.M. Mock, *The potential of diamond and SiC electronic devices for microwave and millimeter-wave power applications.* Proceedings of the IEEE, 1991. **79**(5): p. 598-620.
152. Yasar Gurbuz , O.E., Ibrahim Tekin , Weng P. Kang, Jimmy L. Davidson, *Diamond semiconductor technology for RF device applications.* Solid-State Electronics, 2005. **49**: p. 1055–1070.
153. Shiomi, H., Y. Nishibayashi, and N. Fujimori, *Field-Effect Transistors using Boron-Doped Diamond Epitaxial Films.* Japanese Journal of Applied Physics, 1989. **28**(Part 2, No. 12): p. L2153.
154. Kawarada, H., *Hydrogen-terminated diamond surfaces and interfaces.* Surface Science Reports, 1996. **26**(7): p. 205-206.
155. Hokazono, A., et al., *Enhancement/depletion MESFETs of diamond and their logic circuits.* Diamond and Related Materials, 1997. **6**(2-4): p. 339-343.
156. M. Kubovic, A.A., M. Schreck, Th. Bauer, B. Stritzker, E. Kohn, *Field effect transistor fabricated on hydrogen-terminated diamond grown on SrTiO3 substrate*

and iridium buffer layer. Diamond and Related Materials, 2003. **12**: p. 403–407.
157. M. Kasu, K.U., Y. Yamauchi, and T. Makimoto, *Gate capacitance-voltage characteristics of submicron-long-gate diamond field-effect transistors with hydrogen surface termination.* Applied Physics Letters, 2007. **90**: p. 043509.
158. K. Tsugawa, K.K., H. Noda, A. Hokazono, K. Hirose, M. Tajima, H. Kawarada, *High-performance diamond surface-channel field-effect transistors and their operation mechanism.* Diamond and Related Materials, 1999. **8**: p. 927-933.
159. Kimura, K., et al., *Hydrogen depth-profiling in chemical-vapor-deposited diamond films by high-resolution elastic recoil detection.* Applied Physics Letters, 2001. **78**(12): p. 1679-1681.
160. Shockley, W., *A Unipolar Field Effect Transistor.* Proc. IRE, Nov. 1952. **40**: p. 1365-1376.
161. Tsugawa, K., et al., *Schottky barrier heights, carrier density, and negative electron affinity of hydrogen-terminated diamond.* Physical Review B, 2010. **81**(4): p. 045303.
162. C.E. Nebel and J. Ristein, *Thin-Film Diamond II, Semiconductors and Semimetals*. 2004, Elsevier/Academic Press,.
163. Koizumi, S., C. Nebel, and M. Nesladek, *Physics and Applications of CVD Diamond*. 2008: Wiley-VCH.
164. Poh, W.C., et al., *Biosensing Properties of Diamond and Carbon Nanotubes.* Langmuir, 2004. **20**(13): p. 5484-5492.
165. DasA, et al., *Monitoring dopants by Raman scattering in an electrochemically top-gated graphene transistor.* Nat Nano, 2008. **3**(4): p. 210-215.
166. Ang, P.K., et al., *Solution-Gated Epitaxial Graphene as pH Sensor.* Journal of the American Chemical Society, 2008. **130**(44): p. 14392-14393.
167. Ohno, Y., et al., *Electrolyte-Gated Graphene Field-Effect Transistors for Detecting pH and Protein Adsorption.* Nano Letters, 2009. **9**(9): p. 3318-3322.
168. Jose A. Garrido, A.H., Stefan Kuch, and Martin Stutzmann, Oliver A. Williams and R. B. Jackmann,, Appl. Phys. Lett. , (2005). **86**: p. 073504.
169. H. Kanazawa, K.S.S., T. Sakai, Y. Nakamura, H. Umezawa, M. Tachiki, H. Kawarada, , Diam. Relat. Mater., (2003). **12**: p. 618.
170. Andreas Härtl, J.A.G., Stefan Nowy, Ralf Zimmermann, Carsten Werner, Dominik Horinek, Roland Netz, and Martin Stutzmann,, J. Am. Chem. Soc. , (2007). **129**: p. 1287.
171. A. Dankerl, A.R., M. Stutzmann and J.A. Garrido,, phys. stat. sol. (RRL) (2008). **2**: p. 31.
172. M. Dankerl, A.R., M. Stutzmann, and J.A. Garrido, , phys. stat. sol. (RRL), 2008. **2**(31).
173. Ristein, J., W. Zhang, and L. Ley, *Hydrogen-terminated diamond electrodes. I. Charges, potentials, and energies.* Physical Review E, 2008. **78**(4): p. 8.
174. Seyller, T., et al., *Schottky barrier between 6H-SiC and graphite: Implications for metal/SiC contact formation.* Applied Physics Letters, 2006. **88**(24): p. 242103-3.
175. Ohta, T., et al., *Interlayer Interaction and Electronic Screening in Multilayer Graphene Investigated with Angle-Resolved Photoemission Spectroscopy.* Physical Review Letters, 2007. **98**(20): p. 206802-4.
176. Emtsev, K.V., et al., *Interaction, growth, and ordering of epitaxial graphene on SiC{0001} surfaces: A comparative photoelectron spectroscopy study.* Physical

Review B (Condensed Matter and Materials Physics), 2008. **77**(15): p. 155303-10.
177. Gerischer, H., et al., *Density of the electronic states of graphite: derivation from differential capacitance measurements.* The Journal of Physical Chemistry, 1987. **91**(7): p. 1930-1935.
178. T. Kondo, K.H., D. A. Tryk, A. Fujishima, Elctrochimica Acta, 2003. **48**: p. 2739.
179. J. A. Garrido, S.N., A. Härtl, and M. Stutzmann,, Langmuir 2008. **24**: p. 3897.
180. Zhihong, C. and J. Appenzeller. *Mobility extraction and quantum capacitance impact in high performance graphene field-effect transistor devices*. in *Electron Devices Meeting, 2008. IEDM 2008. IEEE International*. 2008.
181. Ganguly, J., *Thermodynamics in earth and planetary sciences*. 2008, Springer. p. 396-403.

Acknowledgement

It is a pleasure to express my gratitude to those who made this thesis possible:

I am heartily thankful to my supervisor, **Prof. Jürgen Ristein**, for his abundantly assistance and invaluable guidance. I am really impressed by his deep insight in scientific research, accuracy and insistence for the truth under the phenomenon. I have learned from him experimental skills and procedure on solving problem during my study. I have also learned from him to be more patient and precise. I appreciate his understanding and the influential discussions that helped me pass the hard time, especially his novel view in quantum mechanics and statistical physics. I am grateful for his ideas in this thesis and helping me modify the content, correct many errors and translate the summary into German. Without his patience and inspiration, this thesis can't be finished.

I would like to express my deepest gratitude to **Prof. Lothar Ley**. During my phD study, he has helped me to see life and science in their full depth. He has enlightened me through his wide knowledge and his deep intuitions about where it should go and what is necessary to get there. He always has good ideas. I am very impressed by his passion for scientific research. His encouragement, guidance and support from the initial to the final level enabled me to develop an understanding of the subject. His interesting lecture on semiconductor and solid state physics, his guidance, wisdom and excellent advice throughout my study will embed in my memory about the time of phD study.

I would like to express my gratitude to **Prof. Patrik Schmuki** for his time and efforts in judging my thesis.

It was a pleasure to share doctoral studies and life with wonderful colleagues in Lehrstuhl für Technische Physik. I would like to thank **Prof. Martin Hundhausen**, and **Prof. Thomas Seyller** for their scientific and organization matters. I would like to thank **Florian Speck**, **Markus Ostler**, and **Felix Fromm** for preparing the graphene samples. I really appreciate the kind support and understanding from many former and present colleges in the institute: **Peter Wehrfritz**, **Jonas Röhrl**, **Roland Püsche**, **Ellen Fischermeier**, **Daniel Niesner**, **Kunyuan Gao** and **PD Dr. Ralf Graupner**. My special thanks go to **Peter Geithner**, **Paul Strobel**, and **Peter Lauffer** for their kindness and efforts in assistance and encouragement.

I would like to express my sincere thanks to the friendly people in mechanical workshop and electronic workshop of the physics department. I appreciate **Mr. Gerhard Schlosser** and our secretary, **Jutta Zintchenko**, for their kindness help.

I would like to show my gratitude to the colleagues in DRIVE project, especially **Carsten Pietzka**, **Dr.Jose Garrido** for the introduction to me electrochemistry.

Finally, none of this would have been possible without the love and support from my family. I can't express my love and gratitude to them in short sentences.

Thank you all for your support and with all the Best wishes!

Curriculum Vitae

Personal

Name	Wenying Zhang
Birth date	24, Sept. 1980
Birth place	Foshan, Guangdong Province, P.R.China
Present address	Schwabacher Str. 35, 90762 Fürth (BAY) Germany

Education

1988-1994	Diejiao Elementary School in Foshan, China
1994-1997	Diejiao Middle School in Foshan, China
1997-2000	Guihua High School in Foshan, China Certificate of college study
2000-2004	Undergraduate study in Materials Science and Engineering Materials Engineering Department Southwest Jiaotong University, Chengdu, China Bachelor's Thesis "Fabrication and Tribological Characterization of Multilayer Diamond-like Carbon Coatings Prepared by Filtered Cathodic Vacuum Arc Technology" Bachelorship
2004-2005	Graduate study in Materials for Microelectronics (MATMIC) Department Metallurgy and Materials Engineering Katholieke Universiteit Leuven, Leuven, Belgium Master's Thesis "Wear Behavior of Diamond-like Carbon Coatings at Clevated Temperature" Mastership
since 2005	phD study Lehrstuhl für Technische Physik, Institut für Physik der Kondensierten Materie, Friedrich-Alexander Universität Erlangen-Nürnberg, Germany